Living Experiences, Updating Memories: on the Role of Parvalbumin Interneurons in the Dentate Gyrus

Doctoral Thesis presented by

Elena Pérez Montoyo

- 2024 –

Thesis Director:

Dr. Santiago Canals Gamoneda

PhD Program in Neuroscience

Universidad Miguel Hernández de Elche

Instituto de Neurociencias

INSTITUTO DE NEUROCIENCIAS

UNIVERSITAS Miguel Hernández

La presente Tesis Doctoral, titulada *"Living experiences, updating memories: on the role of parvalbumin interneurons in the Dentate Gyrus"*, se presenta bajo la modalidad de tesis convencional con el siguiente criterio de calidad:

López-Madrona, V.J., Pérez-Montoyo, E., Álvarez-Salvado, E., Moratal, D., Herreras, O., Pereda, E., Mirasso, C.R & Canals, S. (2020). Different theta frameworks coexist in the rat hippocampus and are coordinated during memory-guided and novelty tasks. eLife 9:e57313. https://doi.org/10.7554/eLife.57313

Dr. D. Santiago Canals Gamoneda, director de la Tesis Doctoral titulada *"Living experiences, updating memories: on the role of parvalbumin interneurons in the dentate gyrus"*,

AUTORIZO

La presentación de la Tesis Doctoral *"Living experiences, updating memories: on the role of parvalbumin interneurons in the dentate gyrus"* realizada por Dª Elena Pérez Montoyo bajo mi inmediata dirección y supervisión como director de su Tesis Doctoral en el Instituto de Neurociencias (UMH-CSIC) y que presenta para la obtención del grado de Doctor por la Universidad Miguel Hernández.

Y para que conste, a los efectos oportunos, firmo el presente certificado.

Dr. Santiago Canals Gamoneda

La Dra. Dña. Mª Cruz Morenilla Palao, Coordinadora del Programa de Doctorado en Neurociencias del Instituto de Neurociencias de Alicante, centroid mixto de la Universidad Miguel Hernández (UMH) y de la Agencia Estatal Consejo Superior de Investigaciones Científicas (CSIC),

CERTIFICO:

Que D./Dña. Elena Pérez Montoyo ha realizado bajo la supervisión de nuestro Programa de Doctorado el trabajo titulado *"Living experiences, updating memories: on the role of parvalbumin interneurons in the dentate gyrus"* conforme a los términos y condiciones definidos en su Plan de Investigación y de acuerdo al Código de Buenas Prácticas de la Universidad Miguel Hernández de Elche, cumpliendo los objetivos previstos de forma satisfactoria para su defensa pública como tesis doctoral.

Y para que conste, a los efectos oportunos, firmo el presente certificado.

Dra. Dña. Mª Cruz Morenilla Palao

Coordinadora del Programa de Doctorado en Neurociencias

The Doctoral thesis entitled "*Living experiences, updating memories: on the role of parvalbumin interneurons in the dentate gyrus*" carried out by Elena Pérez Montoyo in the Instituto de Neurociencias de Alicante (UMH/CSIC), has been supported by a ValI+D grant from the Generalitat Valenciana, Consellería de Educación, Investigación, Cultura y Deporte, with reference ACIF/2016/110.

A *Papá*

"Like the entomologist hunting for brightly colored butterflies,
my attention was drawn to the flower garden of the grey matter,
which contained cells with delicate and elegant forms,
the mysterious butterflies of the soul,
the beating of whose wings may someday (who knows?)
clarify the secret of mental life."

Santiago Ramón y Cajal

INDEX

LIST OF ABBREVIATIONS

AI	Artificial intelligence
AMPA	α-amino-3-hydroxy-5-methyl-4-isoxazolepropionic acid
AP	Antero-posterior axis
BOLD	Blood-oxygen-level dependent
CA1/2/3	Cornu ammonis region 1/2/3
CaM	Calmodulin (calcium-binding protein)
CFC	Cross-frequency coupling
ChR2	Channelrhodopsin-2
CNO	Clozapine-N-oxide
DAPI	4′,6-diamidino-2-phenylindole
DG	Dentate gyrus
DI	Discrimination ratio
DREADD	Designer receptor exclusively activated by designer drugs
DV	Dorso-ventral axis
E/I	Excitation/Inhibition
EC	Entorhinal cortex
fMRI	Functional magnetic resonance imaging
fps	Frames per second
GABA	Gamma-aminobutyric acid
GC	Granule cell
GCaMP	GECI based on GFP, CaM and M13 peptide sequence
GECI	Genetically encoded calcium indicators
GFP	Green fluorescence protein
i.p.	Intraperitoneal
ICA	Independent component analysis
ITI	Inter-trial interval
LEC	Lateral entorhinal cortex
LFP	Local field potential
LM	Latero-medial axis
LTD	Long-term depression
LTM	Long-term memory

LTP	Long-term potentiation
MEC	Medial entorhinal cortex
MIP	Multiple Input Patterns task
NAc	Nucleus accumbens
NMDA	N-methyl-D-aspartate
NOL	Novel object location
NOR	Novel object recognition
PBS	Phosphate-buffered saline
PETH	Peri-Exploration Time Histogram
PFA	Paraformaldehyde
PFC	Prefrontal cortex
PP	Perforant pathway
PSTH	Peri-Stimulus Time Histogram
PV	Parvalbumin
PV-Gi	PV-Cre mice injected with hiM4 DREADD
PV-Gq	PV-Cre mice injected with hqM3 DREADD
ROI	Region of interest
s.c.	Subcutaneous
SDT	Social discrimination task
SST	Somatostatin
STM	Short-term memory
th	Threshold
VTA	Ventral tegmental area
WT	Wild-type

LIST OF FIGURES AND TABLES

I. INTRODUCTION

III. METHODS

IV. RESULTS

V. DISCUSION

ABSTRACT

Episodic memories contain information about our daily personal experiences and define who we are and how we perceive the world around us. The storage and retrieval of such information is known to be distributed across different brain regions. This distribution of memory formation involves the linking of the separated neuronal ensembles, but how the brain orchestrates this coordinated activity within the memory network is still an unresolved question. This thesis delves into the complex mechanisms of episodic memory, exploring how the brain encodes new information and updates previously consolidated memories. Focusing on the hippocampal dentate gyrus (DG), known for local conjunctive encoding of multimodal inputs ("local binding"), we propose that it also orchestrates a systems-level coordination of the distributed brain regions ("long-range binding"), allowing for memory formation. We hypothesize that local and transient periods of DG disinhibition, mainly mediated by parvalbumin (PV) interneurons, contribute to enhanced long-range functional connectivity within the memory network.

To unravel the specific role of PV interneurons in memory processes, we employed behavioral assays alongside pharmacogenetic manipulations or calcium-based monitoring of neuronal activity. Additionally, we have developed the MATLAB-based RodEx tool that facilitates the automatic quantification of rodent exploratory behaviors, refining behavioral analysis and improving its interpretation.

Firstly, experiments using DREADDs to upregulate (PV-Gq mice) or downregulate (PV-Gi mice) the activity of DG-PV interneurons in the dorsal hippocampus during memory encoding reveal a restricted impact on spatial components of episodic memory, leaving object and social recognition largely unaffected. We found that the level PV activity has a key role determining the threshold to discriminate subtle changes in the environment, where lower or higher levels of PV inhibition directly improving or impairing, respectively, spatial pattern separation. However, a relevant finding was that the improved spatial memory encoding provided by DG disinhibition, came at the expense of reduced memory capacity.

In a following set of experiments, we used fiber photometry recordings of GCaMP6s-expressing PV interneurons to study the dynamics of these inhibitory neurons in memory-related processes. We found reduced PV activity during Mismatch Novelty task, in good

agreement with a role of these interneurons in detecting contextual novelty and updating the existing memory base.

In summary, our findings shed light on the intricate role of DG-PV interneurons in encoding spatial information and updating contextual memories, suggesting an optimal range for PV inhibition-disinhibition interplay that enables the formation of stable memory traces without compromising their flexibility for subsequent reconsolidation processes.

RESUMEN

La memoria episódica contiene información sobre nuestras experiencias personales y definen quiénes somos y cómo percibimos el mundo que nos rodea. Se sabe que el almacenamiento y la recuperación de esta información se distribuyen en diferentes regiones cerebrales. Esta distribución de la memoria implica la conexión de conjuntos neuronales separados, pero cómo el cerebro coordina esta actividad dentro de la red de memoria sigue siendo una pregunta sin resolver. Esta tesis profundiza en los mecanismos complejos de la memoria episódica, explorando cómo el cerebro codifica nueva información y actualiza memorias previamente consolidadas. Centrándonos en el giro dentado del hipocampo (DG), conocido por la codificación conjuntiva local de inputs multimodales ("unión local"), proponemos que también es responsable de una coordinación a nivel de sistemas de las regiones cerebrales distribuidas ("unión global"), permitiendo la formación de memoria. Hipotetizamos que los períodos locales y transitorios de desinhibición del DG, principalmente mediados por interneuronas parvalbúmina (PV), contribuyen a una mayor conectividad funcional a larga distancia dentro de la red de memoria.

Para desentrañar el papel específico de las interneuronas PV en los procesos de memoria, utilizamos ensayos conductuales junto con manipulaciones farmacogenéticas o monitorización de la actividad neuronal basada en calcio. Además, hemos desarrollado la herramienta RodEx basada en MATLAB que facilita la cuantificación automática de los comportamientos exploratorios de roedores, refinando el análisis conductual y mejorando su interpretación.

En primer lugar, los experimentos utilizando DREADDs para aumentar (ratones PV-Gq) o disminuir (ratones PV-Gi) la actividad de las interneuronas PV del DG en el hipocampo dorsal durante la codificación de la memoria revelan un impacto específico sobre el componente espacial de la memoria (“dónde”), dejando en gran medida intacta la memoria no espacial, como es el reconocimiento de objetos (“qué”) o de estímulos sociales (“quién”). Descubrimos que el nivel de actividad de PV tiene un papel clave en determinar el umbral para discriminar cambios sutiles en el entorno, donde niveles más bajos o más altos de inhibición de PV mejoran o perjudican, respectivamente, la separación espacial de patrones. Sin embargo, un hallazgo relevante fue que la mejora en

la codificación de la memoria espacial proporcionada por la desinhibición del DG se produjo a expensas de una capacidad de memoria reducida.

En segundo lugar, realizamos registros de actividad neuronal basada en calcio mediante técnicas de fotometría, expresando el sensor GCaMP6s en las interneuronas PV para estudiar la dinámica de estas neuronas inhibitorias en procesos relacionados con la memoria. Encontramos una reducción de la actividad de PV durante una tarea de Novedad de Desajuste, de acuerdo con un papel de estas interneuronas en la detección de novedades contextuales y la actualización de la base de memoria existente.

En resumen, nuestros hallazgos arrojan luz sobre el papel de las interneuronas PV del DG en la codificación de información espacial y la actualización de memorias contextuales, sugiriendo un rango óptimo para la interacción de la inhibición-desinhibición de PV que permite la formación de representaciones de memoria estables sin comprometer su flexibilidad para procesos posteriores de reconsolidación.

I. INTRODUCTION

1.1. Brief overview of memory research

Memory is a complex and fascinating phenomenon of human cognition, defined as the ability of our brains to store and later remember vast amounts of information. Yet, memory retains a selective and finite resource, leading us to preserve merely a fraction of what we encounter in the continuous influx of daily experiences. Despite the considerable research studying the underlying mechanisms, how memories are formed and stored for long periods of time remains a significant and unresolved question.

Historically, the interest in understanding how memories are stored in our brains dates back to the late 19th century, when Herman Ebbinghaus (1885) pioneered the experimental study of learning and forgetting processes. He introduced the concept of serial position effects, showing the propensity to remember information at the beginning (*primacy effect*) or end (*recency effect*) of a series, while often forgetting what lies in between. Another significant contribution was made by William James in his book "The Principles of Psychology" (James, 1890), distinguishing between primary and secondary memory, concepts that are now referred to as short- and long-term memory, respectively.

The first half of the 20th century witnessed remarkable contributions to the understanding of associative learning, laying a solid foundation for this field. Behaviorists like Pavlov (1927) and Skinner (1938) elucidated *classical* and *operant conditioning*, respectively, emphasizing the role of associations and consequences in learning. Under a more cognitive perspective, Tolman (1948) introduced the concept of a *cognitive map*, an internal representation of the external environment that individuals can develop and remember without the need for immediate reinforcement or consequences, highlighting the role of mental processes in learning and memory formation.

However, it was in the second half of the 20th century, primarily through studies involving amnesic and brain-damaged patients, that memory research made significant breakthroughs. One of the most revolutionary cases was that of patient Henry Molaison, commonly known as H.M. (Scoville and Milner, 1957). Due to the severe epilepsy that H.M. suffered, he underwent surgery to remove the epileptogenic locus. The removal of both hippocampi resulted in a substantial reduction of the epilepsy but a significant

inability to form new memories. Remarkably, he retained the ability to recall past experiences and learn new motor skills without conscious awareness.

This was one of the seminal studies that paved the way for the classification of different types of memory relying on different brain regions. Depending on the nature of what is being learnt, memory can be categorized into two main types. On the one hand, non-declarative memory encompasses learned skills and habits (*procedural* memory) and conditioned responses typically acquired and expressed without conscious awareness (Cohen and Squire, 1980; Tulving, 1972). On the other hand, declarative memory includes memory for concepts or facts (*semantic* memory) and memory for personal experiences or events (called *episodic* memory). Particularly, episodic memory has been widely studied in humans as well as rodents, where extensive behavioral research has demonstrated that rats and mice are able to remember "what" happened, "where" it happened and "when" such an event occurred (Barbosa and Castelo-Branco, 2022; Dere et al., 2005; Eichenbaum and Fortin, 2005; Fellini and Morellini, 2013; Panoz-brown et al., 2016; Zhou and Crystal, 2009).

Memory can also be classified according to its durability: short-term memory (STM) refers to the temporary storage of information, typically lasting seconds to minutes, whereas long-term memory (LTM) involves retaining information over an extended period of time (Bahrick et al., 1975; Peterson and Peterson, 1959). Finally, the process of memory has been broadly divided into three main stages: *encoding* (the initial acquisition of information), *consolidation* (the storage of information over time) and *retrieval* (the recall of stored information) (Melton, 1963).

Overall, this thesis focuses on the mechanisms underlying episodic memory formation. More specifically, it seeks to address the complex question of how the brain stores new memories and which are the mechanisms involved in the updating of previously consolidated memories. In the following section, I will provide a review of the hippocampus, an indispensable brain region for the acquisition of episodic memories.

1.2. The hippocampus: anatomy, connectivity and functionality

The term hippocampus originates from the Greeks seahorse: *ιππος* ('hippos', horse) and *καμπος* ('kampus', sea monster). It is located in the medial temporal lobe (Figure 1.1A, *top* and *middle* panels) and can be further subdivided into the hippocampus proper, which encompasses *cornu ammonis* or CA regions (CA1, CA2 and CA3), and the dentate gyrus (DG). Together with the entorhinal cortex (EC) and the subicular complex (subiculum, presubiculum and parasubiculum), they constitute the hippocampal formation, considered part of the *limbic system*, which in turn involves several brain regions (i.e., prefrontal cortex (PFC), nucleus accumbens (NAc), ventral tegmental area (VTA), cingulate cortex or amygdala) that are highly interconnected to participate in complex cognitive processes, including emotion, motivation and memory (Morgane et al., 2005).

Pioneers in the study of the hippocampus were Santiago Ramon y Cajal (1852-1934) and his pupil Rafael Lorente de Nó (1902-1990) who, through meticulous observations utilizing Golgi staining techniques, made relevant contributions with their detailed descriptions of the hippocampus anatomy and functional connectivity (Figure 1.1B).

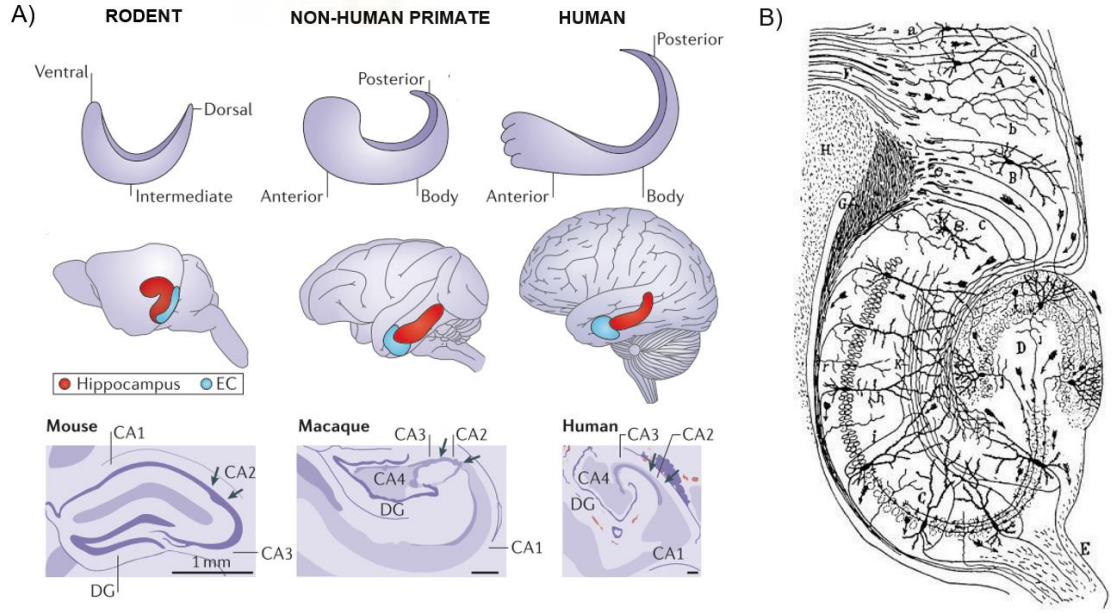

Figure 1.1. The hippocampus. **(A)** Anatomical localization of the hippocampus across different species (top and middle) and drawings of Nissl-stained hippocampal sections (bottom). From Strange et al. (2014). **(B)** Cajal's anatomical drawing of the hippocampus.

1.2.1. Hippocampal cellular organization

The laminar cytoarchitecture of the hippocampus exhibits a highly organized and conserved structure across many mammal species (Andersen et al., 2006). Its characteristic three-layer structure, in contrast to the six-layer neocortical organization, together with its intricate internal circuitry, enables the integration of different types of information and favors the flow of information, ideal for sustaining the formation of episodic memories (Lorente De Nó, 1934; Marr, 1971).

CA regions share their main laminar topology. The somas of the principal neurons in these regions, the pyramidal cells, are densely packed forming the *pyramidal layer,* and their dendrites form two opposite branches: basal dendrites located in the *stratum oriens***,** and apical dendrites crossing the *stratum radiatum* followed by the stratum *lacunosum-moleculare*. In CA3, the most proximal portion of *str. radiatum* is differentiated in *stratum lucidum*.

The characteristic shape of the DG varies from dorsal (V-shaped) to ventral (U-shaped) portions of the hippocampus, being well organized in three layers (Amaral et al., 2007). The somas of the principal excitatory neurons, called granule cells (GCs), are densely located in the *granular layer,* extending their dendrites through the *molecular layer* and projecting their axons, the mossy fibers, through the *polymorphic layer*. This internal part of the DG, also known as *hilus*, contains more than 20 different subtypes of interneurons and the glutamatergic mossy cells (MCs), which innervates inhibitory neurons as well as excitatory GCs (Houser, 2007; Scharfman and Myers, 2012).

1.2.2. Hippocampal connectivity: more than a trisynaptic circuit

Regarding its internal connectivity, the hippocampus is characterized by three main circuits. One of the most well-known pathways is the ***trisynaptic circuit***, initially described by Ramón y Cajal (1899), demonstrating a sequential flow of information through the hippocampus. The perforant pathway (PP), considered the main input to the hippocampus, originates in the EC layer II and arrives at the molecular layer of the DG, where the first synapse occurs (Figure 1.2). From there, dentate GCs send their mossy fibers to CA3 *stratum lucidum*, forming the second synapse. CA3 pyramidal cells, in turn,

send their Schaffer collaterals that terminate in the *stratum radiatum* of CA1, completing the third synapse (ECII → DG → CA3 → CA1). Moreover, there are also some collaterals that backproject from CA3 to DG, targeting especially hilar MCs and GABAergic interneurons (Scharfman, 2007). Finally, CA1 pyramidal neurons project direct and indirectly, via the subiculum, to EC layer V/VI, providing the main output of the hippocampus (Amaral, 1993; Amaral et al., 2007; Andersen et al., 2006).

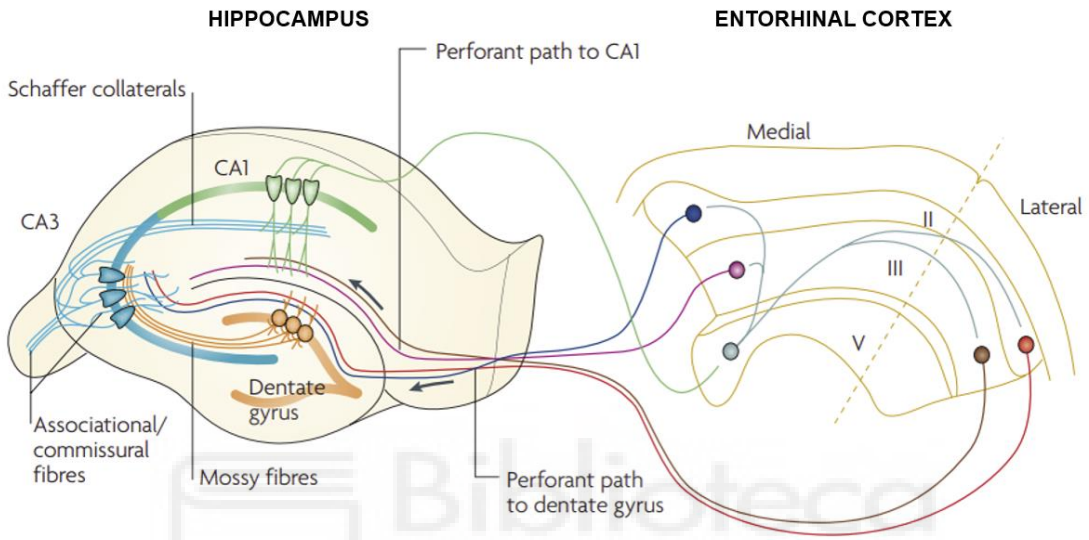

Figure 1.2. Diagram of local hippocampal circuits and main inputs from the EC.
The main input to the hippocampus originates in the medial (MEC) and lateral (LEC) entorhinal cortex. Layer II neurons in MEC and LEC send axons to the DG (and CA3). Layer III neurons project directly to CA1, also known as *temporoammonic pathway*. Within the hippocampus, the diagram shows the traditional trisynaptic loop, where DG mossy fibers (orange) contact CA3 pyramidal cells (blue), that in turn send their Schaffer collaterals to CA1 region (green). CA1 closes the loop projecting to layer V neurons in the EC. The subiculum is omitted in this diagram. Adapted from Neves et al. (2008).

Despite the CA2 subregion being classically overlooked, it is clearly differentiated from neighboring CA3 and CA1 (Dudek et al., 2016; Ishizuka et al., 1995) and has received more attention during the last years. It is also involved in the trisynaptic circuit, receiving weak inputs from DG (Kohara et al., 2014) and weak excitation but strongly feedforward inhibition from CA3 Schaffer collaterals (Chevaleyre and Siegelbaum, 2010), while mainly projecting to CA1 *stratum oriens at* basal dendrites of pyramidal neurons (Kohara et al., 2014; Shinohara et al., 2012).

The second hippocampal circuit arises from those PP axons and follows a ***disynaptic pathway***, bypassing DG and directly projecting to CA3 (ECII → CA3 → CA1). Thirdly, there is a monosynaptic input from EC layer III to CA1, also known as the

temporoammonic pathway (ECIII → CA1), specifically targeting the dendrites of pyramidal neurons at the level of the *stratum lacunosum-moleculare.* Finally, the hippocampal commissure contains axons that cross from one hippocampus to the contralateral one, connecting both hippocampi (Steward and Scoville, 1976; Voneida et al., 1981).

Regarding external connectivity (Figure 1.3), the hippocampus extensively interacts with multiple distributed cortical and subcortical regions (Dickerson and Eichenbaum, 2010; Eichenbaum, 2000). While EC acts as an interface between the hippocampus and neocortex, *fimbria/fornix* is the main efferent pathway to subcortical areas, also containing axons entering into the hippocampus mainly from septal nuclei, thalamus and hypothalamus (Adelmann et al., 1996; Senova et al., 2020; Wyss et al., 1980).

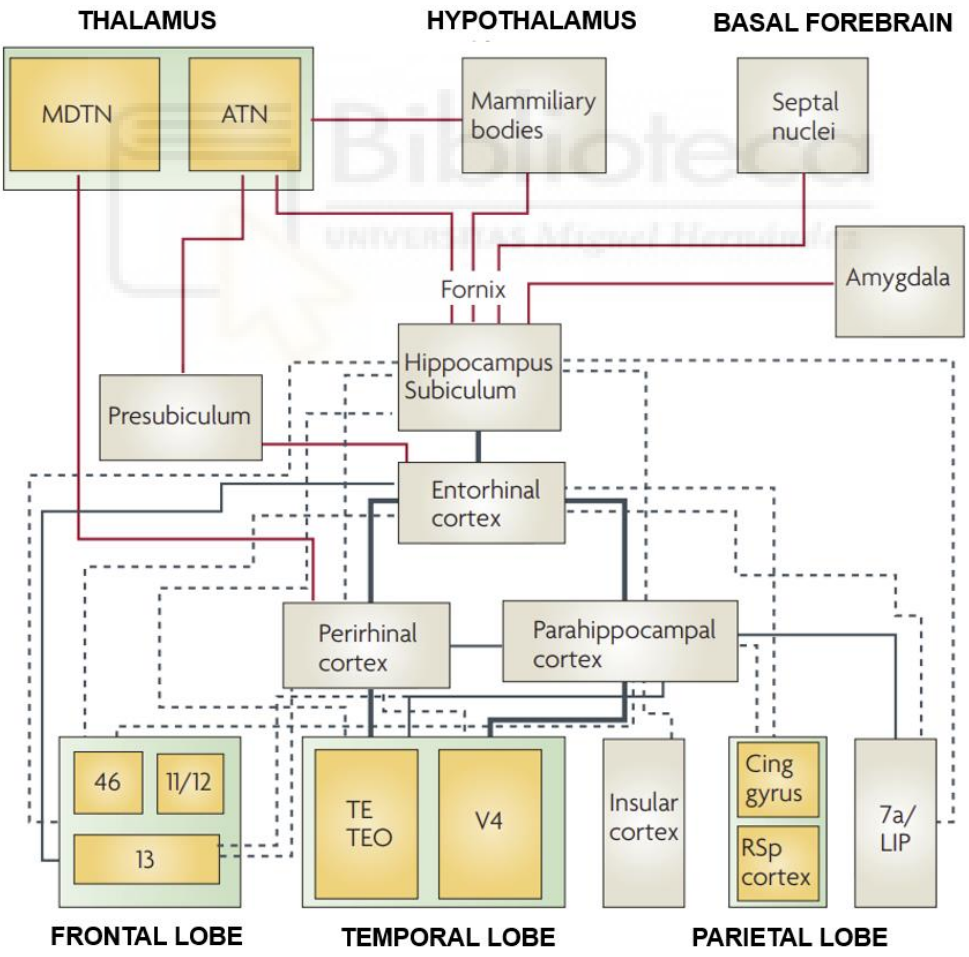

Figure 1.3. Diagram of cortical and subcortical connections of the hippocampus. Red lines depict subcortical connections and cortical connections are indicated by black lines, while the thickness of the black lines approximates to the strength of the connections. From Bird and Burgess (2008).

Overall, the intricate circuitry of the hippocampus provides diverse routes of information that significantly contribute to the integration of different information streams, establishing a robust framework for the formation of episodic memories (Buzsáki, 2006).

1.2.3. Hippocampal mnemonic functions

Decades of research have emphasized the specific role of the hippocampus in spatial memory and navigation through two main approaches: electrophysiology and behavior. As specific examples, electrophysiological recordings of hippocampal activity in freely-moving rats led to the discovery of place cells, neurons firing at specific environmental locations or place fields (O'Keefe, 1976; O'Keefe and Dostrovsky, 1971; O'Keefe and Nadel, 1978). Concurrently, the development of behavioral tests like the radial-arm maze (Olton and Samuelson, 1976) or the water maze (Morris, 1981) not only confirmed the hippocampal role in spatial memories but also introduced more advanced behavioral procedures and analyses, substantially enhancing behavioral approaches to study memory processes.

However, the diverse extrinsic connectivity patterns, molecular expressions and electrophysiological properties along the dorsoventral (or septotemporal) axis have led to functional segregation of the hippocampus (Fanselow and Dong, 2010; Kheirbek et al., 2013; Moser and Moser, 1998; Strange et al., 2014; Wyss et al., 1980). The dorsal region primarily handles spatial processing, interacting with regions like the retrosplenial and anterior cingulate cortex, whereas the ventral hippocampus is related to anxiety and emotional responses, interacting directly with the amygdala, PFC and ventral lateral septum (Bannerman et al., 2003; Ciocchi et al., 2015; Henke, 1990; Kjelstrup et al., 2002; Moser et al., 1993, 1995). In good agreement with this dissociation, there is higher density of place cells with more well-defined place fields in the dorsal compared to the ventral region (Ciocchi et al., 2015; Jung et al., 1994; Kjelstrup et al., 2008).

Furthermore, theoretical and empirical findings have demonstrated that each hippocampal subregion supports specific processing functions:

The DG, also known as the "gatekeeper" of the hippocampus, is characterized by the sparse activity of GCs (Diamantaki et al., 2016; Jung and McNaughton, 1993; Leutgeb et al., 2007; Marr, 1971; Neunuebel and Knierim, 2012; Treves and Rolls, 1992, 1994), which allows the orthogonalization of incoming input patterns into non-overlapping

output patterns, a function called *pattern separation*. This process involves distinguishing between similar inputs and encoding them into distinct neural representations, preventing the interference between memories and ensuring that individual experiences are stored separately (Leutgeb et al., 2007; Marr, 1971; Treves and Rolls, 1992).

CA3 is considered an auto-associative network due to the extensive recurrent collaterals connecting CA3 pyramidal neurons (Amaral, 1993; Ishizuka et al., 1990; Witter, 2007), which supports the rapid formation of arbitrary associations and the ability to recall a complete memory from partial inputs, a function called *pattern completion* (Gilbert and Brushfield, 2009; Guzman et al., 2016; Rolls, 2013). This process enables CA3 to retrieve and reconstruct the whole memory even when presented with incomplete cues.

CA1 serves as the "output gateway" of the hippocampus and plays a critical role in the *temporal integration* of events within episodic memories, linking temporal information with spatial and contextual data to create comprehensive and coherent memory representations (Eichenbaum, 2017; MacDonald et al., 2011; Sellami et al., 2017; Shimbo et al., 2021). It is suggested that CA1 compares temporally coincident inputs with new incoming sensory information (input from EC) and already stored representations (input from CA3) (Barrientos and Tiznado, 2016; Duncan et al., 2012; Kesner and Rolls, 2015; Lisman and Grace, 2005), a relevant function for updating memories.

Notably, a classic distinction has been made between the roles of DG and CA1 in the different stages of memory formation, with the DG primarily linked to encoding (Lassalle et al., 2000; Lee and Kesner, 2004) and CA1 often involved in consolidation and retrieval processes (Remondes and Schuman, 2004; Vago and Kesner, 2008). However, the role of DG in retrieval remains controversial, as recent research has also involved it in the retrieval of spatial (Li et al., 2020; Mendez-Couz et al., 2015), social (Leung et al., 2018) and contextual fear memories (Bernier et al., 2017; Ramirez et al., 2013).

Finally, DG and CA1 have been also classically dissociated in the processing of different aspects of episodic memory, associating the "where" component with the DG and the "what" component with CA1. Pharmacological lesion studies have demonstrated that DG-lesioned rats exhibit impairment in object-location associations, while CA1-lesioned rats show deficits in object recognition (Barker and Warburton, 2011; Gilbert et al., 2001; Kesner and Rolls, 2015; Lee and Solivan, 2010).

In the following section, I review the current understanding of how memories are formed and maintained at a systems-level, for what the interaction between the hippocampus and other relevant regions within the memory network is crucial.

1.3. The distributed and dynamic nature of memories

When an event unfolds, a multitude of sensory, spatiotemporal, emotional and interoceptive information arrives at, and is processed by, diverse brain regions, leading to the coactivation of sparse neuronal ensembles. These interconnected assemblies, shaped by experience-induced synaptic modifications, constitute what is termed a memory trace or *engram,* being the substrate for memory encoding and storage (Guskjolen and Cembrowski, 2023; Josselyn and Tonegawa, 2020; Josselyn et al., 2015; Ryan et al., 2015; Tonegawa et al., 2015a, 2018). This spatially distributed information storage necessitates coordination to link the coactivated and dispersed neurons into comprehensive memory representations. To this aim, the hippocampus is thought to play a pivotal role in binding these distributed cell assemblies. Particularly, the indexing theory suggests that the hippocampus creates associations between disperse brain regions, acting as an index that enables the synchronized reactivation of relevant memory traces across the brain (Tanaka et al., 2018; Teyler and Rudy, 2007).

The concept of distributed memory is not a recent story. In the early 20th century, Richard Semon (1904) introduced the term *engram* to describe the physical and enduring changes in the brain following an experience. Subsequent pioneering experiments, such as those by Lashley and Franz (1917), failed to find the memory engram but supported that memory storage is dispersed throughout the cortex rather than localized in a single region. Influenced by the work of Lorente de Nó (1933) on self-exciting reverberatory circuits, Donald Hebb (1949) proposed that synaptic strengthening increases between neurons simultaneously activated (*"cells that fire together wire together")*. These interconnected neurons form a cell assembly, serving as the mechanism for memory acquisition. Furthermore, the reactivation of such cell assembly would provide the basis for memory retrieval.

Recent molecular engineering advances have allowed the identification of experience-activated neurons based on immediate early genes expression (e.g., *cFos*) and the targeted manipulation of these engram neurons (e.g., via cFos-dependent expression of channelrhodopsin2 (ChR2)). These advancements provide deeper insights into circuit interactions (Liu et al., 2012, 2014; Reijmers et al., 2007; Tonegawa et al., 2015a).

Importantly, although this thesis primarily focuses on the mechanisms supporting memory formation at a network level, the creation of an engram involves experience-induced physical changes occurring at various levels. These alterations range from brain-wide network reorganizations to synaptic and nuclear changes, including transcriptional and epigenetic modifications (Figure 1.4).

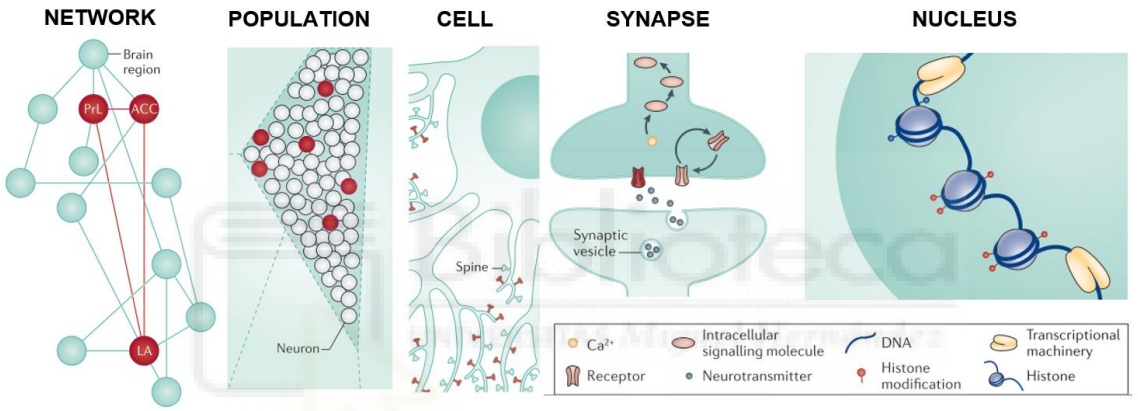

Figure 1.4. Multi-level engram memory formation. Schematic pictures of a given engram at different levels. From brain network level, the involved specific regions (red dots) are connected functionally (red lines) and anatomically (cyan lines). At neuronal population level, subsets of neurons are identified contributing to the engram (red dots). At individual level, neurons undergo changes in connectivity patters with engram formation. Synaptic subsets experience alterations such as strengthening. At the nuclear level, the engram manifests in transcriptional and epigenetic modifications. This diagram highlights the diverse dimensions at which engrams can be divided. Adapted from Josselyn et al., (2015).

Furthermore, memory engrams are known to dynamically change over time (Figure 1.5A). During memory encoding, coactivated neurons are associated (experience-induced cell ensembles) and recruited into the memory engram. The dialogue between the hippocampus and its interconnected regions, especially with EC and PFC, are essential during the early stages of memory formation (Churchwell et al., 2010; Eichenbaum, 2017; Takehara-Nishiuchi, 2020). Then, memory consolidation supposes a network reorganization, where synaptic connections and their weights are modified in order to strengthen the memory representation to become more stable and resistant to interference

or forgetting (Frankland and Bontempi, 2005; Rao-Ruiz et al., 2021; Squire and Alvarez, 1995; Squire et al., 2015; Wang and Morris, 2010).

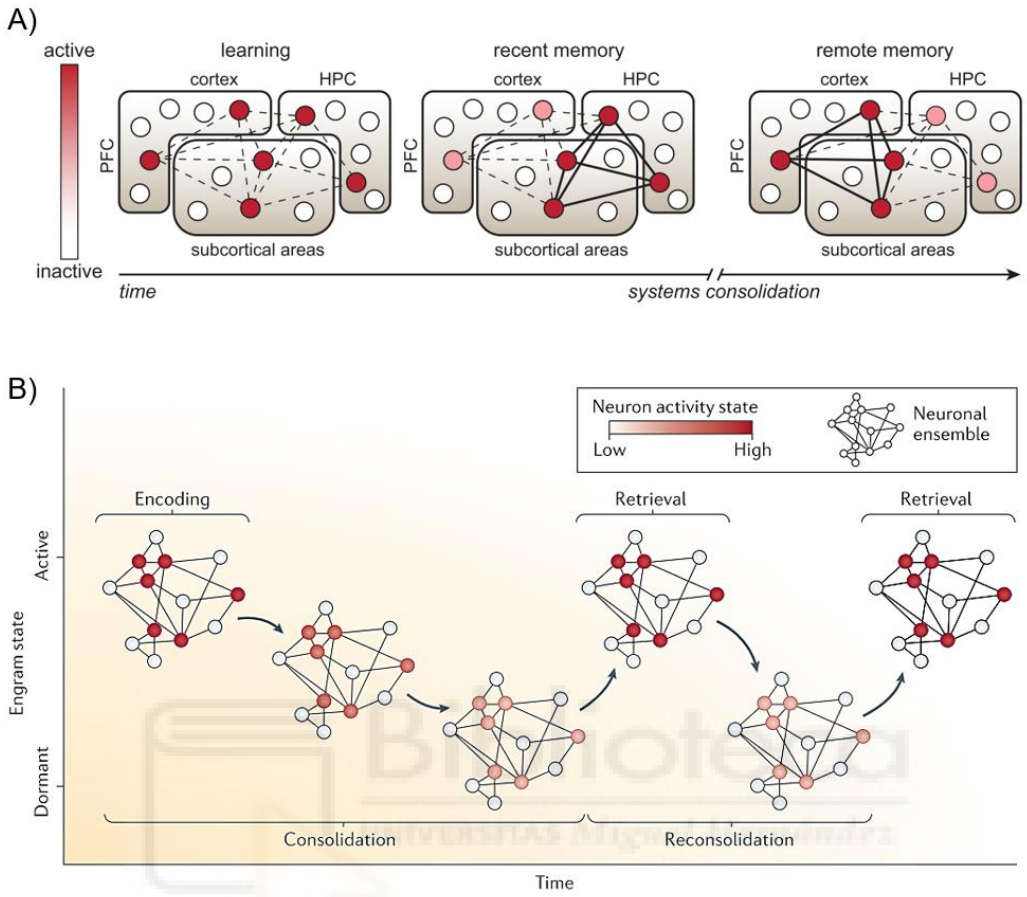

Figure 1.5. Dynamics of memory formation. **(A)** Temporal reorganization of an engram. Neuronal ensembles in memory-related brain regions, including the hippocampus, cortex and subcortical areas, consolidate physical changes supporting memory storage. In the post-learning period, synaptic connectivity strengthens among hippocampal engram cells and other for recent memory expression. Over days to weeks, systems consolidation involves replay and synchronization of activity patterns, promoting maturation of cortical engram cells. This results in strengthen connectivity within cortical-cortical and cortical-subcortical engram cells, shifting the network's dependance towards cortical engram cells for remote memory expression. (**B)** Different states of the engram along its lifespan. Engram formation involves strengthening connections among active neurons (red dots) during an event. Consolidation further enhances these connections, increasing the likelihood of recreating the same activity pattern for successful memory retrieval. During consolidation, the engram becomes mainly dormant. Memory retrieval reactivates the engram, transiently destabilizing its connection pattern. Reconsolidation stabilizes the engram, returning it to a more dormant state. Thus, the engram exists in a dormant phase between the active processes of encoding and retrieval essential for memory formation and recovery. It serves as the groundwork for a memory to emerge without being a memory itself. Colored circles represent the learning-activated neurons in the brain regions related to the given memory. (Images taken from Josselyn et al., 2015 and Rao-Ruiz et al., 2021).

Classically, it was assumed that the hippocampus becomes less relevant with time, as memories have been gradually transferred and stabilized into the neocortex. However, contrary to this standard model of systems consolidation (Moscovitch, 1995; Moscovitch and Winocur, 1995; Squire and Alvarez, 1995), there is evidence supporting the

engagement of the hippocampus when remembering remote memories, being particularly relevant for recalling detailed information (Atucha et al., 2021; Nadel and Moscovitch, 1997; Nadel et al., 2000; Wiltgen et al., 2010).

Once a memory has been consolidated, its retrieval is associated with the reactivation of the involved neurons during its encoding. Thus, it has been experimentally demonstrated that activating or silencing engram cells can promote or disrupt, respectively, memory retrieval (Frankland et al., 2019; Liu et al., 2014; Redondo et al., 2014; Tonegawa et al., 2015a). Additionally, a previously consolidated memory engram is thought to be destabilized during its retrieval, a process called reconsolidation (Figure 1.5B), resulting in a more labile state of the engram that enables its modification, either to be strengthened, updated or deleted (Dudai, 2004; Nadel et al., 2012; Silva and Gräff, 2023; Wang and Morris, 2010).

Overall, memory engrams are not only spatially distributed but also temporally dynamic. This means that they should be flexible enough to accommodate transformations over time, and synaptic plasticity is thought to be the key mechanism mediating the changes in synaptic strengthening and connectivity.

1.3.1. Synaptic plasticity and memory formation

Since a long time ago, it has been accepted that information flow in the brain is mediated by synaptic transmission, and the modification in the efficiency of such transmission, known as *synaptic plasticity*, underlies the storage of new information (Cajal, 1894; Lorente de Nó, 1934). These changes in the strength of synaptic connections can last a short period of time, from milliseconds to minutes (short-term plasticity) (Goldman-Rakic, 1995; Squire and Zola-Morgan, 1991) or can be more permanent in time (long-term plasticity), lasting hours, days or even years. These changes, moreover, could involve the connections between neurons becoming stronger (long-term potentiation, LTP) or weaker (long-term depression, LTD).

Despite it was Erik Kandel the first to empirically link simple forms of learning (i.e., habituation and sensitization) to a change in synaptic efficacy in the mollusc *Aplysia californica* (Kandel and Tauc, 1965; Klein and Kandel, 1978), the discovery and description of LTP was first performed by (Bliss and Lomo, 1973). After applying high-frequency electrical stimulation on the PP, the main cortical afference to the hippocampus,

they observed a very stable and long-lasting synaptic strengthening in the hippocampal DG of rabbits. Although LTP can occur in different ways, this form of potentiation on the DG depends on the activation of N-methyl-D-aspartate (NMDA) receptors, which are voltage-dependent channels permeable to Ca^{2+} but blocked by Mg^{2+} in basal conditions or under weak stimulation. With stimulus of sufficient strength or frequency, NMDA receptors release Mg+ and allow a momentary increase in Ca^{2+}, activating signal-transduction pathways that result in an increase of α-amino-3-hydroxy-5-methyl-4-isoxazolepropionic acid (AMPA) receptors in the postsynaptic membrane. This semi-permanent change leads to an increased sensitivity to glutamate and enhanced synaptic transmission. Furthermore, the long-lasting maintenance of LTP requires the synthesis of new plasticity-related proteins to stabilize the expressed change (Frey and Morris, 1997; Redondo and Morris, 2011; Shires et al., 2012; Takeuchi et al., 2014).

The accumulated experimental evidence during the last 50 years has led to the so far accepted *synaptic plasticity and memory hypothesis* (Marr, 1971; Martin et al., 2000; McNaughton and Morris, 1987; Takeuchi et al., 2014), stating that activity-dependent synaptic plasticity is both necessary and sufficient for the encoding and storage of a memory trace. The blockade of LTP with NMDA receptor antagonists has been shown to impair learning and retention of spatial memories (Davis et al., 1992; McNaughton and Morris, 1987; Morris et al., 1986), while rodents performing hippocampal-dependent memory tasks have shown LTP-like enhancement of CA3-CA1 connections (Sánchez-Rodríguez et al., 2022). Thus, LTP is considered the physiological substrate for learning, while the opposite effect, LTD, has been proposed as the mechanism underlying forgetting (Ito, 1989; Malenka and Bear, 2004; Moreno, 2021; Nabavi et al., 2014).

In summary, synaptic plasticity is essential for the emergence and maintenance of memory engrams, where the DG has been pointed out as a crucial region for the encoding of new memory traces. In the following section, I focus on the specific role of the DG in supporting the binding of distributed cell ensembles that enable memory formation.

1.3.2. Binding mechanisms in the DG

As the main entrance to the hippocampus, the DG receives direct inputs from the lateral (LEC) and medial (MEC) portions of the EC (Amaral, 1993; van Strien et al., 2009), where the "*what*" and the "*where*" features of the episodic memory converge before

reaching the DG: the LEC receives non-spatial information from the perirhinal cortex, while the MEC routes spatial information that receives from the postrhinal cortex (or parahippocampal cortex in humans) (Deshmukh and Knierim, 2011; Eichenbaum et al., 2007; Kerr et al., 2007; Knierim et al., 2006). Thus, the DG has been proposed to conjunctively encode the multimodal inputs it receives, binding spatial and non-spatial information in the dendrite of the granule cells, and supporting the formation of a unified neural representation of the experience (Hainmueller and Bartos, 2020; Kesner, 2007; Lee and Jung, 2017; O'Reilly and McClelland, 1994).

Moreover, other direct inputs from subcortical regions arrive to the DG via fimbria-fornix, as the cholinergic and GABAergic projections to the hilus from the medial septal nucleus and the diagonal band of Broca (Lübke et al., 1997; Ogando et al., 2021); glutamatergic hypothalamic projections mainly from the supramammillar area (Borhegyi and Leranth, 1997; Leranth et al., 1999); and projections from brainstem nuclei, as locus coeruleus (noradrenergic input), VTA (dopaminergic) and raphe nuclei (serotoninergic) (Aznar et al., 2004; McKenna and Vertes, 2001; Swanson and Hartman, 1975).

Serving as the main framework for this thesis, previous studies of the laboratory have already evidenced the potential role of the DG in the coordination of brain circuits. Based on functional magnetic resonance imaging (fMRI), Canals et al. (2009) revealed that the induction of LTP in the rat PP not only causes the expected potentiation in the DG itself (Figure 1.6A) but also enhances the functional coupling of a distributed network, involving neocortical and subcortical structures important for memory formation (Figure 1.6B-C). Specifically, the measured blood-oxygen-level-dependent (BOLD) activity showed significant changes in frontal, association or perirhinal cortices and other subcortical regions like the NAc, memory-related structures that are remote from the site of plasticity (Álvarez-Salvado et al., 2014; Del Ferraro et al., 2018).

In a following study (Álvarez-Salvado, 2015; Estarellas et al., 2023), focused on the local effects of LTP by combining *in vivo* electrophysiological recordings with source separation technique, known as independent component analysis (ICA) (Benito et al., 2014; Fernández-Ruiz and Herreras, 2013; Makarov et al., 2010). The recorded LFP at the DG was decomposed in 2 main generators: *PP-IC* and *Hilar-IC*, mainly reflecting excitatory and inhibitory activity, respectively, induced by PP activation (Figure 1.6 D-F). After LTP induction, they found not only an increased excitability (observed as the potentiation of the PP-IC) but also a decreased inhibitory activity (reduced amplitude of

the Hilar-IC), reflecting a decreased feedforward inhibitory input over GCs (Figure 1.6G). Further current source density (CSD) analysis of the *Hilar-IC* revealed that the reduced inhibitory currents depressed by LTP were spatially localized around the somas of the GCs (Figure 1.6F), pointing to the involvement of perisomatic GABAergic interneurons in the resulting increased excitatory/inhibitory (E/I) ratio (Figure 1.6E).

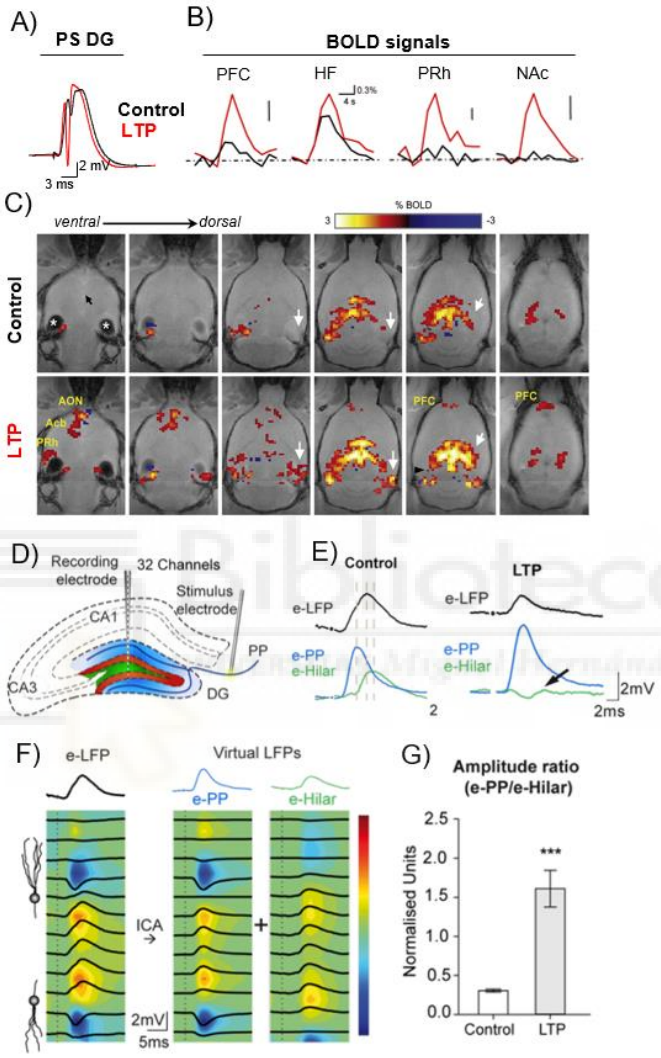

Figure 1.6. Local and brain-wide reorganizations after PP-DG potentiation.
(A) Induction of LTP in the rat PP induces a potentiation of the recorded population spikes in the DG. **(B)** The induction of LTP enhanced functional coupling among distributed brain structures associated with memory formation, like in frontal, association, and perirhinal cortices, along with subcortical regions like the Nucleus Accumbens (NAc), revealed by blood-oxygen-level-dependent (BOLD) activity measured via functional magnetic resonance imaging (fMRI). **(C)** Functional maps overlaid on horizontal anatomical scans, revealing brain regions active before (control) and after inducing potentiation through high-frequency stimulation of the PP, where extrahippocampal were engaged. White arrows indicate brain areas opposite to the stimulated perforant path. The black arrow marks the anterior commissure, while asterisks indicate image distortions from the ear channel. The color scale shows positive and negative BOLD response from baseline. The black arrowhead marks the position of the stimulation electrode tip. **(D)** Illustration of the hippocampus highlighting the different layers of the DG in distinct colors (blue: molecular layer, red: granular layer, green: hilar layers), and displaying the placement of recording and stimulating electrodes for *in vivo* electrophysiological recording of anesthetized rats. **(E)** Comparison between the evoked potentials in the raw LFP (black) and ICs (blue and green) during the control state and after inducing

long-term potentiation (LTP). An arrow indicates the reduced evoked potential in the Hilus-IC following LTP. **(F)** *Left*: Depiction of evoked local field potential (e-LFP) recordings across the DG following perforant path stimulation, presented alongside the corresponding current source density (CSD) map using a color-coded scheme. The upper trace (in black) emphasizes the evoked potential within the hilar region's core. *Right*: Displaying decomposed independent components (ICs), represented as virtual LFPs, overlaid on corresponding CSDs for the PP-IC (e-PP, middle panel) and Hilus-IC (e-Hilus, right panel). Upper traces highlight the e-PP (in blue) and e-Hilar (in green). **(G)** Histogram showing the effects of LTP on the amplitude of excitation/inhibition ratio of evoked ICs normalized to the average value within each experiment ($t(23)=6.6$, $p<0.0001$). The bars represent mean ± SEM. Adapted from Canals et al., (2009) and Estarellas et al., (2023).

Besides the convergence of separated information into the DG ("local binding"), we also found support to our hypothesis on the role of DG in coordinating disperse cell ensembles ("long-range binding") in recent studies involving the use of cFos-dependent expression of ChR2, which enables the targeted manipulation of engram neurons. In these studies, the reactivation of DG engram cells by optogenetic activation of cFos-dependent ChR2 (those GCs neurons that were active during memory encoding) was sufficient to trigger the behavioral expression of memory, being able to recall a contextual fear memory even in the absence of contextual cues to express the conditioned freezing (Liu et al., 2012; Perusini et al., 2017; Ramirez et al., 2015).

In summary, plasticity studies (1) evidenced the potential role of the DG in the system-level coordination of brain circuits and (2) pointed to the feedforward perisomatic inhibition as the underlying mechanism of the DG in the functional reorganization of distributed cell assemblies. Under this framework, we propose that the DG is a critical node for the association of the distributed experience-relevant neuronal assemblies into the memory network. Furthermore, we hypothesize that local changes in the E/I balance of the DG could be the binding mechanism contributing to this network coordination (Deco et al., 2014).

1.4. The role of inhibition on information processing and memory formation

While attention has been predominantly focused on the excitatory activity underlying learning and memory, the importance of inhibition in these processes has been proposed since some time ago (Young, 1964). Moreover, there is a continuously expanding body of evidence supporting the crucial role of GABAergic neurons in memory processes

(Cummings et al., 2021; Giorgi and Marinelli, 2021; Lucas and Clem, 2018; Topolnik and Tamboli, 2022; Tzilivaki et al., 2022, 2023).

Maintaining a balanced interplay between excitation and inhibition is fundamental for the proper functioning of the brain. This equilibrium, referred to as the excitatory/inhibitory (E/I) balance, relies on the activity of GABAergic interneurons shaping the excitatory activity, significantly influencing neuronal communication (Isaacson and Scanziani, 2011; McKenzie, 2018; Pelkey et al., 2017). Disruptions or abnormalities in inhibitory activity, leading to an imbalance in the E/I ratio, have been associated with various neurological and psychiatric disorders, such as epilepsy (Magloire et al., 2019), schizophrenia (Benes and Berretta, 2001; Jahangir et al., 2021; Konradi et al., 2011), Alzheimer's disease (Czéh et al., 2015; Palop and Mucke, 2016), depression (Czéh et al., 2015; Luscher et al., 2011; Umschweif et al., 2021) or posttraumatic stress disorder (PTSD) (Regev-Tsur et al., 2020).

GABAergic interneurons exert their influence on principal cells through two main mechanisms (Figure 1.7A). First, *feedback* inhibition predominantly involves local connectivity, where principal cells activate interneurons, which subsequently inhibit the principal cell population. Second, *feedforward* inhibition arises from excitatory inputs that directly contact interneurons as well as principal cells (Isaacson and Scanziani, 2011; Sloviter, 1991).

Despite GABAergic interneurons only represent about 10-20% of all neuronal population, they are remarkably diverse in molecular, morphological, electrophysiological and connectivity properties (Booker and Vida, 2018; Freund and Buzsáki, 1996; Hosp et al., 2014; Houser, 2007; Klausberger and Somogyi, 2008; Pelkey et al., 2017; Woodson et al., 1989). One of the main classifications is based on their preference for targeting different domains of the principal cell, distinguishing between *perisomatic* and *dendritic* interneurons (Figure 1.7B). Perisomatic interneurons target the soma and the axon initial segment of the postsynaptic neuron, regulating the output of principal cells. Contrarily, dendritic interneurons innervate the dendrites of target neurons, influencing their input integration (Freund and Katona, 2007; Miles et al., 1996).

Two major classes of interneurons are often differentiated due to their distinct, non-overlapping –and complementary– characteristics. Parvalbumin-expressing (PV) interneurons are classified as fast-spiking and *perisomatic* interneurons, while

somatostatin-expressing (SST) cells are considered slow-firing interneurons that preferentially contact the dendrites of target neurons (Figure 1.7B). These differences have led to functional distinctions between PV and SST, suggesting they may differentially impact network plasticity and memory formation (Aery Jones et al., 2021; Caroni, 2015; Kim et al., 2016; Lee et al., 2016; Miao et al., 2017; Royer et al., 2012).

While ongoing research continues to explore the specific contributions of each interneuron subtype, our understanding of inhibitory control and neuronal modulation during memory formation remains incomplete. Nevertheless, a growing body of evidence emphasized the significant role of PV (Hijazi et al., 2023; Miranda et al., 2022; Xia et al., 2017) and SST interneurons (Cummings and Clem, 2020; Honoré et al., 2021; Stefanelli et al., 2016) in the processes of memory encoding, consolidation and retrieval (see review by Raven and Aton, 2021).

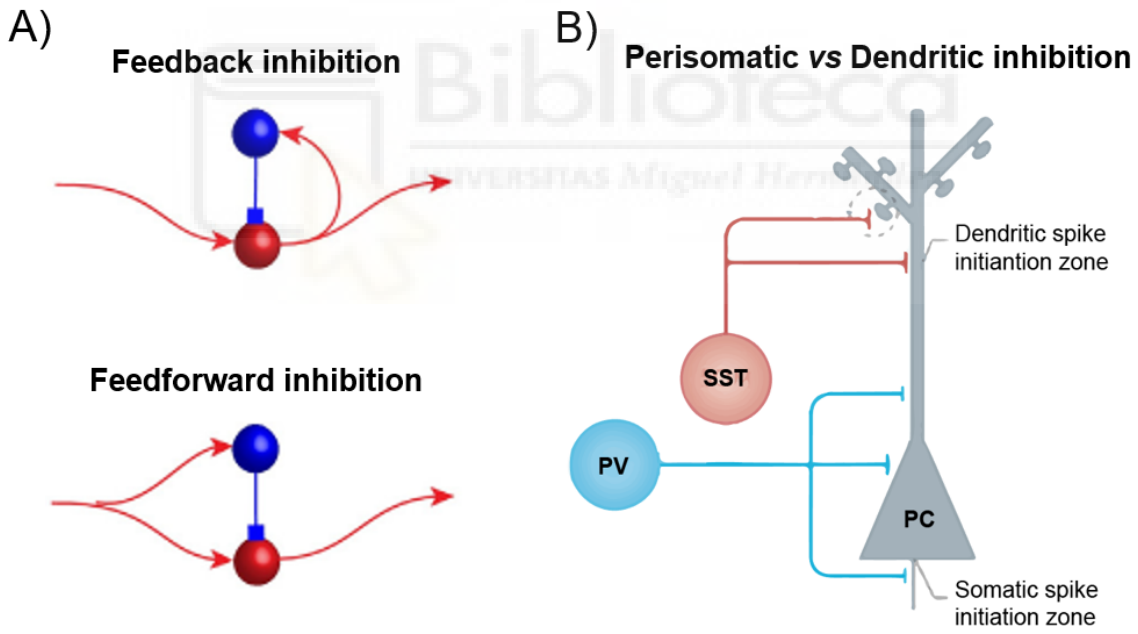

Figure 1.7. Inhibitory circuits and interneurons subtypes
(A) Main mechanisms of influence of GABAergic interneurons (blue) on principal cells (red) by feedback inhibition which primarily operates through local connections and principal cells trigger interneurons, which then inhibit the principal cell population; and by feedforward inhibition which occurs through excitatory inputs directly engaging interneurons as well as principal cells. **(B)** Diagram of a principal cell innervated by perisomatic and dendritic interneurons, contacting at different domains of the principal cells.

1.4.1. Gamma oscillations and Theta-Gamma coupling

Neural oscillations emerge from the synchronized firing of excitatory and inhibitory neurons, leading to rhythmic patterns of activity (Buzsáki, 2006; Pelkey et al., 2017; Whittington et al., 2000). Predominant rhythms in the hippocampus are theta (4-12 Hz) and gamma (30-100 Hz) oscillations. Theta rhythm is associated with the synchronization of separated brain regions and it is prominent during spatial navigation and locomotion. Gamma oscillations are associated with local processes, where higher frequencies enable faster communication and local binding of features. GABAergic neurons, and especially fast-spiking PV interneurons, have been shown to be involved in the generation of gamma oscillations (Antonoudiou et al., 2020; Buzsáki and Wang, 2012; Freund, 2003; Fuchs et al., 2007; Park et al., 2020; Sohal et al., 2009).

The coupling of oscillatory activity is thought to facilitate information processing and effective neuronal communication between brain regions (Fries, 2005). Specifically, the relationship between the amplitude of gamma and the phase of theta oscillations, known as *phase-amplitude cross-frequency coupling* (CFC), or theta-gamma coupling, has been proposed as an essential mechanism to coordinate distributed cortical regions (Canolty et al., 2006; Lisman and Jensen, 2013; Ponzi et al., 2023; Tort et al., 2009). Stronger CFC has been correlated with memory encoding and retrieval (Shirvalkar et al., 2010; Tort et al., 2008, 2009; Vivekananda et al., 2021; Zhang et al., 2016), while decreased strength in theta-gamma coupling has been associated with memory impairments (van den Berg et al., 2023; Kitchigina, 2018).

In this regard, in Lopez-Madrona et al, (2020) we recently found that the strength of CFC and the synchronization of multiple theta oscillations in CA1 are dynamically modulated to support cognitive functions, with stronger CFC and higher synchronization states observed during contextual novelty detection and decision-making epochs. Moreover, we also found a cross-frequency directionality from the faster gamma activity onto the phase of the slower theta rhythm. This result suggests that the coordination of local gamma activity by GABAergic interneurons might facilitate communication between cell assemblies in distant regions by coordinating cell firing into coherent theta waves. These findings proposed a mechanism based on the flexible coordination of different theta frameworks for either integrating (synchronized theta states) or segregating (less synchronized theta states) information within local hippocampal networks.

1.4.2. Disinhibition as a binding mechanism

Growing evidence proposes disinhibition as a fundamental mechanism supporting learning and memory formation (Letzkus et al., 2015; Möhler and Rudolph, 2017), creating critical windows of opportunity that favors the information flow and neural network communication.

Classical studies with pharmacological interventions to increase the inhibitory activity reported impaired hippocampus-dependent memory acquisition (Arolfo and Brioni, 1991; McNaughton and Morris, 1987), while opposite effects were found during periods of mild reductions in inhibitory activity (Chambers et al., 2003; Collinson et al., 2006; Izquierdo et al., 1993). More recently, cell-specific manipulations and electrophysiological recordings have linked transient disinhibition periods with the acquisition and expression of memory (Froemke, 2015; Letzkus et al., 2015; Ogando et al., 2021). Zooming in on DG, reductions of PV+ cell inhibition have been correlated with improved spatial learning in the water maze, although a shift towards a higher PV+ inhibitory network occurred following the completion of learning (Donato et al., 2013).

Taken into account all the aforementioned evidence, and based on the specific reduction of perisomatic feedforward inhibition in the DG reported in Estarellas et al, 2023 (see also Álvarez-Salvado, 2015), we postulated that these alterations in the inhibitory level of the DG would be mediated by perisomatically innervating PV interneurons. We further hypothesized that local reduction of PV inhibition in the DG would impact at a systems-level by increasing activity propagation through distributed cell assemblies, which may well account for the widespread changes in the blood-oxygen-level-dependent (BOLD) signal observed by Canals et al. (2009).

To test this hypothesis, prior to this thesis we used pharmacogenetic manipulation of PV interneurons in the dorsal DG of mice (Caramés et al., 2020). Interestingly, downregulation of PV interneurons increased extra-hippocampal activity propagation (Figure 1.8A), similar to the brain-wide reorganization observed after LTP induction (see Figure 1.6 and Canals et al, 2009). Mice with disinhibited DG activity also showed improved spatial memory, whereas the upregulation of DG-PV activity disrupted memory encoding (Figure 1.8 B-C). Strikingly, cFos staining revealed that despite engram's size remained constant (Figure 1.8D), the functional connectivity between memory-related brain regions was bidirectionally controlled by the level of PV activity (Figure 1.8E):

while less PV inhibition increased the functional coupling, the upregulation of PV activity led to a decreased coupling between hippocampal and extrahippocampal regions.

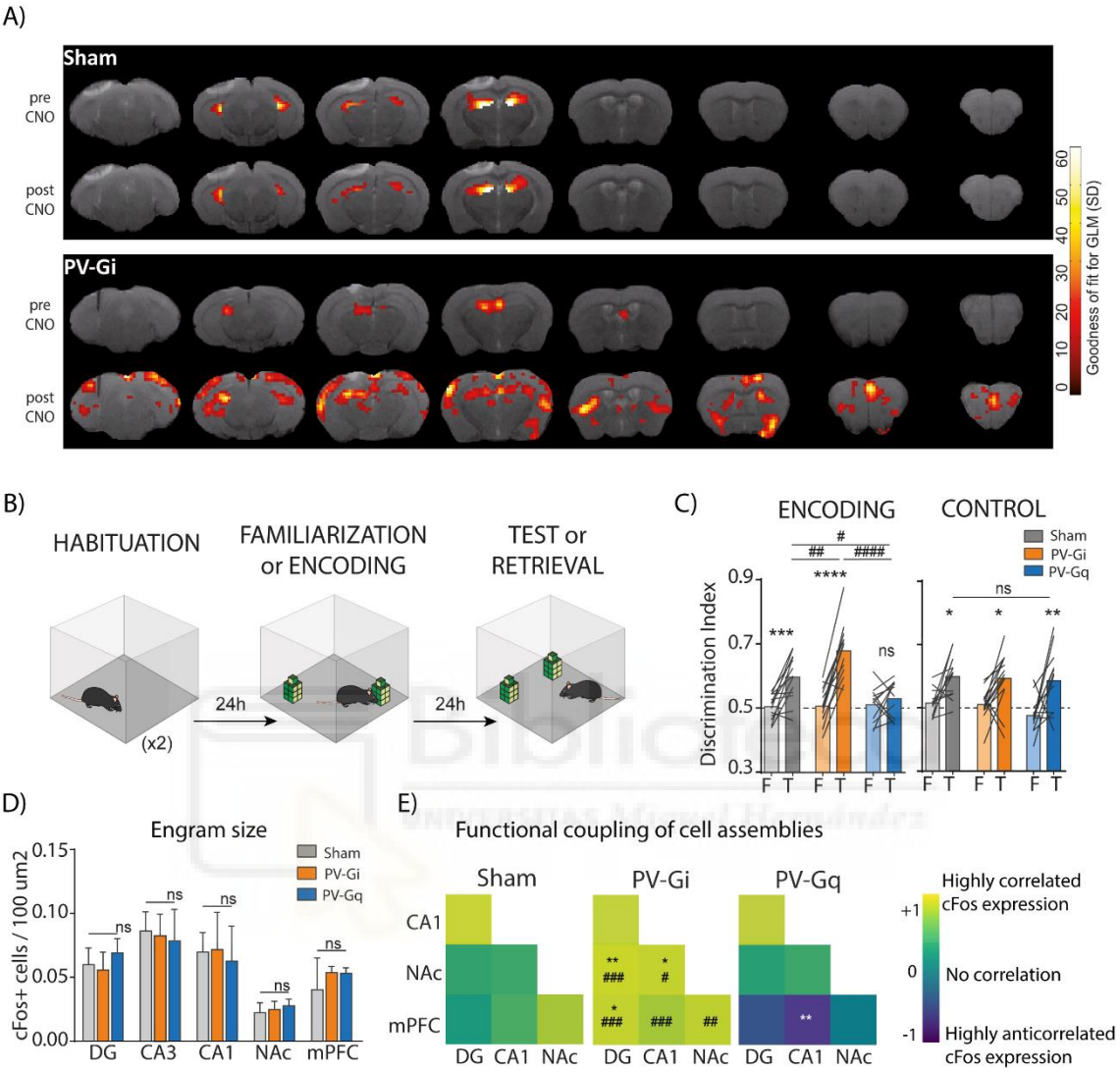

Figure 1.8. PV interneurons in the DG control spatial memory formation and functional connectivity within the memory network.

(A) Functional maps resulting from pre and post CNO injection stimulation, superimposed on T2 anatomical images. The color-coded representation indicates the goodness of fit according to GLM analyses, thresholded at p<0.01. Notably, an increased propagation of extra-hippocampal activity is observed, resembling patterns illustrated in Figure 1.6. **(B)** Schematic illustration of the NOL task design employed to assess spatial memory under manipulated PV interneuron activity. **(C)** Evaluation of performance in the NOL task. Values exceeding 0.5 indicate a preference for the relocated object. Each dot corresponds to paired observations from individual animals, with bars representing mean values. Light and dark colors signify familiarization (F) and test (T) phases, respectively. * denotes within-group comparison (Fam. vs. test), # denotes between-group comparison (Sham vs. PV-Gi vs. PV-Gq). **(D)** Quantification (mean ± SEM) of c-Fos+ cells per 100 µm2 activated during the NOL familiarization phase within the specified ROIs. *#p≤0.05, **##p≤0.01, ***###p≤0.001. **(E)** Co-variation analysis of c-Fos+ expression in the hippocampus, PFC, and NAc. The color-coded scheme represents Pearson-correlation coefficients. * indicates comparisons between Sham and PV-Gi or PV-Gq; # indicates comparisons between PV-Gi and PV-Gq.

These results led us to propose a binding mechanism operated by PV interneurons in the DG. We suggest that this mechanism appears to be particularly crucial for memory updating, fulfilling two complementary functions depending on the level of PV inhibition. On the one hand, to select the relevant information by increasing the coupling between disperse brain regions and allowing the network to add new information. On the other hand, to discard irrelevant or redundant information by decoupling brain areas, thereby preventing from overwriting existing memories and maintaining the integrity of the memory base.

Nevertheless, many questions remain unresolved. For instance, if disinhibition implies transient periods of reduced inhibition, when do these disinhibitory transients occur during the learning process? How do PV interneurons undergo physiological modulation to create stable memory representations by coordinating distributed brain regions? To address these queries, I have broadened our technical methodologies introducing calcium-based neural recordings, which enabled the monitoring of PV interneurons activity in animals engaged in memory-related tasks.

1.5. Recording cell-specific neural dynamics

During the last decades, great advances in genetic tools have empowered neuroscientists to study the contribution of different neuronal populations in memory formation, storage and retrieval (Navabpour et al., 2020). Notably, optogenetic and pharmacogenetic techniques have become extensively used to manipulate specific neural circuits and study the consequences of such perturbation (Ciocchi et al., 2010; Cowansage et al., 2014; Garner et al., 2012; Goshen et al., 2011; Liu et al., 2012; Nguyen-Vu et al., 2013; Redondo et al., 2014; Senn et al., 2014).

Furthermore, calcium imaging tools provide the means to identify specific cell populations and visualize neural dynamics, allowing for the monitoring of neuronal activity at a single-cell resolution. By observing the fluctuations in intracellular calcium levels, which increase when neurons fire action potentials, we can indirectly assess neuronal activity (Kerr et al., 2000; Scanziani and Häusser, 2009). The influx of calcium ions into presynaptic terminals triggers neurotransmitter release (Neher and Sakaba,

2008), while a transient increase in calcium levels within dendritic spines is required for activity-dependent synaptic plasticity (Zucker, 1999).

Although calcium-based activity is typically characterized by lower temporal resolution compared to electrophysiological recordings (for a detailed comparison, see London et al., 2018), in our experiments we took the advantage of the cell specificity offered by calcium imaging techniques in contrast to electrophysiology, allowing us to selectively monitor the activity of PV interneurons (specific cell population) (Deng et al, 2019; Hainmueller et al, 2021; Campos et al., 2020; Twarkowski et al., 2022).

1.5.1. Calcium biosensors

In essence, calcium indicators are fluorescence molecules that exhibit increased brightness (fluorescence intensity) when bound to calcium, enabling the measurement of changes in cytosolic-free calcium levels (Looger and Griesbeck, 2012). It is worth mentioning that, apart from calcium indicators, other types of biosensors are employed to visualize neuronal activity or specific neurotransmitter release, such as voltage (Piatkevich et al., 2018; St-Pierre et al., 2014) or dopamine indicators (Patriarchi et al., 2018).

Traditionally, different calcium sensors have been used, including the chemical indicator *fura-2* (Grynkiewicz et al., 1985) or *Yellow Cameleon (YC) 3.60* (Nagai et al., 2001), a Föster resonance energy transfer (FRET)-based genetically encoded calcium indicator (GECI). More recently, single-fluorophore GECIs have gained popularity due to their extended functionality in the expressing neurons, allowing longitudinal recordings of neuronal activity (Andermann et al., 2010; Mank et al., 2008; Tian et al., 2009).

Specifically, the most currently used single-fluorophore GECIs are GCaMP sensors (see *Methods* for a detailed description), firstly developed by Nakai et al., (2001). Although improved variants with higher sensitivity and faster dynamics are currently available, such as GCaMP7 (Dana et al., 2019) or GCaMP8 families (Zhang et al., 2023) at the onset of this thesis, the GCaMP6 family (Chen et al., 2013) was the most commonly used GECI for *in vivo* calcium imaging (see Figure 3.8).

1.5.2. Calcium imaging techniques for in vivo conditions

In general, calcium imaging techniques entail using a light source to excite a calcium indicator and capturing the emitted fluorescence. To this end, different methods have been developed.

Firstly, *two-photon microscopy* (Figure 1.9A) has been classically used to monitor cortical areas, with the introduction of GRIN lenses providing access to deep-brain regions (Bocarsly et al., 2015; McHenry et al., 2017; Sato et al., 2017; Calhoon et al., 2018). When combined with GECI expression, this method presents a high signal-to-noise ratio. Still, it requires animals to be head-fixed under the microscope when recording in awake conditions, limiting their movement. In recent years, it has often been combined with virtual reality preparations (Forro and Klausberger, 2023; Leinweber et al., 2014; Orlandi et al., 2023).

Secondly, the development of *miniaturized head-mounted microendoscopes* (Figure 1.9B) has facilitated single-cell imaging in freely-moving conditions (Flusberg et al., 2008; Ziv and Ghosh, 2015). This method requires the chronic implantation of GRIN lenses to enable cortical and subcortical imaging (Cai et al., 2016; Kitamura et al., 2015; Pinto and Dan, 2015; Yu et al., 2017). In contrast to the two-photon system, the axial resolution is limited and there is a higher degree of contamination from neuropil fluorescence and out-of-focus signals.

Thirdly, *fiber photometry* (Figure 1.9C) does not provide cellular resolution but, in turn, it captures the bulk fluorescence arising from the summed activity of the GECI-expressing population under the implanted fiber (Cui et al., 2013; Gunaydin et al., 2014; Parker et al., 2019). The typical optic fiber diameter is 400 μm, making it less invasive that GRIN lenses, which typically have a diameter of 1 mm. However, the use of an isosbestic signal or another fluorophore independent of calcium concentrations is recommended to eliminate motion artefacts or non-physiological signaling. In the context of this thesis, fiber photometry was chosen for the recording of GCaMP-expressing PV interneurons due to several reasons. Although PV interneurons possess extensive axonal arborization, they represent a relatively small fraction of the total neuronal population within the DG, with their somas sparsely distributed (mainly) throughout the granular layer. Opting for fiber photometry, rather than other calcium imaging techniques offering cellular resolutions, was deemed advantageous by maximizing the availability of

fluorescence signals captured by the optic fiber. Another important reason motivating our decision was that the use of head-mounted microendoscopes requires a highly invasive surgical procedure compared to fiber photometry, involving, in the case of DG recordings, the removal of parts of the cortex and hippocampal CA1 to enable the GRIN lens implantation. Finally, the simple design of fiber photometry technique also favors its flexible integration with other methodologies, such as simultaneous recordings of electrophysiological or BOLD fMRI signals. Both combinations have a high potential to probe local and global circuits in the brain.

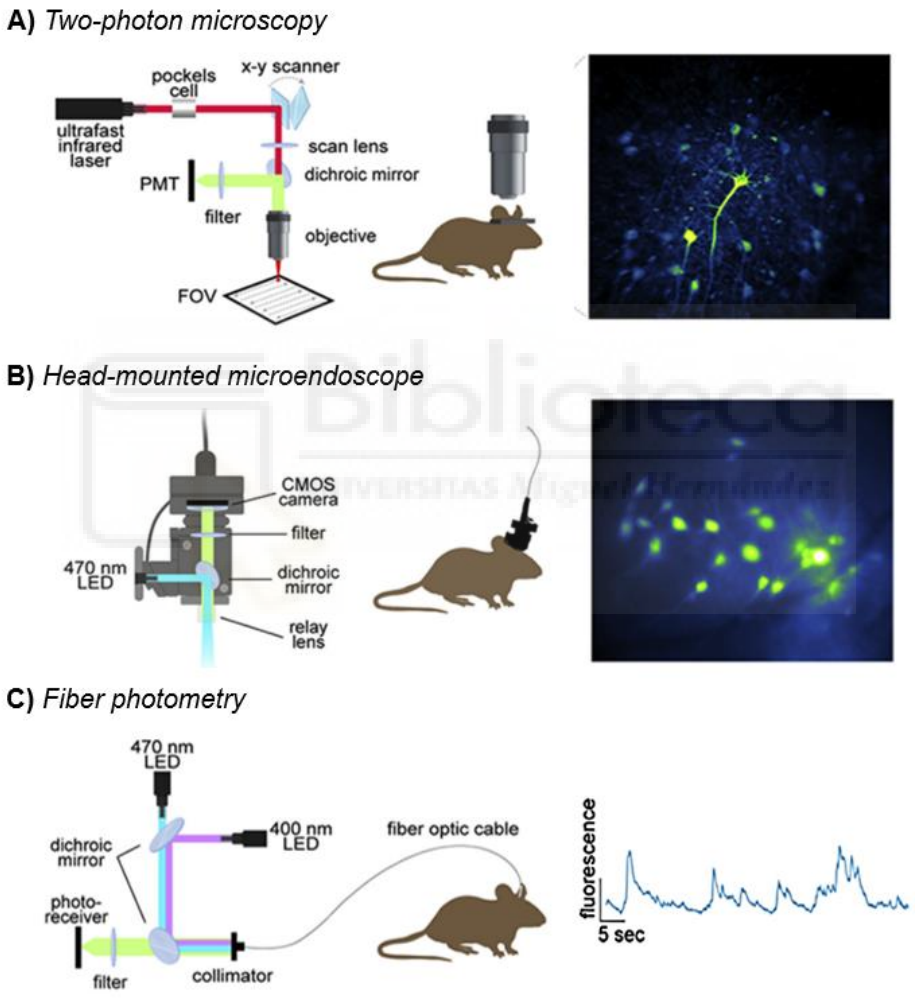

Figure 1.9. Calcium imaging techniques for in vivo conditions
(A) Illustration showing two-photon microscopy technique which involves the utilization of a pulsed near-IR laser optimized. A scanner directs the excitation spot across the specimen, while the emitted fluorescence is captured by a photomultiplier tube (PMT). **(B)** Illustration showing miniaturized head-mounted microendoscopes technique for single-cell imaging in freely-moving conditions. This device contains both the excitation source and sensors, usually a CMOS camera, allowing cellular resolution imaging during free behavior. **(C)** Illustration showing fiber photometry technique, capturing bulk fluorescence from the collective activity of GECI-expressing populations under the implanted fiber. While it lacks cellular resolution, the optic fiber is less invasive than GRIN lenses. Different fluorophores independent of calcium concentrations are used to minimize motion artifacts or non-physiological signaling (adapted from Siciliano and Tye, 2019).

II. OBJECTIVES

The main goal of this thesis was to investigate the mechanisms that govern the coordination of dispersed cell assemblies within the brain's memory network. Our working hypothesis suggests that local and transient increases in the excitation/inhibition balance in the DG, likely involving a reduction in the inhibitory activity, contribute to enhanced long-range functional connectivity in the network. This facilitates the encoding of new information and its integration to update preexisting memories.

1. To investigate the functional consequences of modulating DG-PV interneurons during the encoding of non-spatial memories.

2. To deepen understanding of DG-PV interneurons in spatial pattern separation, a DG-dependent function.

3. To assess the potential side effects of DG disinhibition during memory encoding.

4. To examine how PV inhibitory activity is regulated during memory-related processes, like exploring novel environments or discriminating objects occupying new locations.

An additional technical objective has been set:

5. To develop an open-source and flexible tool for video processing, multi-point tracking and automated quantification of exploratory behaviors.

III. MATERIALS AND METHODS

3.1. Experiments for DG-PV modulation

This section corresponds to the methodological procedures carried out to approach objectives 1, 2 and 3.

3.1.1. Animals

Knock-in mice (B6;129P2-Pvalb$^{tm1(cre)Arbr}$/J) expressing Cre recombinase under parvalbumin promoter (PV-Cre mice) were originally obtained from Jackson Laboratories (RRID: IMSR_JAX:008069) and then bred in our facilities (RMG Animal House, IN-CISC). They were socially housed in groups of 2 to 5 littermates with food and water available *ad libitum* and maintained at 12/12-h light/dark cycle, standard room temperature (22-25ºC) and relative humidity (50-55%).

A total of n = 21 PV-Cre mice (12 males and 9 females) have been used in this set of experiments, being 8-10 weeks old at the time of surgery. A total of n = 8 C57BL/6J wild-type (WT) mice (4 males and 4 females) were used for one specific task. Additionally, we have used data reported in two databases (with a total n = 92 mice, 52 males and 40 females) from previously performed experiments with PV-Cre mice that underwent similar procedures (pharmacogenetic manipulation of DG-PV interneurons). There is a detailed explanation in the following section *3.1.4. Behavioral procedures* (see also Figure 3.3).

All experiments were approved by the Animal Care and Use Committee of the Institute of Neuroscience (IN-CSIC, Alicante, Spain) and comply with the Spanish (law 53/2013) and European regulations (EU Directive 2010/63/EU).

3.1.2. Virus

We have used Designer Receptors Exclusively Activated by Designer Drugs (DREADDs) in order to selectively manipulate the activity of PV interneurons. DREADDs are a family of engineered muscarinic G protein-coupled receptors (Alexander et al., 2009; Armbruster et al., 2007) to which the endogenous ligand acetylcholine is unable to bind,

but are activated by an exogenous and synthetic agonist, Clozapine-N-Oxide (CNO; ENZO Life Science Inc., New York, USA). Based on the subtype of muscarinic receptor and its linked signal transduction mechanism, binding of CNO has potentially different effects on neuronal activity. Specifically, M3 receptor, that couples to the $Gq_{/11}$ mediated signaling pathway (hM3Dq), leads to increased neuronal firing due to a depolarization of membrane potential by phospholipase C activation following CNO binding (Figure 3.1A). DREADDs based on M4 receptors, coupled to Gi protein (hM4Di), are able to hyperpolarize the cell by inhibiting adenylyl cyclase-dependent pathway, leading to neuronal inhibition. Following systemic administration, CNO's peak effect reaches at 20 minutes, being stable for several hours (Alexander et al., 2009; and see Figure 3.1B).

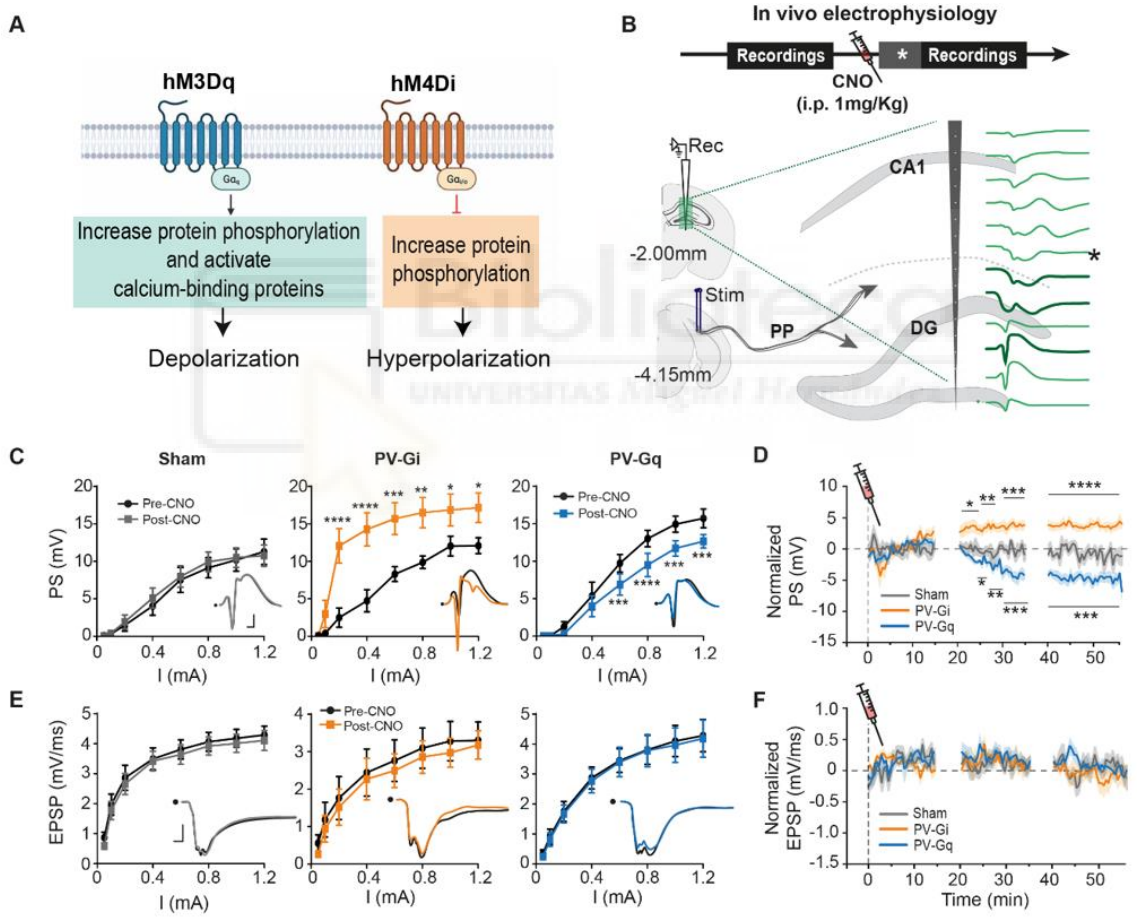

Figure 3.1. Pharmacogenetic manipulations of cell-specific activity by DREADDs.
(A) The administration of CNO in hM3Dq DREADD activates PLC-dependent mechanisms (by stimulating phospholipase C and releasing intracellular calcium stores), resulting in cellular depolarization. In contrast, hM4Di DREADD with CNO leads to cellular hyperpolarization by inhibiting adenylate/adenylyl cyclase and downstream cAMP production. **(B)** Experimental time-course of in vivo electrophysiological recordings before and after the administration of CNO. Grey block with white asterisk indicates the additional baseline recordings post-CNO injection. Schematic representation of the recording and stimulating electrodes and multichannel in vivo electrophysiological recordings (green traces) in response to perforant path (PP) stimulation. Thick traces indicate the selected channels for PS analysis (lower trace) and EPSP (upper two traces). For PV-Gi animals, the larger and faster PS interfered with EPSP measures in the optimal location and a more distal recording is taken (black asterisk). **(C)** Comparison of PP stimulus-

response curves of DG PS amplitude before (black) and after CNO i.p. injection in Sham (grey), PV-Gi (yellow) and PV-Gq (blue) animals. Insets: representative PS waveforms (scale 2 ms, 4 mV). **(D)** Time course of the PS changes after CNO administration. **(E)** Comparison of PP stimulus-response curves of DG EPSP slope before and after CNO i.p. inj-ection (same colour-code as before). Insets: representative EPSP waveforms (scale 1 ms, 1 mV). **(F)**. Time course of the EPSP changes after CNO administration. Group data represent mean ± SEM. *p≤0.05, **p≤0.01, ***p≤0.001, ****p≤0.0001. (See Caramés et al., 2020).

To achieve cell type-specific expression of DREADDs, we have used cre-dependent adeno-associated virus (AAV) vectors, encoding hM3Dq or hM4Di DREADD, intracranially injected in PV-Cre transgenic mice (see next section *3.1.3. Surgical procedures for viral injection*). *AAV5-hSyn-DIO-hM3Dq-mCherry* and *AAV5-hSyn-DIO-hM4Di-mCherry* were used to induce neuronal excitation and inhibition, respectively (Viral Vector Facility, Neuroscience Center Zurich, Switzerland) (Figure 3.2). The efficacy of DG-PV pharmacogenetic manipulation on controlling GCs output has been already demonstrated in previous work (Figure 3.1 C-F).

3.1.3. Surgical procedures for viral injection

For viral injection, mice were anesthetized with isoflurane (4-5% in 0.8 l/min O_2 flow for induction in chamber and 1-2% + 0.8 l/min oxygen for maintenance (IsoFlo, Esteve Laboratorios, Murcia, Spain). When pedal withdrawal reflexes disappear, the animal is removed from the induction chamber to be placed in the stereotaxic frame (David Kopf Instruments, California, USA) and locally anesthetized by subcutaneous (s.c) injection of 0.03-0.04 mL lidocaine (50mg/ml; Braun Medical, Barcelona, Spain) in the incision site. During the whole surgery, the animal's temperature is controlled and maintained at 37±0.5ºC using a heating pad.

After cleaning the incision zone and shaving the fur with a blade, the skin is opened with a scalpel and retracted to expose the skull surface. Under stereotaxic guidance and using bregma and lambda as references, the position of the head is adjusted to achieve correct alignment in DV and LM axis (maximum deviation allowed = 100 μm). Circular trephine holes were carried out bilaterally in dorsal DG hilar coordinates (from bregma: AP +2mm, LM ±1.35mm, DV -1.95mm) by using a 0.5 mm burr in an automatic driller (Fine Science Tools, Germany). Glass micropipettes (ref. 4878, World Precision Instrument, London, UK), which had been previously pulled with puller P-20000 (Sutter Instrument Company, Novato, USA), were filled with mineral oil, attached to an automatic injector (Nanoliter 2010 injector, WPI) and filled with the virus to be injected. Micropipettes are gently

lowered in the brain until reaching the target coordinate, and wait for 10 minutes before injecting 0.5 µl per hemisphere of either *hM3Dq* (n=7, PV-Gq group) or *hM4Di* (n=7, PV-Gi group) virus (Figure 3.2). Once the injection was completed, the micropipette was held in place for an additional 10 minutes to allow the correct virus diffusion, and very gently, was slowly removed. The skin was sutured with silk thread and then mice were removed from the stereotaxic frame and left in a warm cage (tempered with a heating blanket) until they showed complete recovery signs. An additional group of mice were sham-operated to generate the control group (n=7, Sham group).

During the surgery, mice were subcutaneously (s.c.) injected with 3 µl/gr of buprenorphine (0.03 mg/ml; Dechra Veterinaria Products SLU, Barclona, Spain) and 4 µl/gr of meloxicam (0.5mg/ml; Girovet, Barcelona, Spain) at least 15-20 minutes before being awakened from anesthesia. Post-surgical analgesic treatment was orally administered for two days, with 1 ml of buprenorphine 0.03 mg/ml diluted in glucose 5% (GlucosaVet; Braun, Barcelona, Spain) absorbed by a hypercaloric pellet.

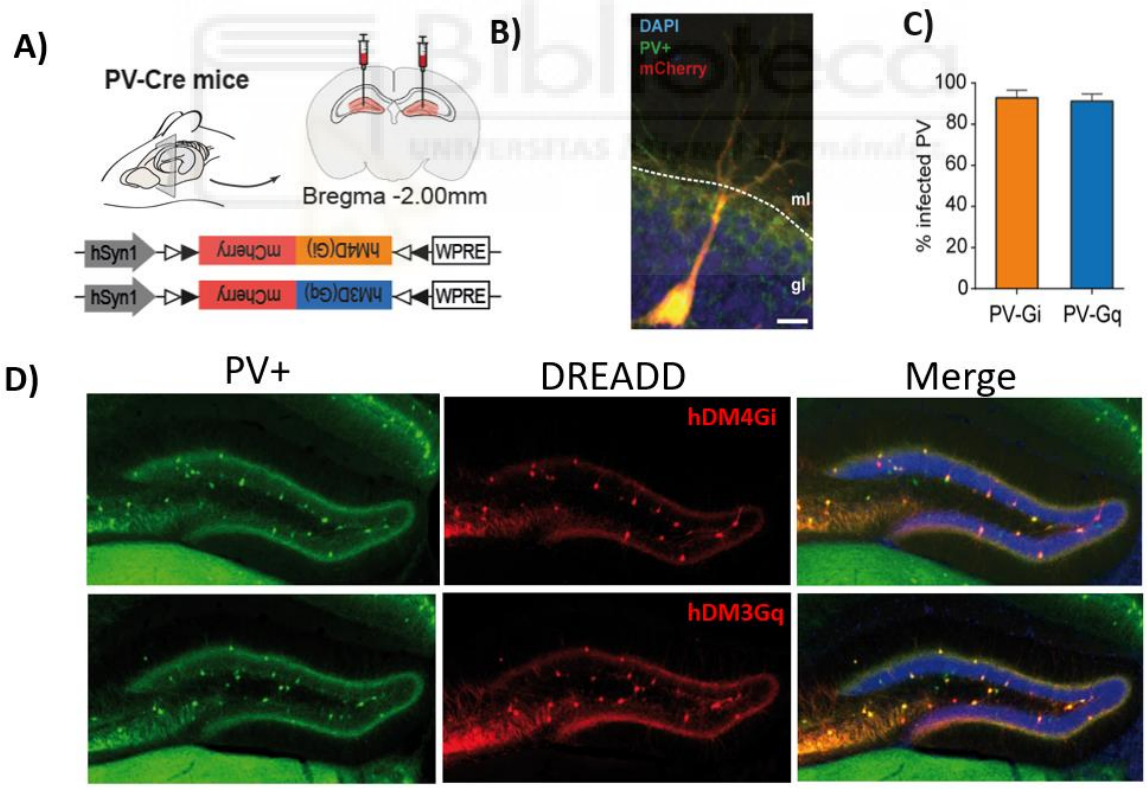

Figure 3.2. DREADDs expression in PV interneurons in dorsal DG.
(A) Schematic representation of bilateral virus injection and viral constructs utilized to inhibit (orange) or activate (blue) PV interneurons. **(B)** Zoom in on a PV+ cell infected with hM3D construct. Scale bar: 10 µm. (C) Efficiency of DREADDs expression in the DG expressed as the % of infected PV-cells in PV-Gi (yellow) and PV-Gq (blue) animals. Data show mean ± SEM. **(D)** Representative pictures showing the reporter of the virus infection (mCherry), immunolabelled against PV protein (green) and counterstained with DAPI (cell nuclei, blue). Scale bar: 100 µm. Adapted from Caramés et al. (2020).

3.1.4. Behavioral procedures

Two weeks after surgery, mice started being habituated to the dimly lit testing room and handled by the experimenter. The experimental room was divided by a curtain to separate the experimenter from the testing zone, where mice perform the tasks. The walls of the testing zone had different visual cues that remained constant until completion of all the experiments.

As general procedures, mice were always acclimated for 20-30 minutes to the testing room before starting any experimental session, and water with ethanol 70% was used to clean behavioral apparatuses between subjects. Importantly, to minimize negative interactions with mice performance, the i.p. injection of CNO was always administered in a different room where mice never perform any behavioral task. A second experimenter was required to sequentially inject the drug at a given time before the encoding session (between 60-90 minutes, depending on the duration of the encoding session), specified below in the description of each experiment.

Behavioral testing started 3-4 weeks after surgery to allow viral infection. Mice performed a battery of memory-related behavioral tasks to assess different aspects of memory, waiting 4-7 days between experiments: NOR ("what" memory), SDT ("who" or social memory) and MIP[1] (memory capacity) tasks (Figure 3.3A). Additionally, 2 databases reporting the results of previously performed NOL ("where" memory) (Figure 3.3B) and SETA[2] (spatial pattern separation) tasks were used in this thesis (Figure 3.3C). These experiments were conducted in collaboration with Raquel Garcia-Hernandez and Dr. José María Caramés (current and former PhD students in the laboratory, respectively).

Note that the choice of trained or rewarded behaviors has been avoided in our experiments. In turn, all the performed tasks were based on the innate preference of mice towards novelty (Eichenbaum et al., 2007; Ennaceur and Delacour, 1988) a measure of memory.

[1] *Multiple Input Patterns* task is explained in detail below. This paradigm has been conceptualized, designed and implemented during the development of this thesis. Raquel Garcia-Hernandez (PhD student) was involved in the conceptualization of the protocol and construction of the apparatus. RGH and Analia Rico (technician) were involved in the performance of pilot studies.

[2] *SETA* task is explained in detail below. This paradigm was co-developed with Dr. Jose María Caramés (former PhD student in the laboratory) and additional data of this task were already presented in his thesis).

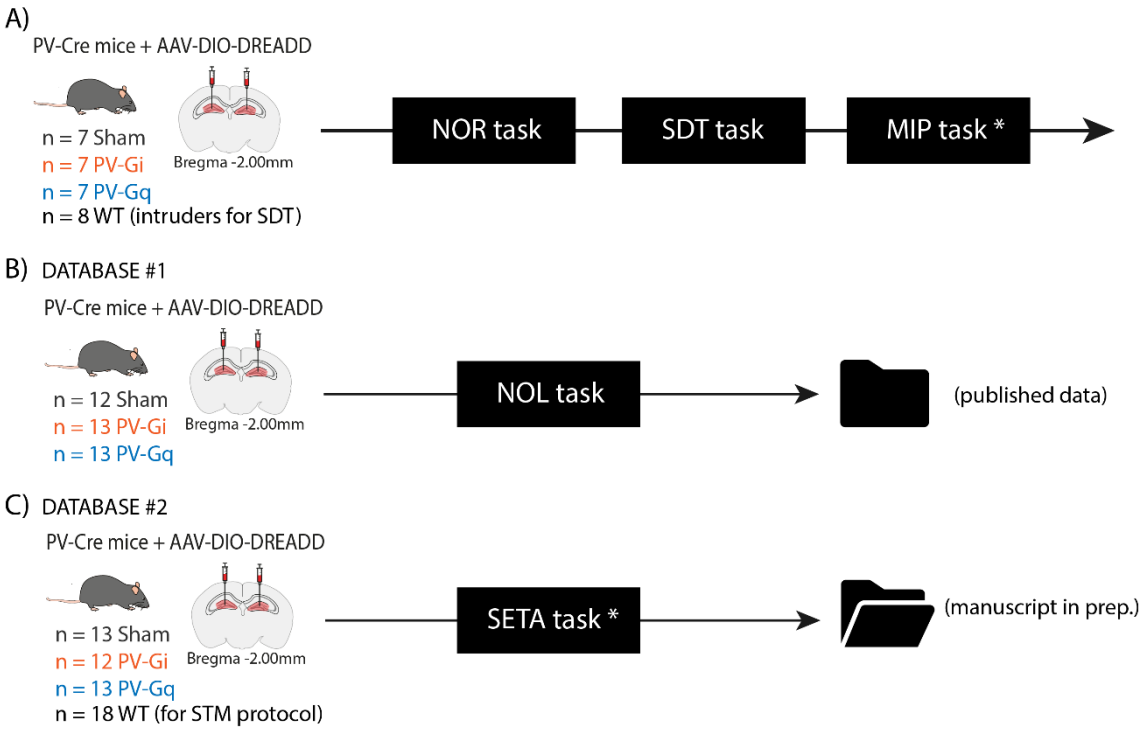

Figure 3.3. Behavioral experimental designs
(A) Batch of animals that conducted NOR, SDT and MIP tasks. **(B)** Database with a batch of animals that conducted the NOL task. Data used to validate RodEx and presented in Figure 1.8 (From Caramés et al., 2020). **(C)** Database with a batch of animals that conducted the SETA tasks. * indicates our developed behavioral tests.

3.1.4.1. Standard behavioral paradigms

In order to assess the role of DG-PV interneurons in the encoding of different types of memory, we conducted three classical paradigms based on mice spontaneous exploration and their preference towards novel stimuli:

Novel Object Location task (NOL). This task was performed by n=37 PV-Cre mice (n=13 PV-Gi, n=13 PV-Gq and n=12 Sham; see Figure 3.3B) to evaluate long-term spatial memory and the obtained results were reported in Caramés et al., (2020). The standard protocol for this task consisted of 3 phases: habituation, encoding and retrieval or test (Figure 3.4A). On day 1, mice performed 2 habituation sessions with an inter-trial interval (ITI) of 3 hours, where they entered into an empty open field and were allowed to freely explore the context for 5 minutes. The apparatus was a white squared box of methacrylate (50 x 50 x 30 cm high) with different visual cues attached at the top center of each wall. On day 2, mice were injected with CNO (1mg/kg i.p.) 90 minutes before starting the encoding session, where they encountered two identical objects in the already familiar

context and were allowed to freely explore them for 10 minutes. On day 3, during the testing session, mice returned to the open field for 10 minutes where one of the objects was displaced to a different location, while the other remained in the same position as the day before. During both encoding and test sessions, objects were equally distanced from the walls (13.5 cm) and the new position of the displaced object was counterbalanced across subjects. The time that the subjects spend exploring each object was first manually scored by double-blind experimenters and then automatically quantified using RodEx (see *4.1.2. Validation* in Results).

Novel Object Recognition task (NOR). This task was performed by n=21 PV-Cre mice (n=7 PV-Gi, n=7 PV-Gq and n=7 Sham; see Figure 3.3A) to test long-term object recognition memory. We followed the same 3-day protocol used to test spatial memory in Caramés et al., (2020) (Figure 3.4B). Habituation and encoding phases were exactly the same as in the NOL task (explained above). But here, during the test session, one of the objects was replaced by a novel one (different shape, texture and color but similar size). Objects' exploration was automatically measured with RodEx (see *4.2.1. On the role of DG-PV interneurons in non-spatial memories* in Results).

Social Discrimination Task (SDT). Following the NOR task, the same animals (Figure 3.3A) performed a slightly modified version of the standard SDT protocol (Nadler et al., 2004) to assess social memory (Figure 3.4C). The task was performed in a typical three-chamber maze (60 x 40 x 22 cm), with free access between chambers, divided by transparent Plexiglas walls. Each side chamber contains a small wire cage (9 cm diameter x 15 cm high) with bars spaced 1 cm, allowing the interaction between mice but avoiding aggressive behaviors between them. On day 1, mice were allowed to explore the 3-chamber arena containing 2 *empty cages* (5-min habituation session). On day 2, mice were injected with CNO (1mg/kg i.p.) 90 minutes before starting the encoding session, composed of 2 identical trials (S1 and S2 trials), where subjects encountered a mouse never seen before (intruder 1) in one of the cages (*social cage*), while the other remained empty (*empty cage*). S1 and S2 lasted 5 minutes, with an ITI of 3 min, and the position of *social* and *empty* cages remained constant but counterbalanced between subjects. Day 3, during the test session, mice encountered the familiar intruder 1 in the same cage than the day before, and a new mouse never met before (intruder 2). The time that mice spent exploring the *empty vs. social* cage (S1 and S2 trials, encoding phase) or the familiar *vs.* novel intruder (social novelty test) was automatically quantified using RodEx (see *4.2.1.*

On the role of DG-PV interneurons in non-spatial memories in Results). In this experiment, 1 subject from the Sham group was excluded from the analysis due to the high levels of anxiety shown (this subject was attacked in its home-cage, probably by the dominant cage mate, before starting the sessions). As intruder, we used C57BL/6J WT mice (n=4 males and n=4 females), who were previously habituated to the experimental room, to be handled by the experimenter and to be introduced within the cages and placed in the three-chamber maze. Intruders were of the same sex and similar age as experimental subjects.

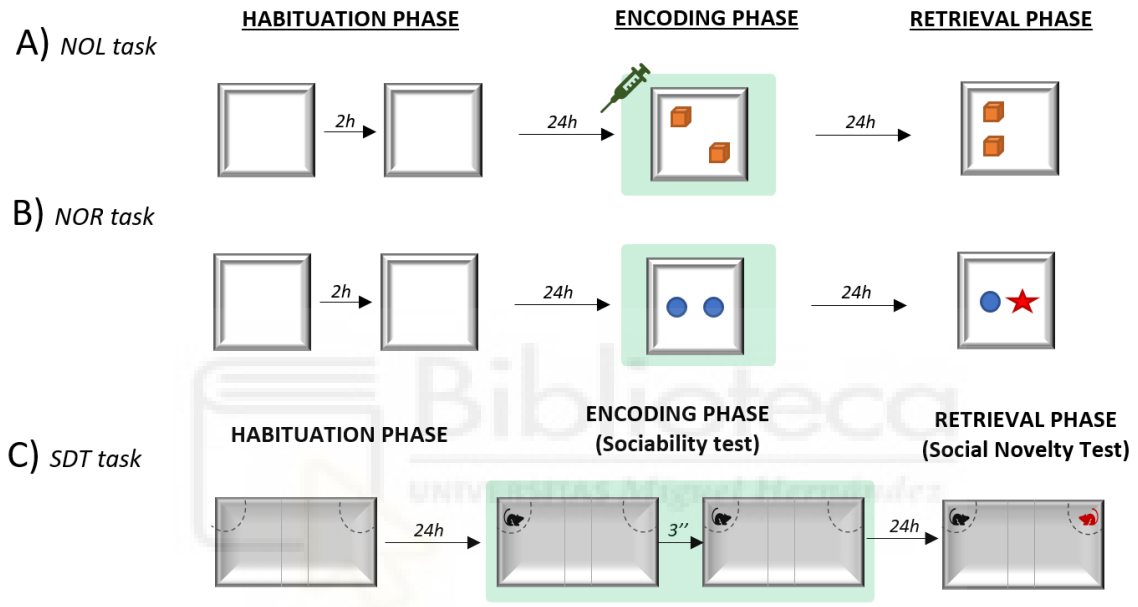

Figure 3.4. Standard behavioral procedures
(A) Schematic representation of the NOL protocol used to assess spatial memory. **(B)** Schematic representation of the NOR protocol used to assess non-spatial memory. **(C)** Schematic representation of the SDT protocol used to assess social memory. Red mouse represents the novel social stimuli. Green shadows represent the specific phase at which PV interneurons are under the effect of CNO (encoding phase).

3.1.4.2. Newly developed behavioral paradigms

In addition to carrying out well-known standard protocols, two different behavioral paradigms have been conceptualized, designed and implemented during the development of this thesis in order to assess spatial pattern separation and memory capacity:

SETA task for pattern separation. This task was designed to assess spatial pattern separation. We based our protocol on previous paradigms (van Hagen et al., 2015), where progressively displacements of objects are used to introduce subtle changes in a familiar environment. Data reported in this thesis were obtained with previous experiments and

preliminarily shown in the Thesis of Dr. Jose María Caramés (2018). The database contains the results of n = 56 mice (n=12 PV-Gi, n=13 PV-Gq, n=13 Sham and n=18 C57BL/6J WT mice; see Figure 3.3C). The behavioral apparatus (Figure 3.5A) was specifically designed and built for this experiment, consisting of a semicircular open field (70 cm length x 35 cm diameter x 40 cm high) of white methacrylate connected to a smaller chamber ("waiting box", 10 cm x 15 cm x 15 cm). We considered this semicircular shape as it allows constant distances between (1) the object and the wall of the maze across the consecutive object displacements and with (2) the animal at the time of the entrance. Moreover, the connected waiting box enables mice transitions without experimenter interventions. The door separating the open field and the waiting box is manually displaced by the experimenter allowing mice freely transitioning, reducing their manipulation during the behavioral performance.

The procedures for the SETA task follow the same 3-stage time flow as in previous tasks: habituation, encoding and testing phases. Habituation session (Figure 3.5B) consists of 5 trials (ITI = 1 min in the waiting box) where mice are allowed to freely explore the semicircular context for 5 minutes. In the single-trial encoding session (Figure 3.5C) mice encounter 2 identical objects located at the starting positions and are allowed to freely explore them for 5 minutes. Finally, the testing session (Figure 3.5D) is composed of 5 consecutive trials with an ITI = 1 min (mice remaining in the waiting box). During the testing trials, one of the objects is gradually displaced 5 cm from its previous location, introducing subtle changes in the spatial information from one trial to the next one. All sessions started placing mice inside the waiting box for 1 minute before opening the door to start the first trial. Mice enter by themselves to the semicircular arena and after 5 minutes, the experimenter opens the door, permitting mice to leave the arena and enter in the waiting box for an additional 1 minute.

The protocol can be performed at short- or long-term (STM and LTM protocols, respectively, see Figure 3.5E), depending on the ITI between encoding and test sessions. Common to both protocols, 2 habituation sessions are performed on consecutive days (day 1 and 2). In the STM protocol, encoding session is carried out on day 3 and testing session takes place immediately after (ITI = 1 min in the waiting box). In the LTM protocol, on day 3, mice are injected with CNO (1 mg/kg i.p.) 90 minutes before starting the encoding session and are tested at day 4 (ITI = 24 hours).

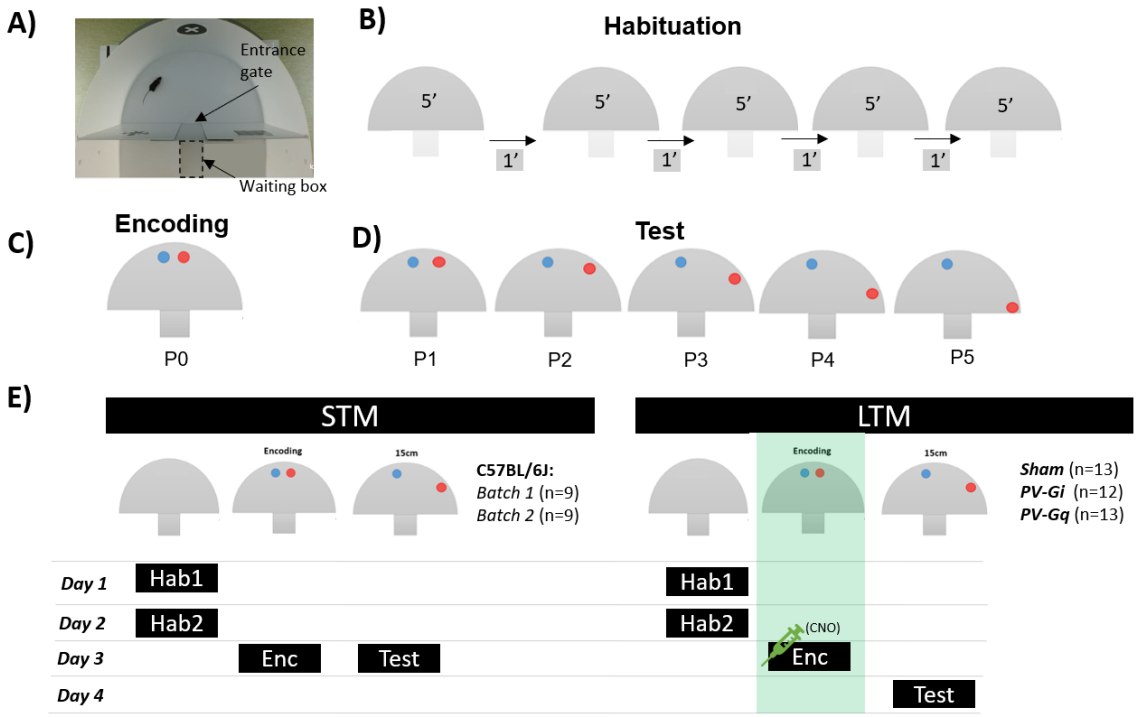

Figure 3.5. SETA task procedures.
(A) Picture of the SETA maze with black arrows indicating the waiting box (dotted square) and the entrance door that separates it from the semicircular arena. **(B-D)** Schematic representation of the different sessions. Semicircular shape permits to maintain the distance between mouse at the beginning of each trial (entrance point), regardless of the objects' position. 12 magnets were placed under the ground in the exact position where objects will be placed. Objects have magnets and are identical, blue and red colors just represent the fixed and the moving object. **(E)** Experimental time flow for the STM and the LTM protocols

Multiple Input Patterns task (MIP). Same animals used in the NOR and STD experiments performed this task (Figure 3.3A), that has been devised as an extension of the NOL task, aiming to assess spatial memory capacity. The objective is to examine the ability of mice to encode and retain information regarding changes in object locations. To achieve this, the mice are subjected to a series of consecutive input patterns that are temporally coincident. Subsequently, their performance is evaluated based on the number of input patterns in which they can successfully encode and accurately recall the altered object locations. We defined the *input pattern* as a single environment with its specific object-context and object-location associations. According to this definition, the standard NOL task can be considered as a single input pattern paradigm. In our MIP procedure (Figure 3.6), object-location recognition is tested in 4 different contexts (4 input patterns). During the development of the protocol, several considerations were taken into account:

→ In order to reduce the manipulation of mice during the performance of the task, the behavioral apparatus consisted of a rectangular corridor of 70 cm length x 12 cm heigh x 10 cm width of white methacrylate connected to a squared box (open field

used in GCaMP experiments, see description in section 2.6) in one extreme and to a semicircular open field (the one used for the SETA task) in the other, as shown in Figure 3.6A. Open fields' entrance gates are manually opened by the experimenter to allow free passage of mice.

→ Two different contexts per open field have been generated to create 4 distinguishable input patterns. Diverse walls and floors were built with methacrylate, polypropylene and textured adhesive tapes materials to be assembled in the square and semicircular open fields, generating different contexts (see Figure 3.6B). We used a color-based nomenclature: '*Red'* and '*Yellow'* contexts were built to be used in the semicircular arena, while '*Blue'* and '*Green'* contexts were used in the square arena.

→ The order of presentation of contexts varied from session to session to avoid the implication of sequence learning mechanisms or strategies.

→ 2 identical objects are presented per context. The 4 pairs of objects are different in shape, material, size and texture to enhance the specificity of object-context association. Initial objects' positions (during encoding session) and the final position of the displaced object (during test session) were intended to differ as much as possible between contexts. Objects' positions were not counterbalanced across subjects due to the relatively small sample size (n = 7 per group).

→ Pilot studies with C57BL/6J wild-type mice (n = 15) and with a batch of PV-Cre mice (n = 8 *PV-Gi*, n = 8 *PV-Gq* and n = 8 *Sham* mice) were performed before setting the final protocol (data not shown in the thesis).

Behavioral protocol followed the same 3-day time flow followed in the NOL task: habituation, encoding and test sessions, where each session consists of 4 trials (the visit to each context) (Figure 3.6C). Day 1 (habituation phase), mice visited sequentially the 4 contexts (*Blue→Yellow→Green→Red*) and were allowed to freely explore them for 10 minutes, waiting 2 minutes in the central corridor at the beginning of the session and between contexts. These timings lead to sessions of 50 minutes per subject (4 trials of 10 minutes + waiting periods). Day 2 (encoding phase), mice received an i.p. injection of CNO (1 mg/kg) 60 minutes before starting the encoding session, in which they visited the 4 contexts in a different order (*Red→Green→Yellow→Blue*). In each context, mice encountered two identical objects at specific locations. Day 3 (testing phase), one object is displaced to a different location at each context (*Green→Red→Blue→Yellow*), while the other object remains immobile. Memory capacity was tested by measuring in how many

contexts mice prefer to explore the novel object location, meaning that they are able to discriminate object's displacement.

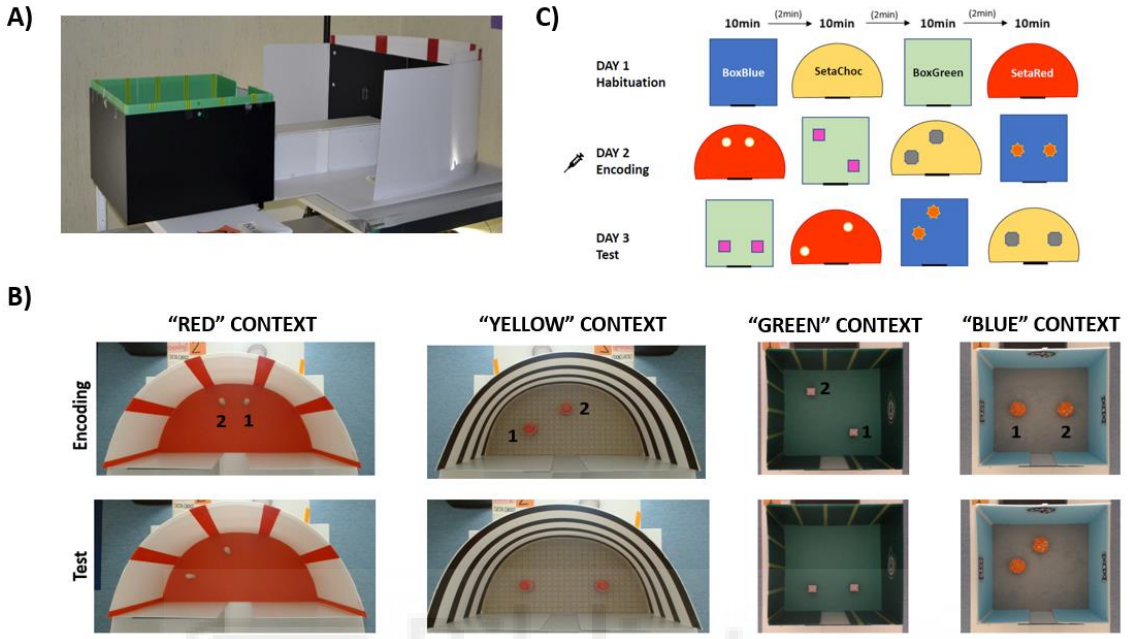

Figure 3.6. Multiple Input Patterns (MIP) designed task to assess memory capacity.
(A) Picture with the behavioral setup. White corridor links both square and semicircular arenas. **(B)** Pictures of the four "input patterns" used in the MIP task. Each input pattern consists of a specific context with its associated pair of objects. Numbers indicate the fixed (1) and the displaced (2) objects. **(C)** Schematic representation of the MIP protocol with the followed sequences of context presentation.

3.1.4.3. Data acquisition and behavioral quantification

A webcam (Logitech HD Pro C920) held by a tripod was placed above the apparatus in the center of the testing zone and was connected to the computer in the experimenter zone to enable live viewing and recording of mice performance. All the recorded video files were processed offline using RodEx (see 4.1 in Results), obtaining (1) centroid and head tracking, (2) measurements of locomotor activity, such as distance traveled, movement velocity or centroid *vs.* periphery occupancy, and (3) automatic quantification of objects' (or conspecifics') exploration.

Then, as a measure of memory performance in NOR ("what" memory), SDT ("who" or social memory), SETA (pattern separation) and MIP (memory capacity) tasks, we

calculated the discrimination index, which reflects the time spent exploring the novel stimulus relative to the total time of exploration, following this formula:

$$DI = \frac{t_{New}}{(t_{New} + t_{Old})}$$

where t_{New} refers to the time exploring the novel object (NOR task), the novel mouse (SDT task) or the displaced object (NOL, SETA and MIP tasks), and t_{Old} the time exploring the familiar one. In encoding sessions, t_{New} refers to the object that will be replaced or displaced in the following testing session. DI values range from 0 to 1, where 0.5 denotes equal preference for both objects and values higher than 0.5 reflect preference for the novel stimulus.

Following data processing and statistical analysis were performed using customized MATLAB scripts and GraphPad Prism software. If any additional measurement has been performed, it is clearly stated in the text.

3.1.5. Computational model

Computational simulations were designed and performed by Dr. Encarni Marcos to assess how changes in DG inhibitory tone could affect spatial memory formation (Figure 3.7). The model consists of two modules, as previously applied in (Ornelas et al., 2022): one module with functionalities related to the hippocampus, such as learning and pattern separation, and another module with functionalities related to the prefrontal cortex, such as decision-making.

The hippocampal module was modelled as a neuronal layer with convergent projection from input patterns to memory space, local competition and stable sparsity (Rennó-Costa et al., 2010, 2019). The local competition is performed through an E%-Max Winner-Take-All mechanism (De Almeida et al., 2009) which simulates different levels of inhibition. This rule implies that only neurons whose activity is within an E% distance from the neuron with the maximum activity will be activated. Thus, higher values of E% result in less inhibition, as the probability of a neuron being active increases, and vice versa. For control conditions, E% is set at 10%. For downregulated inhibition conditions (PV-Gi group), EGi% is increased at 32%, while for upregulated inhibitory activity (PV-Gq group), EGq = 2%.

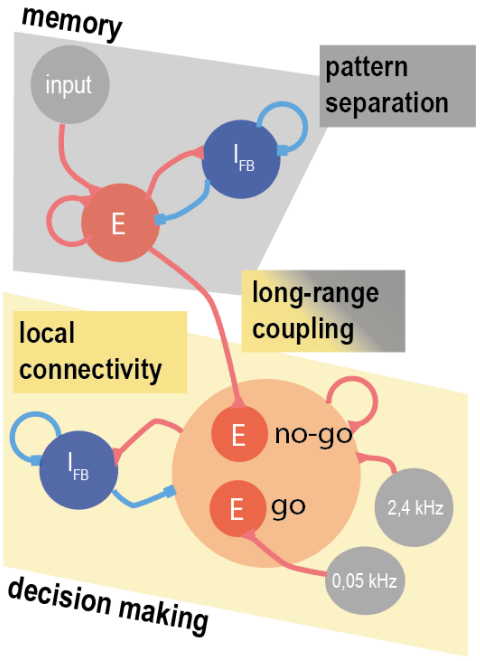

Figure 3.7. Hippocampus-Prefrontal Cortex model.
Architecture of the neuronal circuit with capabilities associated with the hippocampus and prefrontal cortex. The model consists of two modules. The first performs learning through synaptic plasticity and pattern separation, while the second module makes decisions.

In the model, the activity of 200 neurons simulates the "sensory" input pattern projected to the hippocampal module. The activity of each neuron has a random value obtained from a uniform distribution and normalized to a total sum of 1. These neurons connect with a certain probability (25%) to 500 neurons in the hippocampal module. During learning, the synapse of an active neuron contacting another active neuron of the hippocampal module (a_j) increases depending on the activation value of the presynaptic neuron (a_i) and a learning parameter (λ):

$$\Delta W_{i,j}(t) = \lambda * a_i(t) * H(a_j(t))$$

where $H(a_j(t))$ is a Heaviside step function. In these simulations, we have used 50 input patterns (except when investigating memory capacity, where the number of patterns varies) and a learning parameter of λ=0.1 to produce stable representations of learned patterns (Ornelas et al., 2022). This model to simulate the hippocampus was selected based on its previously proven validity to explain some of the dynamics taking place in the hippocampus, such as local competition or rate remapping (De Almeida et al., 2009;

Rennó-Costa et al., 2010). Then, the sum of the hippocampal neurons' activity is projected onto the module associated with the prefrontal cortex, where the decision is made.

The decision-making module is a mean-field approximation of a realistic network of integrate-and-fire neurons (Wilson and Cowan, 1972). The rate-based model is a well-established approximation that allows the study of neuronal activity while reducing the computational expenses of modelling individual neurons. Moreover, it is supported by the fact that neurons are organized in neuronal populations with similar properties (Abbott, 1991). The model consists of two groups of excitatory neurons with recurrent connections ("go" and "no-go" groups) that compete through mutual inhibition (Marcos et al., 2013, 2019). The activity of the excitatory groups varies according to:

$$\tau \frac{dy_1(t)}{dt} = -y_1(t) + f(act_1 + \omega_+ y_1 - \omega_- y_2) + \sigma\xi(t)$$

$$\tau \frac{dy_2(t)}{dt} = -y_2(t) + f(act_2 + \omega_+ y_2 - \omega_- y_1) + \sigma\xi(t),$$

where y represents the activity of each group, ω is the weight of the connections (ω_+ recurrent; ω_- inhibitory), *act* represents the external input to each group, $\sigma\xi$ represents the network fluctuations and *f(.)* is a sigmoidal function of the form:

$$f(x) = \frac{f_{max}}{1 + e^{\frac{-(x-\theta)}{k}}}$$

where f_{max} defines the maximum activity (at which the neuronal network saturates). The network fluctuations are simulated through a Gaussian noise with mean 0 and variance 1 (ξ), which simulates having a finite set of neurons. We use a value of σ = 0.01 spikes·s^{-1} and the strength of the connections is kept constant during the simulations: τ = 20 ms, ω_- = 1, ω_+ = 1, f_{max} = 40 spikes·s^{-1}, θ = 4 spikes·s^{-1} and k = 11 spikes·s^{-1}. The decision is made when the difference in activity between the two groups exceeds a threshold of 30 spikes·s^{-1}.

To simulate the discrimination ratios during the testing sessions, the input to the "go" group in the decision-making module was set constant, simulating the output of the hippocampal module for familiar patterns. The "no go" group received the output of the hippocampal module as the sum of the activity of its neurons. The decision was then considered to be made towards the object when the "go" group won the competition. The DI was calculated as the ratio between the number of decisions towards exploring the

object when the input pattern is the novel one and the number of decisions made towards exploring the object when the pattern is familiar or novel (total cases).

$$DI\ predicted = \frac{Ngo}{Ngo + Nnogo}$$

3.1.6. Histology and Immunohistochemistry

After completion of the experiments, deeply anesthetized mice were perfused intracardially with 40mL 0.9% saline and 50mL of ice-cold 4% paraformaldehyde (PFA) solution. Brains were immediately extracted from the skull and kept for at least 24 h on 4% PFA post-fixation at 4%. Then they were cut in a fixed material vibratome (VT 1000S Leica, Wetzlar, Germany) in 40 μm thick coronal slices.

For immunohistochemical analysis, slices were permeabilized in phosphate-buffered saline (PBS) containing 0.25% Triton and unspecific binding was blocked by adding 5% normal horse serum (NHS) for at least 1 hour. Sections were incubated overnight at 4ºC with monoclonal PV antibody developed in mouse (1:2000, Swant, Switzerland). Then slices were washed in PBS containing 0.25% Triton and incubated for 3 hours with Alexa-488-conjugated goat antibody (anti-mouse, 1:500, Life Technologies, USA). After a final washing with PBS, slices were stained with DAPI, mounted on glass microscope slides (Normax, Portugal) and coverslipped.

3.1.7. Statistical analysis

All statistical analyses were conducted using customized MATLAB scripts (The MathWorks Inc., Massachusetts, USA) and GraphPad Prism version 7.00 for Windows (GraphPad Software, Inc., California, USA). D'Agostino-Pearson test and Levene's test were used to corroborate the normal distribution and the homogeneity of variances of the data, respectively.

To assess intra-group differences, paired t-test for a significance level of $p < 0.05$ was used. To study the differences between experimental groups, we used unpaired one-way ANOVA or two-way ANOVA test, when 2 factors concur (*treatment* and *session*). In case of statistical significance ($p < 0.05$), ANOVA tests were followed by post-hoc Bonferroni's multiple comparison test to check internal relations. In the behavioral

analysis, to compare the similarity between the results obtained from manually extracted data vs. RodEx extracted data, we computed Pearson correlation coefficients, with significance level also set at $p < 0.05$.

If any other statistical approach has been applied, it is clearly stated in the text. Data are expressed in the text as mean ± SEM (unless otherwise specified) and significance levels are expressed in figures with a star-code as follows: * $p < 0.05$, ** $p < 0.01$, *** $p < 0.001$, **** $p < 0.0001$.

3.2. Experiments for PV cell recording

This section explains the methodological procedures to approach objective 4.

3.2.1. Animals

Two animal models have been used for PV cell recordings:

On the one hand, Long-Evans transgenic rats, expressing Cre recombinase under the rat parvalbumin promoter (LE-TG[Pvalb-iCre]2Ottc), from now on called PV-Cre rats, were obtained from the Rat Resource and Research Center (RRRC, #00773, NIDA, USA) to be bred in our facilities. PV-Cre rats were housed in pairs with *ad libitum* access to food and water under a reversed light cycle (12 hours dark/light cycle) with controlled temperature and humidity conditions (22-25ºC and 50-55%). We have used a total of n = 6 PV-Cre rats (4 males and 2 females) to generate the data presented in this thesis.

On the other hand, a total of n = 16 (9 males and 7 females) knock-in PV-Cre mice (see description *3.1.1 Animals*) were used to perform fiber photometry recordings in behaving animals. Mice were socially housed in groups of 2 to 5 littermates with food and water available *ad libitum* and maintained at 12/12-h light/dark cycle, standard room temperature (22-25ºC) and relative humidity (50-55%).

All experimental procedures were approved by the Animal Care and Users Committee of the Institute of Neuroscience (IN-CSIC ethical committee) and performed in accordance with Spanish and European regulations (RD 53/2013 and EU directive 86/609).

3.2.2. Virus

In order to specifically record calcium-based activity specifically from DG-PV interneurons, we have used GCaMP sensors, a single-fluorophore GECI. GCaMP consists of circularly permuted green fluorescent protein (cpGFP), the calcium-binding proteins calmodulin (CaM) and CaM-interacting M13 peptide. Calcium binding causes conformational changes in the CaM-M13 complex, leading to an increased brightness of GFP (Chen et al., 2013) (see Figure 3.8A).

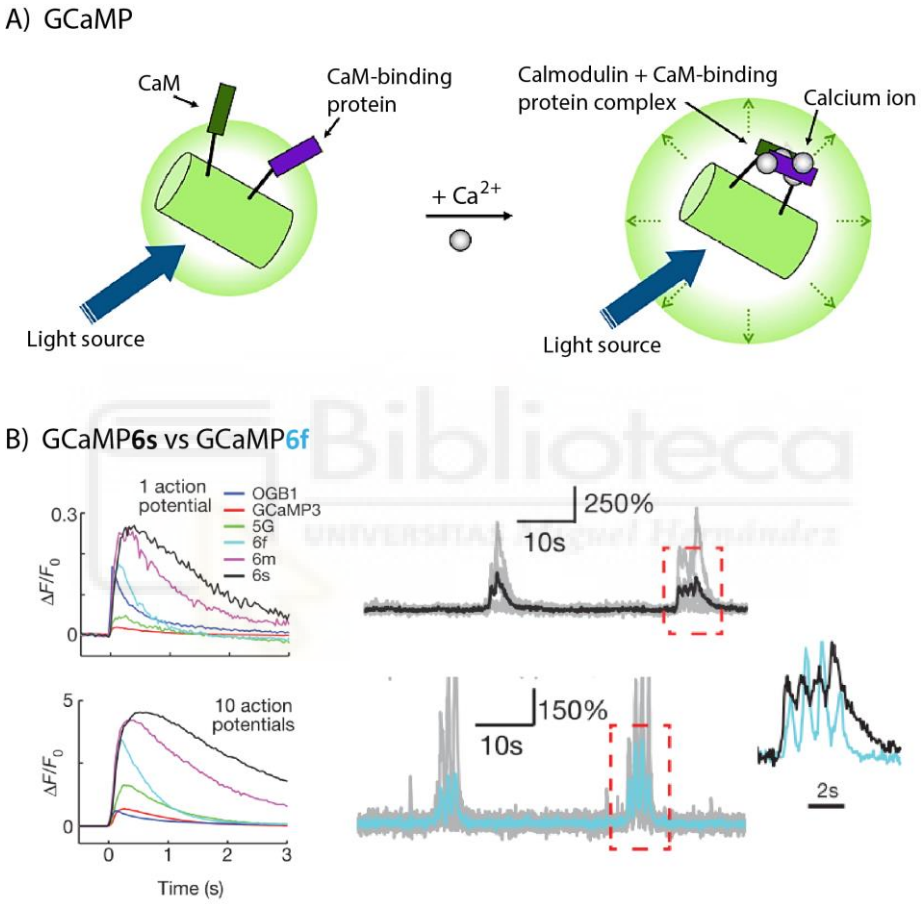

Figure 3.8. GCaMP6 calcium indicators and variants dynamics.
(A) Mechanism of action of GCaMP sensor. GFP brightness increases when calcium binding induces conformation changes in CaM-M13 complex (from Oh et al., 2019). **(B)** Comparison between 6s (black) and 6f (blue) variants. *Left*, averaged responses of different calcium sensors after a one (top) or ten (bottom) action potentials recorded in dissociated cells. *Right*, comparison of evoked responses recorded in the mouse visual cortex after visual stimulation and zoom in of red boxes (modified from Chen et al., 2013).

Despite the fact that we currently have available improved GCaMP variants (i.e., GCaMP7 or jGCaMP8; (Dana et al., 2019; Zhang et al., 2023), during the development of this thesis we used the slow (s) and fast (f) variants of the GCaMP6 sensor, the most

commonly used GECI at the time this thesis was developed. GCaMP6s and GCaMP6f sensors present different kinetics, with lower sensitivity for faster kinetics (Figure 3.8B).

We combined viral transduction of cre-dependent AAVs with transgenic PV-Cre mice and rats by using the following viral constructs: *AAV5-Syn-Flex-GCaMP6s-WPRE.SV40* (#100833, Addgene, USA) and *AAV5-Syn-Flex-GCaMP6f-WPRE.SV40* (#100837, Addgene, USA). In order to avoid GCaMP overexpression, viruses were diluted in PBS (1:8) to a titer of $8x10^{11}$ vg/ml.

3.2.3. Surgical procedures

For GCaMP recordings in anesthetized animals, n = 6 PV-Cre rats, with a weight of 250-350 gr, were injected with 0.5 µl of cre-dependent GCaMP6s (n=3) or GCaMP6f (n=3) AAV in the dorsal DG. Rats were generally anesthetized with isoflurane (4-5% and 1.5-3% in 0.8 l/min O_2 flow for induction and maintenance, respectively) and locally anesthetized by s.c. injection of 0.2 ml lidocaine (50 mg/ml; Braun Medical, Barcelona, Spain). Incision site is cleaned and shaved before cutting the skin to expose the skull bone. Using bregma and lambda references, the position of the head is adjusted to achieve correct alignment in DV and LM axis (maximum deviation allowed = 300 µm). At this point, rats were administered s.c. with 3 µl/gr of buprenorphine (0.003 mg/ml), so that the analgesic effect was maximal at the time of awakening from anesthesia. A manual drill was used to make a trephine hole at left DG coordinates (from bregma: AP+3 LM±2.5 DV– 2.9 mm) and the dura was carefully punctured with a needle to allow the penetration of the infusion cannula (33-gauge, 15 mm length, C1315I/SPC, Plastics One Technologies, USA). It was slowly lowered until the target coordinates and held in place for 10 minutes before starting virus infusion. A flexible plastic tube (Plastics One Technologies, USA) filled with mineral oil connected the cannula to a 1-µl microsyringe (Hamilton, USA) in a microinfusion pump (Legato 101, World Precision Instruments, USA). After virus delivery at an infusion rate of 50 nl/min, the cannula was held in place for 10 minutes before gently removing it. Craniotomy was covered with tissular adhesive and the skin was sutured with silk thread. Then, rats were removed from the stereotaxic frame and left in a warmed cage (tempered with a heating blanket) until they showed complete recovery signs. During the whole surgery, vital parameters (heart and breath

rate and oxygen saturation) were controlled by a paw-clip pulse oximeter (MouseOx Plus, Starr Life Sciences, USA) and temperature was kept constant (37±0.5 ºC).

For GCaMP behavioral experiments, n = 15 PV-Cre mice were injected in the left dorsal DG with cre-dependent AAV-GCaMP6s and chronically implanted with an optic-fiber. Surgical procedures for viral injection were carried out in the same way as previously described for DREADDs injections, with some particularities: (1) before drilling the craniotomies, the surface of the skull was scratched with a scalpel to facilitate further dental cement attachment and increase implant durability; (2) mice were injected unilaterally in the left DG (from bregma: AP +2mm, LM ±1.35mm, DV -1.95mm) and the surgery continued after virus delivery. Once the micropipette had been removed, brain surface was carefully cleaned and the dura was punctured to allow the introduction of the implantable fiber-optic cannula. We used silica mono fiber-optic cannula of 400 µm diameter, NA 0.48 and 3mm length, with SM3 receptacle (MFC, Doric Lenses Inc., Canada) connected to a stereotaxic cannula holder (SCH, Doric Lenses Inc., Canada). The optic-fiber was slowly lowered until 100 µm above the injection site, at the coordinates: AP +2mm, LM ±1.35mm, DV -1.85mm. After waiting 20 minutes for tissue accommodation, we applied several layers (usually 2-4) of dental cement (opaque polymer, Super-Bond C&B, Sun Medical, Japan) until a complete fixation of the optic-fiber. Post-surgical procedures were the same as for DREADDs experiments, taking into account the Mouse Grimace Scale (Langford et al., 2010) to assess mice welfare and recovery. Chronically implanted mice were housed in groups of 3-5 mice per cage.

3.2.4. Fiber photometry setup

The dual-excitation single-detection fiber photometry system (Doric Lenses, Canada) was used to record GCaMP fluorescence activity (Figure 3.9A). In this system, two LEDs (465 and 405 nm wavelengths), controlled by a LED driver (LEDD) are coupled to a fluorescence mini-cube (FMC4), which has 2 dichroic mirrors to combine and separate excitation and emission wavelengths, respectively, and narrow bandpass filters limiting the excitation fluorescence spectrum (Figure 3.9B). The 405-nm light excites GCaMP autofluorescence or calcium-independent fluorescence (isosbestic point), while the 465-nm wavelength excites calcium-dependent fluorescence. Both signals, emitted at 500-550 nm, are reflected on the FMC4 dichroic mirror and sent to a Newport Visible Femtowatt

photoreceiver module (NPM model 2151). Fiber photometry console (FPC) controls and synchronizes light output and the input data acquisition and it integrates with Doric Neuroscience Studio v5 software. Software interface enables the control of FPC and displays real-time recordings of the input signals, including TTL signals.

3.2.4.1. Data acquisition

In order to distinguish 465-nm and 405-nm emitted fluorescence within a single wavelength (500-550 nm), we have used the Lock-in acquisition mode, which allows separating both signals using a single detector. Each LED emits a sinusoidal signal at a given frequency (carrier frequency). Then, GCaMP and isosbestic fluorescence can be separated by targeting the carrier frequencies on the detected signal, a process known as demodulation. (Figure 3.9C).

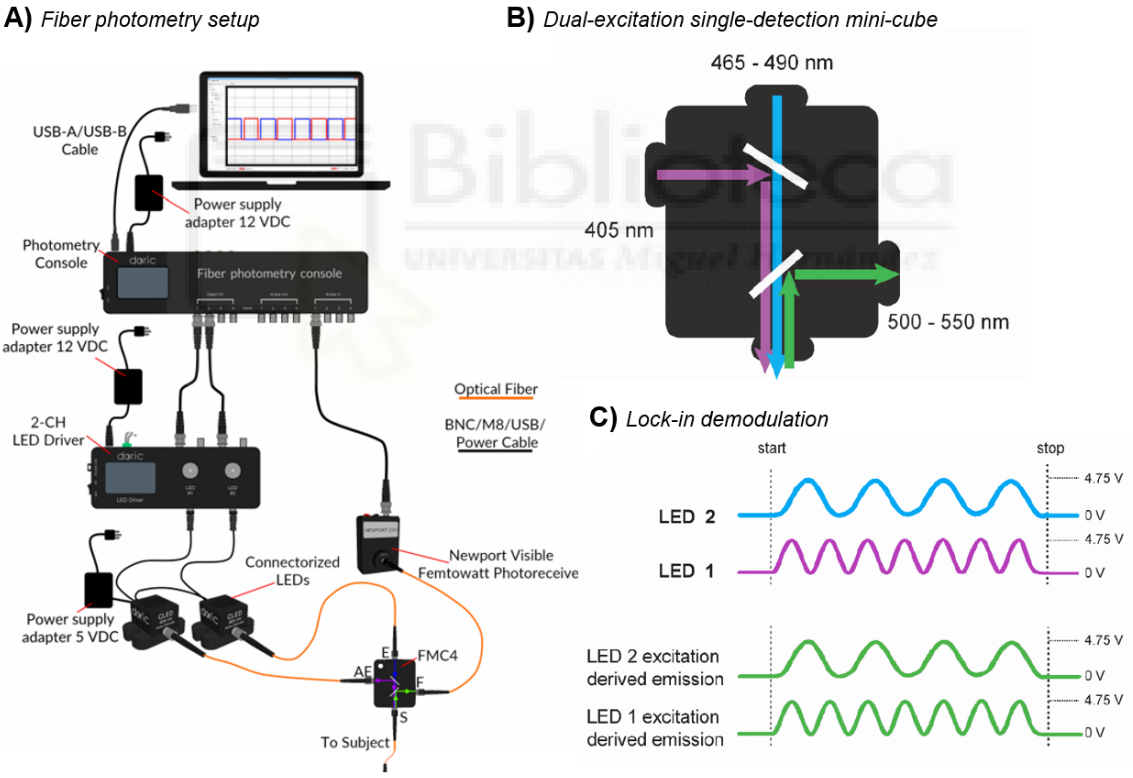

Figure 3.9. Fiber photometry system and Lock-in acquisition mode.
(A) Hardware components of Doric Photometry System. FMC4 excitation ports (405nm and 460-490nm) receive LED light from LED drives (1 and 2 respectively). 500-550 nm port carries received light to the Femtowatt Photoreceiver. A console communicates the acquisition software with the rest of the system. **(B)** Schematic drawing of the fluorescence mini cube with two input ports (405 and 465 nm excitation wavelengths), one output port (500-550 nm emission wavelength) and one bidirectional port (from and towards the sample). Dichroic mirrors (white bars) are used to guide and separate the different lights. **(C)** Lock-in mode acquisition diagram allows simultaneous detection of two signals emitted within the same nm spectrum. Each LED light is delivered at a defined frequency, called carrier frequency. Different sinusoidal carrier frequencies are separated by demodulation process.

For both, anesthetized (in rats) and awake (in mice) experiments, *carrier frequencies* were set at 215Hz and 322Hz for 465-nm and 405-nm LEDs, respectively, based on previous applications (Owen and Kreitzer, 2019). Configuration parameters *Vmax* and *Vmin* defines the output voltage from FPC to LEDD, which determines the final current sent to the LEDs using a conversion factor of 400 mA/V. Initially, all recordings started with a light intensity of ~50 µW at the tip of the fiber-optic patch cord before tethering the animal, with *Vmin* = 0.2 V and *Vmax* = 1 V. These values are settable to adjust the final light intensity, if needed (i.e., when recorded signals were saturated).

3.2.5. GCaMP recordings in anesthetized rats

3.2.5.1. Animals and experimental procedures

PV-Cre rats (n = 3 injected with GCaMP6s and n = 3 injected with GCaMP6f) underwent a second surgery to compare PV-GCaMP6s and PV-GCaMP6f recordings under anesthesia conditions. For this preparation, we electrically stimulated the perforant pathway (PP) while recording PV calcium-based activity and local field potentials (LFP) of the DG (Figure 3.10).

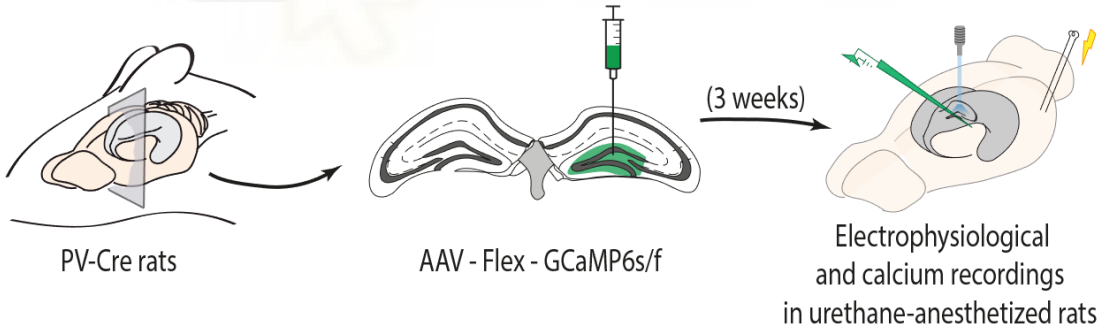

Figure 3.10. Experimental design of fiber photometry recordings in anesthetized animals.
Schematic representation of unilateral viral infection in the left dorsal DG and the position of the electrodes in the brain during combined electrophysiological and GCaMP recordings. Optic fiber (blue) and multichannel recording electrode (green) are place in the dorsal DG to record the evoked responses following PP electrical stimulation (grey electrode).

Four weeks after virus injection, animals were briefly anesthetized with isoflurane (no more than 5 minutes at 4-5% in 0.8 l/min O2) and rapidly injected i.p. with 1.5mg/Kg urethane. Rats were placed in the stereotaxic frame (Narishige, Japan) when showed absence of withdrawal reflexes and 0.2 ml of local anesthetic (lidocaine 50 mg/ml, Braun

Medical, Barcelona, Spain) was applied in the incision site. The skin was cut and retracted to expose the skull surface and make bregma and lambda references visible, which are used to adjust the final head position so that bregma and lambda coordinates coincide in the LM and DV axis (maximum deviation ± 200 μm).

Then, 3 trephine holes were made using a manual drill of 2 mm diameter at the recording and stimulation coordinates (see Table 3.1) and the dura was punctured with a needle to facilitate the penetration of electrodes and optic-fiber.

Table 3.1: Stereotaxic coordinates for main targets in rats

	AP (mm)	LM (mm)	DV (mm)
Medial PP (stimulation electrode)	8.5*	4.1	2.3-2.7
Dorsal DG (recording electrode)	1.5#	2.5	4.3-4.8
Dorsal DG (recording optic-fiber cannula)	3.5	2.4	2.75

* *15º (caudo-rostral)*

\# *30º (rostro-caudal)*

AP= antero-posterior axis, ML= medio-lateral axis, DV=dorso-ventral axis. DV coordinates for stimulation and recording electrodes may vary from subject to subject as the electrode's final location is precisely located using the recorded evoked potentials in the DG. All coordinates are based in an anatomical atlas (Paxinos and Watson, 2007). Values are shown from the reference point bregma as 0.0 coordinate.

First, mono fiber-optic cannula (400 μm Ø, NA 0.48, M3 receptacle) attached to a holder that allows direct recording of fluorescence signal (FPCH, 400 μm, NA 0.57, M3 connector, Doric Lenses), was slowly lowered to be located approximately 100 μm above the injection/recording site (see Table 3.1) and held in place for 20 minutes to allow tissue accommodation. Then, stimulation and recording electrodes were slowly lowered and positioned closed to their target coordinates. Final location of both electrodes was adjusted by using as a reference the evoked potentials at the DG (Andersen et al., 1966) so that a maximal amplitude of the population spiking (PS) activity was recorded in the DG.

Electrical stimulation was delivered through a current source and pulse generator (STG-2004, Multi Channel Systems, Reutlingen, Germany), controlled by MC_Stimulus software (Multi Channel Systems). Several protocols have been applied to stimulate the perforant pathway (PP):

- *Single-pulse stimulation* consisted of 20 biphasic 0.1 ms pulses delivered at a low rate (0.05 Hz). The stimulation intensity was adjusted for each animal, ranging

between 50 – 80 µA (subthreshold for GC firing) and 600-800 µA (suprathreshold intensities).

- *Paired-pulse stimulation* is a protocol often used to study overall inhibition in the hippocampal DG (Andersen et al., 1966; Waldbaum and Dudek, 2009). Following the same protocol as for single-pulse stimulation, we applied two consecutive stimulation pulses with a delay of 20 ms (at suprathreshold intensities), where the first stimulus evokes a PS that recruits feedback inhibition, producing a proportional reduction of the evoked response to the second stimulus.
- *Train stimulation* was used to enhance signal-to-noise ratio by applying trains of single pulses at higher frequencies. The protocol consisted of 3 repetitions of 10 pulses at 5 Hz, delivered at 600-800 µA. The total duration of the protocol was 12 minutes, with 180 seconds between trains.

During the whole surgery, vital parameters (heart and breath rate and oxygen saturation) were controlled by a paw-clip pulse oximeter (MouseOx Plus, Starr Life Sciences, USA), while the animal's temperature was maintained at 37 ± 0.5ºC with a heating blanket. Rats were hydrated with 1 ml glucose 5% (GlucosaVet, Braun Medical, Barcelona, Spain) each 60 minutes and provided with 0.5 l/min O_2 flow. Viral infection and exact position of stimulation electrode and fiber-optic recording cannula were corroborated with further histological analysis (see *3.2.7. Histology and Immunohistochemistry*).

3.2.5.2. Data acquisition and processing

Electrophysiological signals were recorded at 20 kHz sampling rate (ME64 Programmable Gain Amplifier and Filter controlled by MC_Rack software, Multi Channel Systems) using a multichannel electrode (32 recording sites spaced every 50 µm; NeuroNexus Technologies, Michigan, USA) and further analyzed in Spike2 software (Cambridge Electronic Design, Cambridge, UK). In these experiments, LFP recordings were mainly used to (1) ensure the optimal position of stimulation electrode and (2) control spontaneous and evoked hippocampal activity and its stability during fiber photometry recordings. In this preparation, the recording electrode is introduced with an angle of 20º in the sagittal plane, so the recorded CA1 belongs to a more anterior lamella than the recorded DG signals. Thus, the analysis was mainly restricted to the evoked PS recorded in the DG region, following standard criteria to measure the amplitude of evoked

PS calculating the difference (in mV) between the maximum peak of the rising evoked potential and the minimum peak of the spike.

Raw GCaMP signals (calcium-dependent and isosbestic) were recorded at 12 kHz sampling rate using the Doric Neuroscience Studio software and further analyzed with custom MATLAB scripts. To analyze evoked calcium activity, we used basic signal processing: first, 465 nm calcium-dependent and 405 nm isosbestic signals were low-pass filtered at 250 Hz and downsampled to a final sampling frequency of 500 Hz. Second, the change in fluorescence (ΔF/F) was calculated by subtracting and dividing the isosbestic signal from the 465 nm calcium-dependent signal:

$$\Delta F/F = \frac{F_{465} - F_{405}}{F_{405}}$$

where F_{465} is the calcium-dependent fluorescence and F_{405} the isosbestic fluorescence. Third, evoked ΔF responses were averaged in peri-stimulus time histograms (PSTH) with a time window of -5 to +10 seconds.

3.2.6. GCaMP recordings in behaving mice

3.2.6.1. Animals and behavioral procedures

A total of n = 16 PV-Cre mice (9 males and 7 females) were initially injected with cre-dependent AAV-GCaMP6s and chronically implanted with an optic-fiber in the left DG, as previously described in *3.2.3. Surgical procedures.*

Two weeks after surgery, handling and habituation to the experimental room were performed daily during 7-10 days. Handling included periods of animal immobilization to attach the fiber-optic patch cord and 5-min periods of mock recordings to get mice used to freely behave while tethered to a path cord. Once mice were completely habituated, home-cage control recordings were carried out to check fluorescence signals and adjust, if needed, *Vmax* and *Vmin* configuration parameters to improve signal-to-noise ratio (see *3.2.4. Fiber Photometry setup*). Four mice were excluded before starting any behavioral experiment due to lack of calcium-dependent signals, leading to an initial sample size of n = 12 subjects (7 males and 5 females).

Behavioral testing consisted of 2 behavioral tasks typically used to assess contextual novelty and spatial memory, which were carried out in the same behavioral apparatus. It consisted on a modified open field of 45 x 45 x 40 cm high (square box of white methacrylate), with an opening in the center of one of the walls to connect the open field to an adjoining smaller chamber (15 x 15 x 20 cm high, covered with a transparent methacrylate), which we refer to as the "waiting box" (Figure 3.11A). The door separating the waiting box from the open field is manually opened by the experimenter, allowing mice to enter by themselves from the waiting box to the open field, and vice versa. Thus, experimenter manipulation is avoided during animal behavior and we have noticed a better performance of the animals in the subsequent task.

To perform photometry recordings in behaving mice, the recording fiber-optic patch cord (400 μm diameter, NA 0.57, 1.5 m length, Doric Lenses Inc.) is connected to a pigtailed 1x1 rotatory joint (FRJ, 400 μm diameter, NA 0.57, Doric Lenses Inc.). Importantly, all optical fibers possess a baseline fluorescence due to their chemical composition, and this autofluorescence can interfere with photometry measurements by overwhelming the signal. Thus, the patch cord and rotatory joint were bleached overnight before any experimental session to minimize autofluorescence. According to the supplier's recommendations (Doric Lenses Inc., Canada), photobleaching is carried out by setting the current of the blue 465-LED at a maximum value and leaving overnight the light on in continuous mode.

As general procedures, experimental sessions started introducing mice into the experimental room for 20-30 minutes before starting the photometry recordings. Then, mice are tethered to the patch cord and placed in the waiting box of the open field. After 2 mins, the experimenter opens the door and mice enter into the open field (Figure 3.11B). The specific procedures for each behavioral task were as follows:

Novel Object Location (NOL). We used exactly the same protocol as explained for DREADDs experiments (see above in section *3.1.4. Behavioral procedures*), with the exception that mice are not injected with CNO during the encoding phase (Figure 3.11C).

Mismatch Novelty Task. In this experimental paradigm, animals are exposed to an unanticipated alteration within a previously familiar environment. To initially mitigate contextual novelty, visual cues displayed on the walls of the open field, encountered by the animal during the prior NOL task, were retained at the onset of the experiment. This

approach ensured that mice encountered a context with which they were already familiar, starting from the initial trial of the task. We then followed a 2-session protocol carried out in 2 consecutive days. Each session consists of 2 trials of 3 minutes with an ITI = 2 min, in which mice stay in the waiting box, with continuous GCaMP recordings (Figure 3.11C). On day 1, mice were placed on the waiting box for 2 minutes before opening the door and were allowed to freely explore the (familiar) context for 5 minutes (F1 trial). Then, the door was opened again and mice returned back to the waiting box for the 2-min ITI, after which they revisited the familiar context (F2 trial). Day 2 started exactly the same way as the day before with mice visiting for the third time the familiar context (F3 trial). Then, while mice were in the waiting box during the ITI period, a new floor/ground with a different texture and color (44 cm x 44 cm x 3mm green polypropylene) was fitted into the open field, so when the door is opened and the mice enter the open field, they encounter an unexpected ground. Animals are allowed to explore this subtly modified context for 5 minutes (novelty trial).

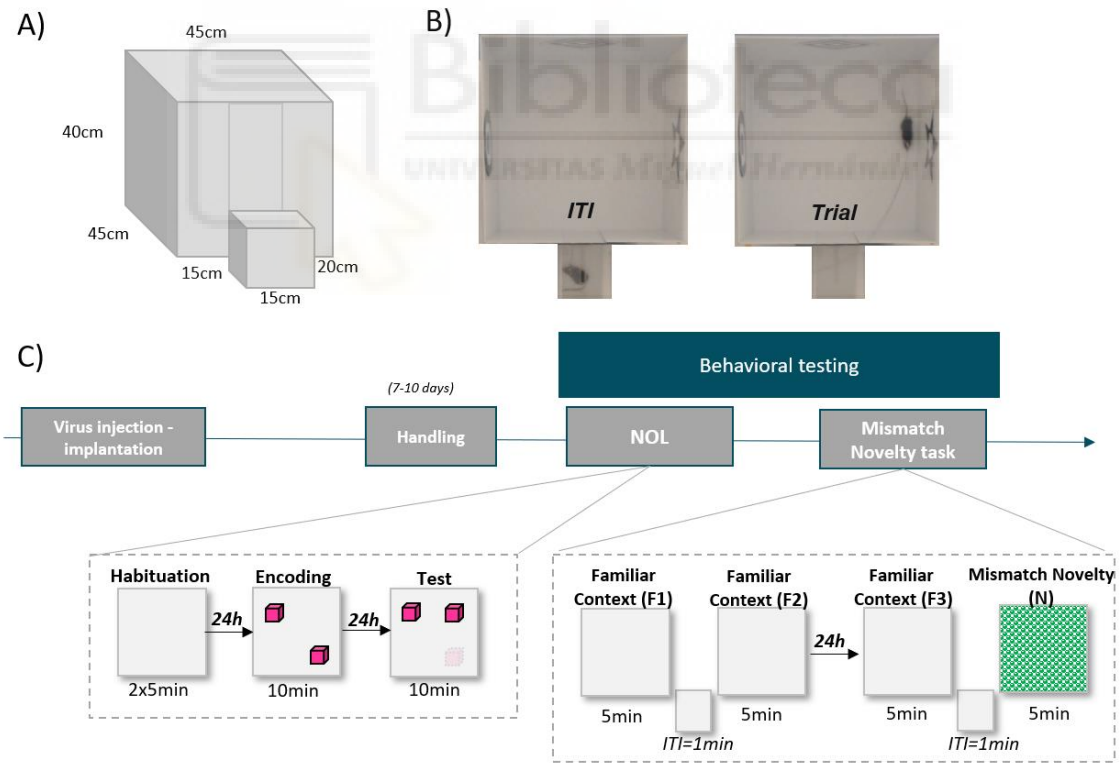

Figure 3.11. Experimental design of fiber photometry recordings during memory tasks.
(A) Schematic representation of the open field utilized for behavioral testing with simultaneous GCAMP fiber photometry recordings. **(B)** Pictures of a mouse in the waiting box (left) and inside the arena (right). The door is opened manually to allow mice transitioning from and towards the open field and the waiting box. **(C)** Time-course of behavioral fiber photometry experiments. Virus injection and fiber optic implantation are performed in the same surgery. Handling started approximately one week after the surgery to ensure a proper habituation of mice to be transiently immobilized prior to the experiment and to be tethered to a patch-cord. Mice first conducted a NOL task and one week later a Mismatch Novelty task

3.2.6.2. Data acquisition, processing and synchronization

Behavioral video files were recorded with a webcam (Logitech HD Pro C920) at 15 Hz and processed offline with our MATLAB-based RodEx tool (see *4.1. Development and implementation of RodEx* in Results).

Fiber photometry GCaMP6s recordings were acquired in Lock-in mode (as explained before) with Doric Studio software and further processed in MATLAB. Calcium signal processing was performed as follows (Figure 3.12A): demodulated raw signals (both 465-calcium signal and 405-isosbestic signal), sampled at a 12 kHz, were first low-pass filtered at 25 Hz and downsampled to a final sampling frequency of 50 Hz. The first 50 seconds of the recording (while the animal is in the waiting box) were removed to eliminate the initial recording artifact (sharp decay in the recorded fluorescence). Then, both signals were corrected subtracting the detected baseline using a polynomial fitting of second-order. Corrected 405-isosbestic signal was then fitted to the corrected 465-calcium signal using a polynomial regression of second order. Then, fitted 405-isosbestic signal (F_{fit405}) was used to calculate the final corrected fluorescence signal (ΔF):

$$\Delta F = F_{corr465} - F_{fit405}$$

ΔF is finally transformed to a z-score to allow comparison of calcium signals between mice. When analyzing discrete behavioral events, such as an object's exploration, PSTHs averaging ΔF responses over 10 seconds before and after the *peak* of the exploration, were performed. Exploration peak was defined as the minimum mouse-to-object distance during the exploration epoch.

Processed behavioral and calcium data were synchronized using *Module V* of RodEx (see *4.1.1. Development* in Results). To this end, we used a programmable TTL pulse generator (PulserPlus, Prizmatix, Israel) to manually define and save critical timestamps, such as the start and the end of the session, and all moments when the gate is opened to define the duration of each trial within the session. The first TTL signal was used to mark the start of the session and trigger the initiation of fiber photometry recording. By contrast, we were unable to use TTL signal to trigger the initiation of the webcam recording. Instead, we used it to illuminate an LED (placed within the camera's field of view but not visible to the animal performing the task, as illustrated in Figure 3.12 B-C). Further image processing to detect when the LED was on or off was used to generate the video

timestamps data. Then, we used the first and the last TTL-defined timestamps to synchronize video and fiber photometry signals, which were acquired at different sampling frequencies. Time vectors from both signals were rescaled (from t=0 to t=100) to be aligned by averaging the data contained in all the ΔF samples that correspond to each video frame (1 frame ≈ 3 samples) (see Figure 4.6 in Results).

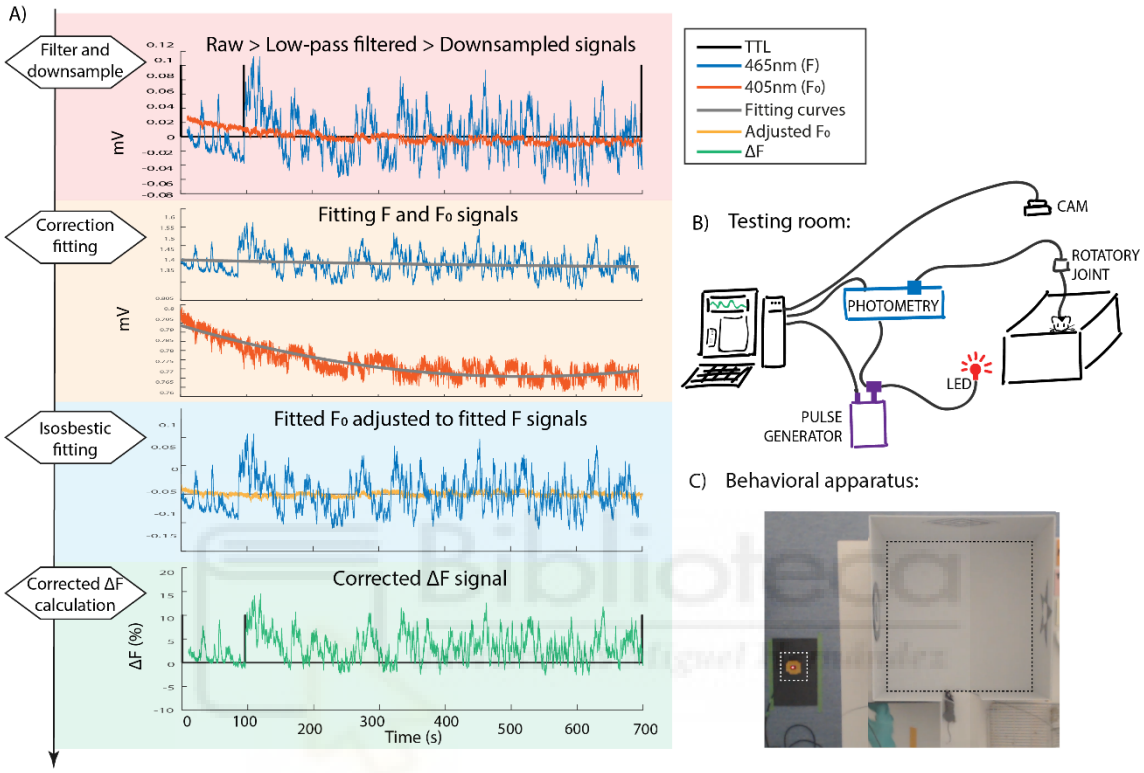

Figure 3.12. GCaMP processing pipeline and behavioral setup.
(A) Schematic workflow of raw data processing and ΔF extraction (different steps have been tested during the establishment of the final analysis pipeline, obtaining similar results irrespective of the method utilized). Traces in the first step correspond to PV-calcium (blue) and PV-isosbestic (orange) signals from a mouse freely behaving in an open field. **(B)** Schematic drawing of hardware configuration to perform fiber photometry recordings in freely-moving rodents. A pulse generator is connected to the photometry console to generate timestamps. Same TTL inputs are used to illuminate a red LED that is recorded by the webcam. The camera, the photometry console and the pulse generator are connected to the computer, where different software are used to control each apparatus. **(C)** Picture showing the field of view of the camera recording the behavioral experiment. Dotted squares define the ROIs for the open field arena and for the LED detection used to synchronize behavior and calcium signal. This example shows the TTL marking the starting of the trial.

3.2.7. Histology and Immunohistochemistry

Perfusion in rats. At the end of each experiment, anesthetized rats were perfused intracardially with 100 ml of 1% PBS and 100 ml of ice-cold 4% PFA solution. Brains

were kept in PFA overnight at 4ºC and cut in a fixed material vibratome (VT 1000S Leica, Wetzlar, Germany) in 50 µm thick coronal or sagittal slices.

Perfusion in mice. After completion of the experiments, mice were anesthetized with pentobarbital (Dolethal 200 mg/ml, Vetoquinol, Madrid, Spain) and perfused intracardially with 40 mL 1% PBS and 50mL of ice-cold 4% PFA solution. Implanted optic-fibers were firmly but carefully removed from the skull and the extracted brain was kept for at least 24 h on 4% PFA post-fixation. Then they were cut in a fixed material vibratome (VT 1000S Leica, Wetzlar, Germany) in 40 µm thick coronal slices.

Immunohistochemical processing was the same for rats and mice. Slices were permeabilized in PBS containing 0.5% Triton and unspecific binding was blocked by adding 10% normal goat serum (NDS) for at least 2 hours. Sections were incubated overnight at 4ºC in blocking solution with monoclonal rabbit anti-PV (1:1000, Swant, Switzerland) and chicken anti-GFP (1:500, Aves Labs, California, USA) antibodies. Then, slices were washed in PBS containing 0.5% Triton and incubated for 2 hours in blocking solution with Alexa-594-conjugated (1:500, goat anti-rabbit, Thermo Fisher Scientific, USA) and Alexa-488-conjugated (goat anti-chicken, Thermo Fisher Scientific, USA) antibodies. After a final washing with PBS, slices were stained with DAPI, mounted on glass microscope slides (Normax, Portugal) and coverslipped.

3.2.8. Statistical analysis

All statistical analyses were conducted using customized MATLAB scripts (The Mathworks Inc., Massachusetts, USA) and GraphPad Prism version 7.00 for Windows (GraphPad Software, Inc., California, USA). The normal distribution of the data was corroborated with the D'Agostino-Pearson test.

To assess the correlation between calcium values and the speed of the animal, we computed Pearson correlation coefficients, with significance level set at $p < 0.05$.

Due to the high correlation found in our recordings, we considered an inferential analysis from the Mismatch-Novelty task data by using the following multivariate regression model to perform inferential analysis from data:

$$\Delta F = Session * ns(Time, 3) + m_{speed} + (time \mid subject) + \varepsilon_i$$

The response variable in the model is ΔF. Regarding the explanatory variables, we include: the variable *session,* the variable *speed* and the effect of *time*. Additionally, exploratory analyses showed that the effect of time on calcium depends on the session (where it was slightly different in the novelty session). Thus, the interaction between session and time variables is considered, where the variable time has been modeled through a non-linear term with cubic splines method. A spline is a piecewise curve derived from the third-order polynomials that fit together perfectly, creating a continuous curve up to its second derivative. Finally, the non-independence of data has been considered through random factors: time | mouse, indicating a random intercept for each mouse and random slope for the time of each mouse. This controls the non-independence of data and the variability between subjects.

Cubic splines have excellent mathematical properties and are easily represented, but the resulting coefficients are hardly interpretable. Thus, we considered to divide the 5-min trial duration into 100-seconds time periods, leading to t_1 (0 – 100 s), t_2 (100 – 200 s) and t_3 (200 – 300 s), and then use repeated measures two-way ANOVA to test whether changes in inhibitory activity occur over time (across the different time periods). In case of statistical significance ($p < 0.05$), ANOVA tests were followed by post-hoc Bonferroni's multiple comparison test to check internal relations. This model was performed in collaboration with Victoria Fornés Ferrer, who provided statistical support from the Responsible Research Office, Research and Innovation Vice-rectorate of the University Miguel Hernández (UMH).

For the NOL task, in order to simplify the statistical analysis, we used the approach to divide the total time of each session in time periods of 150 seconds (t1, t2, t3 and t4, where t3 and t4 are only available for encoding and test sessions). We used repeated-measures two-way ANOVA test to study the differences on PV inhibitory dynamics between different sessions (session and time period factors). As before, Bonferroni's multiple comparison test was used if needed.

If any other statistical approach has been applied, it is clearly stated in the text. Data are expressed in the text as mean ± SEM (unless otherwise specified) and significance levels are expressed in figures with a star-code as follows: * $p < 0.05$, ** $p < 0.01$, *** $p < 0.001$, **** $p < 0.0001$.

IV. RESULTS

4.1. Development and implementation of RodEx

In view of the methodological approach proposed for this thesis (mainly based on behavioral experimentation), this first chapter stemmed from the need to ensure objective and unbiased behavioral analysis, which would lead to better interpretation of measured behaviors and its underlying neural basis.

Therefore, an initial goal was to improve available tracking methods by implementing (1) reliable detection of head coordinates in freely-moving rodents and (2) unsupervised quantification of exploratory behaviors.

For this purpose, we have developed RodEx, a versatile and open-access MATLAB-based code package[3] for video processing, animal tracking and automated quantification of exploratory behavior. To validate our method, we compared the generated results to those that were manually scored by experienced experimenters. Finally, as a proof of concept, our tool was employed to assess its efficacy.

Note: RodEx development started during my master project work (*"Modulating hilar parvalbumin interneurons in behaving mice"*) in 2015, before AI-based methods like DeepLabCut (Mathis et al., 2018) were developed. Although the capabilities of these new tools surpass the present software, especially for recognizing parts of the animal's body that are being tracked, RodEx has some advantages that we will discuss at the end of the chapter.

4.1.1. Development

On the basis of Sensory Orientation Software open-access codes (Gomez-Marin et al., 2012), we have developed a package of MATLAB-based codes that enables unsupervised quantification and further analysis of rodent's exploratory behaviors in freely-moving conditions. To achieve this, we first worked on improving rodents' head tracking (see

[3] We are currently working on an updated version of RodEx, which will soon be available on https://canalslab.com/resources-canalslab/

Module II below) to provide high-resolution measurements of animal posture (i.e., stretching) and orientation (see *Modules III-IV* below).

The entire process is carried out offline and can perform single-video or batch processing. It is organized in consecutive modules as shown in Figure 4.1. Each module is explained in more detail below. Briefly, there is a core script, consisting of *Modules I, II* and *IV*, to compute animal centroid-head-tail tracking and measure postural and locomotor behaviors. Additionally, *Module III* can be also run to quantify exploration of previously defined targets. Finally, there is an optional module (*Module V*) that allows us to synchronize video files with another simultaneously recorded signal, very often sampled at higher frequencies (neural recordings recorded up to 40 kHz while video files are usually recorded at 15-60 frames per second).

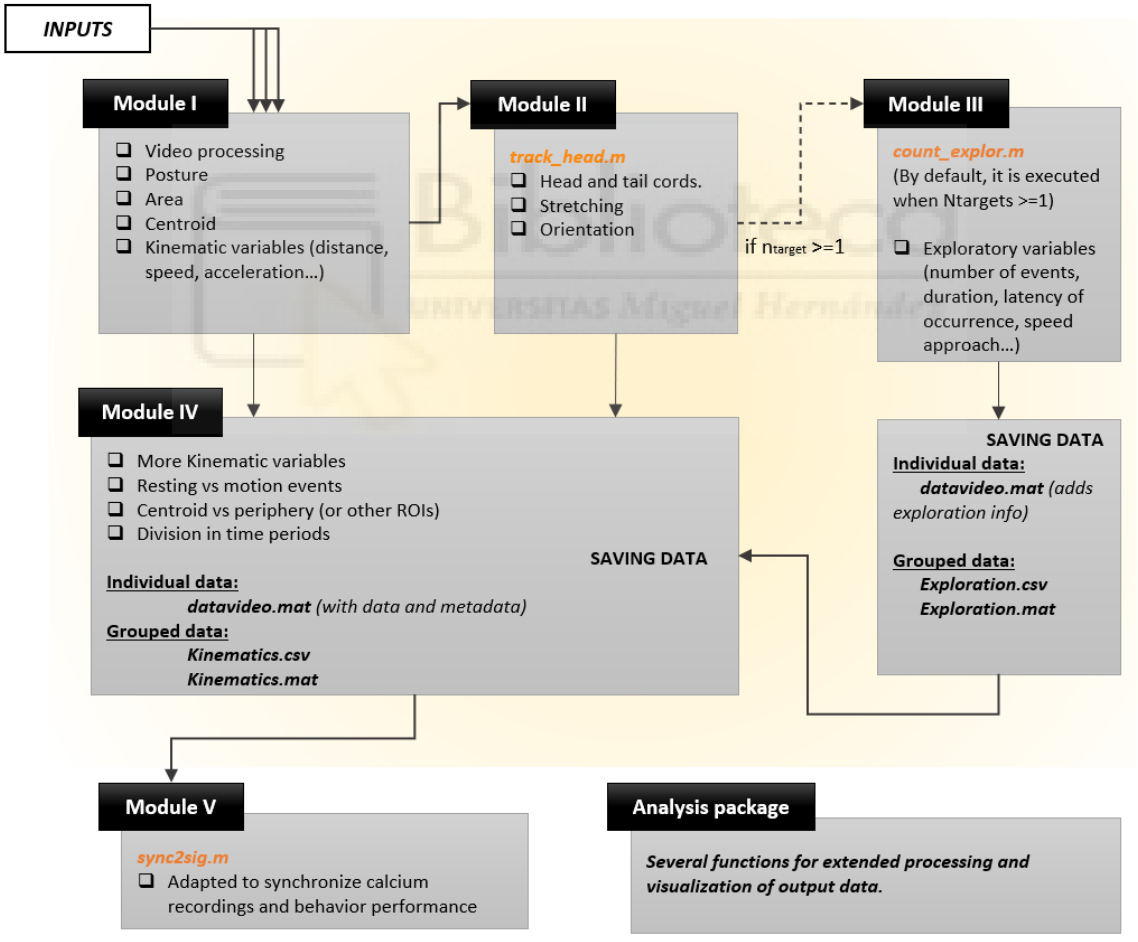

Figure 4.1. Schematic workflow of the RodEx pipeline.
Summary of RodEx modules and the main outputs at each step. Text in orange highlights the primary functions executed within each module. The parameter N_{target} represents the number of objects (or any target to be explored), which is given as one of the input parameters for Module I. If N_{target} equals to 0, Module III and the corresponding saving process are bypassed.

Although our tool does not yet have a graphical user interface (GUI), it has a user-friendly design for inexperienced-MATLAB experimenters. On the other hand, it is flexible enough to be modified or adapted by programming skilled users according to their specific needs.

Module I. Video processing and extraction of animal's posture and position (centroid tracking).

This module consists of two main parts. The first requires user's interaction to set the desired parameters for video processing and for subsequent data analysis, and the latter computes image processing for the entire video, centroid tracking and detection and generation of basic kinematic variables:

Setting input parameters. First, establishment of fundamental input parameters is required for proper loading, image calibration and processing and saving functions. A second set of input parameters are asked to the user with pop-up MATLAB windows, such as selecting the region of interest (ROI) from the whole image (e.g., the maze arena, objects, etc.) or the threshold for mice to be detectable and trackable (Figure 4.2 A-B). For batch processing, the same parameters will be applied to all video files, unless otherwise specified by the user. Once all inputs have been stated, the program starts running an iteration loop that permits loading, processing and saving multiple video files sequentially without further user interaction.

Centroid tracking and generation of kinematic variables: Frame by frame, the mouse is targeted as the biggest detected object within the ROI and its posture, area and position (centroid coordinates) are calculated (Figure 4.2C and Figure 4.3A) and saved in a structured file in *mat* format, called *datavideo*, that will contain the data and metadata for each processed video file.

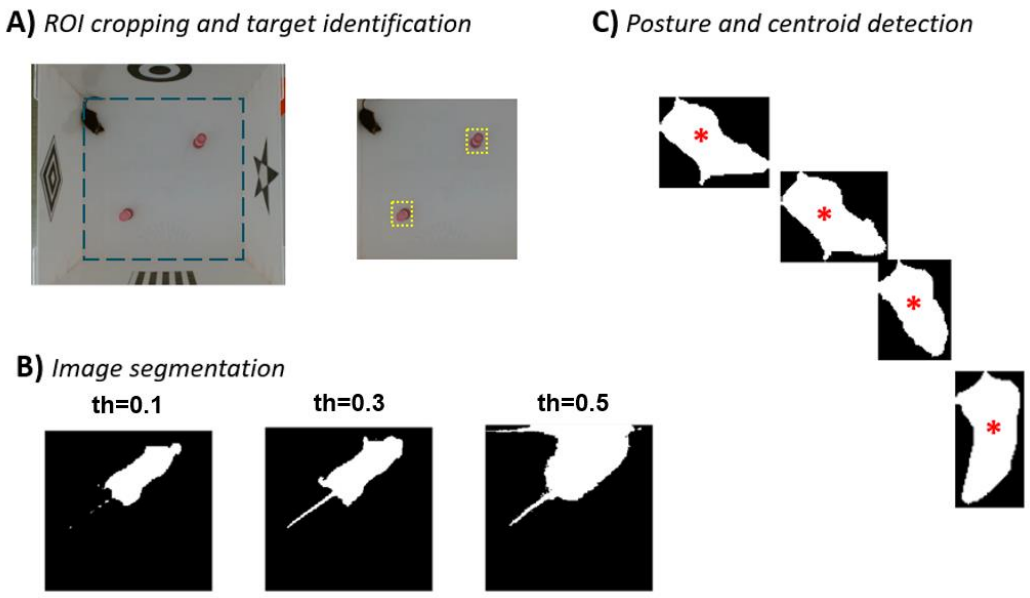

Figure 4.2. Module I.
(A) Users define the required ROIs through initial input parameters by drawing them on the image. **(B)** RodEx displays various default image segmentation thresholds (th=0.1, 0.3 and 0.5). Users can explore other threshold if none of the presented options are suitable. **(C)** Illustrations of animal postures captured in four consecutive frames. Posture and position variables are saved separately (see Figure 4.1).

Module II. Detection of head and tail coordinates and extraction of new postural data (stretching, heading).

After all video frames have been processed, this second module completes the collection of kinematic variables and the detection of head and tail positions. As rodents are ellipse-shaped, head and tail coordinates are extracted by using a *curvature criterion* (Figure 4.3A), which identifies the maximum curvatures along the contour of the detected posture.

However, freely moving rodents present variable postures in shape and size, sometimes adopting non-elliptical shapes and leading to biased head and tail detection. To solve these problems, we introduced two unsupervised correction algorithms, based on directionality and proximity rules, which are combined to improve head and tail detection taking into account the information from previous and following frames. To do so, head and tail coordinates are swapped in the current frame (proximity rule) or in a set of successive frames (directionality rule). The proximity-based algorithm is used to improve the initial decision of head and tail coordinates for each frame. The algorithm identifies inconsistencies when comparing the distance between head coordinates in the current

(H_C) and previous frame (H_{C-1}) with the distance between tail coordinates (T_C - T_{C-1}). The directionality-based algorithm takes into account centroid coordinates in previous, current and following frames to maintain consistency between centroid and head directionality.

Once head and tail coordinates are detected for all the frames, this information is added to *datavideo* file and new variables such as stretches (measured as the distance between head and centroid) or headings (measured as changes in head orientation with static centroid) are now approachable (see Figure 4.3B, *left* and *middle*).

This sequential approach to obtain centroid and head-tail coordinates in separated modules allows us (1) to apply the correction algorithms in order to reduce errors in head detection, (2) to run faster computation and (3) it can be easily skipped in case head positions are not needed (Figure 4.3B, *right*).

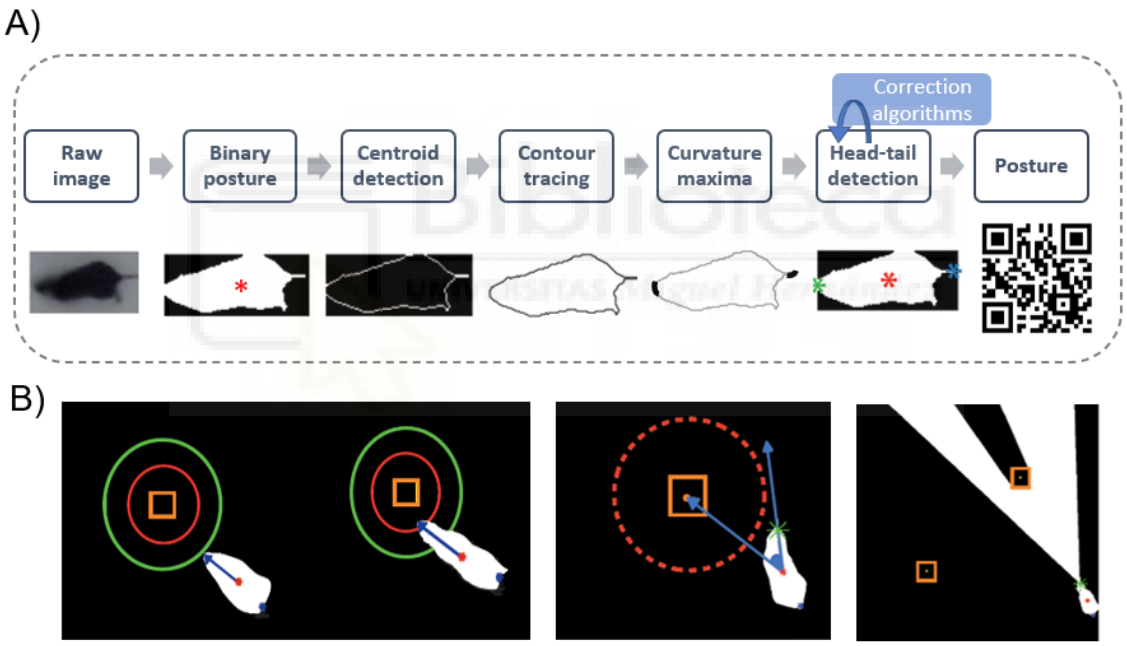

Figure 4.3. Module II.
(A) Schematic workflow of Module II, including main video processing and extraction of postural and spatiotemporal data. The optional function of head and tail detection is computed after processing the entire video. Scan the QR code to view a video example displaying the results of RodEx video processing. **(B)** Examples of frames with typical mouse behaviors, such as stretching (*left*) or animal orientation towards a target (*middle*). Additional measurements, like the binocular field of view (*right*), can be applied with minimal programming expertise.

At this point it should be mentioned that the quality of our recorded videos was good enough to visualize, track and analyze animal position and behavior, but was insufficient to constantly track the tail in all frames, so we do not use this information hereinafter. We expect that tail detection will become more stable in video recordings with better

resolution, therefore improving head tracking and RodEx accuracy: if tail is detectable in all frames, it will be easier to constantly detect its end as the maximum curvature, stabilizing as well the detection of the head point, which is the opposite maximum curvature.

Module III. Quantification of exploratory events

Numerous behavioral tasks that assess learning and memory in rodents rely on their natural tendency to explore novel rather than familiar environments or stimuli. In these paradigms, the preference for exploring novelty, and thus recognizing the familiar, is a measure of memory performance.

To consider that a rodent is actively exploring an object (or any other target) one has to first define what is considered as exploration. We follow Ennaceur and Delacour and consider an act of exploration when the animal is less than 2 cm from the object of exploration and directs its head towards the object (Ennaceur and Delacour, 1988). Based on these criteria, *Module III* basically combines several constraints for a frame to be considered as an *exploration frame* (see Figure 4.4A). These constraints, or thresholds, must be defined by the user in *Module I* as input parameters. The different thresholds are relative to head distance to the object (th_{dh}), orientation towards the object (th_{deg}) and centroid distance to the object (th_{dc}), the latter to control climbing of animals over an object (Figure 4.4A). Those frames in which the detected posture (animal) meets all the above thresholds are classified and reported as exploratory frames (Figure 4.4B and C). The number, size and position of explorable targets (usually objects) were also defined as input parameters in *Module I*.

Access to global navigation (Figure 4.4D) and to the individual exploratory epochs is available (Figure 4.4E). Diverse variables related to exploratory behavior are measured, such as duration of each exploration epoch, number of explorations across time, or the approach speed to the target, among others (Figure 4.4F). This information is added to the structured *datavideo* file and group data is generated at both *mat* and *csv* formats.

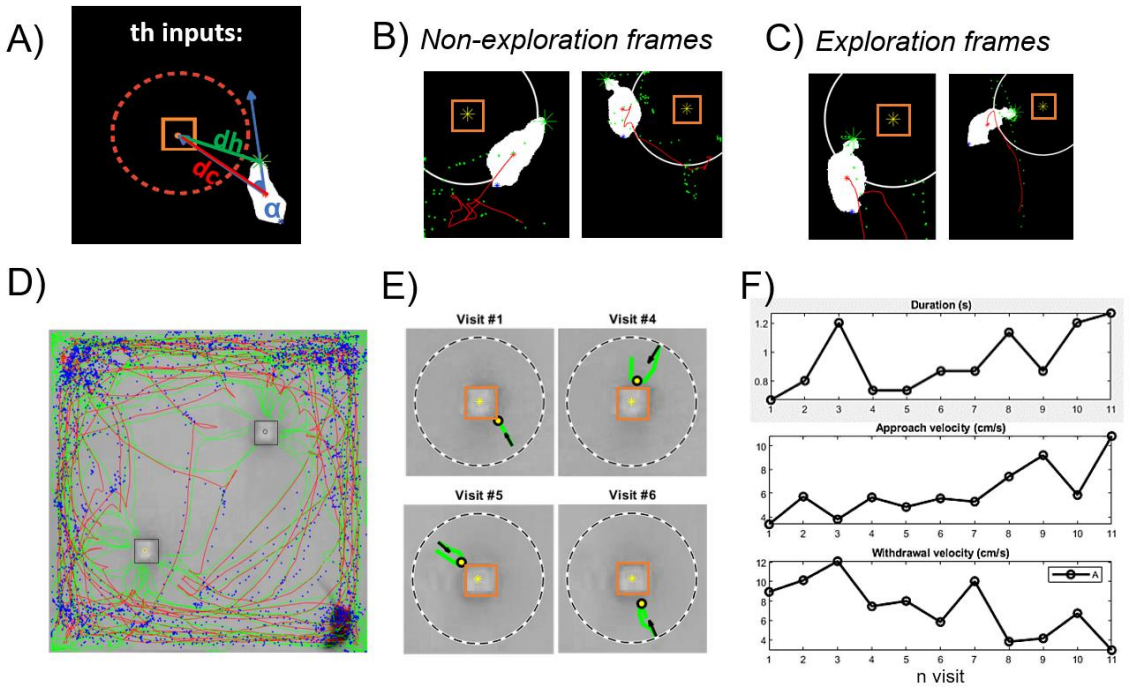

Figure 4.4. Module III.
(A) Combination of constraints determining whether the animal is exploring. A frame is considered an "exploration frame" if it satisfies all specified constraints or thresholds. **(B)** Examples of frames designated as "non-exploration frames". Green dots represent head coordinates and red lines represent centroid coordinates in the previous 5 seconds leading the current frame. On the left, despite the animal being close enough for exploration (th_{dh}), the orientation is not directed towards the object (th_{deg}). On the right, the animal was exploring in previous frames, but the visit has concluded. Orange square defines object position and yellow asterisk its center. **(C)** Examples of frames defined as "exploration frames", showcasing different positions and postures during object exploration. **(D)** Representative example of centroid (red) and head (green) tracking for a complete encoding session of the NOL task. **(E)** Individual object explorations separately, with green traces representing the head trajectory during detected exploratory frames. The arrow indicates the animal's direction, and the yellow dot marks the frame with the minimum head-object distance. **(F)** Representative example of the measured variables, including duration (s), approach velocity (cm/s) and withdrawal velocity (cm/s). The number of the x-axis represents the quantified explorations towards the same object, in this case, 11 visits.

Module IV. Data analysis and visualization

This module is composed of a set of functions to compute group analysis and data visualization. By default, several figures per subject (Figure 4.5A and B) are automatically saved and displayed for quick visualization. Figure 4.5C shows how different ROIs can be defined on different mazes.

It is worth mentioning that we also performed first attempts to automatically classify *rearing* and *grooming* behaviors based on the area of the detected posture for each frame (Figure 4.5E, bottom). Although we have not finally implemented the automatic detection of these behaviors, its future implementation is plausible.

Finally, group data resulting from Module IV is saved in two formats (*mat* and *csv files)*, so the analysis can be continued in MATLAB or performed with any other statistical software (see *4.1.2. Application and added value of RodEx*).

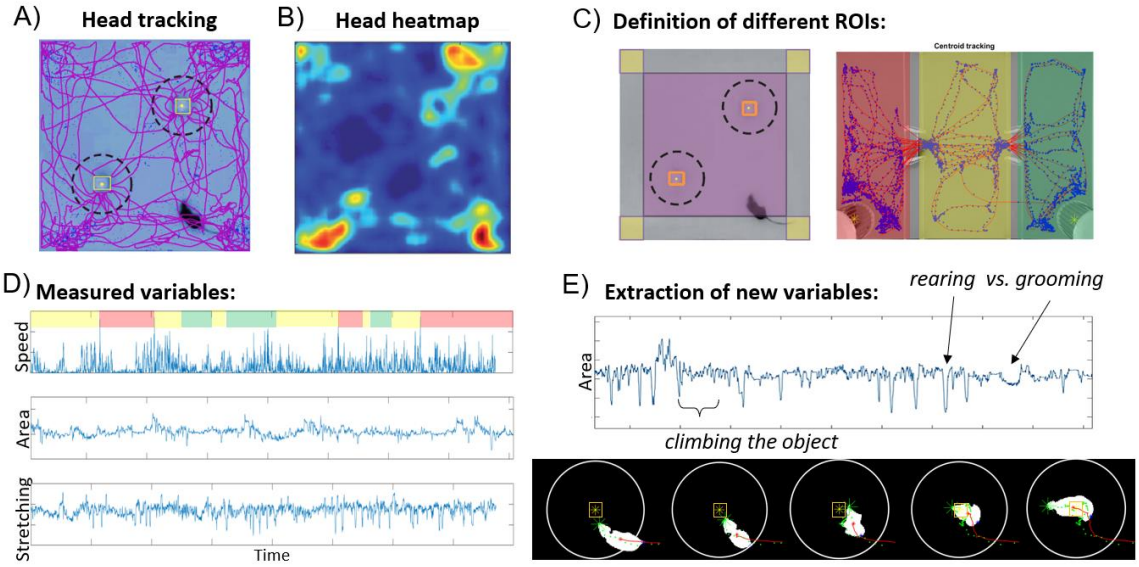

Figure 4.5. Module IV.
(A) Head trajectory in the NOL task and **(B)** respective heatmap. **(C)** Definition of different ROIs. *Left*, within the main ROI, we can distinguish different zones with the function *timeinzone.mat*, computed by default when a square ROI has been defined. This function is flexible the user can adjust the size of each new defined zone. *Right*, three different ROIs are initially defined to distinguish areas in a 3-chamber arena. **(D)** Representative examples of measured variables related to locomotor and postural information in a 10-min session, corresponding to the 3-chamber video processed in panel C (area variable comes from the same animal in a NOL session). From top to bottom, speed (cm/s), area (pixels^2) and stretching (cm). Colored bar at the top of the plots indicates the occupancy of the animal at each time point (red = left chamber, green = right chamber and yellow = middle chamber). **(E)** Other exploratory behaviors can be inferred from the extracted data, such as the area variable. A mouse climbing the objects often coincides with changes in the measured area (with lower values when climbing up and down the object and increased area when the animal is on the object). Rearing and grooming also are usually related to reductions in the area, the former reflected in more transient peaks and the latter reflected in more prolonged but small reduction in the area. On the bottom, cropped frames exemplifying the changes in area while climbing the object.

Module V. Data synchronization

For specific experiments, we could be interested in synchronizing data coming from different sources, usually acquired at different sampling frequencies. In this framework, we have also developed *Module V* that specifically synchronizes already processed video files with any simultaneously recorded signal.

In the present thesis, for instance, we have used fiber photometry calcium recordings, acquired with the DORIC photometry system at 12000 samples per second (12 kHz), while the acquisition rate of the recorded videos was 15 frames per second (15 fps). In a

typical experiment, we use a TTL pulse generator to mark the start and the end of the experiment, or other times of interest. In our example here, the first TTL signal triggers the start of photometry recording, the second TTL marks the beginning of the trial, and the third TTL the end of the behavioral trial (Figure 4.6A).

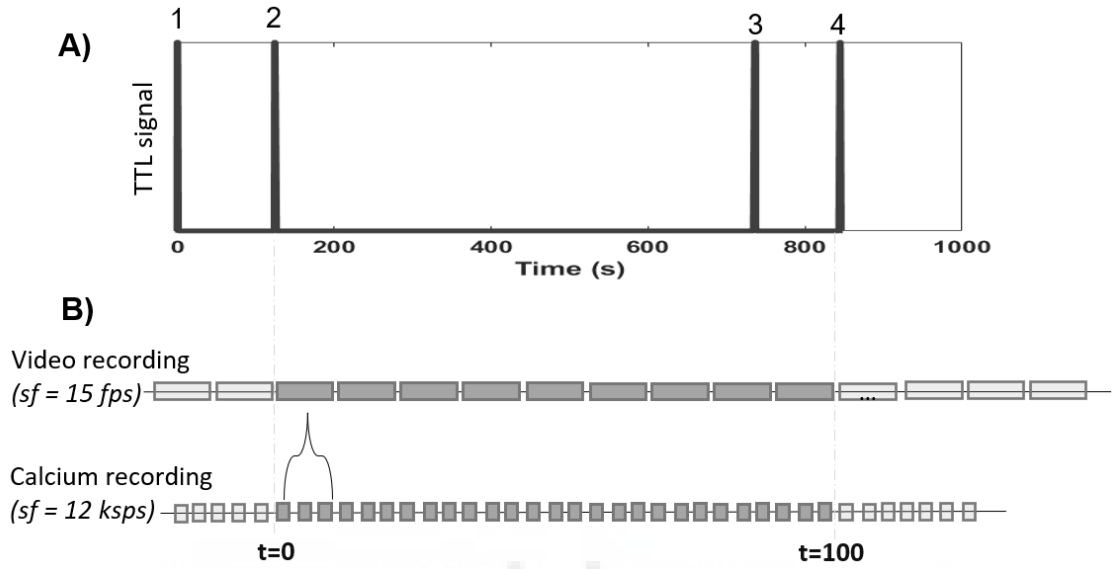

Figure 4.6. Module V.
(A) TTL digital input used to synchronize behavioral (video file) with neuronal (calcium recordings in this example) acquired at different sampling frequencies. **(B)** Schematic representation of signals reescalation and alignment based on the TTL inputs.

The *Module V* defines new time vectors for both signals and rescales them based on the TTL input, allowing their alignment and making them comparable (Figure 4.6B). Again, in the example above, taking into account the slow dynamics of the calcium sensors used we were able to easily align them with the videos by averaging the data contained in all the samples that correspond to each frame (1 frame ≈ 800 samples). At the end of the module, the synchronized information is added to the main structure *datavideo*, but we can alternatively generate a different file to save only the synchronized data.

4.1.2. Validation

In order to validate the proper functioning of our tool to automatically quantify exploration, we have used the database of our previous work (Caramés et al., 2020), which contains the results from a Novel Object Location (NOL) task performed by n=37 mice. This task evaluates spatial memory based on mice preference to spend more time exploring objects encountered in a novel rather than in a familiar position.

Originally, objects exploration was manually scored by two double-blind experienced observers. First step was to compare these results with those obtained from our unsupervised automatic quantification. The criteria for exploration in RodEx were defined/specified as the mouse being oriented towards the object ($th_{deg} \leq 40$) and the distance between mouse's head and the object is less than 2 cm ($th_{dh} \leq 2$), excluding instances where the animal climbed on the object ($th_{dc} \leq 0.5$, or the equivalent to the object's ROI). Conversely, while the experimenters followed common criteria to quantify exploratory events, there always exists a level of subjectivity in manual scoring processes. Arguably, the human experimenters' definition of scanning will be more accurate, and RodEx's less biased.

The first result, measuring absolute exploration time, already shows this difference. The absolute times of RodEx are higher than the consensus time of both experimenters (Figure 4.7A, 2-way ANOVA *Method:* $F_{1,36} = 74.5$, $p < 0.001$). One possible explanation for this result is that the experimenters rely on shorter excursions of the animal, relative to the object, to define a positive exploration. Importantly, RodEx and experimenter measures were highly correlated, regardless of the absolute values (Figure 4.7B, Pearson correlation $r = 0.61$, $p < 0.001$, n = 148). Accordingly, the corresponding discrimination ratios (DI = $\frac{T2}{T1+T2}$) were indistinguishable (Figure 4.7C; $F_{1,36} = 0.728$, $p = 0.399$) and covaried significantly (Figure 4.7D; Pearson's correlation $r = 0.85$, $p<0.001$, n = 74).

Finally, as a complementary validation, a proportion of the used video recordings were manually re-analyzed using MiceChrono software. This is a MATLAB-based software (designed by Dr. Víctor López-Madrona) that allows the experimenter to manually quantify specific events (i.e., exploration of objects or time spent at different chambers) by manual annotations. A representative example of this comparison is shown in Figure 4.7E, reflecting the high reliability of our automatic measurements.

During the validation analysis, for some subjects we observed mismatching results between manual and automatic measurements. For a few of these videos, we requested other experimenters to conduct a manual re-analysis of exploration. Interestingly, we often noticed inconsistent manual quantification between experimenters who conducted the re-analysis of the same sessions, mainly based on moments of uncertainty regarding whether or not to classify a given event as an exploration. Thus, on some occasions, the

advantage of the experimenter's flexible but biased expert eye is outweighed by the fixed criteria programmed into RodEx.

We conclude that the presented method provides a realistic automatic quantification, which makes it an optimal tool to obtain constant and objective results, avoiding the effects of subjectivity or fatigue that experimenters experience during manual scoring.

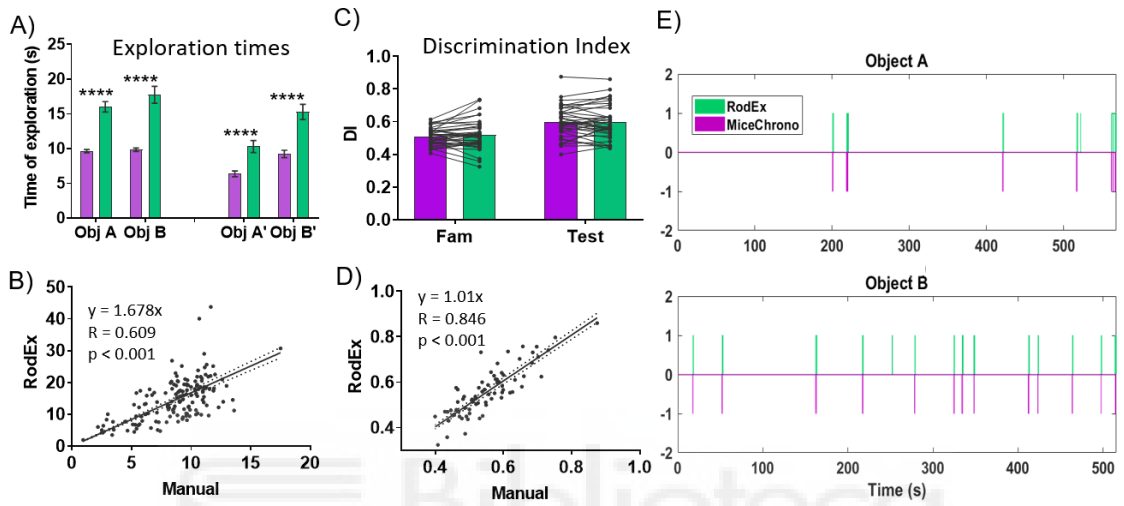

Figure 4.7. Validation of RodEx: comparison between manual scores obtained using MiceChrono and automatic quantification provided by RodEx.
(A) Differences in absolute time of exploration calculated manually (purple) and automatically (green) for each object during encoding (Obj. A and B) and test (Obj. A' and B') sessions in a NOL task. **(B)** Linear correlation of absolute times of exploration shown in A. **(C)** Differences in the discrimination indices (DI) for each session, calculated by the ratio of exploration of the displaced object (t2/(t1+t2)). **(D)** Linear correlation of DIs shown in C. **(E)** Representative example of the differences between both quantification methods showing the fidelity of RodEx quantifying the exploratory behavior compared to the annotations of an expert observer using MiceChrono. Shown mean ± SEM. Significance levels indicated with a star code as follows: **** p<0.0001.

4.1.3. Application and added value of RodEx

Once the feasibility of our method was validated, we used again the aforementioned database to verify RodEx functionality. Briefly, the database contains the results from 3 experimental groups: Sham-control group, PV-Gi group (disinhibited DG) with improved spatial memory and PV-Gq (inhibited DG) with impaired spatial memory (see Figure 1.8 and section 3.1 in Methods for a detailed description of the data).

Without going into a detailed interpretation of results, we would like to highlight some curious observations that we did during the implementation of our method. First, it is worth mentioning the great variability in the way mice explore their surroundings and the

encountered objects, showing very different exploratory profiles and strategies (Figure 4.8A). Additionally, we calculated the cumulative exploration curves and found different profiles of objects' exploration (Figure 4.8B). Strikingly, subjects from different experimental groups were unevenly distributed among this classification.

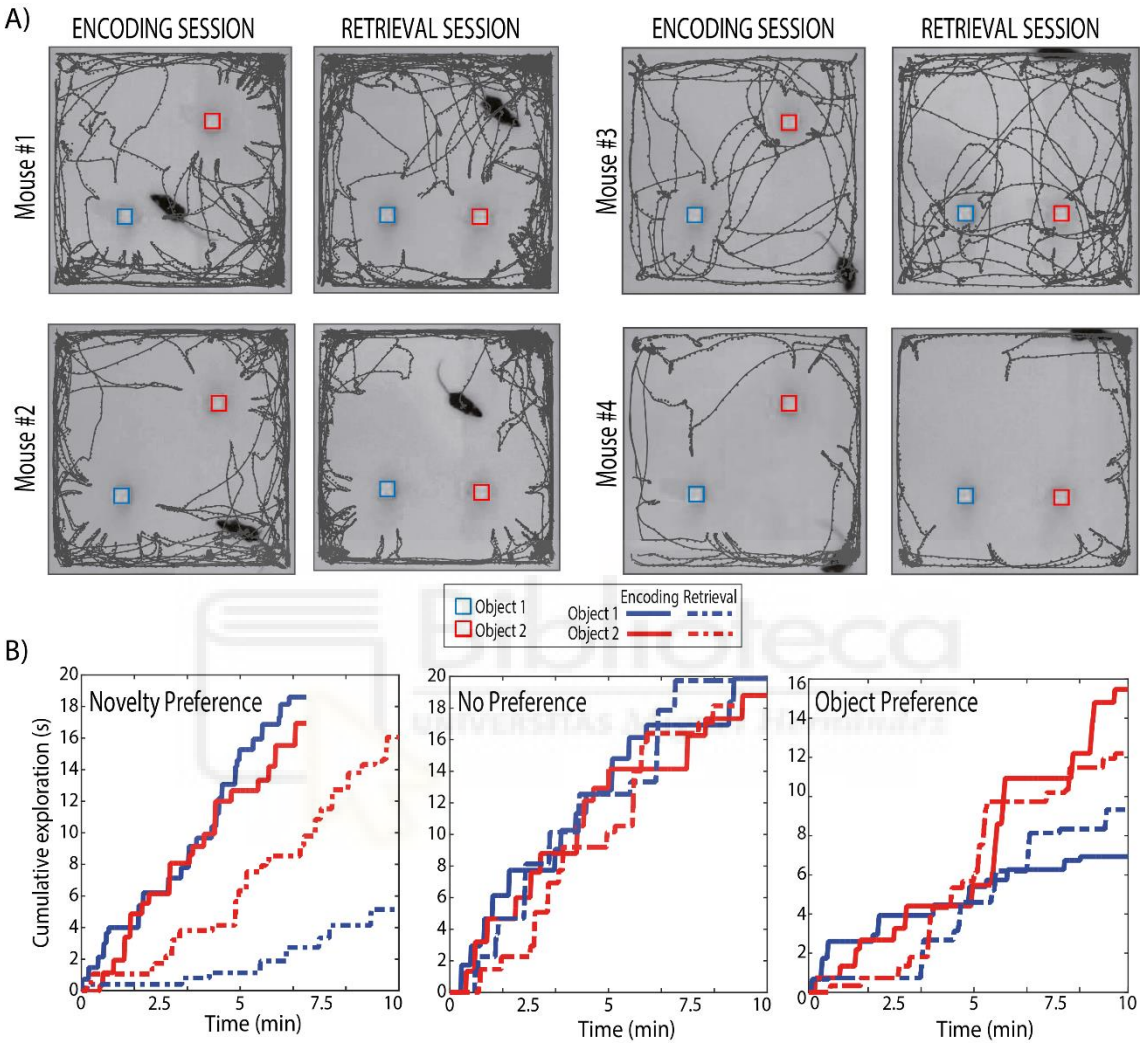

Figure 4.8. Variability in mice NOL performance.
(A) Variability in locomotor behavior. Centroid tracking (grey traces) of 4 mice during the encoding and test sessions of the NOL task. Note that the individual variability is highly constant across sessions. **(B)** Variability in object's exploratory behavior. Different patterns of exploratory behavior based on the slope of the cumulative curves of exploration of each object in the NOL task. Dashed lines represent objects in test session.

Regarding the extended plotting and analysis of object exploration, Figure 4.9 shows some of the event-related variables that we can measure with RodEx to study exploratory behavior. Very interestingly, we identified that in a NOL task, where successful performance implies an increased preference towards the moved object during the

retrieval phase, indeed reflects a full neglect of the immobile object rather than increased attention towards the displaced object (Figure 4.9B).

We further combined different measured variables to obtain relevant information related to the defined exploration targets (object 1 in blue and object 2 in red). General information about the position and the orientation of the animal towards each object during the whole session is available and can be plotted in different ways (Figure 4.9 B-D). Moreover, the important point here is the accessibility to the individual exploratory events that RodEx has identified (Figure 4.9 E-G), which provides additional and valuable information to improve the interpretation of behavioral data.

To summarize this chapter, we conclude that we have developed a versatile tool that provides high-resolution measurements and quantitative data of rodent locomotor and exploratory behaviors. The extended results obtained with RodEx provides not only reliable measurements compared to the manual scorings but also meaningful information overlooked under the traditional analysis, enabling a more detailed characterization of our experimental phenotypes. We have used this method to analyze all the behavioral experiments in the present thesis.

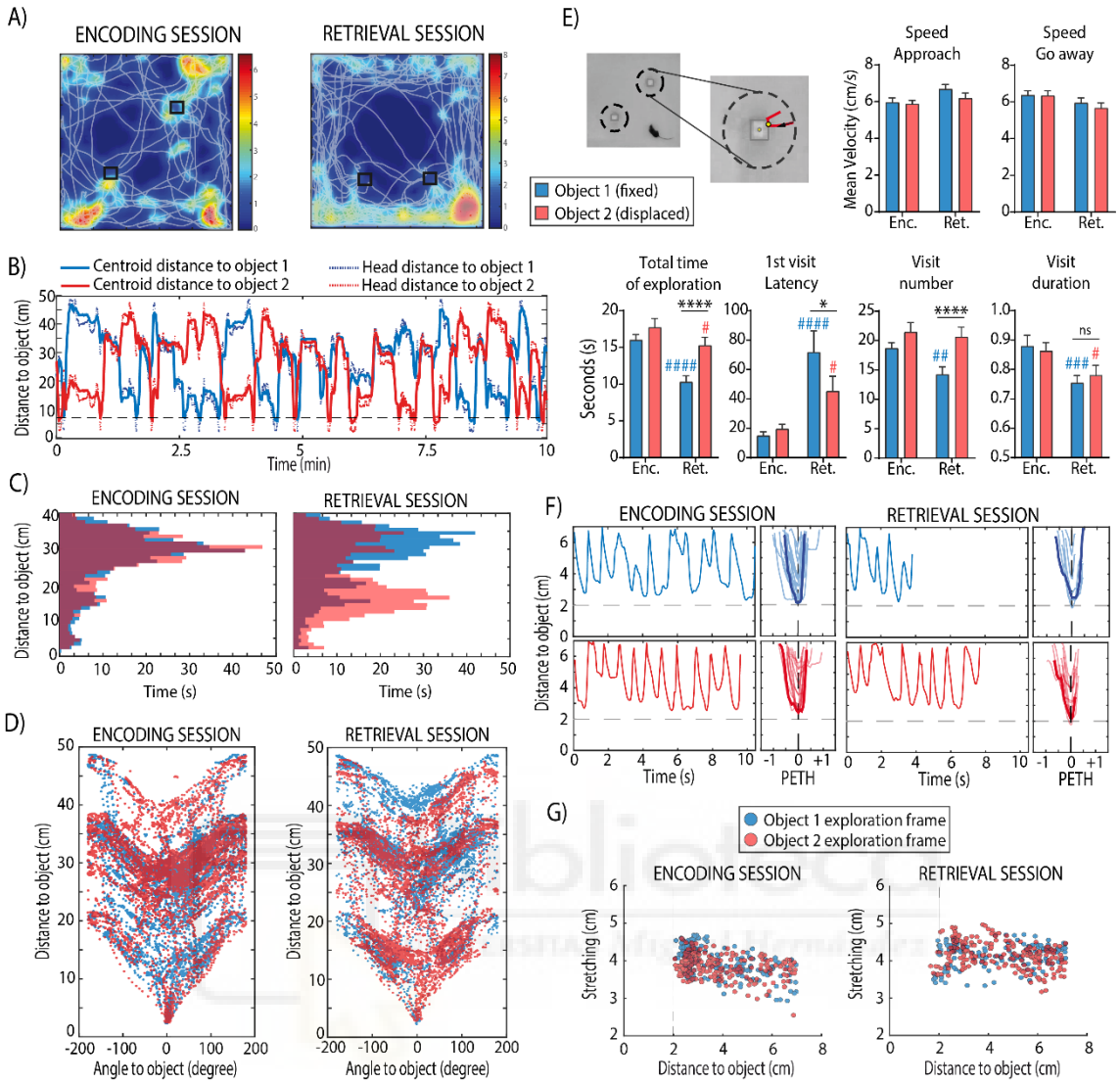

Figure 4.9. Examples of available analysis and data visualization with RodEx.
Examples of measured variables relative to object exploration that can be easily extracted using RodEx. All analyses shown were extracted from the same animal, with the only exception of panel E that shows group averages. **(A)** Representative example of head trajectories (white) overlapped on the corresponding heatmaps of the encoding and retrieval sessions of a NOL task. **(B)** Traces depict the relative distance between the subject and each object along the whole encoding session (blue traces for object 1 or "fixed"; red traces for object 2 or "displaced"). **(C)** Frequency histograms of head-to-object distance. Specifically, this mouse spends more time closer to the displaced object during the retrieval session, while its distance to both objects is similar during the encoding session. **(D)** Orientation towards each object during the whole session. Each dot represents the orientation value (in degrees) for each video frame. **(E)** Typical NOL arena with a zoom in on one of the objects, where dashed line around the object defines th_{dh} and the overlapped red trace represents a single visit. Bar charts show the quantification of different measurements relative to the individual visits to each object. Data show mean ± SEM of the total sample, without differentiating experimental groups (n = 36). Significance levels indicated with star- or hash-code as follows: * $p<0.05$, ** $p<0.01$, *** $p<0.001$, **** $p<0.0001$. * indicates comparison between objects and # indicates comparison between sessions. **(F)** Profiles of individual visits to each object during encoding and test sessions. All visits to each object appear concatenated (*left*) and overlapped (*right*) with t=0 at the maximum proximity to the object during the visit. **(G)** Scatter plots showing how the subject stretched during exploration epochs.

4.2. Manipulating DG-PV interneurons during memory encoding

In Caramés et al., (2020) we already demonstrated that GC perisomatic inhibition plays a critical role in the encoding of spatial memories: while pharmacogenetic inhibition of DG-PV interneurons improved mice performance, PV activation prevented memory encoding in a NOL task. We also evidenced that these localized changes in DG-PV inhibitory activity strongly modulated activity at the network level, increasing (or decreasing) functional connectivity between hippocampus and other memory-related brain regions. However, we did not characterize in detail the mnemonic effect nor distinguish between memory types, so the specificity of the phenomenon remained unknown.

Then, our main goal here was to investigate the effect of manipulating DG-PV cell activity during the encoding of different types of memory. To this end, on the one hand we performed a battery of memory-related behavioral tasks while pharmacogenetically modulating DG-PV interneurons specifically during the encoding phase of each task (see following section 4.2.1). On the other hand, we carried out extended analysis on previously performed experiments (data not published) in order to unveil the role of these interneurons in pattern separation, a DG-dependent function (see following section 4.2.2). Finally, we developed a computational model to integrate previous results and experimentally tested its predictions to explain the likely side effects of downregulating DG inhibitory tone during memory encoding (see following section 4.2.3).

4.2.1. On the role of DG-PV interneurons in non-spatial memories

Extensive empirical evidence from studies on learning and memory studies highlights the specific role of the DG in spatial memories (*"where"* information), while non-spatial memories are typically associated with other hippocampal regions. The recognition of novel objects, or "what" information, is considered DG-independent, relying on CA1 integrity (Gilbert et al., 2001). Hence, we predicted that our DG-PV manipulations would not affect object recognition performance.

On the other hand, although social recognition memory, related to "*who*" information, is mainly attributed to CA2 and the ventral regions of the hippocampus (Hitti and Siegelbaum, 2014; Meira et al., 2018; Okuyama et al., 2016), the involvement of the dorsal DG is not conclusively ruled out. Leung et al., (2018) reported that optogenetically inactivating EC inputs to the dorsal DG during encoding or retrieval phases directly impaired social memory. Therefore, our predictions regarding the effects of manipulating dorsal DG-PV interneurons during social memory encoding were not as definitive as those for other non-spatial memories.

A total of 21 PV-Cre mice, previously injected with DREADDs or sham-operated (n= 7 Sham, n= 7 PV-Gi, n= 7 PV-Gq), were first tested on a Novel Object Recognition (NOR) task (Figure 4.10A). This task evaluates memory for object identity by replacing one of the objects by a new one during the test session, contrarily to the NOL test, where one of the objects is displaced to a new location. As shown in Figure 4.10B, two-way repeated measures ANOVA revealed that all groups preferentially explored the novel object during the test session, without differences between groups regardless PV modulation during the encoding phase (*Session* $F_{1,18}$= 85.55, p<0.001; *Treatment* $F_{2,18}$= 0.08437, p=0.9195).

Two weeks later, we performed a Social Discrimination Task (SDT) with the same animals to assess social recognition memory (Figure 4.10C). We slightly modified the standard SDT protocol adding a second trial during the encoding phase (see Figure 3.4C and section 3.1.4.1 in Methods for a detailed explanation) to additionally test whether PV manipulation has any effect on sociability, which is the preference of rodents to explore conspecifics more than inanimate objects (social cage *vs.* empty cage). We found that all mice preferentially explored the social cage rather than the empty cage during S1 and S2 trials (Figure 4.10D), meaning an intact sociability regardless of DG-PV modulation. During the social novelty trial, although PV-Gi mice exhibited a tendency towards increased preference for exploring the novel mouse (higher DI), there were no significant differences between the experimental groups' performance (*Interaction* $F_{4,34}$= 0.483, p=0.747; *Treatment* $F_{2,17}$= 0.356, p=0.706; *Session* $F_{2,34}$= 8.527, p=0.001).

Despite the absence of statistical differences between groups, we proceeded with the analysis to delve deeper into the behavior of these mice. On the one hand, we expected a better performance on the Novelty session. On the other hand, the previous result is restricted to the averaged DI, without taking into account interaction times individually, which could be overlooking different behaviors. For these reasons, in order to better

elucidate the experiment's outcome, we compared the absolute exploration times towards the familiar vs. the novel conspecific (Figure 4.10E). Individual paired t-test analysis for each experimental group revealed that PV-Gi mice significantly spent more time exploring the novel mouse (t_6= 3.25, p=0.017), while PV-Gq mice failed to preferentially explore the novel mouse (t_6= 1.748, p=0.131). Sham mice showed slight preference for the novel mouse, though without reaching statistical significance (t_5= 2.220, p=0.07). Interestingly, cumulative curves of social interaction depicted a different conclusion, as both PV-Gi and PV-Gq seemed to discriminate the novel conspecific more than Sham mice (Figure 4.10F). Again, one-way ANOVA test comparing the area under the curve (AUC) ratio provided no statistical differences between groups ($F_{2,17}$= 0.134 p<0.875; Figure 4.10G).

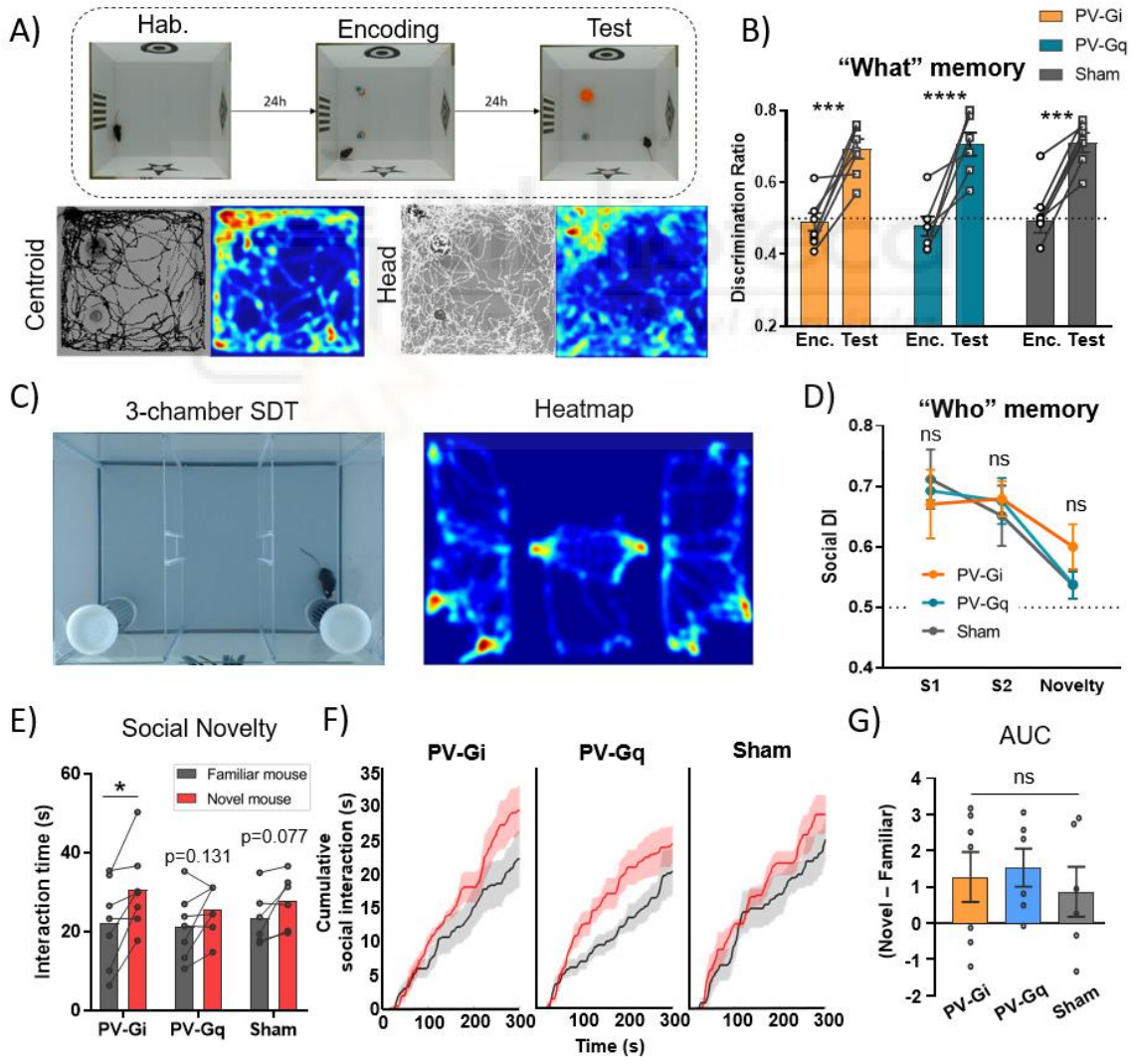

Figure 4.10. DG-PV manipulation during the encoding of non-spatial memories.
(A) NOR task ("what" memory). Schematic representation of the NOR protocol (top) and examples of centroid and head position tracks and heatmaps for the same mouse during a typical test trial (bottom). **(B)** NOR results with paired DI during encoding and test sessions. There are no statistical differences between

groups (*Sham* n=7, *PV-Gi* n=7, *PV-Gq* n=7). **(C)** SDT task ("who" memory) 3-chamber arena (*left)* and a representative heatmap of a 5-min session (*right*). **(D)** Quantification of the averaged social discrimination index, comparing the preference for social *vs.* inanimate stimuli (S1 and S2 trials) or novel *vs.* familiar mouse (Novelty trial) between experimental groups. Two-way ANOVA shows no differences between Sham, PV-Gi and PV-Gq mice in either sociability (S1 and S2 trials) or social novelty preference (Novelty trial). **(E)** Comparison of absolute exploration times during social Novelty test session, comparing times exploring a familiar (black) *vs.* a novel conspecific (red) in Sham, PV-Gi and PV-Gq mice. Paired t-test analyses are calculated independently for each experimental group. **(F)** Cumulative exploration curves of familiar (black) and novel (red) intruders over the 5-min trial (mean ± SEM of n = 7 mice per group). **(G)** Quantification of the area under the cumulative curves (AUC). Results from the one-way ANOVA comparing the difference between novel and familiar curves per each animal, indicating a lack of significant differences between the experimental groups. Note that for SDT, 1 animal was excluded from the analysis (*Sham* n=6, *PV-Gi* n=7, *PV-Gq* n=7). Significance levels indicated with star code as follows: * p<0.05, ** p<0.01, *** p<0.001, **** p<0.0001.

Overall, we considered these results not fully conclusive and further experiments must address this question to clarify whether PV manipulation could affect social memory. Together with the NOL results, we conclude that decreasing or increasing DG-PV activity primarily impacts the encoding of long-term spatial memories, leading to enhanced or impaired memory for object-location associations, respectively.

4.2.2. On the role of DG-PV interneurons in pattern separation

Our second objective for this chapter was to deepen into the role of DG-PV interneurons in pattern separation, the ability of mice to discriminate among similar but slightly different experiences or stimuli. There is numerous computational and empirical evidence relating this function to the DG (Leutgeb et al., 2007; Marr, 1971; Treves and Rolls, 1992). We reasoned that better coordination between experience-relevant sets of activated neurons, as seen under PV-cell inhibition (Caramés et al., 2020), will facilitate the strengthening of synaptic connections between them, allowing more efficient association of experience features within memory engrams. In turn, pattern discrimination will improve, since the more accurate and complete the memory representation of an experience is, the easier it will be to discriminate it from previously stored experiences with overlapping features. Therefore, we used our experimental tools to test this hypothesis.

For this purpose, we conceptualized and designed a new behavioral protocol, called SETA task (see Figure 3.5 and section 3.1.4.2 in Methods), with which we have already obtained some evidence of the implication of DG-PV on pattern separation (preliminary data

presented in the Thesis of Dr. José María Caramés). Briefly, we used a semicircular arena (SETA maze) where mice encountered two identical objects during the encoding phase (initial position, P_0); in the following trials, one object is gradually displaced in small steps while the other remains in a constant location (Figure 4.11A, for a detailed description see Methods). With this paradigm, we can evaluate pattern separation by measuring which displacement (from P_1 to P_5) is required for mice to be able to detect spatial changes in the environment, which is reflected in a preferential exploration of the displaced object. The protocol can be used to test short- and long-term memory (STM and LTM protocols; see Methods).

4.2.2.1. DG-PV inhibitory tone controls spatial pattern separation

Figure 4.11 illustrates the outcomes of the SETA protocols, where n = 18 C57BL/6J WT mice were used as control animals for the STM protocol (ISI = 2 min between P_0 and P_1 trials). In this experiment, mice showed a preference for the displaced object (DI > 0.5) when it had moved at least 15 cm (Figure 4.11B). This preference resulted from reduced habituation toward the moving object compared to the immobile one, rather than a substantial increase in exploration of the moving object (Figure 4.11F). Notably, once the animal recognized the change in the context, its interest in the moving object remained consistent for the subsequent trials.

In the LTM protocol, when 24 hours elapse between the encoding and the test trials (ISI = 24 hours min between P_0 and P_1 trials), we tested the effect of modulating DG-PV interneurons in pattern separation (see Figure 3.5 in Methods for a detailed description). In this LTM protocol at control conditions (Sham group), several things are noteworthy. First, the discrimination of the object's movement occurred again at P_3 (15 cm from the position seen the day before) and not at P_4 (15 from the first position seen on the day) (Figure 4.11C). This indicated a constructive interaction between long-term and short-term memory buffers, where the animal discriminated the context by combining memory stored from the previous day with the present information.

Second, while the DI behaved similarly in both STM and LTM tasks under control conditions (Figure 4.11 B vs. C), the absolute exploration times tell a different story (Figure 4.11 F vs. G). The time spent exploring the objects during the first trial after the 24h-delay in the LTM task (P_1) dropped dramatically (Figure 4.11G and J). This level of

exploration mirrored the familiarity achieved towards the immobile object by the end of STM test at P_5 (Figure 4.11F), reflecting the animal's habituation to an already familiar object. Thus, although mice did not discriminate the movement of the object at P_1 in the LTM test, they already demonstrated familiarity with the objects. Therefore, "what" and "where" can be dissociated in the developed task: the animal has formed a memory representation of the objects (a memory of "what"), but the displacement (5 cm) is insufficient to be identified as a new pattern (memory of "where").

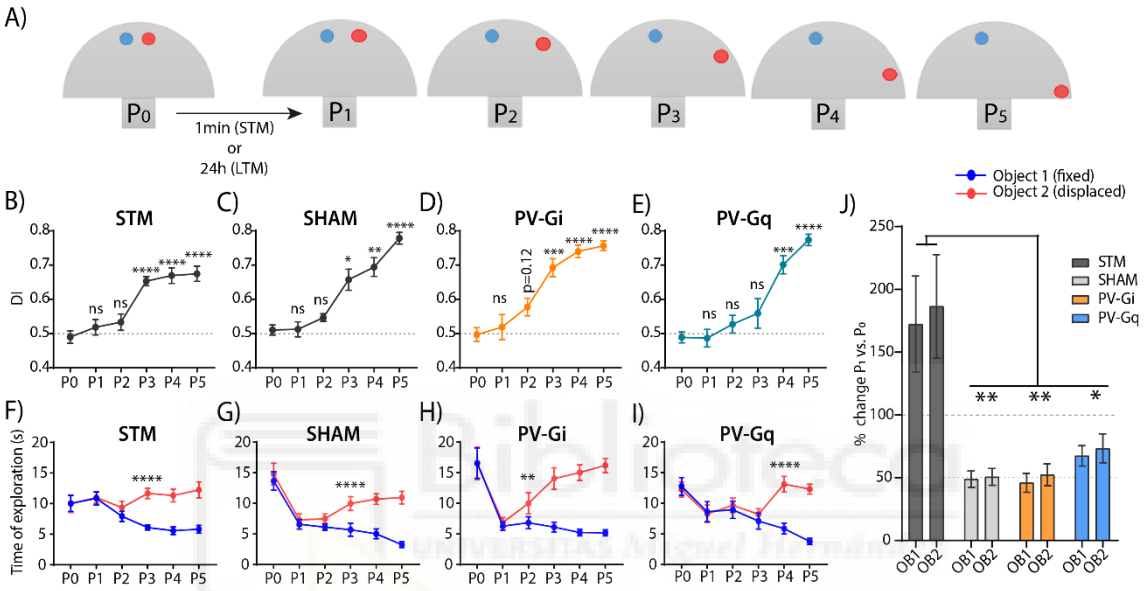

Figure 4.11. Behavioral Assessment of Spatial Pattern Separation with SETA task.
(A) Schematic representation of the SETA task protocol to assess spatial pattern separation. **(B)** Graphical quantification of averaged discrimination index across trials for control mice in STM protocol (n = 18). Values higher than 0.5 denotes preference for the displaced object. **(C-E)** Same than B for Sham (n = 13), PV-Gi (n = 12) and PV-Gq (n = 13) mice in LTM protocol. **(F)** At STM protocol, comparison of the time of exploration of the fixed (blue) and the moving (red) object across trials. **(G-I)** Same than in F for LTM protocol in Sham, PV-Gi and PV-Gq mice. All statistical analysis were done using 2-way ANOVA and show mean ± SEM. **(J)** Percentage of change from P_0 to P_1 trials in the time of exploration of each object. Data show mean ± SEM. Significance levels indicated with star code as follows: * $p<0.05$, ** $p<0.01$, *** $p<0.001$, **** $p<0.0001$.

Then, our investigation delved into the effects of modulating DG inhibitory tone during the encoding phase (P_0) of the LTM protocol. In a first exploration, reduced PV inhibition seemed not to enhance pattern separation (Figure 4.11D). DI curve indicated a significant preference for the displaced object again at P_3, showing a similar DI progression than that observed in Sham mice (see Figure 4.12A). However, a slight tendency to a preference for the displaced object at P_2 was also evident. Indeed, further exploration of the absolute times revealed that PV-Gi animals spent significantly more time exploring the displaced vs. immobile object already at P_2 (Figure 4.11H), reflecting an improvement in pattern

separation that was overlooked in the DI analysis. Moreover, the marked reduction in exploration times at P_1 was comparable to that observed in the Sham group (Figure 4.11J), highlighting the specific enhancement of the "where" memory when DG inhibition was decreased.

In contrast, increased activation of DG-PV activity during the encoding phase resulted in impaired pattern separation, delaying the detection of spatial changes to P_4 (20 cm from the position seen the day before) (Figure 4.11I). Exploration by PV-Gq mice at P_1 was reduced compared to P_0, although not as drastically as for the previous groups, which could be potentially reflecting an interaction between the "where" and "what" information (Figure 4.11J). If we omit the data at P_0, the trend of the exploration curves aligns entirely with the STM control mice (merge Figure 4.11F from P_0-P_4 with Figure 4.11I from P_1-P_5), which was the expected outcome considering that the upregulation of PV activity in PV-Gq animals would interfere with the encoding of spatial information (see Figure 1.8). In this scenario, later pattern separation at P_4 would be assisted by ongoing (CNO free) STM.

4.2.2.2. DG-PV level of inhibition sets the threshold for spatial pattern separation

To better understand how the activity of PV interneurons influences pattern separation, we performed a more detailed behavioral analysis at the individual level. We calculated the probability of each subject to discriminate object's displacement at each position. We considered that a subject has detected the spatial change when the DI at a given position is greater than 2 SD from the mean DI at the encoding phase. Mice were then re-classified according to this criterion, leading to 5 possible subclasses per group attending to the discrimination thresholds (Figure 4.12B and E-H), named accordingly to the position at which they first detect object's displacement ('*5cm'*, '*10cm'*, '*15cm'*, '*20cm'* and '*25cm'*). Under this re-classification, each subject belongs to a unique subgroup, so although they could present significant preference for the displaced object in more than one trial, it would be classified in the first displacement detection (see DI curves in Figure 4.12 E-H). Indeed, it seems that they maintained their preference for the displaced object once they have realized the movement (see DI curves in Figure 4.12 I-L) regardless DG-PV manipulation.

Although most of the subjects at control conditions detected object displacement at P_3 (‘*15cm’* subgroup), a small proportion of animals were able to discriminate displacements at P_2 (‘*10cm’*) or even P_1 (‘*5cm’*), whilst some others required more than 3 steps (‘*20cm’* subgroup at P_4 and ‘*25cm’* subgroup at P_5) to realize the difference in object’s location (Figure 4.12 B,E,F). Interestingly, this distribution shifted by modulating PV cell activity (Figure 4.12C). When mice encoded the initial position of the objects with a reduced PV-inhibitory tone in the DG, this distribution shifted to the left as an increased number of subjects realized spatial changes before the third displacement (Figure 4.12 B,C,G), reflecting an enhanced pattern separation capacity. Contrarily, when activating DG-PV interneurons during encoding at P0, very few animals detected the movement before 20cm (Figure 4.12 B,C,H). Cumulative probability curves (Figure 4.12D) highlight the differences in discrimination probability between groups: while approximately 60% of mice have already discriminated the change in object location at 15 cm under control conditions (n = 12/18 in STM and n = 8/13 in Sham), it increases up to 90% (n = 11/12) on PV-Gi mice and reduces to 30% (n = 4/13) in PV-Gq.

We then compared the performance of our experimental groups using the new classification (Figure 4.12 I-L). Broadly, our findings revealed that mice classified within a particular discrimination threshold subgroup showed consistent performance, irrespective of the experimental group they belonged to (STM, Sham, PV-Gi or PV-Gq). All groups exhibit similar patterns of exploration (DI) across trials, suggesting that the extent of PV inhibition influences the ability to discriminate (Figure 4.12 C-D) but does not alter the manner in which objects are explored (Figure 4.12 I-L).

Overall, with this extended analysis that accounts for the individual variability, we have demonstrated the existence of different discrimination profiles, with mice presenting variable thresholds for pattern separation. The relevant finding was that inhibition or activation of DG-PV increased or reduced, respectively, the ability to detect spatial changes at the individual level. That is, it is not a cumulative change in the time devoted to exploring one object over the other, but an all-or-none effect on the individual's awareness of the change.

From the perspective of pattern separation, the results may lead one to question why, if a lower inhibitory tone facilitates pattern separation, such a tone has not been selected throughout evolution. However, from the perspective of updating memory with new information, the system may be optimal, as it allows both updating when there are

significant changes, and preserving memory (avoiding continuous updating) when changes are minor, thus optimizing resources. In any case, in the next chapter we asked what are the potential trade-offs of decreasing inhibitory tone in the DG.

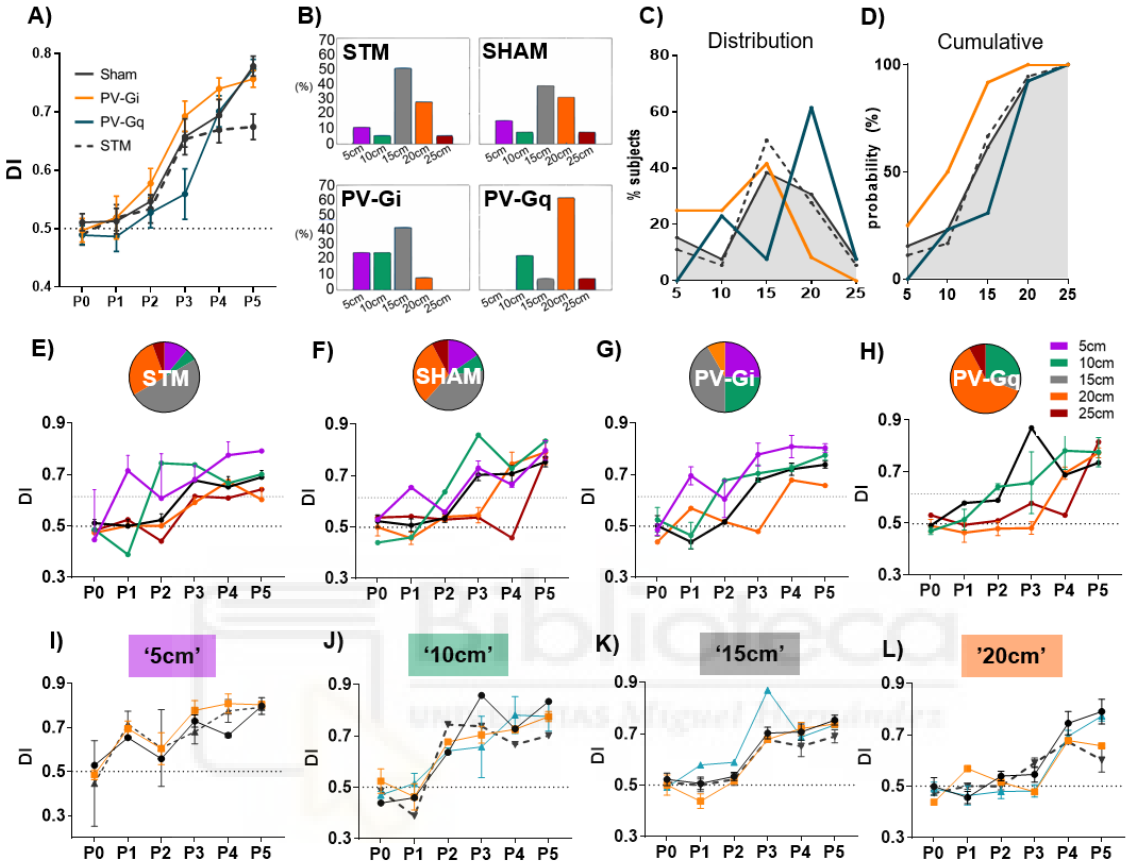

Figure 4.12: Individual analyses reveal different discrimination profiles in pattern separation
(A) Graphic showing the comparison of average DI between STM (n = 18) and LTM groups (*Sham* n = 13, *PV-Gi* n = 12 and *PV-Gq* n = 12; showed in Figure 4.11 separately). **(B)** Discrimination profile distribution of mice across the different spatial discrimination threshold denoted as '5cm' (purple), '10cm' (green), '15cm' (grey), '20cm' (orange), and '25cm' (red) depicting the position at which mice first detected object displacement. **(C)** Effect of PV cell activity modulation showing a shift in the distribution of discrimination thresholds subjects. While STM and Sham distributions are overlapped, PV-Gi and PV-Gq curves appear left- and right-shifted, respectively **(D)** Cumulative probability curves from C showing the discrimination probability between group**s. (E-H)** Pie charts showing the distribution of each experimental group into the subclasses based on the discrimination threshold and intragroup comparative DI curves for the 5 possible subclasses: **(E)** Mice from STM group are divided as follows: STM_{5cm} n=2, STM_{10cm} n=1, STM_{15cm} n=9, STM_{20cm} n=5, STM_{25cm} n=1. **(F)** Mice from Sham group are divided as follows: $Sham_{5cm}$ n=2, $Sham_{10cm}$ n=1, $Sham_{15cm}$ n=5, $Sham_{20cm}$ n=4, $Sham_{25cm}$ n=1. **(G)** Mice from PV-Gi group are divided as follows: $PV\text{-}Gi_{5cm}$ n=3, $PV\text{-}Gi_{10cm}$ n=3, $PV\text{-}Gi_{15cm}$ n=5, $PV\text{-}Gi_{20cm}$ n=1, $PV\text{-}Gi_{25cm}$ n=0. **(H)** Mice from PV-Gq group are divided as follows: $PV\text{-}Gq_{5cm}$ n=0, $PV\text{-}Gq_{10cm}$ n=3, $PV\text{-}Gq_{15cm}$ n=1, $PV\text{-}Gq_{20cm}$ n=8, $PV\text{-}Gq_{25cm}$ n=1. **(I-L)** For each discrimination threshold, comparison between STM, Sham, PV-Gi and PV-Gq groups ($F_{2,4}$= 0.488, p = 0.646 for *5cm*; $F_{3,4}$= 0.075, p = 0.970 for *10cm*; $F_{3,16}$= 1.612, p = 0.226 for *15cm*; $F_{3,14}$= 1.109, p = 0.379 for *20cm*). Data shown as mean ± SEM (*STM* n = 18, *Sham* n = 13, *PV-Gi* n = 12, *PV-Gq* n = 13).

4.2.3. Benefits and trade-offs of reduced DG inhibitory tone during encoding of spatial memories

4.2.3.1. From experimental data to computational model

Taking together the previous results, we moved to a computational approach to further understand how changes in DG inhibitory tone could affect spatial memory formation. Computational model was designed and performed by Dr. Encarni Marcos.

To this end, we modelled a cortico-hippocampal neural network that aims to emulate the decision-making of an animal exploring a familiar environment in which it may encounter novel or familiar objects. The level of novelty of a "sensory" input pattern will determine whether the model outputs a command to explore the novel object or not. The model consisted of two modules (Figure 4.13A), related to hippocampal and prefrontal cortex functions: the first one performs Hebbian learning and pattern separation, while the second module makes the decision towards exploring or not the spatial novelty.

In the hippocampal module, we used an E%-max winner-take-all rule, that determine which neurons are activated based on the excitability of neurons with maximum activity (De Almeida et al., 2009) (see *3.1.5. Computational model* in Methods). In the model, the parameter E% is used to adjust network inhibition. A higher value of E% reduces inhibition and facilitates neuronal recruitment, while a lower value of E% increases inhibition and hinders neuronal activation.

To simulate the discrimination ratios during the NOL task, the input to the “go” group in the decision-making module was set constant, simulating the output of the hippocampal module for familiar patterns. The “no go” group received the output of the hippocampal module as the sum of the activity of its neurons. The decision was then considered to be made towards the object when the “go” group won the competition. The DI was calculated as the ratio between the number of decisions towards exploring the object when the input pattern is the novel one and the number of decisions made towards exploring the object when the pattern is familiar or novel (total cases).

$$DI\ predicted = \frac{Ngo}{Ngo + Nnogo}$$

The model showed that the inhibitory tone of the DG directly influences the output representation of a learned pattern, in terms of correlation, when gradual changes are made to the pattern (Figure 4.13B). With lower levels of inhibition, the network is able to detect more subtle differences between the current and the learned patterns, discriminating them even when input correlation is as high as 0.8. These subtle differences are overlooked with higher levels of inhibition, resulting in generalization and decreased pattern separation (Figure 4.13C). This result could explain the observed experimental data where inhibition of DG-PV during the encoding phase resulted in a higher number of novelty choices compared to controls in a NOL task. However, although the results suggest an improvement in memory performance, the change in the level of inhibition could also impact the robustness of the network because excessive sensitivity to change in a system with noisy connections, such as the brain, may also destabilize pattern representation. To test this possibility, we added synaptic noise to the neural network by allowing fluctuations in the synapses' strengths. As expected, this manipulation had a higher impact on low levels of inhibition compared to high ones, resulting in a rapid decrease in the stability of the output for a learned pattern (Figure 4.13D). Therefore, the simulated results highlight the fundamental role of local competition (inhibition) in maintaining the stability of memory representations in the network.

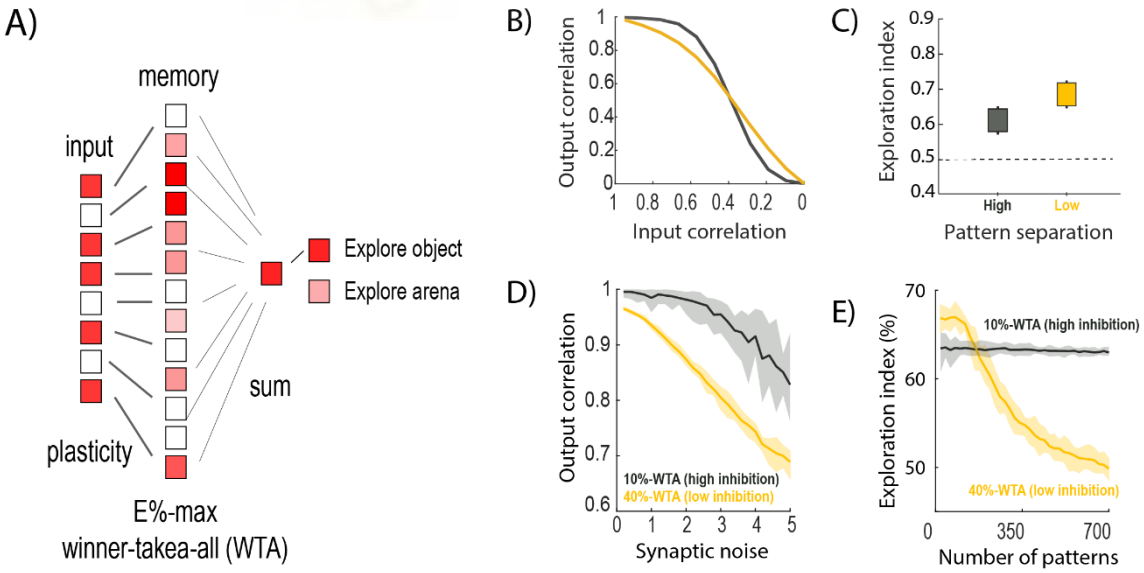

Figure 4.13. Simulations of the hippocampus-prefrontal cortex model for different levels of inhibition. **(A)** Computational model architecture illustrating the two-module computational neural network simulating cortico-hippocampal interactions under different levels of inhibition. **(B)** Pattern separation (measured as the correlation of activity among excitatory neurons associated with different levels of input correlation) is influenced by the level of inhibition within the hippocampus. **(C)** Novelty exploration index obtained after decision-making, for either high (black) or low (yellow) inhibition levels, when the input

pattern correlation is 0.6. **(D)** Simulation of the pattern separation measure, calculated through the correlation between the output produced for a pattern that has been previously learned and the output for that same pattern when noise is added to the plastic synapses**. (E)** Simulations of the discrimination index of the novel object for different numbers of learned patterns. The inhibition level is 10%-WTA (high) and 40%-WTA (low inhibition). Mean ± SEM represented.

The change in network stability opens the question of whether lower inhibitory tone might impact memory capacity, as the representation of previously learned patterns seemed to be less robust to noise. To assess this, we systematically increased the number of learned patterns in the network and estimated the DI for each condition. Our results show that the level of DG inhibition directly impacts memory capacity. Specifically, when inhibition in the hippocampal module is low, the novel object exploration (DI) drops dramatically as the number of learned patterns increases (Figure 4.13E), reaching a chance level. This indicates that novel and familiar objects are no longer distinguishable by the model (DI = 0.5). Conversely, the DI remains constant when the number of learned patterns increases but the level of inhibition is high.

Thus, the model predicted that low levels of inhibition would improve pattern separation, but as a consequence, would impair memory capacity. In the next section we experimentally approached these predictions.

4.2.3.2. From computational model to experimental data: modulating DG inhibitory tone impairs spatial memory of multiple patterns.

The following step was to test the predictions of the computational simulations. To this end, we designed a new behavioral protocol that we called Multiple Input Patterns task (MIP task). The goal behind this task was to increase the number of input patterns during the encoding phase of the memory. To achieve this objective, we have designed 4 different contexts with different features and specific object-context and object-location associations (see 3.1.4.2 in Methods for a detailed description), considering each context a different input pattern. After performing several pilot studies (data not shown), we adapted the final protocol to a 3-days task (Figure 4.14A).

Same n = 21 mice that performed NOR and SDT experiments (in previous section 4.2.1) were used to carry out the MIP task. The first day, mice visited sequentially the 4 contexts and were allowed to freely explore them for 10 minutes, waiting for 2 minutes in the

central corridor in between contexts. The next day, mice received an i.p. injection of 1mg/kg CNO 1h before starting the encoding trials, in which they visited the 4 contexts, in a different order. In each context mice encountered two identical objects at specific locations. One day after, one of the objects is displaced to a different location at each context, and memory capacity was tested by measuring in how many contexts mice are able to discriminate object's displacement.

In control conditions, mice successfully learned 2 to 3 out of 4 contexts (*Treatment* $F_{3,18}$=0.529, p = 0.669; *Session* $F_{1,6}$= 80.35, p = 0.0001; *Interaction* $F_{3,18}$=9.95, p = 0.0004), with clear preference for the displaced object in "Blue" and "Yellow" contexts and a mild preference in "Green" context. Nevertheless, they were not able to discriminate object displacement in the "Red" context (Figure 4.14B, left). We considered this performance to be the most appropriate for the sham-operated control group, as it allows us to detect both improvement or reduction of memory capacity.

Interestingly, consistent with the prediction of the computational model, PV-Gi animals (with inhibited PV interneurons) critically reduced their performance (Figure 4.14B, middle), showing no significant preference for the displaced object in any of the 4 contexts (*Treatment* $F_{3,18}$=9.752, p=0.0005; *Session* $F_{1,6}$=4.29, p=0.084; *Interaction* $F_{3,18}$=1.037, p = 0.399). We also tested PV-Gq animals with increased inhibitory activity of PV cells, which also showed an impaired memory, being able to detect spatial novelty only at one context (Figure 4.14B, right).

In an attempt to simplify the analysis of these results, we summarized the performance of each subject by using the averaged discrimination index (aDI), which takes into account the mean performance of the subject for all the contexts (Figure 4.14C):

$$aDI = \frac{(DIred + DIgreen + DIyellow + DIblue)}{4}$$

One-way ANOVA test showed significant differences between Sham group and PV-Gi or PV-Gq ($F_{2,18}$=6.659, p=0.007; Dunnett's multiple comparisons Sham vs Gi p = 0.004 and Sham vs Gq p = 0.049). These results demonstrated that up- or downregulating DG inhibitory tone reduced memory capacity as the number of input patterns increased, corroborating the predictions of the computational model.

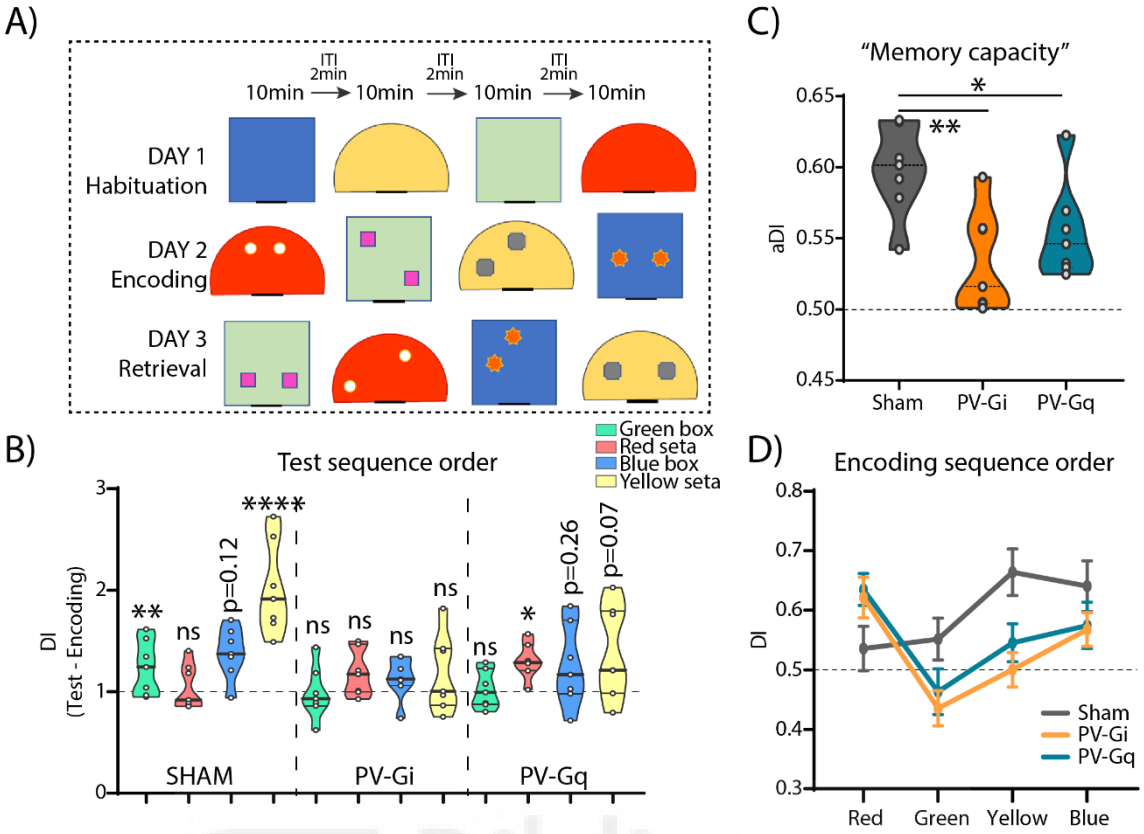

Figure 4.14. Impact of DG-PV modulation in memory capacity.
(A) Experimental protocol for Multiple Input Patterns (MIP) Task, describing the three-day task designed to assess memory capacity by introducing multiple input patterns (up to 4 different contexts). **(B)** Intra group comparison: DI ratio between encoding and test sessions for Sham (n = 7), PV-Gi (n = 7), and PV-Gq (n = 7) groups is used to simplify data visualization. Two-way ANOVA is comparing DI from encoding *vs.* test session. **(C)** Comparison between groups: averaged DI (aDI) is calculated from the mean performance across all four contexts for each subject. **(D)** Comparison of retrieval performance based on the order in which the contexts were visited during the encoding phase. Two-way ANOVA reveal differences between groups and between contexts (*Treatment* $F_{2,18}$=6.669, p=0.0068; *Context* $F_{2.65,47.66}$=6.238, p=0.0017; *Interaction* $F_{6,54}$=2.621, p = 0.0265). Post-hoc multiple comparison highlights the significant difference at 'Yellow' context between Sham and PV-Gi (p=0.016) and PV-Gq (p=0.089) groups. (Statistical analyses were done using one-way (panel C) or 2-way ANOVA (panel B and D). ns: no significative, *=p<0.01, **=p<0.001.

Moreover, we finally compared mice performance throughout the different contexts, based on the order in which the contexts were visited during the encoding phase, where the manipulation of PV inhibitory activity occurred (Figure 4.14D). The retrieval of the Sham group reflects a typical recency, scoring higher DI in the last visited contexts compared to the first ones. Contrarily, PV-Gi animals showed the opposite performance, exhibiting a primacy effect in their retrieval DI values, which we interpreted as an increased proactive interference, where the encoding of first patterns (visited contexts) hinders the encoding of the following ones. Intriguingly, PV-Gq animals showed the same performance as the PV-Gi group. This was an unexpected result as opposite PV

manipulations, with clear and bidirectional effects on memory encoding and pattern separation, had the same effect in terms of interference in memory capacity.

Overall, reduction of perisomatic inhibition of granule cells enhances memory formation and facilitates pattern separation of single episodes, but the cost is high in memory capacity. This makes a balanced tandem of inhibition/disinhibition fundamental in the mechanism of memory updating. In the final Chapter of results, we will present our attempts to investigate this balance in more natural conditions.

4.3. Recording DG-PV interneurons

Following the outcome of the previous experiments, our next goal was to investigate the functional and physiological regulation of DG-PV interneurons during memory formation.

In contrast to electrophysiological recordings, calcium imaging techniques allow us to selectively record the activity of specific neuronal populations. During the development of this thesis, we introduced fiber photometry technique in the laboratory to measure calcium-based activity in PV-Cre animals, by virally expressing calcium sensors (GCaMP6s).

In this chapter, we first implemented fiber photometry technique performing GCaMP recordings in anesthetized animals (see following section 4.3.1). Then, we performed GCaMP recordings under freely-moving conditions to study the dynamics of DG-PV interneurons during memory formation (see following section 4.3.2).

Upon initiating photometry experiments, we introduced the use of transgenic PV-Cre rats in our laboratory. This addition was of great interest as rats, compared to mice, consistently yield more stable results in behavioral experiments and offer better conditions for imaging tests like fMRI (larger brain areas improve resolution and signal-to-noise ratios). To explore and leverage these advantages, we performed parallel experiments with both rats and mice to examine GCaMP expression and recordings. Vanesa Salazar, a master's student in the lab, conducted mice experiments (which were presented in her master project *"Recording in vivo cell-specific activity signals from parvalbumin interneurons",* 2019), while I performed the same procedures in rats. In the following chapter, I present the implementation experiments using PV-Cre rats.

4.3.1. Implementing GCaMP fiber photometry recordings

Before-conducting fiber photometry recordings in freely-moving animals, we performed a series of *in vivo* preliminary experiments (Figure 4.15A) with two primary objectives. First, we established technical and procedural protocols to ensure optimal fiber photometry recordings. These protocols encompassed the establishment of precise stereotaxic coordinates for injection and fiber-implantation in both mice and rats (Figure

4.15B), as well as the choice of the concentration and volume of the delivered virus to verify its functional expression (Figure 4.15C).

Second, we assessed the functionality of GCaMP6s and GCaMP6f sensors expressed in DG-PV interneurons to validate their suitability for our experimental requirements (Figure 4.15 D-E). Given the faster kinetic properties of GCaMP6f relative to GCaMP6s, we hypothesized that GCaMP6f would be the optimal calcium sensor for expression in fast-spiking PV interneurons.

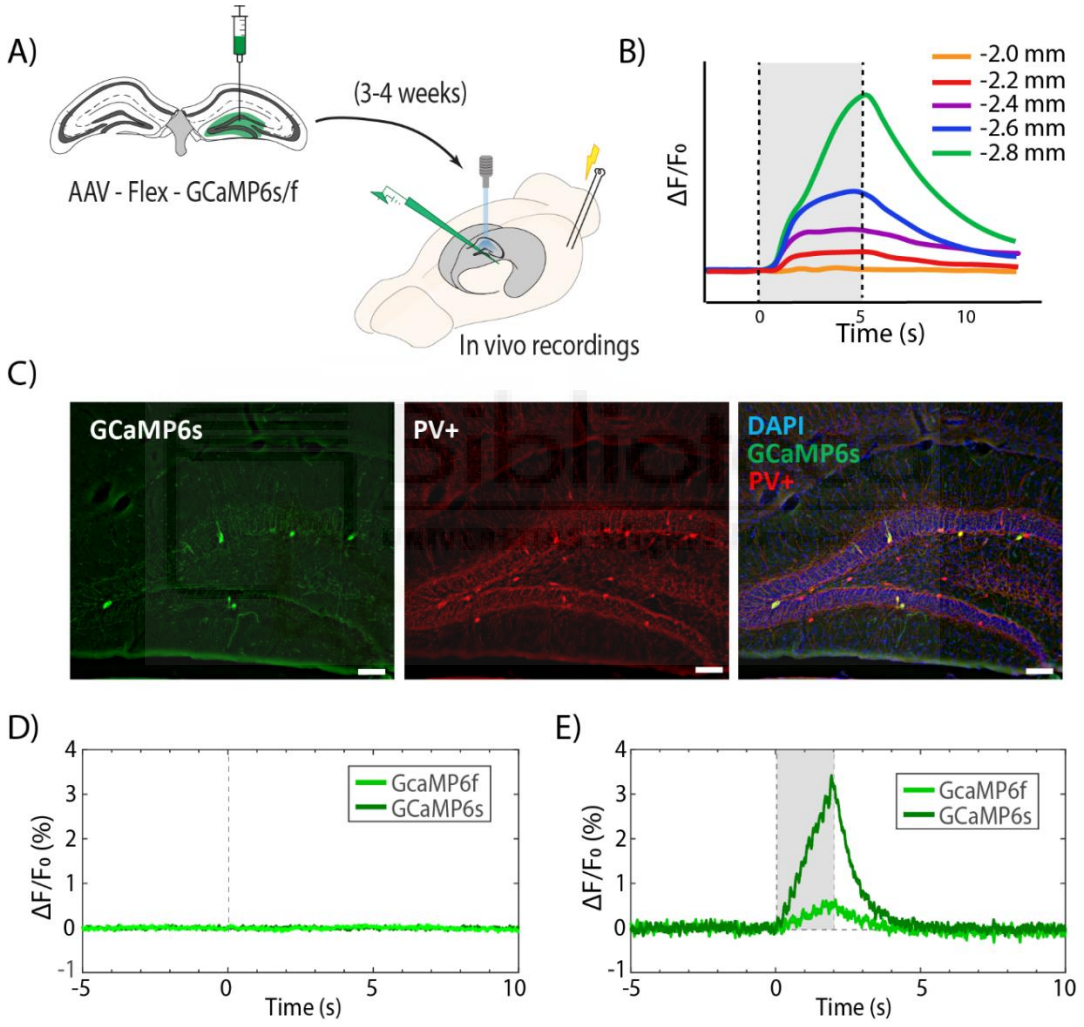

Figure 4.15. PV-calcium signals in response to different PP electrical stimulation protocols using fiber photometry. **(A)** Schematic representation of the stereotaxic injection and electrical stimulation of the perforant pathway in anesthetized PV-Cre rats expressing GCaMP6s or GCaMP6f. Local field potentials and PV-calcium activity were simultaneously recorded in the DG. **(B)** Representative examples of evoked calcium responses recorded at different depths from the brain surface (in the DV axis) while reaching the DG with the recording optic-fiber. Grey shadow represents the stimulation time to evoke calcium responses. **(C)** Immunofluorescence staining against GFP (to enhance fluorescence from GCaMP), against PV (red) and nuclear staining (DAPI in blue). **(D)** Single-pulse electric stimulation of the PP at suprathreshold intensities showing no detectable changes in the intensity of the GCaMP signal of any sensor (6s or 6f). **(E)** Graphic showing the successful evocation of Ca2+ responses in DG-PV interneurons with 5 Hz pulse trains in GCaMP6s and GCaMP6f-expressing PV interneurons.

PV-Cre rats were stereotaxically injected with 0.5µl of cre-dependent AAV-GCaMP6s (n = 3) or AAV-GCaMP6f (n = 3) in the left dorsal DG. After 3 weeks for viral expression, we combined fiber photometry recordings of DG-PV interneurons in urethane-anesthetized rats with electrical stimulation of the perforant pathway (PP), the main input to the DG (Figure 4.15A). To correctly place the stimulation electrode and ensure the activation of DG-PV interneurons by PP input, we used simultaneous recordings of local field potentials (LFP) in the DG.

We started checking whether we could differentiate feedforward from feedback inhibition in GCaMP-expressing PV interneurons. We applied single-pulse electric stimulation to the PP at intensities subthreshold for GC firing (40-80 µA), as demonstrated by the absence of a population spike, to recruit PV-cells mainly in a feedforward manner. Unfortunately, this stimulation protocol was not sufficient to produce detectable changes in the intensity of the GCaMP signal of any sensor (6s or 6f). Indeed, a single suprathreshold stimulus (600-900 µA) evoking a strong population spike was also unable to evoke Ca^{2+} transients (Figure 4.15D), suggesting either a low sensitivity of the calcium sensors or a strong effect of anesthesia.

As an alternative strategy, we applied paired-pulse stimulation in order to enhance the recruitment of feedforward inhibition. Briefly, this protocol consists of two consecutive supra-threshold stimulation pulses, separated by 20-ms delay. Each pulse is expected to recruit feedforward inhibition. However, the first pulse elicits a full-sized population spike, reflecting the firing of granule cells in the DG, that also activates feedback inhibition and largely reduces granule cell firing in response to the second stimulation (see section 3.2.5 in Methods). Therefore, simply speaking, each paired-pulse stimulation protocol recruits two times feed-forward inhibition, one time feed-back inhibition and one time granule cell firing. Unfortunately, at least in anesthetized animals, this protocol also failed to produce consistent Ca^{2+} responses. We concluded that single or paired-pulse stimulation may produce very dim changes in PV-cell driven fluorescence intensity unable to be detected in our preparation.

As an internal check that the system was working, we used more intense stimulation by applying repeated electrical pulses at a frequency of 5 Hz (see Methods for detailed description of the stimulation protocols). As can be seen in Figure 4.15E, these protocols evoked clear Ca2+ responses. In good agreement with previous evidence (Chen et al., 2013), GCaMP6s-expressing PV interneurons showed greater responses to 5Hz trains of

stimulation than those evoked by GCaMP6f-expressing PV cells. This result dispelled doubts about possible technical problems with the preparation and demonstrated the possibility of obtaining specific calcium activity signals from PV interneurons, although it did not allow us to distinguish between feed-forward and feed-back events, as both are mixed in a prototype stimulus train.

Furthermore, in none of the animals recorded under anesthesia with either calcium sensor, we recorded large nor medium size fluctuations in the basal signal (see Figure 4.15 D-E pre-stimulus period), so we could not perform resting state or spontaneous activity analysis. We conclude that the effect of anesthesia is critical on the calcium signal. Subsequently, we found that an anesthesia combining medetomidine and ketamine allows us to record calcium signals of greater amplitude (data not shown). At the time of writing this thesis, we are using this anesthesia in combined fiber photometry and fMRI experiments (see Further Directions in Discussion).

4.3.2. Recording DG-PV Ca^{2+} dynamics during spatial processing and memory formation

Throughout the previous chapters we have shown the impact of decreasing or increasing the activity of DG-PVs in the encoding of spatial memories. We therefore wondered how PV activity is naturally modulated during the formation of such memories. In other words, we have shown what PV cells can do on memory encoding, but not what they actually do during those periods. To answer this question, we used the implemented PV-cell specific calcium recordings and focused on investigating their activity during spatial information processing and contextual novelty detection.

We hypothesized that DG-PV inhibition would be downregulated to facilitate encoding of novel information, while increased PV activity would prevent encoding of irrelevant (or unchanged) spatial information.

To test our hypothesis, we injected and implanted n = 16 PV-Cre mice with cre-dependent AAV-GCaMP6s in the left DG to perform a battery of behavioral tests while simultaneously recording PV activity with fiber photometry. Although behavioral tasks were performed as shown in Figure 3.11, the presentation of the results follows a different order to facilitate the narrative.

Prior to any experimental test, mice were habituated during 2 weeks to the experimental room and to experimenter's manipulations, including periods of handling and immobilization to connect the fiber patch-cord (see 3.2.6 in Methods for a detailed explanation of behavioral procedures).

4.3.2.1. PV-calcium activity highly correlates with running speed in behaving animals

Our first observation was the strong correlation between the amplitude of the calcium signal and the velocity of the animal while exploring the arena (Figure 4.16 A-B). The faster the animal was moving in the arena, the higher the intensity of the recorded fluorescence (ΔF) signal. Although there was not a perfect linear relationship, Pearson correlation coefficient showed that the two variables correlated significantly (Figure 4.16C).This was not a surprising finding though, as hippocampal activity is known to regulate locomotion and running speed (Ahmed and Mehta, 2012; Bender et al., 2015; Furtunato et al., 2020), and we have shown that the input from the entorhinal cortex to the DG, as recorded in the theta power of the LFP signal and extracted by independent component analysis (ICA), strongly correlates with the velocity of the animal (López-Madrona et al., 2020). Therefore, a higher input to the DG is expected to recruit both, in a feedforward and feedback manner, more PV cells. This fact complicated the analysis of the calcium signal in freely behaving experiments. As an intriguing observation, we found systematically that the raising in PV-GCaMP6s activity preceded the increase in the velocity of the animal (Figure 4.16D).

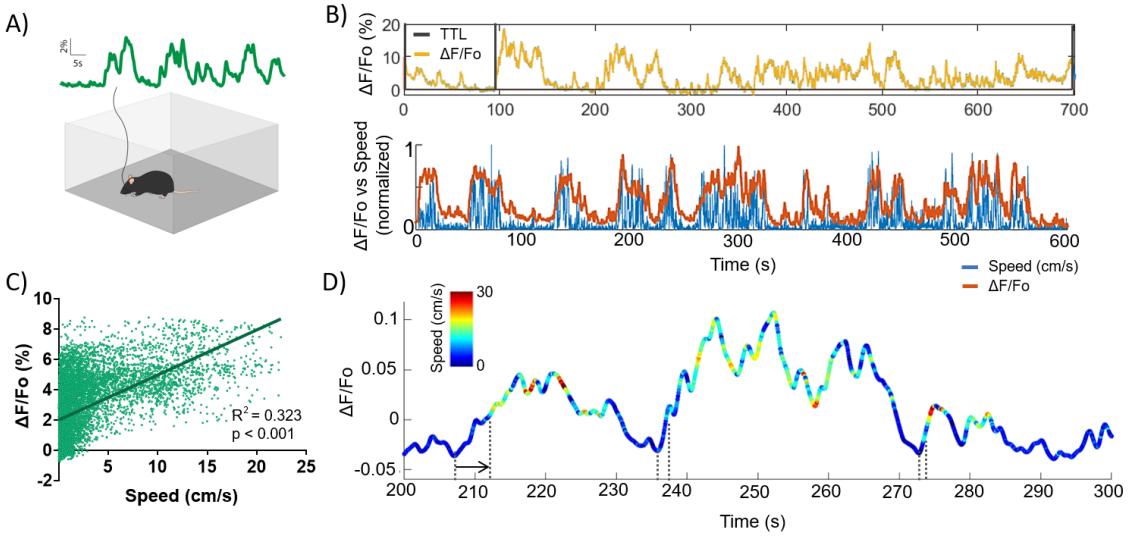

Figure 4.16. Correlation between PV-GCaMP6s activity and speed of the animal
(A) Graphic showing an example of the recording of an animal's activity in an open field. **(B)** On the top, downsampled and synchronized GCaMP signal (yellow) based on TTL inputs, which define the initiation and finalization of the trial, using RodEx. On the bottom, relationship between PV-GCaMP6s signal (orange) recorded in a freely-moving mouse and the running velocity of the animal (blue). **(C)** Scatter plot showing the correlation of the animal's running speed with the intensity of the fluorescence signal (ΔF). **(D)** Graphic showing 100 seconds of recording. Colormap is used to represent the value of the speed. Dotted lines and arrow highlight the increase in calcium response preceding the increase in the animal velocity.

4.3.2.2. DG-PV activity decreases with contextual novelty

Being aware of the strong correlation between our PV-GCaMP6s signals and the animal's velocity, we always included in our analysis the comparison between ΔF and speed variables, thus trying to avoid biased interpretations of changes in PV-calcium dynamics that are indeed reflecting changes in mean speed.

Based on the contribution of the DG in spatial novelty discrimination (Fredes et al., 2021; Hunsaker et al., 2008; Lee et al., 2005), we next used a Mismatch Novelty task (Figure 4.17A, see methods for details) to investigate how DG-PV inhibitory activity is regulated while the animal explores novel *vs.* familiar contexts. After 3 trials visiting a familiar arena (F1, F2 and F3 trials), we changed the floor (different color and texture) to introduce contextual novel information (novelty trial). Each trial lasted 5 min. Based on our working hypothesis, we were expecting a reduced PV inhibitory activity during novelty conditions *vs.* the exploration of familiar contexts.

Initially, we compared the averaged ΔF (Figure 4.17B) and speed (Figure 4.17C) from the full 5-min trials. Repeated-measures 1-way ANOVA revealed that PV activity was different between trials ($F_{2,18.37} = 3.617$, $p = 0.047$; Figure 4.17B), although a post-hoc

multiple comparisons-corrected analysis did not show any significant differences between specific trials. We also found that the averaged movement velocity in the 5-min trials differed between conditions ($F_{1.5,13.65} = 5.003$, $p = 0.031$; Figure 4.17C), where post-hoc Tukey's multiple comparisons test corroborated that mice displayed a tendency to move faster during the novelty trial (N *vs.* F1/F2/F3: p = 0.125/0.124/0.192; rest of comparisons p > 0.700).

Then, to further address the different regulation of PV-inhibitory activity across trials, we compared the time evolution of PV activity in each trial, as we reasoned that salience of the novel context would decrease over time, becoming more familiar at the end of the trial. To this aim, we averaged the recorded ΔF of all the subjects for each trial using a sliding-time window method (Figure 4.17D and E). Interestingly, we observed that the dynamics of PV interneurons are differently modulated when mice are exploring the mismatch novelty compared to the exploration of familiar contexts, especially during the first 200 seconds of the sessions (Figure 4.17D). Mean speed also differed from novelty to familiar conditions (Figure 4.17E), as suggested by the previous one-way ANOVA analysis in panel C.

In an attempt to control the unavoidable effect of speed on DG-PV calcium signals, we used a multivariate regression model (see *3.2.8. Statistical Analysis* in Methods) to study the differences in PV dynamics between sessions. The predicted ΔF values are shown in Figure 4.17F, corroborating that the observed differences between novelty and familiar sessions are still significant when the effect of the speed is controlled as an explanatory variable in the model. The results of the model showed that the interaction between session and time is statistically significant ($p < 0.0001$), leading us to conclude that the effect of time on calcium (ΔF) is session-dependent.

In order to simplify the statistical analyses, we divided the total trial duration into three 100-second time periods (t1, t2 and t3) and grouped the 3 familiar sessions to compare with the novelty condition (Figure 4.17G and H). A two-way ANOVA analysis revealed comparable PV-calcium activity during the first (t1) and last (t3) periods of the sessions (Figure 4.17G), where the higher values of ΔF are recorded during t1 (*Session* $F_{1,40} = 2.64$, $p = 0.112$; *Time-period* $F_{2,80} = 10.22$, $p = 0.0001$; *Interaction* $F_{2,80} = 4.76$, $p = 0.011$). However, at t2 there is a significant reduction specifically during the novelty condition, compared to the dynamics observed during the familiar trials.

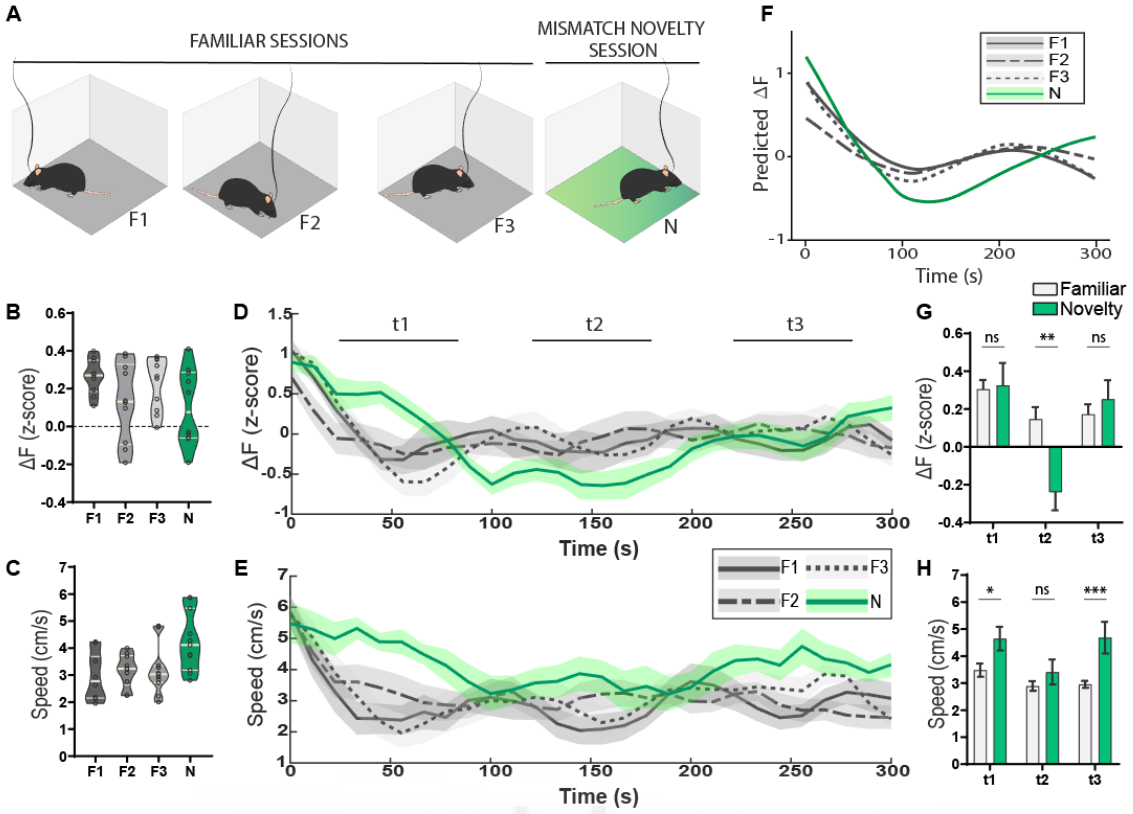

Figure 4.17: DG-PV dynamics in a Mismatch Novelty task.
(A) Experimental design of the mismatch novelty task where mice explored both familiar (F1, F2, F3) and novelty conditions in an open field with simultaneous fiber photometry recording of PV-GcaMP6s interneurons. **(B)** Average ΔF (calcium signal) in the 5-minute trial for familiar and novelty conditions. **(C)** Average velocity in the 5-minute trial for familiar and novelty conditions. **(D)** Time evolution of PV activity using a sliding-time window method across the trials for familiar and novelty conditions. **(E)** Time evolution of mean speed using a sliding-time window method across the trials for familiar and novelty conditions. **(F)** Regression model predicted ΔF values corroborates the differences in novelty *vs.* familiar conditions. **(G)** Histogram showing mean ΔF for each time period (t1 = (0-100s), t2 = (100-200s) and t3 = (200-300s)). **(H)** Histogram showing mean velocity for the three 100-second time periods for familiar and novelty conditions. Statistical analyses were done using 1-way ANOVA (B and C) and 2-way ANOVA (G and H). Dots in violin plots represent individual values. Grey and green traces represent averaged values for familiar and novelty conditions, respectively, and shadows represents the dispersion of the data (mean ± SEM). Bar plots and error bars also show mean ± SEM.

The mean velocity of mice at period t2 remained constant for all trials (Figure 4.17H), thus indicating that differences in Ca^{2+} dynamics at t2 were not explained by differences in the locomotor activity of mice. Furthermore, we could also observe an increased mean speed at t1 and t3 during the novelty trial (explaining the upward trend in averaged speed in Figure 4.17C) which was not accompanied by an increase in the calcium signal. We interpret the latter result as indicating a lower PV cell activity also at t1 and t3 that is masked by the increase in velocity (compare t1 and t3 in Figure 4.17, panel G vs. H). These results might be interpreted as reduced inhibitory activity compared to the familiar trials, showing higher ΔF values for the same speed.

In summary, novelty mismatch is associated with reduced activity of DG-PV interneurons, probably indicating the establishment of a DG circuit state favorable for memory encoding.

4.3.2.3. DG-PV activity increases during novel object-location exploration

Based on our previous results, where the level of DG-PV inhibition controlled the encoding of spatial information in a NOL task, our next step was to study the regulation of DG-PV activity during spontaneous object exploration paradigms (Figure 4.18). The difficulty here was the brevity and infrequency of the animal's visits to explore the objects, which limits the amount of calcium signals that can be recorded. Once again, RodEx proved to be a great help in identifying, selecting, and aligning behavior and calcium recordings in these experiments (Figure 4.19).

We hypothesized that PV interneurons would be more silent when exploring new object-location associations (this is, exploring both objects during the encoding phase and the displaced object during retrieval), thus allowing successful encoding of this information into memory. In contrast, we expected upregulation of PV activity when re-exploring an immobile object, thus avoiding overwriting the already existing memory when the information has not changed.

We started analyzing the calcium signals along the different trials, with no special focus on object exploration events. As we did for the Novelty task in the previous section, we analyzed the time evolution of averaged ΔF and speed in the NOL sessions. We approached these comparisons by dividing the sessions into periods of 150 seconds (see Figure 4.18B). The 5-min (habituation) sessions are divided into two periods (t1 and t2), while the 10-min (encoding and test) sessions lead to four time periods (t1, t2, t3 and t4). To simplify the analysis, we focused on t1 and t2, as t3 and t4 periods were not available for habituation sessions.

We did not find differences when comparing averaged PV activity between sessions (*Session* $F_{3,21}$= 1.564, p = 0.228), but we again observed a significant reduction of ΔF from t1 to t2 (*Time period* $F_{1,7}$= 43.85, p = 0.0003) (Figure 4.18D). Post-hoc Bonferroni's multiple comparisons test revealed that this decline was less significant in the second habituation session (p = 0.07 for Hab2 vs. p < 0.003 for the other sessions). Our findings

in the previous section *4.3.2.2* may help explain these results, as this session is the only session without novelty processing: while the first habituation session introduces a completely novel context, the second habituation involves encountering an already familiar context. Furthermore, in the encoding and retrieval sessions, although the context remains familiar, novel stimuli are presented to mice.

Then, we compared these results with the averaged velocity as a control for ΔF-Speed correlation (Figure 4.18G). We observed significantly higher mean speed in the first habituation session compared to the others (*Session* $F_{3,21}$= 13.26, $p < 0.0001$), probably as a consequence of being a novel context never encountered before, as indicated before. Due to the high correlation between ΔF amplitude and running speed, one could expect higher average ΔF during this first session concomitant to the increased mean speed, compared with the rest of the sessions. However, this was not the case, as similar levels of inhibition were recorded across sessions, at both t1 and t2 (Figure 4.18D). We interpreted this result as a reduced PV inhibitory activity during the first habituation session, the most novel condition.

The dispersion in the measures of calcium activation was consistently higher during encoding and test sessions than during the habituation sessions (Figure 4.18D and Table 4.1). As the context remains constant across sessions, the key difference is the presence or absence of explorable objects. This additional information, that can be encoded and updated into the existing contextual memory, might explain the increased ΔF variance during encoding and test sessions, as if there were two distinct processing streams that differentially activates PV interneurons: the first processing stream related to the spatial navigation (highly speed-dependent) and a second one related to the explorable targets (allowing object-context associations). Another more parsimonious explanation might be that the behavioral repertoire to explore objects could be more diverse that those for exploring an empty environment.

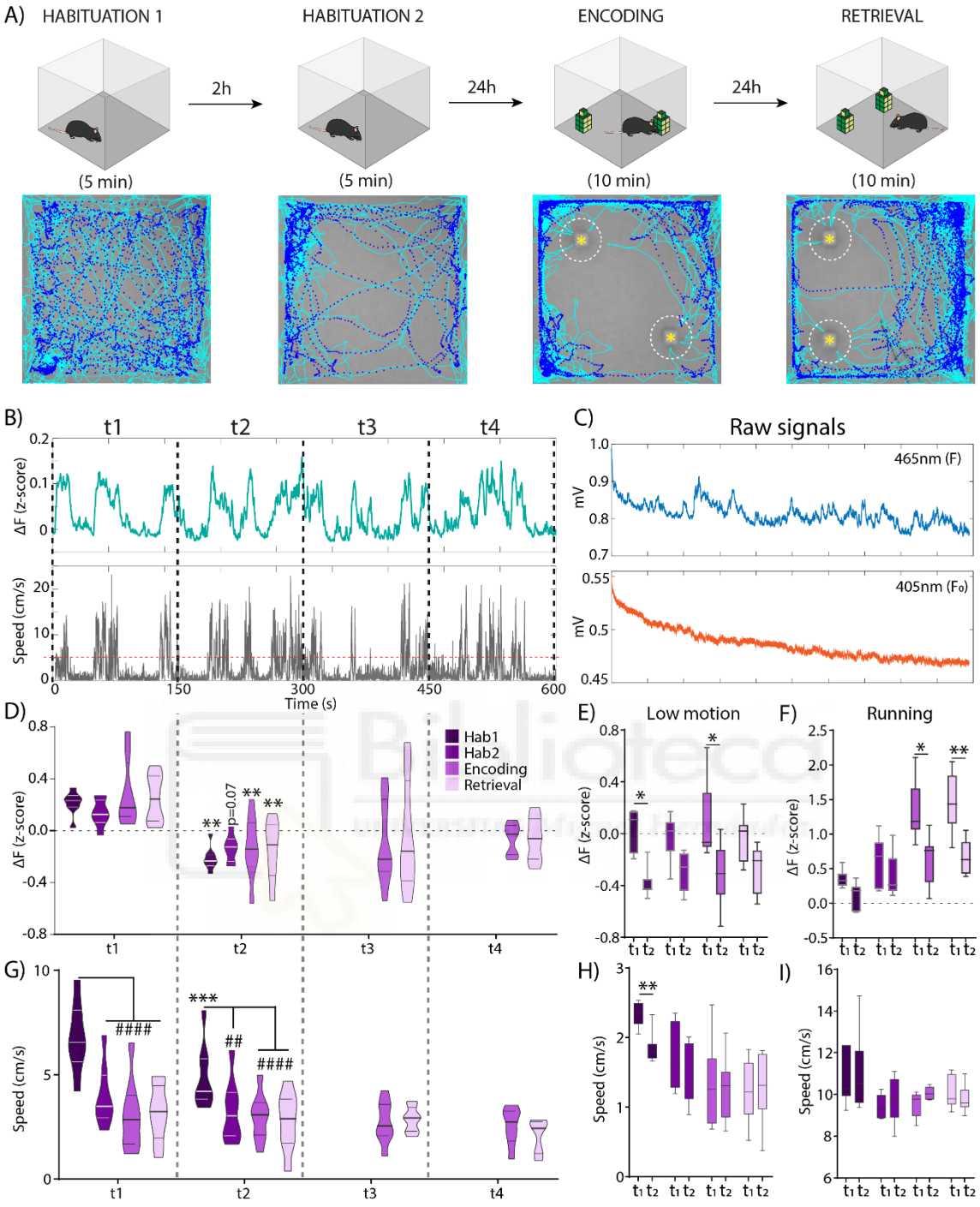

Figure 4.18. Dynamic regulation of DG-PV activity during NOL task

(A) Schematic representation of the NOL task with a representative example of centroid (blue dots) and head (cyan traces) tracking from the same animal. **(B)** Detail of the division of sessions into periods of 150 seconds and the differentiation of periods. The 5-min (habituation) sessions are divided into two periods (t1 and t2) and the 10-min (encoding and test) sessions are divided into four time periods (t1 = 0 – 150 s; t2 = 150 – 300 s; t3 = 300 – 450 s; t4 = 450-600 s). Horizontal dashed line represents the threshold of speed = 5cm/s for locomotor activity classification (low motion *vs* running epochs). **(C)** Raw 465nm (calcium-dependent) and 405nm (isosbestic) signals recorded in a typical habituation session. **(D)** Time evolution of the averaged ΔF (calcium signal). Violin plots represent the average ΔF for each time period. Repeated-measures two-way ANOVA are done without including t3 and t4 (only available for encoding and test sessions). **(E)** Averaged ΔF at low-motion epochs (speed < 5cm/s) periods across sessions. **(F)** Averaged ΔF during running epochs (speed > 5cm/s). **(G)** Time evolution of the averaged speed. **(H)** Averaged speed during low-motion epochs. **(I)** Averaged speed during running epochs. Only significant results are shown

in the figure for simplicity, where * are used to intragroup comparisons (t1 vs t2 time periods) and # are used to between-groups comparisons (Hab1 vs Hab2 vs Encoding vs Test sessions).

Table 4.1. Coefficient of variation (%) for ΔF and speed across time periods within each session

		Hab. 1	**Hab. 2**	**Encoding**	**Retrieval**
ΔF Coefficient of variation (%)	***t1***	42.13	75.20	90.16	72.49
	t2	42.29	75.13	193.40	154.20
	t3	---	---	340.20	1118
	t4	---	---	186.90	268.80
Speed Coefficient of variation (%)	***t1***	24.51	36.96	55.92	42.83
	t2	31.63	46.02	38.27	50.62
	t3	---	---	37.15	21.19
	t4	---	---	34.93	37.92

To gain insight into our findings, we focused on t1 and t2 periods and further differentiated between *low-motion* (speed < 5cm/s) and *running* periods (speed ≥ 5cm/s) Figure 4.18 E-F and H-I). Repeated-measures two-way ANOVA results were as follows:

(1) When comparing the inhibitory PV activity between-sessions, we found no differences in the averaged ΔF during low-motion epochs (Figure 4.18E, *Session:* $F_{3,21}$= 0.516, p = 0.676). However, at running epochs, PV activity was differently regulated (*Session:* $F_{3,18}$= 18.58, p < 0.0001), being significantly more active during encoding and retrieval compared to habituation phases (Figure 4.18F).

(2) Regarding speed analysis and as mentioned before, mean speed during the first habitation was significantly higher (at both low-motion and running epochs) than in the other sessions (Figure 4.18H and I).

(3) When comparing the progression of DG-PV activity over time (t1 *vs.* t2 periods), we found a significant downregulation of this inhibitory activity at both low-motion (Figure 4.18H*, Time period:* $F_{1,7}$= 32.75, p = 0.0007) and running epochs (Figure 4.18I, *Time period:* $F_{1,6}$= 94.54, p < 0.0001). Notably, at low-motion epochs, this reduction occurred specifically during first habituation and encoding sessions. However, the differences in the former session were considered meaningless due to the concomitant reduction in speed (Figure 4.18H, *Time period:* $F_{1,7}$= 6.04, p = 0.044). At running epochs, this inhibitory downregulation was observed during both encoding and retrieval phases (Figure 4.18I).

(4) Intra-session analysis of mean speed at faster motion epochs showed that mice exhibited constant velocity over time in all sessions (Figure 4.18I, *Time period:* $F_{1,6}$= 0.42, p = 0.541).

In our last analysis, we directed the efforts to investigate the activity of PV interneurons during the active exploration of objects (Figure 4.19). For the analysis, due to the individuality in exploratory events (i.e., variability in the number and duration of the visits to the objects), we took into account only the first 3 explorations to each object (Figure 4.19B).

The initial expectation with this analysis was a reduction of recorded PV activity while exploring novel spatial information (both objects during encoding and only the displaced object during retrieval). However, we found the opposite result, this is, that DG-PV interneurons increase their activity when exploring novel objects (Figure 4.19B left*, both objects in encoding session*), as well as to familiar objects occupying novel locations (Figure 4.19B right, *object 2 in test session*). Conversely, PV interneurons are less active when exploring a familiar object in a previously visited location (Figure 4.19B right, *object 1 in test session*). Regarding the averaged speed during the first 3 explorations to each object (Figure 4.19C), we can consider that mice approached objects and withdrew from them after exploration at very similar velocities.

Taken together, despite these results might suggest that PV interneurons are actively involved, instead of transiently inhibited, in the encoding of novel spatial information, a resulting downregulated excitatory/inhibitory balance still remains a possibility. The clear finding is that PV interneurons are not silenced during the exploration of novel spatial information (e.g., exploring the displaced object in the test session), but how excitation is regulated during these same events is not known. Depending on the concomitant excitatory activity, the increase in the inhibitory signal from PV interneurons could be interpreted in different ways (see Figure 5.4 in Discussion).

Overall, these results highly emphasized the necessity to improve our technical approach by implementing the simultaneous recording of excitatory (GCs) and inhibitory (PV) activity. This would allow us to calculate an E/I ratio that would provide an improved approach to study local disinhibition in the DG.

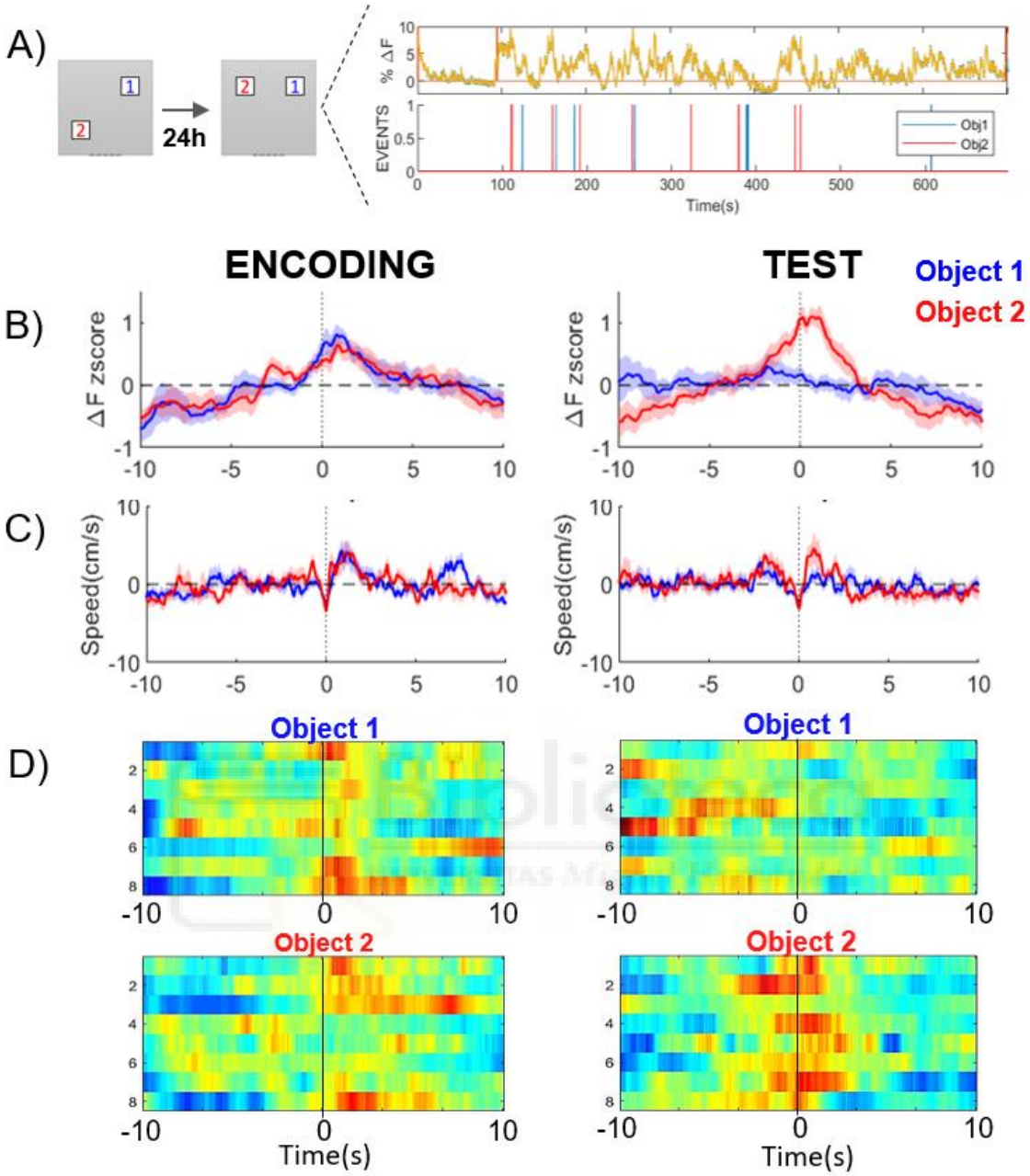

Figure 4.19. DG-PV interneuron activity during objects exploration in the NOL task
(A) On the left, experimental design showing object localization during the encoding (left) and retrieval (right) sessions of the NOL task, showcasing the arrangement of objects. On the right, representative example of the recorded ΔF signal in a test session. Signal is processed and synchronized with RodEx, quantifies exploratory behavior, detecting specific events (visits to objects). **(B)** Average PETH of PV activity during the first three visits to each object in both encoding (left) and retrieval (right) sessions. (C) Average PETH of running speed during object exploration in both encoding (left) and retrieval (right) sessions, indicating the speed of mouse movements during exploration **(D)** Color-coded PETH plots of PV activity during object exploration, offering a detailed visual representation of PV interneuron activity during the task. Each row contains the averaged responses for one animal.

V. DISCUSSION

In our daily lives, we encounter countless experiences and are bombarded with a wealth of information. Although we are able to store lots of information in our memory, we are not able to remember every single detail of these experiences. While our understanding of how memories are formed and the underlying mechanism has advanced significantly, there are still many unresolved questions that continue to challenge researchers in the field of neuroscience. Recently, a pivotal role played by GABAergic interneurons and hippocampal disinhibition in modulating the establishment and persistence of memory engrams has been postulated (see review by Raven and Aton, 2021).

Building upon previous research (Canals et al., 2009; Caramés et al., 2020; Estarellas et al., 2023; Del Ferraro et al., 2018), this thesis delves into the role of local perisomatic inhibition in the DG, mediated by PV+ interneurons, as the mechanism underlying network communication during memory formation. I have used pharmacogenetic and fiber-photometry calcium imaging techniques to unveil the specific role of DG-PV interneurons in the encoding of episodic memories, spatial pattern separation, contextual novelty detection and binding of object-location associations (see review by Hainmueller and Bartos, 2020b). Additionally, I have dedicated a section to present RodEx, a tool I developed during my thesis to automate quantitative and objective analysis of rodents' exploratory behavior.

In the initial experiments, we used DREADDs to modulate the activity of PV interneurons during the encoding phase of various memory tasks. We found that the effect of modulating the level of DG perisomatic inhibition on memory encoding is restricted to the spatial component (*"where"*) of episodic memory, with no discernible impact on object (*"what"*) or social (*"who"*) recognition tasks. Subsequently, we investigated the role of PV interneurons in spatial pattern separation, another function dependent on the DG (Leutgeb et al., 2007; Marr, 1971; Treves and Rolls, 1994). Again, we found that decreasing or increasing the activity of DG- PV interneurons enhanced or impaired, respectively, mice's ability to discriminate subtle changes in the environment. However, the cost of the enhanced spatial memory and pattern separation is high, as memory capacity is reduced in mice with less PV activity.

In the second phase of experiments, we performed PV-GCaMP6s fiber photometry recording in order to uncover the dynamics of DG-PV interneurons during contextual

novelty detection and spatial memory formation. We observed a significant reduction in PV activity when mice encountered a different floor within a familiar environment, indicating their ability to detect contextual mismatches. In contrast, PV+ interneurons exhibited a notable increase in activity when exploring novel object-location associations, indicative of their involvement in binding spatial and non-spatial information.

In summary, our findings propose that the activity of DG-PV interneurons controls the encoding and updating of spatial-dependent memories. The data also suggest the existence of an optimal range for PV inhibition-disinhibition interplay that enables the proper formation of stable memory traces without compromising their flexibility for subsequent reconsolidation processes (Mau et al., 2020; Rao-Ruiz et al., 2021; Umbach et al., 2022). However, it remains unclear whether the conjunctive encoding of object-location associations relies on transient disinhibitory events in the DG. I discuss below the results that led to these conclusions.

5.1. RodEx: a new tool for unsupervised automated quantification of exploratory behavior

Behavioral testing in neuroscience is a fundamental tool that provides researchers with valuable insights into the complex relationship between brain, behavior and cognition (Krakauer et al., 2017). As such, the accurate quantification, classification and analysis of the observed behaviors is essential for their proper interpretation (Pereira et al., 2020).

There is a large number of behavioral paradigms to assess the different stages of learning and memory and their underlying neural mechanisms, often involving long periods of training along multiple trials and/or the administration of rewards or punishments (as in the Morris water maze, Barnes maze, aversive fear conditioning or delayed alternation tasks). Other types of paradigms, usually involving one-trial encoding phase, are based on the innate preference of rodents to explore novel rather than familiar environments or objects (Berlyne, 1950) and do not require the learning of contingency rules. Thus, the time that mice spend exploring novel vs familiar stimuli is used as an index of memory.

In this thesis, we have mainly used novelty-preference paradigms in order to assess the role of DG-PV interneurons in memory formation. The simplicity of these tasks, such as

the object recognition test (Ennaceur and Delacour, 1988; Leger et al., 2013) and its variants (Dix and Aggleton, 1999; Reichelt et al., 2021; Vogel-Ciernia and Wood, 2014), contrasts to the vast repertoire of spontaneous behaviors that mice could perform and the complexity of automatizing the analysis of exploration. However, at the time I started this thesis, we were faced with a lack of resources for the automated quantification of exploratory behavior. Although some commercial software (such as *SMART Video Tracking* by Panlab or *EthoVision XT* by Noldus) already offered the possibility to perform multi-point tracking, which allows a better characterization of behavior based on postural features (not available in centroid-based tracking), they presented a high percentage of errors in head-point detection, which in turn biased the quantification of objects' exploration. As a result, many experimenters still resort to manual quantification to obtain valid object exploration scores. However, manual scoring is very time-consuming for researchers and entails a higher degree of subjectivity, which reduces the reproducibility and consistency of results.

In the opening chapter of results, I introduced RodEx, a set of MATLAB written codes that I meticulously developed during the initial years of this thesis. Initially derived from the open-source tracking package designed by Gomez-Marin et al., (2012), RodEx allows (i) three-point tracking (head-centroid-tail) of freely moving rodents, (ii) the automated and unsupervised quantification of object exploration and (iii) high-resolution behavioral analysis (see Figures 4.8 and 4.9). The detection of head coordinates in addition to centroid coordinates complements the study of locomotion by providing not only the typical kinematic variables (e.g., distance, velocity and acceleration) but also measures of postural features (e.g., orientation, stretching or head casts). This additional dimension opens avenues for the generation of different criteria to define and classify exploration events (Benice and Raber, 2008).

Despite lacking a graphical user interface, RodEx is structured into modules that ensure accessibility, as users without programming expertise can readily utilize it. For those researchers with programming skills, this modular design also accommodates customizations, further enhancing its flexibility and adaptation to specific requirements. Nonetheless, it is important to acknowledge certain limitations. Precision in head tracking is critical, particularly when rodents are in close proximity to objects or targets for exploration, and inaccuracies in head-point tracking could potentially bias the quantification of exploration. Thus, when implementing a new experimental setup, a

validation process by cross-referencing automatic results with manual scoring in a small subset of samples, is recommended.

More recently, the integration of artificial intelligence (AI) tools and deep-learning based methods has substantially improved behavioral analysis during the last years (Isik and Unal, 2023; Sturman et al., 2020), presenting more accurate tracking systems (Mathis et al., 2018) and automated behavior classifiers for spatial trajectories (Donnarumma et al., 2021), social interactions (Nilsson et al., 2020; Segalin et al., 2021) and object exploration (Gabriel et al., 2022; Ibañez et al., 2023). In contrast to these sophisticated methods, RodEx maintains a streamlined design with tight operator control, while offering a complete set of tools for both multi-point tracking and classification of behavioral events, making it a valuable complement or stand-alone tool for performing advanced behavioral analysis.

5.2. Disinhibition of the DG enhances spatial memory and pattern separation

Memories are thought to be encoded through the strengthening of synaptic connections between experience-induced cell assemblies, also called memory trace or engram (Carrillo-Reid, 2022; Guskjolen and Cembrowski, 2023; Josselyn et al., 2015; Lavi et al., 2023; Litwin-Kumar and Doiron, 2014; Ortega-de San Luis and Ryan, 2022; Tonegawa et al., 2015b). However, how these distributed subsets of neurons are synchronized and coordinated to enable the emergence and maintenance of memory engrams is still a matter of research. The DG emerges as a pivotal region to compress and conjunctively encode spatial (from the MEC) and non-spatial (from the LEC) information, locally binding these multimodal inputs in order to create an integrated and comprehensive representation of the episodic memory (Goode et al., 2020; Kesner, 2007; Sugar and Moser, 2019; Teyler and Rudy, 2007). We further posit the role of DG in long-range network binding during memory formation. Specifically, we propose that the DG, through PV-mediated disinhibition, has the capacity to coordinate widely dispersed cell assemblies (Canals et al., 2009; Caramés et al., 2020; Del Ferraro et al., 2018).

Under this framework, we have previously evidenced the key role of DG PV interneurons as a gating mechanism controlling spatial memory formation and the functional coupling

within the memory network (Caramés et al., 2020). Pharmacogenetic modulation to decrease (PV-Gi mice) or increase (PV-Gq mice) the level of perisomatic inhibition in the DG was sufficient to improve or impair, respectively, spatial memory encoding in a NOL task (Figure 1.8C). Notably, while the size of the encoding-induced engram remained unaltered, functional coupling between distant brain regions, such as PFC or NAc, was also bidirectionally controlled (Figure 1.8E). These findings led us to suggest that DG-PV interneurons are compelling candidates for orchestrating distributed experience-induced cell ensembles during the initial encoding of spatial information. They provide a bidirectional mechanism by which the system can selectively incorporate information to update the memory base (by enhancing coupling between cell assemblies) while discarding irrelevant information to maintain the memory base intact (by decoupling the activity of the implicated ensembles).

5.2.1. Contribution to non-spatial memories

Firstly, if local changes in the inhibitory level of the DG are able to coordinate downstream brain regions within the memory network (Figure 1.6C), we wondered whether any type of episodic memory would be similarly affected. At first glance, one could consider an affirmative response, but we argued that the effects would be limited to those dorsal DG-dependent functions, mainly related to contextual discrimination and spatial memory (Hainmueller and Bartos, 2020; Kesner, 2007).

As we used the NOL task to assess the *"where"* memory, we selected similar and comparable tasks to evaluate other components of the episode, such as the memory for *"what"* (object) and *"who"* (social stimulus). We performed the novelty-preference paradigms NOR and SDT tasks to assess object and social recognition, respectively, in which the spatial information is neither relevant nor tested during the retrieval phase (Figure 3.4).

The ability to recognize a novel object relative to a familiar one has been shown to be intact in mice with lesioned or altered DG, whereas the performance of CA1-lesioned mice is severely impaired (Gilbert et al., 2001; Kesner et al., 2004). Thus, it has been suggested that *"what"* memory, or object recognition, relies mainly on CA1 and is independent of the DG function. Consistent with this, our results showed that mice performance in the NOR task was unaffected by the manipulation of DG-PV interneurons

(Figure 4.10B). Coherently, in the NOL task we observed a general reduction in the objects exploration time during the retrieval compared to the encoding phase (data not shown in this thesis), suggesting that all groups, including PV-Gq mice (who were unable to discriminate the change in object location – memory for *"where"*), were able to remember the objects themselves (memory for *"what"*).

With respect to the ability of mice to recognize previously encountered versus unfamiliar conspecifics, the role of the DG may be somewhat more controversial, with very little evidence for the involvement of dDG on social memory (Leung et al., 2018) in contrast to the numerous studies showing the direct implication of CA2 subregion (Alexander et al., 2016; Hitti and Siegelbaum, 2014; Tzakis and Holahan, 2019) and the ventral hippocampus, particularly vCA1 (Deng et al., 2019; Okuyama et al., 2016). Therefore, we hypothesized that DG-PV manipulations would not affect the encoding of the *"who"* information of the episodic memory. We found no statistical differences in the social recognition of mice regardless DG-PV modulation when tested in the SDT (see Figure 4.10D), which led us to assume that social memory is not affected by the level of DG inhibition in the dorsal hippocampus. However, I do not consider these results to be fully conclusive, as there is no clear preference for the novel mouse by control mice (Figure 4.10E). I argue that one of the most important limitations of this experiment is the relatively small sample size (n = 6 Sham and n = 7 per experimental group), that together with the substantial interindividual variability in behavioral assessments, might have underestimated potential significant differences between the experimental groups. A future comprehensive study could aim to: (i) ensure proper performance of the control group, which will allow better interpretations; (ii) increase the sample size; and (iii) paying particular attention to individual differences in mouse performance, which in turn are likely to correlate with viral diffusion to ventral hippocampal areas, more associated with anxiety and emotional processing (Moser et al., 1993; Strange et al., 2014).

There is compelling evidence highlighting the significance of PV interneurons in social novelty detection (Deng et al., 2019) and mood regulation in more ventral areas of the hippocampus. Specifically, while increased PV inhibition in the intermediate DG induces anxiolytic effects (Zou et al., 2016), a reduced density of PV interneurons in ventral DG leads to depression-like behaviors (Chen et al., 2022b). Our manipulations predominantly occurred in the dorsal DG, possibly explaining the absence of anxiolytic or anxiogenic effects in our experiments (Caramés et al., 2020). Nonetheless, recent findings have

demonstrated that pharmacogenetic sustained inhibition of PV activity in the dorsal DG can induce anxiety and depression-like behaviors (Zhou et al., 2022), suggesting the involvement of the dorsal DG also in emotional processing, especially when its activity is dysregulated for extended periods, contributing to various psychiatric disorders (Sun et al., 2023).

In summary, the pharmacogenetic manipulation of DG-PV interneurons in the dorsal hippocampus appears to specifically regulate the encoding of spatial memories, with no discernable impact on tasks where spatial information is irrelevant and becomes DG-independent. Consequently, we hypothesize that modulating DG inhibitory levels will also influence context-dependent memories (Dees and Kesner, 2013; Frankland et al., 1998; Hernández-Rabaza et al., 2008; Rivera et al., 2015; Shirazy et al., 2020) and episodic-like memories in which the different features of the episode (*What-Where-Which* task) are tested jointly (Davis et al., 2013; Inostroza et al., 2013).

5.2.2. Contribution to spatial pattern separation

Secondly, despite the enhanced spatial memory when PV interneurons are inhibited in the NOL task, a negative consequence of this reduced inhibition would be an increased number of GCs activated by the experience, which could lead to overlapping representations, reducing orthogonalization of outputs to CA3 and impairing pattern separation (Marr, 1971; Treves and Rolls, 1994; Yassa and Stark, 2011). However, our previous work showed an intact engram size in the DG and other memory-related regions regardless of the up- or downregulation of DG-PV interneurons, as reflected by a constant number of cFos-activated neurons (Figure 1.8; Caramés et al, 2020), leading us to hypothesize that pattern separation, like spatial memory, would be improved in PV-Gi mice and impaired in PV-Gq mice.

Although there was not a standardized protocol, we found some behavioral approaches in the literature to specifically assess spatial pattern separation (Clelland et al., 2009; Gilbert and Kesner, 2003, 2006; Gilbert et al., 2001; Goodrich-Hunsaker et al., 2005; van Hagen et al., 2015; Poucet, 1989). However, these tasks often require multiple learning trials or are focused on comparing the ability to detect low *vs* high spatial changes. Therefore, we designed the SETA maze and the protocol for the SETA task (Figure 3.5), which procedure overcomes the previously used by Van Hagen et al., (2015). The main feature

of the constructed apparatus is its semicircular shape, which allows constant distances (object-to-wall and object-to-entrance gate) to be maintained despite object displacements, and the addition of the waiting box to allow mice to freely transit to and from the SETA maze without experimenter's intervention. After being habituated to the empty context, mice were able to explore two identical objects during the encoding phase and, after an ITI of 2 min (STM protocol) or 24 hours (LTM protocol), mice were tested in 5 consecutive trials where one of the objects is sequentially displaced in steps of 5 cm.

In our test, the pattern to be separated is given by the distance between the objects. Trials in which the object has moved little generate a pattern that is difficult to distinguish from the one stored in memory, and vice versa. As hypothesized, an increased perisomatic inhibition in PV-Gq mice precluded pattern separation, delaying the spatial discrimination from 15 to 20 cm, while PV-Gi mice with a disinhibited DG showed improved pattern separation, preferentially exploring the displaced object already at 10 cm (Figure 4.11). However, the relevant finding here was the existence of a gradient of thresholds for spatial pattern separation. Under control conditions, although on average mice detect object displacement at 15 cm, some mice were able to distinguish more subtle changes (th < 15 cm), while other mice require more dissimilar experiences to discriminate between them (th > 15 cm). When increasing or decreasing the activity of PV interneurons, this variability is maintained but its distribution is right-shifted (impaired pattern separation) or left-shifted (improved pattern separation), respectively (Figure 4.12 B-D).

Overall, our results support the idea that DG-PV interneurons play a key role in the emergence of spatial memory engrams, specifically, by enhancing or weakening the representation of object-location associations into the brain-wide memory trace. At physiological conditions, a given level of PV+ perisomatic inhibition in the DG permits the required strengthening of synaptic connections to encode a stable memory representation capable of being retrieved in the future (Guskjolen and Cembrowski, 2023; Josselyn et al., 2015; Rao-Ruiz et al., 2021). On the one hand, a disinhibited DG would lead to highly strengthened memory representation. This "stronger encoding" of the memory trace facilitates its retrieval and the discrimination of subtle changes in the spatial information (object displacement), explaining why pattern separation is improved in PV-Gi mice. On the other hand, an increased inhibitory level in the DG would generate a poorer object-location representation in the involved brain structures, hindering its subsequent consolidation into long-term memory. The impaired pattern separation in PV-

Gq mice, observed in the delayed discrimination of novelty, may be explained due to the "lack" of a memory reference from the encoding session.

Indeed, based on the different discrimination thresholds, our data yield additional insights into the changes in pattern separation and their behavioral correlates. Irrespective of the mice's discrimination threshold, different exploration patterns of fixed and moving objects following the detection of object's displacement (shaded column in plots) were observed during STM and LTM tests (Figure 5.1 STM and SHAM). When mice were tested at STM, a subtle "sawtooth profile" in the exploration of the moving object might suggest mice comparing the current object's position with the immediately previous encounter. In contrast, Sham mice at LTM exhibit a consistent preference for the moving object after detecting the displacement, suggesting that mice compare the current position with a previously consolidated reference, encoded the day before. Notably, PV-Gi mice demonstrated an enhanced LTM-like performance, progressively increasing the preference for the moving object once they have detected the displacement (Figure 5.1 PV-Gi), while PV-Gq mice showed a STM-like performance (Figure 5.1 PV-Gq), characterized by a "sawtooth preference" for the moving object, confirming the suggested lack of memory reference aforementioned.

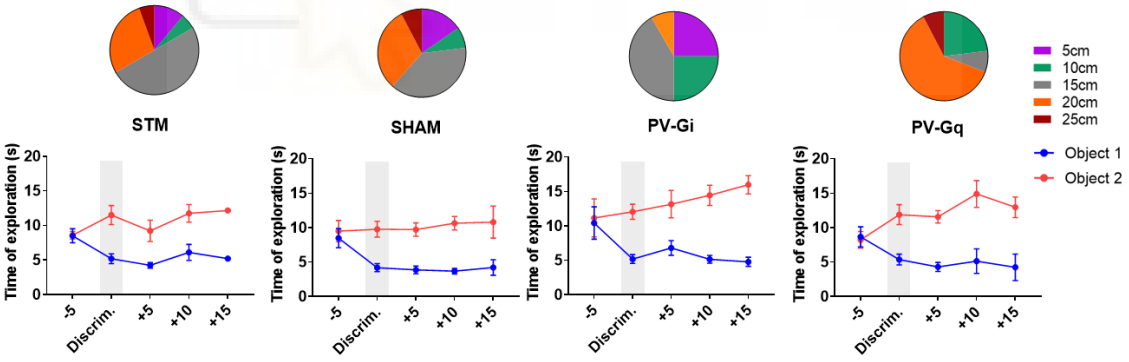

Figure 5.1. Exploratory performance before and after the discrimination point.
The data shown in this figure is a combination of results shown in Figure 4.11 and 4.12 in results. Pie charts depict the percentage of mice in each subgroup (based on the different discrimination thresholds, from 5cm to 25cm) within each group of mice (STM, Sham, PV-Gi and PV-Gq). Plots below show the progression of the exploration towards each object after the discrimination. All mice of one group are aligned to their discrimination point (grey column), regardless the subgroup they belong to.

Furthermore, while a less inhibited DG network may be interpreted as more advantageous for enhancing spatial memory formation and pattern separation, persistent loss of perisomatic inhibitory control could potentially have detrimental effects on normal brain function. Indeed, this could be an evolutionary factor that limits the extent of basal DG

disinhibition, given the area's well-known susceptibility to epilepsy (Botterill et al., 2019; Krook-Magnuson et al., 2015; Sloviter, 1994). Although we cannot rule out the possibility that an extended period of disinhibition might have such an impact (Ribak et al., 1979; Scharfman, 2019), our experiments did not reveal any epileptogenic effects associated with CNO-induced disinhibition in PV-Gi animals. So, what might be the trade-offs that prevent the DG from down-regulating its inhibition?

5.3. The dark side of perisomatic disinhibition: reduced memory capacity… and flexibility?

To gain insight into the potential side effects of dorsal DG disinhibition during memory encoding, we used a computational approach to model the outcomes of reducing inhibitory network levels on spatial novelty detection. Our simulations predicted that a disinhibited DG enhances spatial discrimination when encoding involves a low information load. However, the ability to detect spatial novelty is drastically impaired as the information load increases, represented in our modes as the *number of input patterns* (Figure 4.13). Therefore, we propose that improved memory encoding in mice with lower PV inhibition (PV-Gi mice) may come at the cost of reduced memory capacity.

These predictions were experimentally confirmed in the MIP task (Figure 4.14), a modified version of the NOL task with a higher number of input patterns to be encoded and retrieved (see 3.1.4.2 in Methods). One advantage of our MIP task, in contrast to another recently developed test to assess memory capacity (Harkotte et al., 2022), is that it tested object-location memory for all encountered contexts during the encoding phase. This allows us to assess not only memory capacity but also factors like serial position and interference effects (Lee et al., 2020; Roberts and Smythe, 1979; Watanabe and Yanagisawa, 2000). An interesting finding with the MIP task was the observed order-dependent memory differences between experimental groups. Under control conditions, memory performance exhibited a recency effect, where the most recently visited contexts during encoding were better recalled. Conversely, PV-Gi mice recalled the earliest encoded context better than the others, indicating a shift toward a primacy-biased pattern (Figure 4.14D). This suggests that decreased DG-PV activity may reduce memory capacity by promoting proactive interference (Barron, 2021; Costa and Friedrich, 2012;

Engin et al., 2015; Tello-Ramos et al., 2019), priming earlier encoded memories and hindering the formation of new competing memories. In line with these results, recent theoretical simulations based on human data have evidenced how stable or flexible encoding induces, respectively, primacy or recency effects on memory (Lee et al., 2020), supporting our hypothesis on DG disinhibition leading to 'stronger' or more stable memory representations.

These assumptions imply that a disinhibited DG not only reduces memory capacity in PV-Gi mice but may also limit memory flexibility. From the perspective of memory updating, although stable, memory traces should be flexible enough to permit reconsolidation processes, where the memory trace becomes labile and malleable (Grella et al., 2020; Hainmueller and Bartos, 2018; Lee, 2010; Nader, 2015). Therefore, a stronger representation resulting from DG disinhibition during encoding may impair or difficult the introduction of new information into the existing representation. We propose that the strengthened memory representation encoded by PV-Gi mice might be "too fixed", favoring its maintenance in long-term memory but hindering its updating with new information (Wang et al, 2005). In contrast, the weaker memory representation encoded with fully active PV-cells in the DG may facilitate its forgetting during reconsolidation, leaving the existing memory intact instead of updating the existing one. In the delicate balance between these two conditions would exist the formation of adaptive memory, sufficiently stable and necessarily flexible. The possibility of regulating this balance up or down offers innumerable possibilities to the circuit, from persistently recording events critical to survival to preventing the continuous updating of memory with irrelevant changes in what is known (see Figure 5.2).

In accordance, several studies have already highlighted the importance of inhibition for cognitive flexibility, showing that animals with poor memory retention, associated with higher levels of inhibition, tend to be more flexible and perform well in reversal learning tasks, and *vice versa* (Akers et al., 2014; Barron, 2021; Tello-Ramos et al., 2019). Indeed, increased levels of PV inhibition in the dDG have previously been linked to better reversal learning (Morellini et al., 2010) and fear extinction (Zou et al., 2016), suggesting enhanced memory flexibility with higher perisomatic inhibition. Furthermore, although neurogenesis is beyond the scope of this thesis, the role of adult-born GCs should not be underestimated, as several experimental pieces of evidence support the connection

between PV interneurons and new-born cells with pattern separation and reversal learning functions (Fölsz et al., 2023; Hvoslef-Eide and Oomen, 2016; Yun et al., 2023).

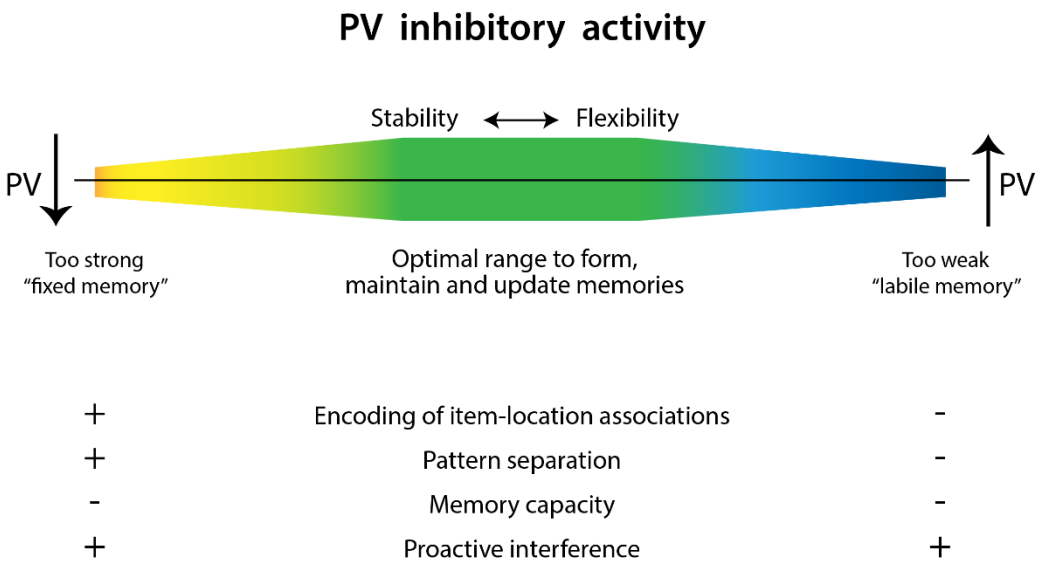

Figure 5.2. Hypothetical framework for the role of PV interneurons in the updating of memories.

While we did not perform any task specifically designed to assess memory flexibility while manipulating DG-PV activity, we did test the effects of increased PV activity on memory capacity that, so far, we have not yet discussed. Although we did not explicitly model the effects of increasing inhibition in the DG, the impaired performance of PV-Gq mice in NOL and SETA tasks led us to postulate a potential impairment in their memory capacity. Indeed, increased PV activity impaired memory capacity compared to control animals (Figure 4.14B and C). We further hypothesize the absence of serial-position effects, indicating an overall poor performance across all contexts. However, PV-Gq mice showed a clear primacy effect in their retrieval, similar to that observed in PV-Gi mice (Figure 4.14D).

This unexpected outcome of the MIP task appears to contrast with our proposed mechanism based on the *'stability-flexibility'* of the encoded memory trace. It also seems inconsistent with previous findings from the NOL and SETA tasks, where PV-Gq mice failed to effectively encode object-location associations involving a single "input pattern". I propose an interpretation for this apparently contradictory scenario when

comparing PV-Gq performance in the MIP versus the NOL and SETA tasks: the nature of the MIP task's environment might inherently possess greater "predictable variability" because the order of context presentation varies from day to day. Thus, although the change itself is unpredictable, mice may exhibit a higher degree of expectation or anticipation than in the NOL task. Under these conditions, mice would benefit from more flexible learning, as previously suggested by Tello-Ramos et al. (2018), likely explaining why PV-Gq mice performed better in the MIP task compared to the NOL task. Nevertheless, this explanation is tentative and requires a more comprehensive investigation before definitive conclusions can be drawn.

To conclude, disinhibition-based mechanisms supporting learning and memory processes (reviewed in Letzkus et al, 2015) does not imply prolonged periods of disinhibition. Instead, transient decreases of inhibition, mediated by perisomatic PV interneurons, are likely to occur to support the acquisition of memory representations (Raven and Aton, 2021; Xia et al., 2017). Indeed, specific evidence suggests that PV activity should be able to dynamically change during the different processes of memory, such as learning, consolidation or reconsolidation (Donato et al., 2013; Hainmueller and Bartos, 2018; Ognjanovski et al., 2017). However, how PV+ interneurons are intrinsically regulated to allow these transient E/I imbalances remains unclear. Consequently, the focus now shifts towards understanding the modulation of these disinhibitory transients during memory formation.

5.4. Limitations of fiber photometry recordings of PV GCaMP6s-expressing interneurons in the DG under anesthesia conditions.

Over the past few decades, significant advances in electrophysiological and optical imaging techniques, coupled with genetically-engineered mouse models, have greatly enhanced our capacity to monitor and manipulate neuronal activity in both anesthetized and behaving animals (Chen et al., 2022a; Zhang et al., 2022) and thereby facilitating the study of neural circuit function and dynamics. In particular, calcium imaging constitutes an indirect method for assessing neuronal activity, wherein calcium availability is transformed into a fluorescent signal. Consequently, this approach tends to exhibit poorer

temporal resolution when compared to electrophysiology. In contrast, the main advantage of calcium imaging is the cell specificity that it presents, providing higher cellular specificity than electrophysiological recordings (Campos et al., 2020; Hartung and Gold, 2020; Scanziani and Häusser, 2009).

In this thesis, we have used fiber photometry technique to specifically record the dynamics of DG-PV interneurons expressing GCaMP6s sensor. Prior to recording these signals in behaving animals, we conducted preliminary fiber photometry experiments in anesthetized animals, in combination with electrical stimulation and electrophysiological readout. Our motivation for those experiments relied on the possibility to distinguish between feedforward and feedback inhibition (Buzsáki, 1984; Sloviter, 1991). Through subthreshold electrical stimulation of the PP, configured to evoke minimal GCs firing, we sought to isolate feedforward inhibition while avoiding feedback inhibition due to GCs firing (Buzsáki, 1984; McKenzie, 2018). We aimed to confirm whether the reduction of feedforward inhibition in the DG at potentiated conditions (*'postLTP'* in Figure 1.6, see also Álvarez-Salvado, 2015; Estarellas et al, 2023) is controlled by perisomatic PV interneurons.

Unfortunately, we encountered certain limitations that hindered the testing of our hypothesis, as we were (1) unable to elicit a detectable calcium response by single-pulse PP stimulation (neither at sub- nor at suprathreshold intensity), necessitating the use of stimulation trains (see Figure 4.15) which in turn increases the likelihood of GCs firing and the recruitment of feedback inhibition. This limitation may be attributed to the slow kinetics that characterize GCaMP6s sensor (Chen et al., 2013). We also (2) faced challenges in recording spontaneous Ca^{2+} events in the absence of electrically driven activity, which might be explained by the use of anesthesia (Guo et al., 2021; Huh and Cho, 2013; Tort-Colet et al., 2023). This "basal PV silence" was evident in our recordings with isoflurane and urethane anesthesia, both of which are known to suppress neuronal activity, including hippocampal firing and synchronization (Guo et al., 2021; Hara and Harris, 2002; Huh and Cho, 2013; Shumkova et al., 2021; Yagishita et al., 2020).

For future experiments involving the recording of DG-PV interneurons, especially under anesthetized conditions, we recommend considering the use of a different calcium sensor. In recent years, improved calcium sensors with higher sensitivity and a better signal-to-noise ratio have been developed (Zhang et al., 2023). Furthermore, sensors with enriched expression in specific cellular compartments, such as axons (Broussard et al., 2018) or

cell bodies (Shemesh et al., 2020) could provide more precise signals and interpretations when using fiber photometry, where cellular resolution is compromised, and bulk signals are recorded. Any of these modern sensors would greatly enhance the functionality compared to previous GCaMP6 versions and would potentially allow for the recording of evoked calcium responses to PP single pulse stimulation. In this regard, although soma-targeted calcium singling is considered a good proxy of spiking activity in fast-spiking neurons to measure decreases in firing rate (Ali and Kwan, 2019), the use of axon-GCaMP could be beneficial due to the sparse anatomical organization of the PV interneurons in the DG and their dense axonal arborization through the granular layer (Amaral et al., 2007).

5.5. DG-PV dynamics: perisomatic inhibition is differentially regulated during the encoding of contextual novelty and the binding of object-location associations.

So far, our findings provide compelling evidence on the role of DG PV-mediated disinhibition in the encoding and updating of spatial memories. In line with previous research (Donato et al., 2013; Letzkus et al., 2015; Ogando et al., 2021), it becomes evident that the activity of PV interneurons should be dynamically modulated to ensure proper formation of memory representations. However, while this sheds light on the relevance of PV interneurons, the mechanisms underlying their contribution to the emergence and allocation of memory engram is still unknown (Sauer and Bartos, 2020).

One of the main questions that arises is whether PV inhibition undergoes transient downregulation to facilitate information processing and encoding. If indeed this is the case, then when do these E/I imbalances occur, and what is the overall temporal profile of this perisomatic inhibitory activity during contextual-dependent memory formation? To address these questions, we performed fiber photometry recordings in freely-moving mice in order to characterize the dynamics of PV-GCaMP6s interneurons during two DG-dependent tasks: novelty detection and spatial memory (Fredes et al., 2021; Gómez-Ocádiz et al., 2022; Hunsaker et al., 2008; Kesner et al., 2016; Li et al., 2020).

One critical observation was the strong correlation between running speed and the amplitude of the recorded PV-GCaMP6s signal (Figure 4.16). This observation agrees with prior research that has already established a tight relationship between animal velocity and hippocampal GABAergic interneurons (Iwase et al., 2020; McNaughton et al., 1983; Nitz and McNaughton, 2004). More specifically, recent studies employing calcium imaging, which offers cell specificity, have shown that PV+ interneurons in CA1 (Dudok et al., 2021) as well as in DG (Hainmueller et al., 2021) increase their activity with running speed. Thus, the observed positive correlation was not unexpected, but it is an interference that deserves careful consideration in the analysis and interpretation of the calcium data, prompting us to control for the variable of speed (see 3.2.8 in Methods).

5.5.1. Decreased activity of DG-PV interneurons to detect contextual novel information

The hippocampus plays a pivotal role in detecting novelty (Kumaran and Maguire, 2006; Thakral et al., 2015), with the DG being particularly relevant in discriminating similar contextual information (Hunsaker et al., 2008). Thus, instead of employing Uncharted Novelty tasks, where the novel context is entirely different from the familiar one (Barth et al., 2018), we conducted a Mismatch Novelty task, where mice visit a slightly modified version of the familiar context during the novelty trial (Lever et al., 2006). The 'mismatch' condition requires the coordination between incoming sensory inputs and the retrieval of previously stored contextual information (Buzsáki and Moser, 2013; Dudai and Morris, 2013; Wang and Morris, 2010). Therefore, we aimed to understand how PV interneurons are regulated when new contextual information is encountered and should be integrated into the existing memory representation.

Previous studies involving electrophysiological recordings in CA1 have shown that GABAergic interneurons decrease their activity during contextual novelty (Nitz and McNaughton, 2004; Wilson and McNaughton, 1993). Interestingly, Niz and McNaughton (2004) also reported an increase in firing rate of DG interneurons in novel environments. However, this increase was noted among the total population of GABAergic neurons in the DG. More recent findings have revealed how specific types of interneurons respond to novelty. Using virtual environments and two-photon calcium imaging in head-fixed animals, it has been demonstrated that PV activity decreases during contextual novelty in both CA1 (Arriaga and Han, 2019) and DG (Hainmueller et al, 2021).

It is worth noting that in previous work (López-Madrona et al., 2020), we demonstrated that the synchronization of different pathway-specific theta oscillations in CA1 is enhanced during mismatch contextual novelty (Figure 5.3A), supporting the flexible integration of the novel information (EC-CA1 pathway) with the previous context representation from memory (CA3-CA1 pathway) (Buzsáki and Moser, 2013; Hasselmo et al., 2002; Lisman and Grace, 2005). In the current study using the same task, we observed a significant reduction in the activity of DG-PV interneurons during contextual novelty detection (Figure 5.3B), in line with Hainmueller et al., (2021). Strikingly, we discovered a robust matching between the time courses of CA1 synchronization and DG disinhibition, time courses that particularly change during the middle phase of the trial (see "*t2"*). These parallel changes in DG and CA1 dynamics correspond to the progression of novelty during the trial: familiarity with the environment is initially high (t1); then, as the trial progresses, 'mismatches' become salient, signifying the processing of novelty (t2) and, towards the end of the trial, novelty gradually diminishes as it transforms into familiarity (t3).

These findings underscore the key role of DG PV+ interneurons in memory updating, detecting and processing novel contextual information that mismatches with the previously stored spatial representation. DG detects and processes novelty, transferring this information to CA1, which in turn integrates and routes hippocampal information to downstream regions (Guardamagna et al., 2023; Larkin et al., 2014; Twarkowski et al., 2022). Thus, our data also highlight how local changes in the inhibitory tone of the DG have an impact not only on CA1 computations but also on the functional connectivity of the memory network, affecting the coupling between distributed cell ensembles.

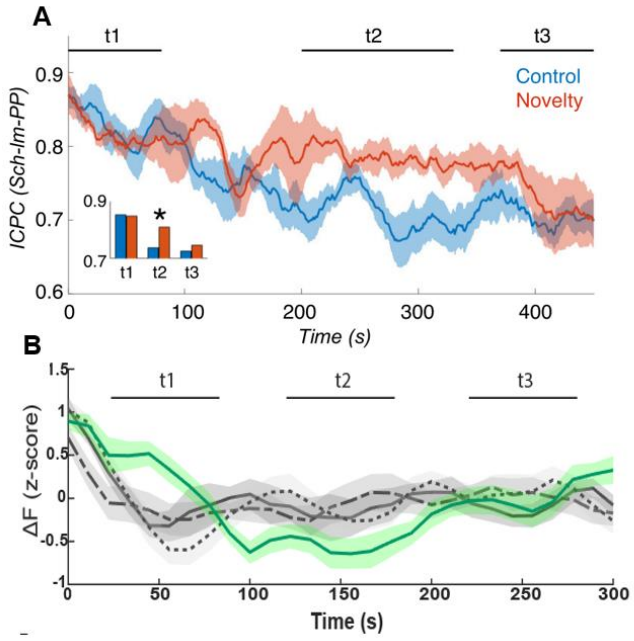

Figure 5.3. Contextual mismatch novelty in CA1 and DG. **(A)** Time evolution of dynamic synchronization between layer-specific theta oscillations in CA1 during exploration of a familiar environment before (blue) and after (red) introducing novel tactile stimuli. Both familiar and mismatch novelty conditions show maximum synchronization during the initial exploration (t1) followed by a decay in familiar but not in novelty (t2). Both conditions show again similar (and reduced) synchronization at the end of the trial (t3). Taken from López-Madrona et al, 2020. **(B)** Dynamics of PV interneurons in the DG during exploration of a familiar environment before (grey) and after (green) introducing novel tactile stimuli (panel D from Figure 4.17). Mean ± s.e.m. across all subjects

5.5.2. Increased activity of DG-PV interneurons to encode novel object-location associations

The hippocampus in humans is activated during the encoding of object-location associations (Burgess et al., 2002; Maguire et al., 1998; Manelis et al., 2012; Thakral et al., 2015), and research with rodents have particularly pointed the specific role of DG in encoding object-location memories based on the conjunctive encoding of spatial and non-spatial information (Gilbert et al., 2001; Kesner et al., 2015; Kim et al., 2020).

In a second experiment, we recorded the dynamics of DG-PV interneurons while mice were engaged in a NOL task. We wondered whether PV+ interneurons exhibited transient decreases in their activity to encode novel object-location associations. We identified the exploration of objects as specific events where we hypothesized a decline in PV activity, presuming these events to involve the encoding of new spatial information. Conversely, we anticipated an increased PV activity when mice interacted with familiar stimuli, where

the binding of novel object-location associations was not expected to occur. Intriguingly, our data revealed precisely the opposite results (Figure 4.19): while the exploration of a familiar object in a previously visited location did not trigger any response by PV interneurons expressing GCaMP6s, exploration of both familiar and novel objects positioned in new locations significantly increased PV-GCaMP6s activity. These results lead us to suggest that DG-PV interneurons play a key role in the encoding of memories that necessitate the integration of novel "where" information (spatial location) with a "what" stimulus (object identity) into the memory representation (Burgess et al., 2002; Lee and Jung, 2017; Manelis et al., 2012; Postma et al., 2008; Ranganath, 2010; Yonelinas et al., 2019).

Overall, PV interneurons increased their activity during the exploration of novel spatial stimuli but not during encounters with familiar ones. A priori, this finding might appear contradictory to our hypothesis regarding the downregulation of perisomatic inhibition as the mechanism facilitating the encoding of spatial memories. However, these data only allow us to conclude that DG-PV interneurons (1) are presumably required to encode novel object-location associations and (2) do not undergo inactivation to encode such associations. Indeed, a complete silencing of PV inhibitory activity is not presumable, as, at least, a subset of GCs will be active when animals explore objects at specific locations within the environment (Deshmukh and Knierim, 2013; GoodSmith et al., 2022). These object-related excitatory responses will inevitably recruit feedback and lateral inhibition from GCs to PV+ interneurons, among other GABAergic interneurons (Espinoza et al., 2018; Sloviter and Brisman, 1995), leading to the increased PV calcium-based signal observed in our experiments.

Furthermore, the resultant balance between excitation and inhibition in the DG during these exploration-triggered events remains unknown. Is this increased inhibitory PV activity compatible with a disinhibitory final effect on DG network? In our experiments, we are able to observe changes in the inhibitory activity of PV interneurons, but we lack information on the excitatory output. The intriguing question that now arises is how excitatory activity from GCs is simultaneously modulated with PV inhibitory activity, potentially allowing for the calculation of an E/I ratio, as illustrated in Figure 5.4. This example demonstrates how the same level of inhibitory activity can yield different E/I balance in the DG. Consequently, obtaining this ratio could help us to confirm the

presence of transient disinhibitory events and, more importantly, their timing and occurrence.

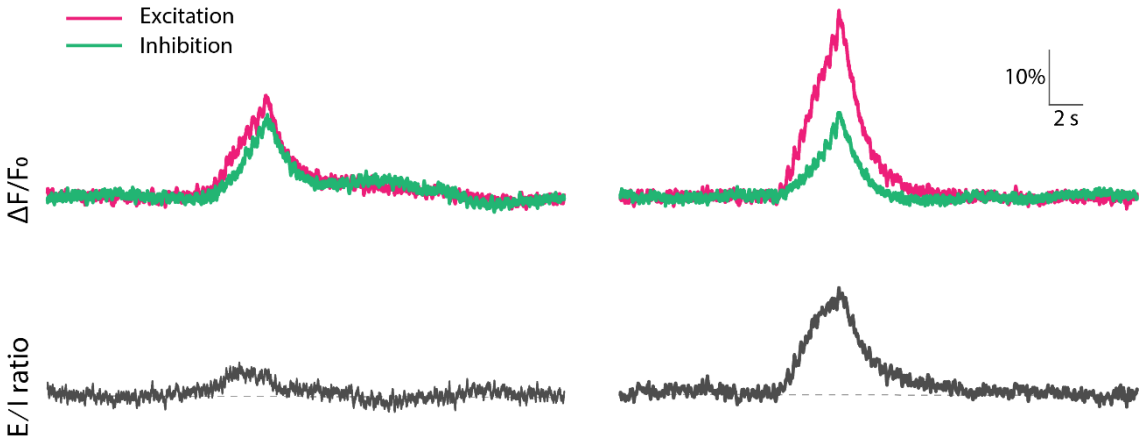

Figure 5.4. Theoretical network responses where same inhibitory level results in different E/I ratios. ***Left:*** Excitatory and inhibitory signals show similar responses, thus E/I ratio remains constant. ***Right:*** Despite the level of inhibition is the same as in the left panel, these calcium responses show an increased E/I ratio.

Lastly, while the interaction between PV+ interneurons and other GABAergic neurons or mossy cells has been described (Bernstein et al., 2019), the regulation of the inhibitory network in the DG is not completely understood. Investigating the potential interplay or balance among interneurons is not a trivial matter and should be thoroughly considered if we aspire to gain a comprehensive understanding of how perisomatic inhibition is regulated during the formation and updating of spatial or context-dependent memories.

5.6. Global remarks and future perspectives

Taken together, the findings presented in this discussion support the assertion that the level of PV inhibition within the DG plays a pivotal role in determining the stability of encoded representations or memory traces. This influence is exerted both locally within the DG, by controlling GCs excitability and the strength of object-location representations, and at a broader, long-range network level, by regulating the interactions between distributed hippocampal and extrahippocampal cell assemblies. Consequently, the activity of DG-PV interneurons directly impacts subsequent memory transformations, either facilitating memory consolidation or promoting forgetting, and controls the ability of a memory engram to be updated in response to changing contingencies.

It is essential to recognize that an optimal range of PV inhibition-disinhibition exists to facilitate the effective encoding of new memories and the modification of preexisting memory representations. Indeed, the advantage of the described PV-dependent mechanism lies in its ability to bidirectionally adjust the balance between excitation and inhibition, thereby enabling the selective integration of new information into memory while simultaneously discarding irrelevant data. This delicate control prevents the inefficient overwriting of memory, ensuring that the system functions efficiently.

Furthermore, during the development of this thesis, I have implemented innovative experimental techniques, such as fiber photometry calcium recordings, and analytical tools, like the automated quantification of exploratory behavior. These tools will be invaluable in future laboratory work. However, despite the progress made in understanding the role of DG-PV interneurons in memory formation, numerous unanswered questions persist, motivating further research in two key directions:

I. To enhance the interpretability of data obtained from fiber photometry experiments, it would be highly beneficial to implement dual-wavelength recordings that combine green and red calcium sensors. This approach allows for the simultaneous monitoring of PV+ inhibitory and GCs excitatory activity. Calculating the ratio between excitatory and inhibitory signals would allow us to investigate dynamic changes in this ratio during the learning process. This will provide insights into how the E/I balance is regulated and modulated during memory formation.
II. Our overarching hypothesis suggests that reduced PV activity leads to increased coupling between the hippocampus and other brain regions. However, this causal relationship has not yet been empirically tested. To explore the role and implications of DG-PV interneurons in coordinating the functional connectivity of distant cell assemblies across the brain, it would be intriguing to combine resting-state functional magnetic resonance imaging (fMRI) with local recordings of DG-PV calcium activity. This combined approach will enable researchers to verify whether DG disinhibition epochs correlate with increased BOLD (Blood Oxygen Level Dependent) signals in extrahippocampal areas, shedding light on the role of local inhibition in binding and orchestrating distributed cell ensembles during memory processes.

VI. CONCLUSIONS

1. The functional consequences of manipulating perisomatic PV interneurons in the dDG during memory encoding seems to be restricted to the processing of spatial (‘*where’*) information, whereas mice showed intact non-spatial memory when tested at low dDG demanding processes, such as the recognition of a novel object in the NOR task (‘*what’* memory).

2. The inhibitory tone of the DG directly controls the ability of mice to discriminate subtle spatial changes in familiar environments. The activity of PV interneurons sets the threshold for pattern separation: while less PV inhibition leads to an improved pattern separation in PV-Gi mice, exhibiting lower thresholds to detect small object displacements, higher levels of PV inhibition increase these thresholds in PV-Gq, thereby impairing pattern separation.

3. Despite the positive consequences on memory encoding and pattern separation, DG perisomatic disinhibition drastically reduces memory capacity by promoting proactive interference, unlike the retroactive interference observed in control Sham mice.

4. Fiber-photometry recordings of GCaMP6s-expressing PV interneurons revealed a strong correlation between PV-calcium dynamics and locomotor activity.

5. PV-GCaMP6s activity in the DG is downregulated when mice update an existing memory with novel contextual information in a Mismatch Novelty task. This DG disinhibition correlates with periods of higher theta synchronization and CFC in CA1 of rats performing a similar Mismatch Novelty task, as we previously reported in López-Madrona et al. (2020).

6. In a typical NOL task, DG-PV interneurons are activated during the exploration of objects occupying novel locations (irrespective of whether the object is familiar or unknown), while no responses are evoked when exploring familiar objects in previously visited locations. These results reflect the engagement of PV interneurons

in forming new object-location associations, but the resulting E/I balance in the DG remains unknown.

7. The developed RodEx tool is a versatile tool that has been successfully validated to automatically quantify exploratory behavior of freely-moving rodents, significantly reducing the time invested by experimenters and the possible subjectivity from manual scoring. It provides high resolution measurements of rodent's locomotor and exploratory behaviors, valuable information that improves the interpretation and characterization of our behavioral data.

VI. CONCLUSIONES

1. Las consecuencias funcionales de manipular las interneuronas PV perisomáticas en el giro dentado dorsal (dDG) durante la codificación de la memoria parecen estar restringidas al procesamiento de información espacial (memoria del "dónde"), mientras que los ratones mostraron una memoria no espacial intacta cuando se sometieron a procesos de baja demanda del dDG, como el reconocimiento de un objeto novedoso en la tarea NOR (memoria del "qué").

2. El tono inhibitorio del DG controla directamente la capacidad de los ratones para discriminar cambios sutiles en entornos familiares. La actividad de las interneuronas PV establece el umbral para la separación de patrones: mientras que una menor inhibición perisomática conduce a una mejora en la separación de patrones en ratones PV-Gi, que muestran umbrales más bajos para detectar pequeños desplazamientos de objetos, niveles más altos de inhibición de PV aumentan estos umbrales en PV-Gq, dificultando la separación de patrones.

3. A pesar de las consecuencias positivas en la codificación de la memoria y la separación de patrones, la desinhibición perisomática del DG reduce drásticamente la capacidad de memoria al promover interferencia proactiva, a diferencia de la interferencia retroactiva observada en condiciones controles.

4. Los registros de calcio mediante fotometría de fibra de interneuronas PV que expresan GCaMP6s revelaron una fuerte correlación entre la dinámica de calcio de PV y la actividad locomotora.

5. La actividad de PV-GCaMP6s se regula a la baja cuando los ratones actualizan una memoria existente con información contextual novedosa en una tarea de Novedad de Desajuste. Esta desinhibición que tiene lugar en DG se correlaciona con periodos de mayor sincronización theta y CFC en CA1 de ratas que realizan una tarea similar de Novedad de Desajuste, como mostramos en López-Madrona et al. (2020).

6. En una tarea típica de NOL, las interneuronas PV-GCaMP6s se activan durante la exploración de objetos en localizaciones novedosas (ya sea con un objeto familiar o

desconocido), mientras que no se evocan respuestas al explorar objetos familiares en ubicaciones previamente visitadas. Estos resultados reflejan la participación de las interneuronas PV en la formación de nuevas asociaciones entre objetos y ubicaciones (asociación entre "qué" y "dónde"), pero el equilibrio excitatorio/inhibitorio resultante en el DG sigue siendo desconocido.

7. La herramienta desarrollada RodEx es versátil y se ha validado con éxito para cuantificar automáticamente el comportamiento exploratorio de roedores, reduciendo significativamente el tiempo invertido por los experimentadores y la subjetividad posible de la cuantificación manual. Proporciona mediciones de alta resolución de los comportamientos locomotores y exploratorios de los roedores, información valiosa que mejora la interpretación y caracterización de nuestros datos conductuales.

VII. REFERENCES

Abbott, L.F. (1991). Realistic synaptic inputs for model neural networks. Netw. Comput. Neural Syst. *2*, 245–258.

Adelmann, G., Deller, T., and Frotscher, M. (1996). Organization of identified fiber tracts in the rat fimbria-fornix: an anterograde tracing and electron microscopic study. Anat. Embryol. (Berl). *193*, 481–493.

Aery Jones, E.A., Rao, A., Zilberter, M., Djukic, B., Bant, J.S., Gillespie, A.K., Koutsodendris, N., Nelson, M., Yoon, S.Y., Huang, K., et al. (2021). Dentate gyrus and CA3 GABAergic interneurons bidirectionally modulate signatures of internal and external drive to CA1. Cell Rep. *37*.

Ahmed, O.J., and Mehta, M.R. (2012). Running speed alters the frequency of hippocampal gamma oscillations. J. Neurosci. *32*, 7373–7383.

Akers, K.G., Martinez-Canabal, A., Restivo, L., Yiu, A.P., De Cristofaro, A., Hsiang, H.-L.L., Wheeler, A.L., Guskjolen, A., Niibori, Y., Shoji, H., et al. (2014). Hippocampal neurogenesis regulates forgetting during adulthood and infancy. Science *344*, 598–602.

Alexander, G.M., Rogan, S.C., Abbas, A.I., Armbruster, B.N., Pei, Y., Allen, J.A., Nonneman, R.J., Hartmann, J., Moy, S.S., Nicolelis, M.A., et al. (2009). Remote control of neuronal activity in transgenic mice expressing evolved G protein-coupled receptors. Neuron *63*, 27–39.

Alexander, G.M., Farris, S., Pirone, J.R., Zheng, C., Colgin, L.L., and Dudek, S.M. (2016). Social and novel contexts modify hippocampal CA2 representations of space. Nat. Commun. *7*, 10300.

Ali, F., and Kwan, A.C. (2019). Interpreting in vivo calcium signals from neuronal cell bodies, axons, and dendrites: a review. Neurophotonics *7*, 1.

De Almeida, L., Idiart, M., and Lisman, J.E. (2009). A second function of gamma frequency oscillations: An E%-max winner-take-all mechanism selects which cells fire. J. Neurosci. *29*, 7497–7503.

Álvarez-Salvado, E. (2015). Synapse-To-Network Plasticity in the Hippocampus. Universidad Miguel Hernandez de Elche.

Álvarez-Salvado, E., Pallarés, V., Moreno, A., and Canals, S. (2014). Functional MRI of long-term potentiation: Imaging network plasticity. Philos. Trans. R. Soc. B Biol. Sci. *369*.

Amaral, D.G. (1993). Emerging principles of intrinsic hippocampal organization. Curr. Opin. Neurobiol. *3*, 225–229.

Amaral, D.G., Scharfman, H.E., and Lavenex, P. (2007). The dentate gyrus: fundamental neuroanatomical organization (dentate gyrus for dummies). Prog. Brain Res. *163*, 3–22.

Andermann, M.L., Kerlin, A.M., and Reid, R.C. (2010). Chronic cellular imaging of mouse visual cortex during operant behavior and passive viewing. Front. Cell. Neurosci. *4*, 3.

Andersen, P., Holmqvist, B., and Voorhoeve, P.E. (1966). Entorhinal activation of dentate granule cells. Acta Physiol. Scand. *66*, 448–460.

Andersen, P., Morris, R., Amaral, D., Bliss, T., and O'Keefe, J. (2006). The Hippocampus Book (Oxford University Press).

Antonoudiou, P., Tan, Y.L., Kontou, G., Upton, A.L., and Mann, E.O. (2020). Parvalbumin and Somatostatin Interneurons Contribute to the Generation of Hippocampal Gamma Oscillations. J. Neurosci. Off. J. Soc. Neurosci. *40*, 7668–7687.

Armbruster, B.N., Li, X., Pausch, M.H., Herlitze, S., and Roth, B.L. (2007). Evolving the lock to fit the key to create a family of G protein-coupled receptors potently activated by an inert ligand. Proc. Natl. Acad. Sci. U. S. A. *104*, 5163–5168.

Arolfo, M.P., and Brioni, J.D. (1991). Diazepam impairs place learning in the Morris water maze. Behav. Neural Biol. *55*, 131–136.

Arriaga, M., and Han, E.B. (2019). Structured inhibitory activity dynamics in new virtual environments. Elife *8*, e47611.

Atucha, E., Ku, S.-P., Lippert, M.T., and Sauvage, M.M. (2021). Remembering the gist of an event over a lifetime depends on the hippocampus. BioRxiv 2021.04.14.439803.

Aznar, S., Qian, Z.-X., and Knudsen, G.M. (2004). Non-serotonergic dorsal and median raphe projection onto parvalbumin- and calbindin-containing neurons in hippocampus and septum. Neuroscience *124*, 573–581.

Bahrick, H.P., Bahrick, P.O., and Wittlinger, R.P. (1975). Fifty years of memory for names and faces: A cross-sectional approach. J. Exp. Psychol. Gen. *104*, 54–75.

Bannerman, D.M., Grubb, M., Deacon, R.M.J., Yee, B.K., Feldon, J., and Rawlins, J.N.P. (2003). Ventral hippocampal lesions affect anxiety but not spatial learning. Behav. Brain Res. *139*, 197–213.

Barbosa, F.F., and Castelo-Branco, R. (2022). Assessing episodic memory in rodents using spontaneous object recognition tasks. Emerg. Top. Life Sci.

Barker, G.R.I., and Warburton, E.C. (2011). When is the hippocampus involved in recognition memory? J. Neurosci. Off. J. Soc. Neurosci. *31*, 10721–10731.

Barrientos, S.A., and Tiznado, V. (2016). Hippocampal CA1 Subregion as a Context Decoder. J. Neurosci. Off. J. Soc. Neurosci. *36*, 6602–6604.

Barron, H.C. (2021). Neural inhibition for continual learning and memory. Curr. Opin. Neurobiol. *67*, 85–94.

Barth, A.M., Domonkos, A., Fernandez-Ruiz, A., Freund, T.F., and Varga, V. (2018). Hippocampal Network Dynamics during Rearing Episodes. Cell Rep. *23*, 1706–1715.

Bender, F., Gorbati, M., Cadavieco, M.C., Denisova, N., Gao, X., Holman, C., Korotkova, T., and Ponomarenko, A. (2015). Theta oscillations regulate the speed of locomotion via a hippocampus to lateral septum pathway. Nat. Commun. *6*, 1–11.

Benes, F.M., and Berretta, S. (2001). GABAergic Interneurons: Implications for Understanding Schizophrenia and Bipolar Disorder. Neuropsychopharmacology *25*, 1–27.

Benice, T.S., and Raber, J. (2008). Object recognition analysis in mice using nose-point digital video tracking. J. Neurosci. Methods *168*, 422–430.

Benito, E., Oliver, A., Galiana, L., Barreto, P., Pascual, A., Gomis, C., and Barbero, J. (2014). Development and validation of a new tool for the assessment and spiritual care of palliative care patients. J. Pain Symptom Manage. *47*, 1008-1018.e1.

van den Berg, M., Toen, D., Verhoye, M., and Keliris, G.A. (2023). Alterations in theta-gamma coupling and sharp wave-ripple, signs of prodromal hippocampal network impairment in the TgF344-AD rat model. Front. Aging Neurosci. *15*, 1081058.

Berlyne, D.E. (1950). NOVELTY AND CURIOSITY AS DETERMINANTS OF EXPLORATORY BEHAVIOUR1. Br. J. Psychol. Gen. Sect. *41*, 68–80.

Bernier, B.E., Lacagnina, A.F., Ayoub, A., Shue, F., Zemelman, B. V., Krasne, F.B., and Drew,

M.R. (2017). Dentate Gyrus Contributes to Retrieval as well as Encoding: Evidence from Context Fear Conditioning, Recall, and Extinction. J. Neurosci. *37*, 6359–6371.

Bernstein, H.L., Lu, Y.L., Botterill, J.J., and Scharfman, H.E. (2019). Novelty and novel objects increase c-fos immunoreactivity in mossy cells in the mouse dentate gyrus. Neural Plast. *2019*.

Bird, C.M., and Burgess, N. (2008). The hippocampus and memory: insights from spatial processing. Nat. Rev. Neurosci. *9*, 182–194.

Bliss, T. V, and Lomo, T. (1973). Long-lasting potentiation of synaptic transmission in the dentate area of the anaesthetized rabbit following stimulation of the perforant path. J. Physiol. *232*, 331–356.

Bocarsly, M.E., Jiang, W.-C., Wang, C., Dudman, J.T., Ji, N., and Aponte, Y. (2015). Minimally invasive microendoscopy system for in vivo functional imaging of deep nuclei in the mouse brain. Biomed. Opt. Express *6*, 4546–4556.

Booker, S.A., and Vida, I. (2018). Morphological diversity and connectivity of hippocampal interneurons. Cell Tissue Res. *373*, 619–641.

Borhegyi, Z., and Leranth, C. (1997). Distinct substance P- and calretinin-containing projections from the supramammillary area to the hippocampus in rats; a species difference between rats and monkeys. Exp. Brain Res. *115*, 369–374.

Botterill, J.J., Lu, Y.-L., LaFrancois, J.J., Bernstein, H.L., Alcantara-Gonzalez, D., Jain, S., Leary, P., and Scharfman, H.E. (2019). An Excitatory and Epileptogenic Effect of Dentate Gyrus Mossy Cells in a Mouse Model of Epilepsy. Cell Rep. *29*, 2875-2889.e6.

Broussard, G.J., Liang, Y., Fridman, M., Unger, E.K., Meng, G., Xiao, X., Ji, N., Petreanu, L., and Tian, L. (2018). In vivo measurement of afferent activity with axon-specific calcium imaging. Nat. Neurosci. *21*, 1272–1280.

Burgess, N., Maguire, E.A., and O'Keefe, J. (2002). The human hippocampus and spatial and episodic memory. Neuron *35*, 625–641.

Buzsáki, G. (1984). Feed-forward inhibition in the hippocampal formation. Prog. Neurobiol. *22*, 131–153.

Buzsáki, G. (2006). Rhythms of the brain. (New York, NY, US: Oxford University Press).

Buzsáki, G., and Moser, E.I. (2013). Memory, navigation and theta rhythm in the hippocampal-entorhinal system. Nat. Neurosci. *16*, 130–138.

Buzsáki, G., and Wang, X.-J. (2012). Mechanisms of Gamma Oscillations. Annu. Rev. Neurosci. *35*, 203–225.

Cai, D.J., Aharoni, D., Shuman, T., Shobe, J., Biane, J., Song, W., Wei, B., Veshkini, M., La-Vu, M., Lou, J., et al. (2016). A shared neural ensemble links distinct contextual memories encoded close in time. Nature *534*, 115–118.

Campos, P., Walker, J.J., and Mollard, P. (2020). Diving into the brain: deep-brain imaging techniques in conscious animals. J. Endocrinol. *246*, R33–R50.

Canals, S., Beyerlein, M., Merkle, H., and Logothetis, N.K. (2009). Functional MRI Evidence for LTP-Induced Neural Network Reorganization. Curr. Biol. *19*, 398–403.

Canolty, R.T., Edwards, E., Dalal, S.S., Soltani, M., Nagarajan, S.S., Kirsch, H.E., Berger, M.S., Barbaro, N.M., and Knight, R.T. (2006). High gamma power is phase-locked to theta oscillations in human neocortex. Science *313*, 1626–1628.

Caramés, J.M., Pérez-Montoyo, E., Garcia-Hernandez, R., and Canals, S. (2020). Hippocampal

dentate gyrus coordinates brain-wide communication and memory updating through an inhibitory gating. BioRxiv 2020.07.14.202218.

Caroni, P. (2015). Regulation of Parvalbumin Basket cell plasticity in rule learning. Biochem. Biophys. Res. Commun. *460*, 100–103.

Carrillo-Reid, L. (2022). Neuronal ensembles in memory processes. Semin. Cell Dev. Biol. *125*, 136–143.

Chambers, M.S., Atack, J.R., Broughton, H.B., Collinson, N., Cook, S., Dawson, G.R., Hobbs, S.C., Marshall, G., Maubach, K.A., Pillai, G. V., et al. (2003). Identification of a novel, selective GABAa α5 receptor inverse agonist which enhances cognition. J. Med. Chem. *46*, 2227–2240.

Chen, K., Tian, Z., and Kong, L. (2022a). Advances of optical miniscopes for in vivo imaging of neural activity in freely moving animals . Front. Neurosci. *16*.

Chen, S., Chen, F., Amin, N., Ren, Q., Ye, S., Hu, Z., Tan, X., Jiang, M., and Fang, M. (2022b). Defects of parvalbumin-positive interneurons in the ventral dentate gyrus region are implicated depression-like behavior in mice. Brain. Behav. Immun. *99*, 27–42.

Chen, T.W., Wardill, T.J., Sun, Y., Pulver, S.R., Renninger, S.L., Baohan, A., Schreiter, E.R., Kerr, R.A., Orger, M.B., Jayaraman, V., et al. (2013). Ultrasensitive fluorescent proteins for imaging neuronal activity. Nature *499*, 295–300.

Chevaleyre, V., and Siegelbaum, S.A. (2010). Strong CA2 pyramidal neuron synapses define a powerful disynaptic cortico-hippocampal loop. Neuron *66*, 560–572.

Churchwell, J.C., Morris, A.M., Musso, N.D., and Kesner, R.P. (2010). Prefrontal and hippocampal contributions to encoding and retrieval of spatial memory. Neurobiol. Learn. Mem. *93*, 415–421.

Ciocchi, S., Herry, C., Grenier, F., Wolff, S.B.E., Letzkus, J.J., Vlachos, I., Ehrlich, I., Sprengel, R., Deisseroth, K., Stadler, M.B., et al. (2010). Encoding of conditioned fear in central amygdala inhibitory circuits. Nature *468*, 277–282.

Ciocchi, S., Passecker, J., Malagon-Vina, H., Mikus, N., and Klausberger, T. (2015). Brain computation. Selective information routing by ventral hippocampal CA1 projection neurons. Science *348*, 560–563.

Clelland, C.D., Choi, M., Romberg, C., Fragniere, A., Tyers, P., Jessberger, S., Saksida, L.M., Barker, R.A., and Gage, F.H. (2009). A Functional Role for Adult Hippocampal Neurogenesis in Spatial Pattern Separation. *247*.

Cohen, N.J., and Squire, L.R. (1980). Preserved learning and retention of pattern-analyzing skill in amnesia: dissociation of knowing how and knowing that. Science *210*, 207–210.

Collinson, N., Atack, J.R., Laughton, P., Dawson, G.R., and Stephens, D.N. (2006). An inverse agonist selective for α5 subunit-containing GABA A receptors improves encoding and recall but not consolidation in the Morris water maze. Psychopharmacology (Berl). *188*, 619–628.

Costa, R.E., and Friedrich, F.J. (2012). Inhibition, interference, and conflict in task switching. Psychon. Bull. Rev. *19*, 1193–1201.

Cowansage, K.K., Shuman, T., Dillingham, B.C., Chang, A., Golshani, P., and Mayford, M. (2014). Direct reactivation of a coherent neocortical memory of context. Neuron *84*, 432–441.

Cui, G., Jun, S.B., Jin, X., Pham, M.D., Vogel, S.S., Lovinger, D.M., and Costa, R.M. (2013). Concurrent activation of striatal direct and indirect pathways during action initiation. Nature *494*, 238–242.

Cummings, K.A., and Clem, R.L. (2020). Prefrontal somatostatin interneurons encode fear

memory. Nat. Neurosci. *23*, 61–74.

Cummings, K.A., Lacagnina, A.F., and Clem, R.L. (2021). GABAergic microcircuitry of fear memory encoding. Neurobiol. Learn. Mem. *184*, 107504.

Czéh, B., Varga, Z.K.K., Henningsen, K., Kovács, G.L., Miseta, A., and Wiborg, O. (2015). Chronic stress reduces the number of GABAergic interneurons in the adult rat hippocampus, dorsal-ventral and region-specific differences. Hippocampus *25*, 393–405.

Dana, H., Sun, Y., Mohar, B., Hulse, B.K., Kerlin, A.M., Hasseman, J.P., Tsegaye, G., Tsang, A., Wong, A., Patel, R., et al. (2019). High-performance calcium sensors for imaging activity in neuronal populations and microcompartments. Nat. Methods *16*, 649–657.

Davis, K.E., Easton, A., Eacott, M.J., and Gigg, J. (2013). Episodic-like memory for what-where-which occasion is selectively impaired in the 3xTgAD mouse model of Alzheimer's disease. J. Alzheimers. Dis. *33*, 681–698.

Davis, S., Butcher, S.P., and Morris, R.G.M. (1992). The NMDA receptor antagonist D-2-amino-5-phosphonopentanoate (D-AP5) impairs spatial learning and LTP in vivo at intracerebral concentrations comparable to those that block LTP in vitro. J. Neurosci. *12*, 21–34.

Deco, G., Ponce-Alvarez, A., Hagmann, P., Romani, G.L., Mantini, D., and Corbetta, M. (2014). How Local Excitation–Inhibition Ratio Impacts the Whole Brain Dynamics. J. Neurosci. *34*, 7886 LP – 7898.

Dees, R.L., and Kesner, R.P. (2013). The role of the dorsal dentate gyrus in object and object-context recognition. Neurobiol. Learn. Mem. *106*, 112–117.

Deng, X., Gu, L., Sui, N., Guo, J., and Liang, J. (2019). Parvalbumin interneuron in the ventral hippocampus functions as a discriminator in social memory. Proc. Natl. Acad. Sci. U. S. A. *116*, 16583–16592.

Dere, E., Huston, J.P., and De Souza Silva, M.A. (2005). Episodic-like memory in mice: simultaneous assessment of object, place and temporal order memory. Brain Res. Brain Res. Protoc. *16*, 10–19.

Deshmukh, S.S., and Knierim, J.J. (2011). Representation of non-spatial and spatial information in the lateral entorhinal cortex. Front. Behav. Neurosci. *5*, 69.

Deshmukh, S.S., and Knierim, J.J. (2013). Influence of local objects on hippocampal representations: Landmark vectors and memory. Hippocampus *23*, 253–267.

Diamantaki, M., Frey, M., Berens, P., Preston-Ferrer, P., and Burgalossi, A. (2016). Sparse activity of identified dentate granule cells during spatial exploration. Elife *5*.

Dickerson, B.C., and Eichenbaum, H. (2010). The Episodic Memory System: Neurocircuitry and Disorders. Neuropsychopharmacology *35*, 86–104.

Dix, S.L., and Aggleton, J.P. (1999). Extending the spontaneous preference test of recognition: evidence of object-location and object-context recognition. Behav. Brain Res. *99*, 191–200.

Donato, F., Rompani, S.B., and Caroni, P. (2013). Parvalbumin-expressing basket-cell network plasticity induced by experience regulates adult learning. Nature *504*, 272–276.

Donnarumma, F., Prevete, R., Maisto, D., Fuscone, S., Irvine, E.M., van der Meer, M.A.A., Kemere, C., and Pezzulo, G. (2021). A framework to identify structured behavioral patterns within rodent spatial trajectories. Sci. Rep. *11*, 468.

Dudai, Y. (2004). The neurobiology of consolidations, or, how stable is the engram? Annu. Rev. Psychol. *55*, 51–86.

Dudai, Y., and Morris, R.G.M. (2013). Memorable trends. Neuron *80*, 742–750.

Dudek, S.M., Alexander, G.M., and Farris, S. (2016). Rediscovering area CA2: unique properties and functions. Nat. Rev. Neurosci. *17*, 89–102.

Dudok, B., Klein, P.M., Hwaun, E., Lee, B.R., Yao, Z., Fong, O., Bowler, J.C., Terada, S., Sparks, F.T., Szabo, G.G., et al. (2021). Alternating sources of perisomatic inhibition during behavior. Neuron *109*, 997-1012.e9.

Duncan, K., Ketz, N., Inati, S.J., and Davachi, L. (2012). Evidence for area CA1 as a match/mismatch detector: a high-resolution fMRI study of the human hippocampus. Hippocampus *22*, 389–398.

Ebbinghaus, H. (1885). Memory: A Contribution to Experimental Psychology. Ann. Neurosci. *20*, 155–156.

Eichenbaum, H. (2000). A cortical-hippocampal system for declarative memory. Nat. Rev. Neurosci. *1*, 41–50.

Eichenbaum, H. (2017). Prefrontal–hippocampal interactions in episodic memory. Nat. Publ. Gr.

Eichenbaum, H., and Fortin, N.J. (2005). Bridging the gap between brain and behavior: cognitive and neural mechanisms of episodic memory. J. Exp. Anal. Behav. *84*, 619–629.

Eichenbaum, H., Yonelinas, A.P., and Ranganath, C. (2007). The medial temporal lobe and recognition memory. Annu. Rev. Neurosci. *30*, 123–152.

Engin, E., Zarnowska, E.D., Benke, D., Tsvetkov, E., Sigal, M., Keist, R., Bolshakov, V.Y., Pearce, R.A., and Rudolph, U. (2015). Tonic Inhibitory Control of Dentate Gyrus Granule Cells by α5-Containing GABA_A Receptors Reduces Memory Interference. J. Neurosci. *35*, 13698 LP – 13712.

Ennaceur, A., and Delacour, J. (1988). A new one-trial test for neurobiological studies of memory in rats. 1: Behavioral data. Behav. Brain Res. *31*, 47–59.

Espinoza, C., Guzman, S.J., Zhang, X., and Jonas, P. (2018). Parvalbumin+ interneurons obey unique connectivity rules and establish a powerful lateral-inhibition microcircuit in dentate gyrus. Nat. Commun. *9*, 4605.

Estarellas, C., Álvarez-Salvado, E., Pérez-Cervera, L., Mirasso, C.R., and Canals, S. (2023). Somatic disinhibition of granule cells improves information transmission and pattern separation in the dentate gyrus. BioRxiv 2023.02.16.528800.

Fanselow, M.S., and Dong, H.W. (2010). Are the Dorsal and Ventral Hippocampus Functionally Distinct Structures? Neuron *65*, 7–19.

Fellini, L., and Morellini, F. (2013). Mice create what-where-when hippocampus-dependent memories of unique experiences. J. Neurosci. *33*, 1038–1043.

Fernández-Ruiz, A., and Herreras, O. (2013). Identifying the synaptic origin of ongoing neuronal oscillations through spatial discrimination of electric fields. Front. Comput. Neurosci. *7*, 5–10.

Del Ferraro, G., Moreno, A., Min, B., Morone, F., Pérez-Ramírez, Ú., Pérez-Cervera, L., Parra, L.C., Holodny, A., Canals, S., and Makse, H.A. (2018). Finding influential nodes for integration in brain networks using optimal percolation theory. Nat. Commun. *9*.

Flusberg, B.A., Nimmerjahn, A., Cocker, E.D., Mukamel, E.A., Barretto, R.P.J., Ko, T.H., Burns, L.D., Jung, J.C., and Schnitzer, M.J. (2008). High-speed, miniaturized fluorescence microscopy in freely moving mice. Nat. Methods *5*, 935–938.

Fölsz, O., Trouche, S., and Croset, V. (2023). Adult-born neurons add flexibility to hippocampal

memories. Front. Neurosci. *17*.

Forro, T., and Klausberger, T. (2023). Differential behavior-related activity of distinct hippocampal interneuron types during odor-associated spatial navigation. Neuron *111*, 2399-2413.e5.

Frankland, P.W., and Bontempi, B. (2005). The organization of recent and remote memories. Nat. Rev. Neurosci. *6*, 119–130.

Frankland, P.W., Cestari, V., Filipkowski, R.K., McDonald, R.J., and Silva, A.J. (1998). The dorsal hippocampus is essential for context discrimination but not for contextual conditioning. Behav. Neurosci. *112*, 863–874.

Frankland, P.W., Josselyn, S.A., and Köhler, S. (2019). The neurobiological foundation of memory retrieval. Nat. Neurosci. *22*, 1576–1585.

Fredes, F., Silva, M.A., Koppensteiner, P., Kobayashi, K., Joesch, M., and Shigemoto, R. (2021). Ventro-dorsal Hippocampal Pathway Gates Novelty-Induced Contextual Memory Formation. Curr. Biol. *31*, 25-38.e5.

Freund, T.F. (2003). Interneuron Diversity series: Rhythm and mood in perisomatic inhibition. Trends Neurosci. *26*, 489–495.

Freund, T.F., and Buzsáki, G. (1996). Interneurons of the hippocampus. Hippocampus *6*, 347–470.

Freund, T.F., and Katona, I. (2007). Perisomatic inhibition. Neuron *56*, 33–42.

Frey, U., and Morris, R.G. (1997). Synaptic tagging and long-term potentiation. Nature *385*, 533–536.

Fries, P. (2005). A mechanism for cognitive dynamics: neuronal communication through neuronal coherence. Trends Cogn. Sci. *9*, 474–480.

Froemke, R.C. (2015). Plasticity of Cortical Excitatory-Inhibitory Balance. Annu. Rev. Neurosci. *38*, 195–219.

Fuchs, E.C., Zivkovic, A.R., Cunningham, M.O., Middleton, S., Lebeau, F.E.N., Bannerman, D.M., Rozov, A., Whittington, M.A., Traub, R.D., Rawlins, J.N.P., et al. (2007). Recruitment of parvalbumin-positive interneurons determines hippocampal function and associated behavior. Neuron *53*, 591–604.

Furtunato, A.M.B., Lobão-Soares, B., Tort, A.B.L., and Belchior, H. (2020). Specific Increase of Hippocampal Delta Oscillations Across Consecutive Treadmill Runs. Front. Behav. Neurosci. *14*, 1–13.

Gabriel, C.J., Zeidler, Z., Jin, B., Guo, C., Goodpaster, C.M., Kashay, A.Q., Wu, A., Delaney, M., Cheung, J., DiFazio, L.E., et al. (2022). BehaviorDEPOT is a simple, flexible tool for automated behavioral detection based on markerless pose tracking. Elife *11*, e74314.

Garner, A.R., Rowland, D.C., Hwang, S.Y., Baumgaertel, K., Roth, B.L., Kentros, C., and Mayford, M. (2012). Generation of a synthetic memory trace. Science *335*, 1513–1516.

Gilbert, P.E., and Brushfield, A.M. (2009). The role of the CA3 hippocampal subregion in spatial memory: a process oriented behavioral assessment. Prog. Neuropsychopharmacol. Biol. Psychiatry *33*, 774–781.

Gilbert, P.E., and Kesner, R.P. (2003). Recognition Memory for Complex Visual Discriminations Is Influenced by Stimulus Interference in Rodents With Perirhinal Cortex Damage. Learn. Mem. *10*, 525–530.

Gilbert, P.E., and Kesner, R.P. (2006). The role of the dorsal CA3 hippocampal subregion in spatial working memory and pattern separation. Behav. Brain Res. *169*, 142–149.

Gilbert, P.E., Kesner, R.P., and Lee, I. (2001). Dissociating hippocampal subregions: double dissociation between dentate gyrus and CA1. Hippocampus *11*, 626–636.

Giorgi, C., and Marinelli, S. (2021). Roles and Transcriptional Responses of Inhibitory Neurons in Learning and Memory. Front. Mol. Neurosci. *14*, 689952.

Goldman-Rakic, P.S. (1995). Cellular basis of working memory. Neuron *14*, 477–485.

Gomez-Marin, A., Partoune, N., Stephens, G.J., and Louis, M. (2012). Automated tracking of animal posture and movement during exploration and sensory orientation behaviors. PLoS One *7*.

Gómez-Ocádiz, R., Trippa, M., Zhang, C.-L., Posani, L., Cocco, S., Monasson, R., and Schmidt-Hieber, C. (2022). A synaptic signal for novelty processing in the hippocampus. Nat. Commun. *13*, 4122.

Goode, T.D., Tanaka, K.Z., Sahay, A., and McHugh, T.J. (2020). An Integrated Index: Engrams, Place Cells, and Hippocampal Memory. Neuron *107*, 805–820.

Goodrich-Hunsaker, N.J., Hunsaker, M.R., and Kesner, R.P. (2005). Dissociating the role of the parietal cortex and dorsal hippocampus for spatial information processing. Behav. Neurosci. *119*, 1307–1315.

GoodSmith, D., Kim, S.H., Puliyadi, V., Ming, G. li, Song, H., Knierim, J.J., and Christian, K.M. (2022). Flexible encoding of objects and space in single cells of the dentate gyrus. Curr. Biol. *32*, 1088-1101.e5.

Goshen, I., Brodsky, M., Prakash, R., Wallace, J., Gradinaru, V., Ramakrishnan, C., and Deisseroth, K. (2011). Dynamics of retrieval strategies for remote memories. Cell *147*, 678–689.

Grella, S.L., Fortin, A.H., McKissick, O., Leblanc, H., and Ramirez, S. (2020). Odor modulates the temporal dynamics of fear memory consolidation. Learn. Mem. *27*, 150–163.

Grynkiewicz, G., Poenie, M., and Tsien, R.Y. (1985). A new generation of Ca2+ indicators with greatly improved fluorescence properties. J. Biol. Chem. *260*, 3440–3450.

Guardamagna, M., Chadney, O., Stella, F., Zhang, Q., Kentros, C., and Battaglia, F.P. (2023). Direct Entorhinal Control of CA1 Temporal Coding. BioRxiv 2023.05.27.542579.

Gunaydin, L.A., Grosenick, L., Finkelstein, J.C., Kauvar, I. V, Fenno, L.E., Adhikari, A., Lammel, S., Mirzabekov, J.J., Airan, R.D., Zalocusky, K.A., et al. (2014). Natural neural projection dynamics underlying social behavior. Cell *157*, 1535–1551.

Guo, J., Ran, M., Gao, Z., Zhang, X., Wang, D., Li, H., Zhao, S., Sun, W., Dong, H., and Hu, J. (2021). Cell-type-specific imaging of neurotransmission reveals a disrupted excitatory-inhibitory cortical network in isoflurane anaesthesia. EBioMedicine *65*.

Guskjolen, A., and Cembrowski, M.S. (2023). Engram neurons: Encoding, consolidation, retrieval, and forgetting of memory. Mol. Psychiatry.

Guzman, S.J., Schlögl, A., Frotscher, M., and Jonas, P. (2016). Synaptic mechanisms of pattern completion in the hippocampal CA3 network. Science *353*, 1117–1123.

van Hagen, B.T.J., van Goethem, N.P., Lagatta, D.C., and Prickaerts, J. (2015). The object pattern separation (OPS) task: A behavioral paradigm derived from the object recognition task. Behav. Brain Res. *285*, 44–52.

Hainmueller, T., and Bartos, M. (2018). Parallel emergence of stable and dynamic memory

engrams in the hippocampus. Nature *558*, 292–296.

Hainmueller, T., and Bartos, M. (2020). Dentate gyrus circuits for encoding, retrieval and discrimination of episodic memories. Nat. Rev. Neurosci. *21*, 153–168.

Hainmueller, T., Huang, L.-W., and Bartos, M. (2021). Subfield-Specific Interneuron Circuits Govern the Hippocampal Response to Novelty. SSRN Electron. J.

Hara, K., and Harris, R.A. (2002). The anesthetic mechanism of urethane: the effects on neurotransmitter-gated ion channels. Anesth. Analg. *94*, 313–318, table of contents.

Harkotte, M., Contreras, M.P., Inostroza, M., and Born, J. (2022). Effects of Information Load on Schema and Episodic Memory Formation. Front. Behav. Neurosci. *16*, 923713.

Hartung, J.E., and Gold, M.S. (2020). GCaMP as an indirect measure of electrical activity in rat trigeminal ganglion neurons. Cell Calcium *89*, 102225.

Hasselmo, M.E., Bodelón, C., and Wyble, B.P. (2002). A proposed function for hippocampal theta rhythm: separate phases of encoding and retrieval enhance reversal of prior learning. Neural Comput. *14*, 793–817.

Hebb, D.O. (1949). The first stage of perception: growth of the assembly. Organ. Behav. *4*, 60–78.

Henke, P.G. (1990). Hippocampal pathway to the amygdala and stress ulcer development. Brain Res. Bull. *25*, 691–695.

Hernández-Rabaza, V., Hontecillas-Prieto, L., Velázquez-Sánchez, C., Ferragud, A., Pérez-Villaba, A., Arcusa, A., Barcia, J.A., Trejo, J.L., and Canales, J.J. (2008). The hippocampal dentate gyrus is essential for generating contextual memories of fear and drug-induced reward. Neurobiol. Learn. Mem. *90*, 553–559.

Hijazi, S., Smit, A.B., and van Kesteren, R.E. (2023). Fast-spiking parvalbumin-positive interneurons in brain physiology and Alzheimer's disease. Mol. Psychiatry.

Hitti, F.L., and Siegelbaum, S.A. (2014). The hippocampal CA2 region is essential for social memory. Nature *508*, 88–92.

Honoré, E., Khlaifia, A., Bosson, A., and Lacaille, J.-C. (2021). Hippocampal Somatostatin Interneurons, Long-Term Synaptic Plasticity and Memory. Front. Neural Circuits *15*, 687558.

Hosp, J.A., Strüber, M., Yanagawa, Y., Obata, K., Vida, I., Jonas, P., and Bartos, M. (2014). Morpho-physiological criteria divide dentate gyrus interneurons into classes. Hippocampus *24*, 189–203.

Houser, C.R. (2007). Interneurons of the dentate gyrus: an overview of cell types, terminal fields and neurochemical identity. Prog. Brain Res. *163*, 217–232.

Huh, Y., and Cho, J. (2013). Urethane anesthesia depresses activities of thalamocortical neurons and alters its response to nociception in terms of dual firing modes. Front. Behav. Neurosci. *7*, 141.

Hunsaker, M.R., Rosenberg, J.S., and Kesner, R.P. (2008). The role of the dentate gyrus, CA3a,b, and CA3c for detecting spatial and environmental novelty. Hippocampus *18*, 1064–1073.

Hvoslef-Eide, M., and Oomen, C.A. (2016). Adult neurogenesis and pattern separation in rodents: A critical evaluation of data, tasks and interpretation. Front. Biol. (Beijing). *11*, 168–181.

Ibañez, V., Bohlen, L., Manuella, F., Mansuy, I., Helmchen, F., and Wahl, A.-S. (2023). EXPLORE: a novel deep learning-based analysis method for exploration behaviour in object recognition tests. Sci. Rep. *13*, 4249.

Inostroza, M., Brotons-Mas, J.R., Laurent, F., Cid, E., and de la Prida, L.M. (2013). Specific impairment of "what-where-when" episodic-like memory in experimental models of temporal lobe epilepsy. J. Neurosci. Off. J. Soc. Neurosci. *33*, 17749–17762.

Isaacson, J.S., and Scanziani, M. (2011). How inhibition shapes cortical activity. Neuron *72*, 231–243.

Ishizuka, N., Weber, J., and Amaral, D.G. (1990). Organization of intrahippocampal projections originating from CA3 pyramidal cells in the rat. J. Comp. Neurol. *295*, 580–623.

Ishizuka, N., Cowan, W.M., and Amaral, D.G. (1995). A quantitative analysis of the dendritic organization of pyramidal cells in the rat hippocampus. J. Comp. Neurol. *362*, 17–45.

Isik, S., and Unal, G. (2023). Open-source software for automated rodent behavioral analysis . Front. Neurosci. *17*.

Ito, M. (1989). Long-term depression. Annu. Rev. Neurosci. *12*, 85–102.

Iwase, M., Kitanishi, T., and Mizuseki, K. (2020). Cell type, sub-region, and layer-specific speed representation in the hippocampal–entorhinal circuit. Sci. Rep. *10*, 1407.

Izquierdo, I., Medina, J.H., Bianchin, M., Walz, R., Zanatta, M.S., Da Silva, R.C., Silva, M.B.E., Ruschel, A.C., and Paczko, N. (1993). Memory processing by the limbic system: Role of specific neurotransmitter systems. Behav. Brain Res. *58*, 91–98.

Jahangir, M., Zhou, J.S., Lang, B., and Wang, X.P. (2021). GABAergic System Dysfunction and Challenges in Schizophrenia Research. Front. Cell Dev. Biol. *9*, 1–12.

James, W. (1890). The principles of psychology, Vol I. (New York, NY, US: Henry Holt and Co).

Josselyn, S.A., and Tonegawa, S. (2020). Memory engrams: Recalling the past and imagining the future. Science (80-.). *367*.

Josselyn, S.A., Köhler, S., and Frankland, P.W. (2015). Finding the engram. Nat. Rev. Neurosci. *16*, 521–534.

Jung, M.W., and McNaughton, B.L. (1993). Spatial selectivity of unit activity in the hippocampal granular layer. Hippocampus *3*, 165–182.

Jung, M.W., Wiener, S.I., and McNaughton, B.L. (1994). Comparison of spatial firing characteristics of units in dorsal and ventral hippocampus of the rat. J. Neurosci. *14*, 7347–7356.

Kandel, E.R., and Tauc, L. (1965). Heterosynaptic facilitation in neurones of the abdominal ganglion of Aplysia depilans. J. Physiol. *181*, 1–27.

Kerr, K.M., Agster, K.L., Furtak, S.C., and Burwell, R.D. (2007). Functional neuroanatomy of the parahippocampal region: the lateral and medial entorhinal areas. Hippocampus *17*, 697–708.

Kerr, R., Lev-Ram, V., Baird, G., Vincent, P., Tsien, R.Y., and Schafer, W.R. (2000). Optical imaging of calcium transients in neurons and pharyngeal muscle of C. elegans. Neuron *26*, 583–594.

Kesner, R.P. (2007). A behavioral analysis of dentate gyrus function. Prog. Brain Res. *163*, 567–576.

Kesner, R.P., and Rolls, E.T. (2015). A computational theory of hippocampal function, and tests of the theory: new developments. Neurosci. Biobehav. Rev. *48*, 92–147.

Kesner, R.P., Lee, I., and Gilbert, P. (2004). A behavioral assessment of hippocampal function based on a subregional analysis. Rev. Neurosci. *15*, 333–351.

Kesner, R.P., Taylor, J.O., Hoge, J., and Andy, F. (2015). Role of the dentate gyrus in mediating object-spatial configuration recognition. Neurobiol. Learn. Mem. *118*, 42–48.

Kesner, R.P., Kirk, R.A., Yu, Z., Polansky, C., and Musso, N.D. (2016). Dentate gyrus supports slope recognition memory, shades of grey-context pattern separation and recognition memory, and CA3 supports pattern completion for object memory. Neurobiol. Learn. Mem. *129*, 29–37.

Kheirbek, M.A., Drew, L.J., Burghardt, N.S., Costantini, D.O., Tannenholz, L., Ahmari, S.E., Zeng, H., Fenton, A.A., and Hen, R. (2013). Differential control of learning and anxiety along the dorso-ventral axis of the dentate gyrus. Neuron *77*, 955.

Kim, D., Jeong, H., Lee, J., Ghim, J.-W., Her, E.S., Lee, S.-H., and Jung, M.W. (2016). Distinct Roles of Parvalbumin- and Somatostatin-Expressing Interneurons in Working Memory. Neuron *92*, 902–915.

Kim, S., Jung, D., and Royer, S. (2020). Place cell maps slowly develop via competitive learning and conjunctive coding in the dentate gyrus. Nat. Commun. *11*, 4550.

Kitamura, T., Sun, C., Martin, J., Kitch, L.J., Schnitzer, M.J., and Tonegawa, S. (2015). Entorhinal Cortical Ocean Cells Encode Specific Contexts and Drive Context-Specific Fear Memory. Neuron *87*, 1317–1331.

Kitchigina, V.F. (2018). Alterations of Coherent Theta and Gamma Network Oscillations as an Early Biomarker of Temporal Lobe Epilepsy and Alzheimer's Disease. Front. Integr. Neurosci. *12*, 36.

Kjelstrup, K.B., Solstad, T., Brun, V.H., Hafting, T., Leutgeb, S., Witter, M.P., Moser, E.I., and Moser, M.-B. (2008). Finite scale of spatial representation in the hippocampus. Science *321*, 140–143.

Kjelstrup, K.G., Tuvnes, F.A., Steffenach, H.-A., Murison, R., Moser, E.I., and Moser, M.-B. (2002). Reduced fear expression after lesions of the ventral hippocampus. Proc. Natl. Acad. Sci. U. S. A. *99*, 10825–10830.

Klausberger, T., and Somogyi, P. (2008). Neuronal diversity and temporal dynamics: the unity of hippocampal circuit operations. Science *321*, 53–57.

Klein, M., and Kandel, E.R. (1978). Presynaptic modulation of voltage-dependent Ca2+ current: mechanism for behavioral sensitization in Aplysia californica. Proc. Natl. Acad. Sci. U. S. A. *75*, 3512–3516.

Knierim, J.J., Lee, I., and Hargreaves, E.L. (2006). Hippocampal place cells: parallel input streams, subregional processing, and implications for episodic memory. Hippocampus *16*, 755–764.

Kohara, K., Pignatelli, M., Rivest, A.J., Jung, H.-Y., Kitamura, T., Suh, J., Frank, D., Kajikawa, K., Mise, N., Obata, Y., et al. (2014). Cell type-specific genetic and optogenetic tools reveal hippocampal CA2 circuits. Nat. Neurosci. *17*, 269–279.

Konradi, C., Yang, C.K., Zimmerman, E.I., Lohmann, K.M., Gresch, P., Pantazopoulos, H., Berretta, S., and Heckers, S. (2011). Hippocampal interneurons are abnormal in schizophrenia. Schizophr. Res. *131*, 165–173.

Krakauer, J.W., Ghazanfar, A.A., Gomez-Marin, A., MacIver, M.A., and Poeppel, D. (2017). Neuroscience Needs Behavior: Correcting a Reductionist Bias. Neuron *93*, 480–490.

Krook-Magnuson, E., Armstrong, C., Bui, A., Lew, S., Oijala, M., and Soltesz, I. (2015). In vivo evaluation of the dentate gate theory in epilepsy. J. Physiol. *593*, 2379–2388.

Kumaran, D., and Maguire, E.A. (2006). An unexpected sequence of events: Mismatch detection in the human hippocampus. PLoS Biol. *4*, 2372–2382.

Larkin, M.C., Lykken, C., Tye, L.D., Wickelgren, J.G., and Frank, L.M. (2014). Hippocampal output area CA1 broadcasts a generalized novelty signal during an object-place recognition task. Hippocampus *24*, 773–783.

Lashley, K.S., and Franz, S.I. (1917). The Effects of Cerebral Destruction Upon Habit-Formation and Retention in the Albino Rat. Psychobiology *1*, 71–139.

Lassalle, J.M., Bataille, T., and Halley, H. (2000). Reversible inactivation of the hippocampal mossy fiber synapses in mice impairs spatial learning, but neither consolidation nor memory retrieval, in the Morris navigation task. Neurobiol. Learn. Mem. *73*, 243–257.

Lavi, A., Sehgal, M., de Sousa, A.F., Ter-Mkrtchyan, D., Sisan, F., Luchetti, A., Okabe, A., Bear, C., and Silva, A.J. (2023). Local memory allocation recruits memory ensembles across brain regions. Neuron *111*, 470-480.e5.

Lee, J.L.C. (2010). Memory reconsolidation mediates the updating of hippocampal memory content. Front. Behav. Neurosci. *4*, 168.

Lee, I., and Kesner, R.P. (2004). Differential contributions of dorsal hippocampal subregions to memory acquisition and retrieval in contextual fear-conditioning. Hippocampus *14*, 301–310.

Lee, I., and Solivan, F. (2010). Dentate gyrus is necessary for disambiguating similar object-place representations. Learn. Mem. *17*, 252–258.

Lee, J.W., and Jung, M.W. (2017). Separation or binding? Role of the dentate gyrus in hippocampal mnemonic processing. Neurosci. Biobehav. Rev. *75*, 183–194.

Lee, C.-T., Kao, M.-H., Hou, W.-H., Wei, Y.-T., Chen, C.-L., and Lien, C.-C. (2016). Causal Evidence for the Role of Specific GABAergic Interneuron Types in Entorhinal Recruitment of Dentate Granule Cells. Sci. Rep. *6*, 36885.

Lee, H., Choi, W., Park, Y., and Paik, S.-B. (2020). Distinct role of flexible and stable encodings in sequential working memory. Neural Networks *121*, 419–429.

Lee, I., Hunsaker, M.R., and Kesner, R.P. (2005). The Role of Hippocampal Subregions in Detecting Spatial Novelty. Behav. Neurosci. *119*, 145–153.

Leger, M., Quiedeville, A., Bouet, V., Haelewyn, B., Boulouard, M., Schumann-Bard, P., and Freret, T. (2013). Object recognition test in mice. Nat. Protoc. *8*, 2531–2537.

Leinweber, M., Zmarz, P., Buchmann, P., Argast, P., Hübener, M., Bonhoeffer, T., and Keller, G.B. (2014). Two-photon calcium imaging in mice navigating a virtual reality environment. J. Vis. Exp. e50885.

Leranth, C., Carpi, D., Buzsaki, G., and Kiss, J. (1999). The entorhino-septo-supramammillary nucleus connection in the rat: morphological basis of a feedback mechanism regulating hippocampal theta rhythm. Neuroscience *88*, 701–718.

Letzkus, J.J., Wolff, S.B.E., and Lüthi, A. (2015). Disinhibition, a Circuit Mechanism for Associative Learning and Memory. Neuron *88*, 264–276.

Leung, C., Cao, F., Nguyen, R., Joshi, K., Aqrabawi, A.J., Xia, S., Cortez, M.A., Snead, O.C. 3rd, Kim, J.C., and Jia, Z. (2018). Activation of Entorhinal Cortical Projections to the Dentate Gyrus Underlies Social Memory Retrieval. Cell Rep. *23*, 2379–2391.

Leutgeb, J.K., Leutgeb, S., Moser, M.B., and Moser, E.I. (2007). Pattern separation in the dentate gyrus and CA3 of the hippocampus. Science (80-.). *315*, 961–966.

Lever, C., Burton, S., and O'Keefe, J. (2006). Rearing on hind legs, environmental novelty, and the hippocampal formation. Rev. Neurosci. *17*, 111–133.

Li, Y., Bao, H., Luo, Y., Yoan, C., Sullivan, H.A., Quintanilla, L., Wickersham, I., Lazarus, M., Shih, Y.-Y.I., and Song, J. (2020). Supramammillary nucleus synchronizes with dentate gyrus to regulate spatial memory retrieval through glutamate release. Elife *9*.

Lisman, J.E., and Grace, A.A. (2005). The hippocampal-VTA loop: controlling the entry of information into long-term memory. Neuron *46*, 703–713.

Lisman, J.E., and Jensen, O. (2013). The θ-γ neural code. Neuron *77*, 1002–1016.

Litwin-Kumar, A., and Doiron, B. (2014). Formation and maintenance of neuronal assemblies through synaptic plasticity. Nat. Commun. *5*, 5319.

Liu, X., Ramirez, S., Pang, P.T., Puryear, C.B., Govindarajan, A., Deisseroth, K., and Tonegawa, S. (2012). Optogenetic stimulation of a hippocampal engram activates fear memory recall. Nature *484*, 381–385.

Liu, X., Ramirez, S., Redondo, R.L., and Tonegawa, S. (2014). Identification and manipulation of memory engram cells. Cold Spring Harb. Symp. Quant. Biol. *79*, 59–65.

London, T.D., Licholai, J.A., Szczot, I., Ali, M.A., LeBlanc, K.H., Fobbs, W.C., and Kravitz, A. V (2018). Coordinated ramping of dorsal striatal pathways preceding food approach and consumption. J. Neurosci. 2617–2693.

Looger, L.L., and Griesbeck, O. (2012). Genetically encoded neural activity indicators. Curr. Opin. Neurobiol. *22*, 18–23.

López-Madrona, V.J., Pérez-Montoyo, E., Álvarez-Salvado, E., Moratal, D., Herreras, O., Pereda, E., Mirasso, C.R., and Canals, S. (2020). Different theta frameworks coexist in the rat hippocampus and are coordinated during memory-guided and novelty tasks. Elife *9*, 1–35.

Lorente, D.N. (1933). Vestibulo-ocular reflex arc. Arch Neurol Psychiat *30*, 245–291.

Lorente De Nó, R. (1934). Studies on the structure of the cerebral cortex. II. Continuation of the study of the ammonic system. J. Für Psychol. Und Neurol. *46*, 113–177.

Lübke, J., Deller, T., and Frotscher, M. (1997). Septal innervation of mossy cells in the hilus of the rat dentate gyrus: an anterograde tracing and intracellular labeling study. Exp. Brain Res. *114*, 423–432.

Lucas, E.K., and Clem, R.L. (2018). GABAergic interneurons: The orchestra or the conductor in fear learning and memory? Brain Res. Bull. *141*, 13–19.

Luscher, B., Shen, Q., and Sahir, N. (2011). The GABAergic deficit hypothesis of major depressive disorder. Mol. Psychiatry *16*, 383–406.

MacDonald, C.J., Lepage, K.Q., Eden, U.T., and Eichenbaum, H. (2011). Hippocampal "time cells" bridge the gap in memory for discontiguous events. Neuron *71*, 737–749.

Magloire, V., Mercier, M.S., Kullmann, D.M., and Pavlov, I. (2019). GABAergic Interneurons in Seizures: Investigating Causality With Optogenetics. Neurosci. a Rev. J. Bringing Neurobiol. Neurol. Psychiatry *25*, 344–358.

Maguire, E.A., Frith, C.D., Burgess, N., Donnett, J.G., and O'Keefe, J. (1998). Knowing where things are: Parahippocampal involvement in encoding object locations in virtual large-scale space. J. Cogn. Neurosci. *10*, 61–76.

Makarov, V.A., Makarova, J., and Herreras, O. (2010). Disentanglement of local field potential sources by independent component analysis. J. Comput. Neurosci. *29*, 445–457.

Malenka, R.C., and Bear, M.F. (2004). LTP and LTD: An embarrassment of riches. Neuron *44*, 5–21.

Manelis, A., Reder, L.M., and Hanson, S.J. (2012). Dynamic changes in the medial temporal lobe during incidental learning of object-location associations. Cereb. Cortex *22*, 828–837.

Mank, M., Santos, A.F., Direnberger, S., Mrsic-Flogel, T.D., Hofer, S.B., Stein, V., Hendel, T., Reiff, D.F., Levelt, C., Borst, A., et al. (2008). A genetically encoded calcium indicator for chronic in vivo two-photon imaging. Nat. Methods *5*, 805–811.

Marcos, E., Cos, I., Cisek, P., Girard, B., and Verschure, P.F.M.J. (2013). Biomechanical costs of reaching movements bias perceptual decisions. BMC Neurosci. *14*, P408.

Marcos, E., Tsujimoto, S., Mattia, M., and Genovesio, A. (2019). A Network Activity Reconfiguration Underlies the Transition from Goal to Action. Cell Rep. *27*, 2909-2920.e4.

Marr, D. (1971). Simple memory: a theory for archicortex. Philos. Trans. R. Soc. Lond. B. Biol. Sci. *262*, 23–81.

Martin, S.J., Grimwood, P.D., and Morris, R.G.M. (2000). Synaptic Plasticity and Memory. Ann.Rev.Neurosci 649–711.

Mathis, A., Mamidanna, P., Cury, K.M., Abe, T., Murthy, V.N., Mathis, M.W., and Bethge, M. (2018). DeepLabCut: markerless pose estimation of user-defined body parts with deep learning. Nat. Neurosci. *21*, 1281–1289.

Mau, W., Hasselmo, M.E., and Cai, D.J. (2020). The brain in motion: How ensemble fluidity drives memory-updating and flexibility. Elife *9*.

McHenry, J.A., Otis, J.M., Rossi, M.A., Robinson, J.E., Kosyk, O., Miller, N.W., McElligott, Z.A., Budygin, E.A., Rubinow, D.R., and Stuber, G.D. (2017). Hormonal gain control of a medial preoptic area social reward circuit. Nat. Neurosci. *20*, 449–458.

McKenna, J.T., and Vertes, R.P. (2001). Collateral projections from the median raphe nucleus to the medial septum and hippocampus. Brain Res. Bull. *54*, 619–630.

McKenzie, S. (2018). Inhibition shapes the organization of hippocampal representations. Hippocampus *28*, 659–671.

McNaughton, N., and Morris, R.G.M. (1987). Chlordiazepoxide, an anxiolytic benzodiazepine, impairs place navigation in rats. Behav. Brain Res. *24*, 39–46.

McNaughton, B.L., Barnes, C.A., and O'Keefe, J. (1983). The contributions of position, direction, and velocity to single unit activity in the hippocampus of freely-moving rats. Exp. Brain Res. *52*, 41–49.

Meira, T., Leroy, F., Buss, E.W., Oliva, A., Park, J., and Siegelbaum, S.A. (2018). A hippocampal circuit linking dorsal CA2 to ventral CA1 critical for social memory dynamics. Nat. Commun. *9*, 4163.

Melton, A.W. (1963). Memory. Science *140*, 82–86.

Mendez-Couz, M., Conejo, N.M., Gonzalez-Pardo, H., and Arias, J.L. (2015). Functional interactions between dentate gyrus, striatum and anterior thalamic nuclei on spatial memory retrieval. Brain Res. *1605*, 59–69.

Miao, C., Cao, Q., Moser, M.-B., and Moser, E.I. (2017). Parvalbumin and Somatostatin Interneurons Control Different Space-Coding Networks in the Medial Entorhinal Cortex. Cell *171*, 507-521.e17.

Miles, R., Tóth, K., Gulyás, A.I., Hájos, N., and Freund, T.F. (1996). Differences between Somatic and Dendritic Inhibition in the Hippocampus. Neuron *16*, 815–823.

Miranda, J.M., Cruz, E., Bessières, B., and Alberini, C.M. (2022). Hippocampal parvalbumin

interneurons play a critical role in memory development. Cell Rep. *41*, 111643.

Möhler, H., and Rudolph, U. (2017). Disinhibition, an emerging pharmacology of learning and memory. F1000Research *6*.

Morellini, F., Sivukhina, E., Stoenica, L., Oulianova, E., Bukalo, O., Jakovcevski, I., Dityatev, A., Irintchev, A., and Schachner, M. (2010). Improved reversal learning and working memory and enhanced reactivity to novelty in mice with enhanced GABAergic innervation in the dentate gyrus. Cereb. Cortex *20*, 2712–2727.

Moreno, A. (2021). Molecular mechanisms of forgetting. Eur. J. Neurosci. *54*, 6912–6932.

Morgane, P.J., Galler, J.R., and Mokler, D.J. (2005). A review of systems and networks of the limbic forebrain/limbic midbrain. Prog. Neurobiol. *75*, 143–160.

Morris, R.G.M. (1981). Spatial localization does not require the presence of local cues. Learn. Motiv. *12*, 239–260.

Morris, R.G., Anderson, E., Lynch, G.S., and Baudry, M. (1986). Selective impairment of learning and blockade of long-term potentiation by an N-methyl-D-aspartate receptor antagonist, AP5. Nature *319*, 774–776.

Moscovitch, M. (1995). Recovered consciousness: A hypothesis concerning modularity and episodic memory. J. Clin. Exp. Neuropsychol. *17*, 276–290.

Moscovitch, M., and Winocur, G. (1995). Frontal lobes, memory, and aging. Ann. N. Y. Acad. Sci. *769*, 119–150.

Moser, M.B., and Moser, E.I. (1998). Functional differentiation in the hippocampus. Hippocampus *8*, 608–619.

Moser, E., Moser, M.B., and Andersen, P. (1993). Spatial learning impairment parallels the magnitude of dorsal hippocampal lesions, but is hardly present following ventral lesions. J. Neurosci. Off. J. Soc. Neurosci. *13*, 3916–3925.

Moser, M.B., Moser, E.I., Forrest, E., Andersen, P., and Morris, R.G. (1995). Spatial learning with a minislab in the dorsal hippocampus. Proc. Natl. Acad. Sci. U. S. A. *92*, 9697–9701.

Nabavi, S., Fox, R., Proulx, C.D., Lin, J.Y., Tsien, R.Y., and Malinow, R. (2014). Engineering a memory with LTD and LTP. Nature *511*, 348–352.

Nadel, L., and Moscovitch, M. (1997). Memory consolidation, retrograde amnesia and the hippocampal complex. Curr. Opin. Neurobiol. *7*, 217–227.

Nadel, L., Samsonovich, A., Ryan, L., and Moscovitch, M. (2000). Multiple trace theory of human memory: computational, neuroimaging, and neuropsychological results. Hippocampus *10*, 352–368.

Nadel, L., Hupbach, A., Gomez, R., and Newman-Smith, K. (2012). Memory formation, consolidation and transformation. Neurosci. Biobehav. Rev. *36*, 1640–1645.

Nader, K. (2015). Reconsolidation and the Dynamic Nature of Memory. Cold Spring Harb. Perspect. Biol. *7*, a021782.

Nadler, J.J., Moy, S.S., Dold, G., Trang, D., Simmons, N., Perez, A., Young, N.B., Barbaro, R.P., Piven, J., Magnuson, T.R., et al. (2004). Automated apparatus for quantitation of social approach behaviors in mice. Genes. Brain. Behav. *3*, 303–314.

Nagai, T., Sawano, A., Park, E.S., and Miyawaki, A. (2001). Circularly permuted green fluorescent proteins engineered to sense Ca2+. Proc. Natl. Acad. Sci. U. S. A. *98*, 3197–3202.

Nakai, J., Ohkura, M., and Imoto, K. (2001). A high signal-to-noise Ca2+ probe composed of a

single green fluorescent protein. Nat. Biotechnol. *19*, 137–141.

Navabpour, S., Kwapis, J.L., and Jarome, T.J. (2020). A neuroscientist's guide to transgenic mice and other genetic tools. Neurosci. Biobehav. Rev. *108*, 732–748.

Neher, E., and Sakaba, T. (2008). Multiple roles of calcium ions in the regulation of neurotransmitter release. Neuron *59*, 861–872.

Neunuebel, J.P., and Knierim, J.J. (2012). Spatial firing correlates of physiologically distinct cell types of the rat dentate gyrus. J. Neurosci. *32*, 3848–3858.

Neves, G., Cooke, S.F., and Bliss, T.V.P. (2008). Synaptic plasticity, memory and the hippocampus - a neural network aproach to causality. Nat. Rev. Neurosci. *9*, 65–75.

Nguyen-Vu, T.D.B., Kimpo, R.R., Rinaldi, J.M., Kohli, A., Zeng, H., Deisseroth, K., and Raymond, J.L. (2013). Cerebellar Purkinje cell activity drives motor learning. Nat. Neurosci. *16*, 1734–1736.

Nilsson, S.R.O., Goodwin, N.L., Choong, J.J., Hwang, S., Wright, H.R., Norville, Z.C., Tong, X., Lin, D., Bentzley, B.S., Eshel, N., et al. (2020). Simple Behavioral Analysis (SimBA) – an open source toolkit for computer classification of complex social behaviors in experimental animals. BioRxiv 2020.04.19.049452.

Nitz, D., and McNaughton, B. (2004). Differential modulation of CA1 and dentate gyrus interneurons during exploration of novel environments. J. Neurophysiol. *91*, 863–872.

O'Keefe, J. (1976). Place units in the hippocampus of the freely moving rat. Exp. Neurol. *51*, 78–109.

O'Keefe, J., and Dostrovsky, J. (1971). The hippocampus as a spatial map. Preliminary evidence from unit activity in the freely-moving rat. Brain Res. *34*, 171–175.

O'Keefe, J., and Nadel, L. (1978). The Hippocampus as a Cognitive Map Oxford Univ. Press.

O'Reilly, R.C., and McClelland, J.L. (1994). Hippocampal conjunctive encoding, storage, and recall: avoiding a trade-off. Hippocampus *4*, 661–682.

Ogando, M.B., Pedroncini, O., Federman, N., Romano, S.A., Brum, L.A., Lanuza, G.M., Refojo, D., and Marin-Burgin, A. (2021). Cholinergic modulation of dentate gyrus processing through dynamic reconfiguration of inhibitory circuits. Cell Rep. *36*.

Ognjanovski, N., Schaeffer, S., Wu, J., Mofakham, S., Maruyama, D., Zochowski, M., and Aton, S.J. (2017). Parvalbumin-expressing interneurons coordinate hippocampal network dynamics required for memory consolidation. Nat. Commun. *8*, 15039.

Oh, J., Lee, C., and Kaang, B.K. (2019). Imaging and analysis of genetically encoded calcium indicators linking neural circuits and behaviors. Korean J. Physiol. Pharmacol. *23*, 237–249.

Okuyama, T., Kitamura, T., Roy, D.S., Itohara, S., and Tonegawa, S. (2016). Ventral CA1 neurons store social memory. Science *353*, 1536–1541.

Olton, D.S., and Samuelson, R.J. (1976). Remembrance of places passed: Spatial memory in rats. J. Exp. Psychol. Anim. Behav. Process. *2*, 97–116.

Orlandi, J.G., Abdolrahmani, M., Aoki, R., Lyamzin, D.R., and Benucci, A. (2023). Distributed context-dependent choice information in mouse posterior cortex. Nat. Commun. *14*, 192.

Ornelas, I.M., Cini, F.A., Wießner, I., Marcos, E., Araújo, D.B., Goto-Silva, L., Nascimento, J., Silva, S.R.B., Costa, M.N., Falchi, M., et al. (2022). Nootropic effects of LSD: Behavioral, molecular and computational evidence. Exp. Neurol. *356*.

Ortega-de San Luis, C., and Ryan, T.J. (2022). Understanding the physical basis of memory:

Molecular mechanisms of the engram. J. Biol. Chem. *298*, 101866.

Palop, J.J., and Mucke, L. (2016). Network abnormalities and interneuron dysfunction in Alzheimer disease. Nat. Rev. Neurosci. *17*, 777–792.

Panoz-brown, D., Corbin, H.E., Dalecki, S.J., Sluka, C.M., Wu, J., Crystal, J.D., Sluka, C.M., Wu, J., and Crystal, J.D. (2016). Report Rats Remember Items in Context Using Episodic Memory. Curr. Biol. 1–6.

Park, K., Lee, J., Jang, H.J., Richards, B.A., Kohl, M.M., and Kwag, J. (2020). Optogenetic activation of parvalbumin and somatostatin interneurons selectively restores theta-nested gamma oscillations and oscillation-induced spike timing-dependent long-term potentiation impaired by amyloid β oligomers. BMC Biol. *18*, 7.

Parker, K.E., Pedersen, C.E., Gomez, A.M., Spangler, S.M., Walicki, M.C., Feng, S.Y., Stewart, S.L., Otis, J.M., Al-Hasani, R., McCall, J.G., et al. (2019). A Paranigral VTA Nociceptin Circuit that Constrains Motivation for Reward. Cell *178*, 653-671.e19.

Patriarchi, T., Cho, J.R., Merten, K., Howe, M.W., Marley, A., Xiong, W.-H., Folk, R.W., Broussard, G.J., Liang, R., Jang, M.J., et al. (2018). Ultrafast neuronal imaging of dopamine dynamics with designed genetically encoded sensors. Science *360*.

Pavlov, I. (1927). Conditioned reflexes. (New York, NY, US: Oxford University Press).

Pelkey, K.A., Chittajallu, R., Craig, M.T., Tricoire, L., Wester, J.C., and McBain, C.J. (2017). Hippocampal gabaergic inhibitory interneurons. Physiol. Rev. *97*, 1619–1747.

Pereira, T.D., Shaevitz, J.W., and Murthy, M. (2020). Quantifying behavior to understand the brain. Nat. Neurosci. *23*, 1537–1549.

Perusini, J.N., Cajigas, S.A., Cohensedgh, O., Lim, S.C., Pavlova, I.P., Donaldson, Z.R., and Denny, C.A. (2017). Optogenetic stimulation of dentate gyrus engrams restores memory in Alzheimer's disease mice. Hippocampus *27*, 1110–1122.

Peterson, L., and Peterson, M.J. (1959). Short-term retention of individual verbal items. J. Exp. Psychol. *58*, 193–198.

Piatkevich, K.D., Jung, E.E., Straub, C., Linghu, C., Park, D., Suk, H.-J., Hochbaum, D.R., Goodwin, D., Pnevmatikakis, E., Pak, N., et al. (2018). A robotic multidimensional directed evolution approach applied to fluorescent voltage reporters. Nat. Chem. Biol. *14*, 352–360.

Pinto, L., and Dan, Y. (2015). Cell-Type-Specific Activity in Prefrontal Cortex during Goal-Directed Behavior. Neuron *87*, 437–450.

Ponzi, A., Dura-Bernal, S., and Migliore, M. (2023). Theta-gamma phase amplitude coupling in a hippocampal CA1 microcircuit. PLoS Comput. Biol. *19*, e1010942.

Postma, A., Kessels, R.P.C., and van Asselen, M. (2008). How the brain remembers and forgets where things are: The neurocognition of object-location memory. Neurosci. Biobehav. Rev. *32*, 1339–1345.

Poucet, B. (1989). Object exploration, habituation, and response to a spatial change in rats following septal or medial frontal cortical damage. Behav. Neurosci. *103*, 1009–1016.

Ramirez, S., Liu, X., Lin, P.-A., Suh, J., Pignatelli, M., Redondo, R.L., Ryan, T.J., and Tonegawa, S. (2013). Creating a false memory in the hippocampus. Sci. (New York, NY) *341*, 387–391.

Ramirez, S., Liu, X., MacDonald, C.J., Moffa, A., Zhou, J., Redondo, R.L., and Tonegawa, S. (2015). Activating positive memory engrams suppresses depression-like behaviour. Nature *522*, 335–339.

Ranganath, C. (2010). Binding items and contexts: The cognitive neuroscience of episodic memory. Curr. Dir. Psychol. Sci. *19*, 131–137.

Rao-Ruiz, P., Visser, E., Mitrić, M., Smit, A.B., and van den Oever, M.C. (2021). A Synaptic Framework for the Persistence of Memory Engrams. Front. Synaptic Neurosci. *13*, 661476.

Raven, F., and Aton, S.J. (2021). The Engram ' s Dark Horse : How Interneurons Regulate State-Dependent Memory Processing and Plasticity. *15*, 1–17.

Redondo, R.L., and Morris, R.G.M. (2011). Making memories last: the synaptic tagging and capture hypothesis. Nat. Rev. Neurosci. *12*, 17–30.

Redondo, R.L., Kim, J., Arons, A.L., Ramirez, S., Liu, X., and Tonegawa, S. (2014). Bidirectional switch of the valence associated with a hippocampal contextual memory engram. Nature *513*, 426–430.

Regev-Tsur, S., Demiray, Y.E., Tripathi, K., Stork, O., Richter-Levin, G., and Albrecht, A. (2020). Region-specific involvement of interneuron subpopulations in trauma-related pathology and resilience. Neurobiol. Dis. *143*, 104974.

Reichelt, A.C., Kramar, C.P., Ghosh-Swaby, O.R., Sheppard, P.A.S., Kent, B.A., Bekinschtein, P., Saksida, L.M., and Bussey, T.J. (2021). The spontaneous location recognition task for assessing spatial pattern separation and memory across a delay in rats and mice. Nat. Protoc. *16*, 5616–5633.

Reijmers, L.G., Perkins, B.L., Matsuo, N., and Mayford, M. (2007). Localization of a stable neural correlate of associative memory. Science *317*, 1230–1233.

Remondes, M., and Schuman, E.M. (2004). Role for a cortical input to hippocampal area CA1 in the consolidation of a long-term memory. Nature *431*, 699–703.

Rennó-Costa, C., Lisman, J.E., and Verschure, P.F.M.J. (2010). The mechanism of rate remapping in the dentate gyrus. Neuron *68*, 1051–1058.

Rennó-Costa, C., da Silva, A.C.C., Blanco, W., and Ribeiro, S. (2019). Computational models of memory consolidation and long-term synaptic plasticity during sleep. Neurobiol. Learn. Mem. *160*, 32–47.

Ribak, C.E., Harris, A.B., Vaughn, J.E., and Roberts, E. (1979). Inhibitory, GABAergic nerve terminals decrease at sites of focal epilepsy. Science *205*, 211–214.

Rivera, P.D., Raghavan, R.K., Yun, S., Latchney, S.E., McGovern, M.-K., García, E.F., Birnbaum, S.G., and Eisch, A.J. (2015). Retrieval of morphine-associated context induces cFos in dentate gyrus neurons. Hippocampus *25*, 409–414.

Roberts, W.A., and Smythe, W.E. (1979). Memory for lists of spatial events in the rat. Learn. Motiv. *10*, 313–336.

Rolls, E.T. (2013). The mechanisms for pattern completion and pattern separation in the hippocampus. Front. Syst. Neurosci. *7*, 74.

Royer, S., Zemelman, B. V, Losonczy, A., Kim, J., Chance, F., Magee, J.C., and Buzsáki, G. (2012). Control of timing, rate and bursts of hippocampal place cells by dendritic and somatic inhibition. Nat. Neurosci. *15*, 769–775.

Ryan, T.J., Roy, D.S., Pignatelli, M., Arons, A., and Tonegawa, S. (2015). Memory. Engram cells retain memory under retrograde amnesia. Science *348*, 1007–1013.

Sánchez-Rodríguez, I., Temprano-Carazo, S., Jeremic, D., Delgado-Garcia, J.M., Gruart, A., Navarro-López, J.D., and Jiménez-Díaz, L. (2022). Recognition Memory Induces Natural LTP-like Hippocampal Synaptic Excitation and Inhibition. Int. J. Mol. Sci. *23*.

Sauer, J.F., and Bartos, M. (2020). The role of the dentate gyrus in mnemonic functions. Neuroforum *26*, 247–254.

Scanziani, M., and Häusser, M. (2009). Electrophysiology in the age of light. Nature *461*, 930–939.

Scharfman, H.E. (2007). The CA3 "backprojection" to the dentate gyrus. pp. 627–637.

Scharfman, H.E. (2019). The Dentate Gyrus and Temporal Lobe Epilepsy: An "Exciting" Era. Epilepsy Curr. *19*, 249–255.

Scharfman, H.E., and Myers, C.E. (2012). Hilar mossy cells of the dentate gyrus: a historical perspective. Front. Neural Circuits *6*, 106.

Scoville, W.B., and Milner, B. (1957). Loss of recent memory after bilateral hippocampal lesions. J. Neurol. Neurosurg. Psychiatry *20*, 11–21.

Segalin, C., Williams, J., Karigo, T., Hui, M., Zelikowsky, M., Sun, J.J., Perona, P., Anderson, D.J., and Kennedy, A. (2021). The Mouse Action Recognition System (MARS) software pipeline for automated analysis of social behaviors in mice. Elife *10*.

Sellami, A., Al Abed, A.S., Brayda-Bruno, L., Etchamendy, N., Valério, S., Oulé, M., Pantaléon, L., Lamothe, V., Potier, M., Bernard, K., et al. (2017). Temporal binding function of dorsal CA1 is critical for declarative memory formation. Proc. Natl. Acad. Sci. U. S. A. *114*, 10262–10267.

Semon, R. (1904). Die mneme (Reprinted, 1923).

Senn, V., Wolff, S.B.E., Herry, C., Grenier, F., Ehrlich, I., Gründemann, J., Fadok, J.P., Müller, C., Letzkus, J.J., and Lüthi, A. (2014). Long-Range Connectivity Defines Behavioral Specificity of Amygdala Neurons. Neuron *81*, 428–437.

Senova, S., Fomenko, A., Gondard, E., and Lozano, A.M. (2020). Anatomy and function of the fornix in the context of its potential as a therapeutic target. J. Neurol. Neurosurg. Psychiatry *91*, 547–559.

Shemesh, O.A., Linghu, C., Piatkevich, K.D., Goodwin, D., Celiker, O.T., Gritton, H.J., Romano, M.F., Gao, R., Yu, C.-C.J., Tseng, H.-A., et al. (2020). Precision Calcium Imaging of Dense Neural Populations via a Cell-Body-Targeted Calcium Indicator. Neuron *107*, 470-486.e11.

Shimbo, A., Izawa, E.I., and Fujisawa, S. (2021). Scalable representation of time in the hippocampus. Sci. Adv. *7*.

Shinohara, Y., Hosoya, A., Yahagi, K., Ferecskó, A.S., Yaguchi, K., Sík, A., Itakura, M., Takahashi, M., and Hirase, H. (2012). Hippocampal CA3 and CA2 have distinct bilateral innervation patterns to CA1 in rodents. Eur. J. Neurosci. *35*, 702–710.

Shirazy, M., RayatSanati, K., Jamali, S., Motamedi, F., and Haghparast, A. (2020). Role of orexinergic receptors in the dentate gyrus of the hippocampus in the acquisition and expression of morphine-induced conditioned place preference in rats. Behav. Brain Res. *379*, 112349.

Shires, K.L., Da Silva, B.M., Hawthorne, J.P., Morris, R.G.M., and Martin, S.J. (2012). Synaptic tagging and capture in the living rat. Nat. Commun. *3*, 1246.

Shirvalkar, P.R., Rapp, P.R., and Shapiro, M.L. (2010). Bidirectional changes to hippocampal theta-gamma comodulation predict memory for recent spatial episodes. Proc. Natl. Acad. Sci. U. S. A. *107*, 7054–7059.

Shumkova, V., Sitdikova, V., Rechapov, I., Leukhin, A., and Minlebaev, M. (2021). Effects of urethane and isoflurane on the sensory evoked response and local blood flow in the early postnatal rat somatosensory cortex. Sci. Rep. *11*, 9567.

Siciliano, C.A., and Tye, K.M. (2019). Leveraging calcium imaging to illuminate circuit dysfunction in addiction. Alcohol *74*, 47–63.

Silva, B.A., and Gräff, J. (2023). Face your fears : attenuating remote fear memories by reconsolidation-updating. Trends Cogn. Sci. *27*, 404–416.

Skinner, B.F. (1938). The behavior of organisms: an experimental analysis. (Oxford, England: Appleton-Century).

Sloviter, R.S. (1991). Feedforward and feedback inhibition of hippocampal principal cell activity evoked by perforant path stimulation: GABA-mediated mechanisms that regulate excitability in vivo. Hippocampus *1*, 31–40.

Sloviter, R.S. (1994). The functional organization of the hippocampal dentate gyrus and its relevance to the pathogenesis of temporal lobe epilepsy. Ann. Neurol. *35*, 640–654.

Sloviter, R.S., and Brisman, J.L. (1995). Lateral inhibition and granule cell synchrony in the rat hippocampal dentate gyrus. J. Neurosci. Off. J. Soc. Neurosci. *15*, 811–820.

Sohal, V.S., Zhang, F., Yizhar, O., and Deisseroth, K. (2009). Parvalbumin neurons and gamma rhythms enhance cortical circuit performance. Nature *459*, 698–702.

Squire, L.R., and Alvarez, P. (1995). Retrograde amnesia and memory consolidation: a neurobiological perspective. Curr. Opin. Neurobiol. *5*, 169–177.

Squire, L.R., and Zola-Morgan, S. (1991). The medial temporal lobe memory system. Science *253*, 1380–1386.

Squire, L.R., Genzel, L., Wixted, J.T., and Morris, R.G. (2015). Memory consolidation. Cold Spring Harb. Perspect. Biol. *7*, a021766.

St-Pierre, F., Marshall, J.D., Yang, Y., Gong, Y., Schnitzer, M.J., and Lin, M.Z. (2014). High-fidelity optical reporting of neuronal electrical activity with an ultrafast fluorescent voltage sensor. Nat. Neurosci. *17*, 884–889.

Stefanelli, T., Bertollini, C., Lüscher, C., Muller, D., and Mendez, P. (2016). Hippocampal Somatostatin Interneurons Control the Size of Neuronal Memory Ensembles. Neuron *89*, 1074–1085.

Steward, O., and Scoville, S.A. (1976). Cells of origin of entorhinal cortical afferents to the hippocampus and fascia dentata of the rat. J. Comp. Neurol. *169*, 347–370.

Strange, B.A., Witter, M.P., Lein, E.S., and Moser, E.I. (2014). Functional organization of the hippocampal longitudinal axis. Nat. Rev. Neurosci. *15*, 655–669.

van Strien, N.M., Cappaert, N.L.M., and Witter, M.P. (2009). The anatomy of memory: an interactive overview of the parahippocampal-hippocampal network. Nat. Rev. Neurosci. *10*, 272–282.

Sturman, O., von Ziegler, L., Schläppi, C., Akyol, F., Privitera, M., Slominski, D., Grimm, C., Thieren, L., Zerbi, V., Grewe, B., et al. (2020). Deep learning-based behavioral analysis reaches human accuracy and is capable of outperforming commercial solutions. Neuropsychopharmacology *45*, 1942–1952.

Sugar, J., and Moser, M.-B. (2019). Episodic memory: Neuronal codes for what, where, and when. Hippocampus *29*, 1190–1205.

Sun, D., Mei, L., and Xiong, W.-C. (2023). Dorsal Dentate Gyrus, a Key Regulator for Mood and Psychiatric Disorders. Biol. Psychiatry *93*, 1071–1080.

Swanson, L.W., and Hartman, B.K. (1975). The central adrenergic system. An

immunofluorescence study of the location of cell bodies and their efferent connections in the rat utilizing dopamine-beta-hydroxylase as a marker. J. Comp. Neurol. *163*, 467–505.

Takehara-Nishiuchi, K. (2020). Prefrontal-hippocampal interaction during the encoding of new memories. Brain Neurosci. Adv. *4*, 2398212820925580.

Takeuchi, T., Duszkiewicz, A.J., and Morris, R.G.M. (2014). The synaptic plasticity and memory hypothesis: encoding, storage and persistence. Philos. Trans. R. Soc. Lond. B. Biol. Sci. *369*, 20130288.

Tanaka, K.Z., He, H., Tomar, A., Niisato, K., Huang, A.J.Y., and McHugh, T.J. (2018). The hippocampal engram maps experience but not place. Science *361*, 392–397.

Tello-Ramos, M.C., Branch, C.L., Kozlovsky, D.Y., Pitera, A.M., and Pravosudov, V. V. (2019). Spatial memory and cognitive flexibility trade-offs: to be or not to be flexible, that is the question. Anim. Behav. *147*, 129–136.

Teyler, T.J., and Rudy, J.W. (2007). The Hippocampal Indexing Theory and Episodic Memory: Updating the Index. Hippocampus *1031*.

Thakral, P.P., Yu, S.S., and Rugg, M.D. (2015). The hippocampus is sensitive to the mismatch in novelty between items and their contexts. Brain Res. *1602*, 144–152.

Tian, L., Hires, S.A., Mao, T., Huber, D., Chiappe, M.E., Chalasani, S.H., Petreanu, L., Akerboom, J., McKinney, S.A., Schreiter, E.R., et al. (2009). Imaging neural activity in worms, flies and mice with improved GCaMP calcium indicators. Nat. Methods *6*, 875–881.

Tolman, E.C. (1948). Cognitive maps in rats and men. Psychol. Rev. *55*, 189–208.

Tonegawa, S., Liu, X., Ramirez, S., and Redondo, R. (2015a). Memory Engram Cells Have Come of Age. Neuron *87*, 918–931.

Tonegawa, S., Pignatelli, M., Roy, D.S., and Ryan, T.J. (2015b). Memory engram storage and retrieval. Curr. Opin. Neurobiol. *35*, 101–109.

Tonegawa, S., Morrissey, M.D., and Kitamura, T. (2018). The role of engram cells in the systems consolidation of memory. Nat. Rev. Neurosci. *19*, 485–498.

Topolnik, L., and Tamboli, S. (2022). The role of inhibitory circuits in hippocampal memory processing. Nat. Rev. Neurosci. *23*, 476–492.

Tort-Colet, N., Resta, F., Montagni, E., Pavone, F., Allegra Mascaro, A.L., and Destexhe, A. (2023). Assessing brain state and anesthesia level with two-photon calcium signals. Sci. Rep. *13*, 3183.

Tort, A.B.L., Kramer, M.A., Thorn, C., Gibson, D.J., Kubota, Y., Graybiel, A.M., and Kopell, N.J. (2008). Dynamic cross-frequency couplings of local field potential oscillations in rat striatum and hippocampus during performance of a T-maze task. Proc. Natl. Acad. Sci. U. S. A. *105*, 20517–20522.

Tort, A.B.L., Komorowski, R.W., Manns, J.R., Kopell, N.J., and Eichenbaum, H. (2009). Theta-gamma coupling increases during the learning of item-context associations. Proc. Natl. Acad. Sci. U. S. A. *106*, 20942–20947.

Treves, A., and Rolls, E.T. (1992). Computational Constraints Suggest the Need for Two. Hippocampus *2*, 189–200.

Treves, A., and Rolls, E.T. (1994). Computational analysis of the role of the hippocampus in memory. Hippocampus *4*, 374–391.

Tulving, E. (1972). Episodic and semantic memory. In Organization of Memory., (Oxford,

England: Academic Press), pp. xiii, 423–xiii, 423.

Twarkowski, H., Steininger, V., Kim, M.J., and Sahay, A. (2022). A dentate gyrus-CA3 inhibitory circuit promotes evolution of hippocampal-cortical ensembles during memory consolidation. Elife *11*.

Tzakis, N., and Holahan, M.R. (2019). Social Memory and the Role of the Hippocampal CA2 Region. Front. Behav. Neurosci. *13*, 233.

Tzilivaki, A., Kastellakis, G., Schmitz, D., and Poirazi, P. (2022). GABAergic Interneurons with Nonlinear Dendrites: From Neuronal Computations to Memory Engrams. Neuroscience *489*, 34–43.

Tzilivaki, A., Tukker, J.J., Maier, N., Poirazi, P., Sammons, R.P., and Schmitz, D. (2023). Hippocampal GABAergic interneurons and memory. Neuron 1–22.

Umbach, G., Tan, R., Jacobs, J., Pfeiffer, B.E., and Lega, B. (2022). Flexibility of functional neuronal assemblies supports human memory. Nat. Commun. *13*, 6162.

Umschweif, G., Medrihan, L., Guillén-Samander, A., Wang, W., Sagi, Y., and Greengard, P. (2021). Identification of Neurensin-2 as a novel modulator of emotional behavior. Mol. Psychiatry *26*, 2872–2885.

Vago, D.R., and Kesner, R.P. (2008). Disruption of the direct perforant path input to the CA1 subregion of the dorsal hippocampus interferes with spatial working memory and novelty detection. Behav. Brain Res. *189*, 273–283.

Vivekananda, U., Bush, D., Bisby, J.A., Baxendale, S., Rodionov, R., Diehl, B., Chowdhury, F.A., McEvoy, A.W., Miserocchi, A., Walker, M.C., et al. (2021). Theta power and theta-gamma coupling support long-term spatial memory retrieval. Hippocampus *31*, 213–220.

Vogel-Ciernia, A., and Wood, M.A. (2014). Examining object location and object recognition memory in mice. Curr. Protoc. Neurosci. *2014*, 8.31.1-8.31.17.

Voneida, T.J., Vardaris, R.M., Fish, S.E., and Reiheld, C.T. (1981). The origin of the hippocampal commissure in the rat. Anat. Rec. *201*, 91–103.

Waldbaum, S., and Dudek, F.E. (2009). Single and repetitive paired-pulse suppression: a parametric analysis and assessment of usefulness in epilepsy research. Epilepsia *50*, 904–916.

Wang, S.-H., and Morris, R.G.M. (2010). Hippocampal-Neocortical Interactions in memory Formation, Consolidation and Reconsolidation. Annu. Rev. Psychol.

Watanabe, S., and Yanagisawa, N. (2000). Serial position effect and selective amnesia induced by scopolamine in mice. Nihon Shinkei Seishin Yakurigaku Zasshi *20*, 17–20.

Whittington, M.A., Traub, R.D., Kopell, N., Ermentrout, B., and Buhl, E.H. (2000). Inhibition-based rhythms: experimental and mathematical observations on network dynamics. Int. J. Psychophysiol. Off. J. Int. Organ. Psychophysiol. *38*, 315–336.

Wilson, H.R., and Cowan, J.D. (1972). Excitatory and inhibitory interactions in localized populations of model neurons. Biophys. J. *12*, 1–24.

Wilson, M.A., and McNaughton, B.L. (1993). Dynamics of the hippocampal ensemble code for space. Science *261*, 1055–1058.

Wiltgen, B.J., Zhou, M., Cai, Y., Balaji, J., Karlsson, M.G., Parivash, S.N., Li, W., and Silva, A.J. (2010). The hippocampus plays a selective role in the retrieval of detailed contextual memories. Curr. Biol. *20*, 1336–1344.

Witter, M.P. (2007). Intrinsic and extrinsic wiring of CA3: indications for connectional

heterogeneity. Learn. Mem. *14*, 705–713.

Woodson, W., Nitecka, L., and Ben-Ari, Y. (1989). Organization of the GABAergic system in the rat hippocampal formation: a quantitative immunocytochemical study. J. Comp. Neurol. *280*, 254–271.

Wyss, J.M., Swanson, L.W., and Cowan, W.M. (1980). The organization of the fimbria, dorsal fornix and ventral hippocampal commissure in the rat. Anat. Embryol. (Berl). *158*, 303–316.

Xia, F., Richards, B.A., Tran, M.M., Josselyn, S.A., Takehara-Nishiuchi, K., and Frankland, P.W. (2017). Parvalbumin-positive interneurons mediate neocortical-hippocampal interactions that are necessary for memory consolidation. Elife *6*.

Yagishita, H., Nishimura, Y., Noguchi, A., Shikano, Y., Ikegaya, Y., and Sasaki, T. (2020). Urethane anesthesia suppresses hippocampal subthreshold activity and neuronal synchronization. Brain Res. *1749*, 147137.

Yassa, M.A., and Stark, C.E.L. (2011). Pattern separation in the hippocampus. Trends Neurosci. *34*, 515–525.

Yonelinas, A.P., Ranganath, C., Ekstrom, A.D., and Wiltgen, B.J. (2019). A contextual binding theory of episodic memory: Systems consolidation reconsidered. Nat Rev Neurosci.

Young, J.Z. (1964). A model of the brain (Oxford: Oxford University Press).

Yu, K., Ahrens, S., Zhang, X., Schiff, H., Ramakrishnan, C., Fenno, L., Deisseroth, K., Zhao, F., Luo, M.-H., Gong, L., et al. (2017). The central amygdala controls learning in the lateral amygdala. Nat. Neurosci. *20*, 1680–1685.

Yun, S., Soler, I., Tran, F.H., Haas, H.A., Shi, R., Bancroft, G.L., Suarez, M., de Santis, C.R., Reynolds, R.P., and Eisch, A.J. (2023). Behavioral pattern separation and cognitive flexibility are enhanced in a mouse model of increased lateral entorhinal cortex-dentate gyrus circuit activity. Front. Behav. Neurosci. *17*.

Zhang, K., Pan, J., and Yu, Y. (2022). Regulation of Neural Circuitry under General Anesthesia: New Methods and Findings. Biomolecules *12*.

Zhang, X., Zhong, W., Brankačk, J., Weyer, S.W., Müller, U.C., Tort, A.B.L., and Draguhn, A. (2016). Impaired theta-gamma coupling in APP-deficient mice. Sci. Rep. *6*, 21948.

Zhang, Y., Rózsa, M., Liang, Y., Bushey, D., Wei, Z., Zheng, J., Reep, D., Broussard, G.J., Tsang, A., Tsegaye, G., et al. (2023). Fast and sensitive GCaMP calcium indicators for imaging neural populations. Nature *615*, 884–891.

Zhou, W., and Crystal, J.D. (2009). Evidence for remembering when events occurred in a rodent model of episodic memory. Proc. Natl. Acad. Sci. U. S. A. *106*, 9525–9529.

Zhou, H., Zhu, J., Jia, J., Xiang, W., Peng, H., Zhang, Y., Liu, B., Mu, Y., and Lu, Y. (2022). The antidepressant effect of nucleus accumbens deep brain stimulation is mediated by parvalbumin-positive interneurons in the dorsal dentate gyrus. Neurobiol. Stress *21*, 100492.

Ziv, Y., and Ghosh, K.K. (2015). Miniature microscopes for large-scale imaging of neuronal activity in freely behaving rodents. Curr. Opin. Neurobiol. *32*, 141–147.

Zou, D., Chen, L., Deng, D., Jiang, D., Dong, F., McSweeney, C., Zhou, Y., Liu, L., Chen, G., Wu, Y., et al. (2016). DREADD in parvalbumin interneurons of the dentate gyrus modulates anxiety, social interaction and memory extinction. Curr. Mol. Med. *16*, 91–102.

Zucker, R.S. (1999). Calcium- and activity-dependent synaptic plasticity. Curr. Opin. Neurobiol. *9*, 305–313.